

UNIVERSITY OF OKLAHOMA  
GRADUATE COLLEGE

MECHANICAL DEGRADATION OF WELL CEMENT IN HPHT CARBONIC ACID  
ENVIRONMENT: EXPERIMENTAL STUDIES AND MATHEMATICAL  
MODELING

A DISSERTATION  
SUBMITTED TO THE GRADUATE FACULTY  
in partial fulfillment of the requirements for the  
Degree of  
DOCTOR OF PHILOSOPHY

By  
OMOTAYO ADEDIRAN OMOSEBI  
Norman, Oklahoma  
2016

MECHANICAL DEGRADATION OF WELL CEMENT IN HPHT CARBONIC ACID  
ENVIRONMENT: EXPERIMENTAL STUDIES AND MATHEMATICAL  
MODELING

A DISSERTATION APPROVED FOR THE  
MEWBOURNE SCHOOL OF PETROLEUM AND GEOLOGICAL ENGINEERING

BY

---

Dr. Ramadan Ahmed, Chair

---

Dr. John Pigott

---

Dr. Subhash Shah

---

Dr. Ahmad Ghassemi

---

Dr. Maysam Pournik

© Copyright by OMOTAYO ADEDIRAN OMOSEBI 2016  
All Rights Reserved.

## DEDICATION

To God Almighty I dedicate this work; for He is the source of all wisdom, knowledge, and understanding. Thine, O LORD, is the greatness, and the power, and the glory, and the victory, and the majesty: for all that is in the heaven and in the earth is thine; thine is the kingdom, O LORD, and thou art exalted as head above all. 1 Chronicles 29:11 (KJV).

## **Acknowledgements**

I am very grateful for the mentorship and support I received from my advisor, Professor Ramadan Ahmed, throughout my doctoral study. His guidance and suggestions contribute immensely towards the successful completion of my study at The University of Oklahoma. I am also indebted to Professor Samuel Osisanya who, until his retirement, was my academic advisor. His conviction in my ability to succeed is unflinching, he is always accessible to me even after he has hung up his boots. God bless and reward you bountifully Sir. My appreciation are also due to Professor Subhash Shah, someone I admire. His humility, attention to details, appreciation for excellence and respect for all are values I have internalized while I was under his mentorship and tutelage. Successful completion of this study is not without the invaluable contributions from Professor John Pigott, Professor Ahmad Ghassemi, and Dr. Maysam Pournik, who out of their very busy schedules, volunteered to serve as members of my doctoral research committee.

This research is funded by the Bureau of Safety and Environmental Enforcement (BSEE) under the award contract number E12PC00035. I am very grateful to the organization for the opportunity to conduct this research and for their devotion toward ensuring that the search and recovery of hydrocarbon resources is carried out in the safest manner. In addition, I appreciate the technical contributions from industry advisory board members. My special thanks to Halliburton Energy Services, Mountain Cement Company, Lone Star Portland Cement, Fritz Industries and Schlumberger Limited for donating the materials for this research.

This research could not have been completed without the support of professional organizations, such as the Society of Petroleum Engineers (SPE), Society of

Exploration Geophysicists (SEG), and Artificial Lift Research and Development Council (ALRDC), who awarded me various scholarships to support my graduate studies. I am very grateful to the generosity of these organizations.

I am thankful to the Faculty and Staff of Mewbourne School of Petroleum and Geological Engineering (MPGE). The instruction I received from members of MPGE Faculty helped in conducting this study. Shalli Carnahan Young (Retired) was my school Mum, always looking out for my wellbeing and that of my family. Thank you Shalli, God bless you tremendously! I like to say thank you to Dr. Shokrollah Hassani, who was the Post-Doctoral Research Associate during the early stages of this research. His leadership laid the needed ground works to complete this study. I also acknowledge my fellow student researchers at the Well Construction Technology Center (WCTC), who contributed in one form or the other to this research. Many thanks to Jeffery McCaskill and Joe Flenniken for assisting to setup the equipment used in this research.

Lastly, I am thankful to my support system; my family and friends. To the wife of my youth, I say thank you for being a reliable companion and my greatest fan. To our prince charming and jewel of inestimable worth, daddy says thank you for bearing with him; we earned this milestone together. To my Dad (In Memorial), Mum, Father-In-Law, Mother-In-Law, Sister (and family), Sisters-In-Law, Brothers (and family), and Brothers-In-Law, I am grateful; I hope I made you all proud. To Jide Okunrinboye, a great friend and a brother, thanks for being a golden ally. To the Akumaga family, the Fakoya family, the Omojuwa family, Babatunde Babayemi, Israel Oluwatosin, and members and Pastorate of the RCCG Norman, I thank you. Many thanks to Daddy and Mummy Olaniyan for always checking to ensure that all is well with me and my family.

## Table of Contents

Acknowledgements .....	iv
List of Tables .....	xiii
List of Figures.....	xv
Abstract.....	xxiii
Chapter 1 Introduction.....	1
1.1 Overview of Cement Degradation .....	1
1.2 Statement of Problem.....	6
1.3 Research Objectives.....	8
1.4 Research Methodology .....	8
1.5 Scope of Study .....	9
Chapter 2 Background Study.....	11
2.1 Overview.....	11
2.2 Cement Chemistry .....	11
2.2.1 Hydration of Clinker Compounds .....	11
2.2.2 Reaction between Cement and Carbonic Acid.....	16
2.3 Experimental Studies .....	18
2.3.1 Experimental Studies in the Absence of CO <sub>2</sub> .....	18
2.3.2 Experimental Studies in the Presence of CO <sub>2</sub> .....	27
2.3.3 Summary.....	38
2.4 Theoretical Modeling Studies .....	41
2.4.1 Modeling Studies without CO <sub>2</sub> Effect.....	41
2.4.2 Modeling Studies with CO <sub>2</sub> Effect.....	45

2.4.3	Summary.....	48
Chapter 3 Mechanisms of Cement Degradation in HPHT Carbonic Acid Environment		49
3.1	Overview.....	49
3.2	Hydration and Chemical Shrinkage.....	50
3.3	Structural Transformation of Amorphous CSH.....	52
3.4	Matrix Expansion and Thermally-Induced Pressurization .....	56
3.5	Dissolution of CH and Decalcification of CSH.....	57
3.6	Carbonation.....	59
3.7	Bi-Carbonation and Leaching.....	60
3.8	Interactions between Mechanisms and Propagation of Reaction Fronts .....	62
3.9	Effects of Downhole Parameters on the Mechanisms of Cement Degradation	64
3.9.1	Effect of Temperature.....	65
3.9.2	Effect of Pressure .....	66
3.9.3	Effect of CO <sub>2</sub> Gas Composition .....	67
3.9.4	Effect of NaCl Concentration.....	69
3.10	Summary.....	69
Chapter 4 Experimental Studies .....		71
4.1	Materials .....	71
4.1.1	Slurry Materials .....	71
4.1.2	Slurry Formulation and Preparation .....	71
4.1.3	Slurry Properties.....	72
4.2	Methods .....	74
4.2.1	Curing Procedure and Specimen Preparation.....	74



4.2.2	CO <sub>2</sub> Exposure Tests under HPHT Conditions.....	75
4.2.2.1	Test Setup .....	75
4.2.2.2	Test Procedure .....	75
4.2.2.3	Test Matrix.....	76
4.2.3	Chemical Analysis of Fluid Samples .....	78
4.2.3.1	Measurement of Fluid pH.....	78
4.2.3.2	Measurement of Fluid Calcium Content.....	79
4.2.4	Triaxial Compression Test .....	80
4.2.4.1	Test Setup .....	80
4.2.4.2	Test Procedure .....	81
4.2.5	Transport Properties and Mineralogy.....	83
4.3	Results and Discussion .....	84
4.3.1	Characterization of Mineralogy, Morphology and Microstructure .....	85
4.3.1.1	SEM Images and EDX Elemental Composition.....	85
4.3.1.2	Fourier Transform Infra-Red (FTIR) Analysis.....	89
4.3.1.3	X-Ray Diffraction (XRD) Analysis .....	92
4.3.1.3.1	Unaged Specimen.....	92
4.3.1.3.2	Specimen Aged at 225°F, 6000 psi and 100% CO <sub>2</sub> .....	95
4.3.1.3.3	Specimen Aged at 350°F, 3000 psi and 40% CO <sub>2</sub> .....	100
4.3.2	Bulk Fluid Chemistry .....	104
4.3.3	Effect of Temperature on Cement Integrity .....	106
4.3.3.1	Effect of Temperature at 100% CO <sub>2</sub> .....	106
4.3.3.1.1	FTIR Mineralogy .....	107

4.3.3.1.2	Mechanical Degradation .....	108
4.3.3.1.3	Visual Degradation.....	111
4.3.3.2	Effect of Temperature at 6000 psi .....	113
4.3.3.2.1	FTIR Mineralogy .....	113
4.3.3.2.2	Mechanical Degradation .....	115
4.3.3.2.3	Visual Degradation.....	117
4.3.3.3	Summary.....	119
4.3.4	Effect of CO <sub>2</sub> Gas Composition on Cement Integrity .....	119
4.3.4.1	Effect of CO <sub>2</sub> Gas Composition at 100°F.....	119
4.3.4.1.1	FTIR Mineralogy .....	119
4.3.4.1.2	Mechanical Degradation .....	120
4.3.4.1.3	Visual Degradation.....	123
4.3.4.2	Effect of CO <sub>2</sub> Gas Composition at 225°F.....	124
4.3.4.2.1	FTIR Mineralogy .....	124
4.3.4.2.2	Mechanical Degradation .....	126
4.3.4.2.3	Visual Degradation.....	130
4.3.4.3	.....	132
4.3.4.4	Effect of CO <sub>2</sub> Gas Composition at 350°F.....	132
4.3.4.4.1	FTIR Mineralogy .....	132
4.3.4.4.2	Mechanical Degradation .....	133
4.3.4.4.3	Visual Degradation.....	136
4.3.4.5	Effect of CO <sub>2</sub> Gas Composition at 430°F.....	138
4.3.4.5.1	FTIR Mineralogy .....	138

4.3.4.5.2	Mechanical Degradation .....	139
4.3.4.5.3	Visual Degradation.....	140
4.3.4.6	Summary.....	141
4.3.5	Effect of Pressure on Cement Integrity .....	141
4.3.5.1	Effect of Pressure at 225°F .....	141
4.3.5.1.1	FTIR Mineralogy .....	141
4.3.5.1.2	Mechanical Degradation .....	142
4.3.5.1.3	Visual Degradation.....	143
4.3.5.2	Effect of Pressure at 350°F .....	144
4.3.5.2.1	FTIR Mineralogy .....	144
4.3.5.2.2	Mechanical Degradation .....	144
4.3.5.2.3	Visual Degradation.....	148
4.3.5.3	Effect of Pressure at 430°F .....	148
4.3.5.3.1	FTIR Mineralogy .....	148
4.3.5.3.2	Mechanical Degradation .....	149
4.3.5.3.3	Visual Degradation.....	149
4.3.5.4	Summary.....	150
4.3.6	Effect of Exposure Time on Cement Integrity .....	150
4.3.6.1	Mechanical Degradation.....	150
4.3.6.2	Visual Degradation .....	151
4.3.7	Summary of Experimental Studies.....	152
Chapter 5	Mathematical Modeling and Simulation.....	153
5.1	Overview.....	153

5.2	Model Assumptions .....	153
5.3	Physics of the Problem and Model Formulation .....	153
5.3.1	Mixing and Curing .....	154
5.3.2	Exposure to CO <sub>2</sub> -Saturated Brine in an HPHT Autoclave .....	156
5.3.3	Mechanical Compression Test .....	159
5.4	Cement Degradation Modeling.....	161
5.4.1	Modeling Cement Mixing and Curing .....	161
5.4.1.1	Modeling the Degree of Hydration and Chemical Shrinkage.....	161
5.4.1.2	Modeling Reaction Stoichiometry .....	162
5.4.1.3	Modeling Transport Properties .....	170
5.4.1.4	Modeling Stable Mineral Assemblage in Ca(OH) <sub>2</sub> -SiO <sub>2</sub> -CO <sub>2</sub> -NaCl-H <sub>2</sub> O System .....	171
5.4.2	Modeling Cement Exposure to CO <sub>2</sub> -Saturated Brine in an HPHT Autoclave .....	177
5.4.2.1	Modeling Gas-Liquid Phase Equilibria in CO <sub>2</sub> -H <sub>2</sub> O <sup>v</sup> -CH <sub>4</sub> System ....	177
5.4.2.2	Modeling Bulk Fluid Equilibria in CO <sub>2</sub> -NaCl-H <sub>2</sub> O System.....	179
5.4.2.3	Modeling Reactive Transport of Aqueous Species.....	180
5.4.3	Modeling Mechanical Compression Test.....	182
5.4.3.1	Compressive Strength Model before CO <sub>2</sub> Exposure Test .....	182
5.4.3.2	Compressive Strength Models after CO <sub>2</sub> Exposure Test.....	183
5.4.3.2.1	Model 1 .....	183
5.4.3.2.2	Model 2 .....	187
5.5	Model Results and Validation.....	188

5.5.1	Degree of Hydration and Chemical Shrinkage.....	188
5.5.2	Composition of Cement after Hydration .....	190
5.5.3	Transport and Mechanical Properties before CO <sub>2</sub> Exposure.....	193
5.5.4	Stable Mineral Assemblage and Pore Chemistry after Curing.....	194
5.5.5	Gas Fugacity and Solubility .....	197
5.5.6	Molality of Bulk Fluid Aqueous Species .....	199
5.5.7	Mineral Assemblage and Pore Chemistry after CO <sub>2</sub> Exposure.....	200
5.5.8	Mechanical Strength after CO <sub>2</sub> Exposure.....	204
Chapter 6 Conclusions and Recommendations .....		206
6.1	Conclusions.....	206
6.2	Recommendations.....	208
Nomenclature .....		209
References .....		212
Appendix – Compressive Strength Model .....		228

## List of Tables

Table 2.1 API cement classification (Bourgoyne et al. 1986).....	12
Table 2.2 Fineness and water-to-cement ratio of Classes G and H cement (Hewlett 2004).....	13
Table 2.3 Summary of experimental studies on oil well cement degradation.....	39
Table 2.4 Operational conditions of CCUS projects .....	40
Table 3.1 Mole numbers of lime, silica, and water in some crystalline C-S-H phases ..	53
Table 3.2 Effect of 35% BWOC silica flour on C/S ratio in C-S-H .....	54
Table 4.1 Manufacturer, density and clinker composition of Classes G and H cement.	71
Table 4.2 Compositions of cement, water and additives.....	72
Table 4.3. Slurry properties (Omosebi et al., 2015) .....	73
Table 4.4 Test matrix for aging experiment .....	77
Table 4.5 Correction factor for compressive strength measurements. ....	82
Table 4.6 Comparison between XRD data of unaged specimen and specimen aged at 225°F, 6000 psi and 100% CO <sub>2</sub> (Omosebi et al., 2015).....	98
Table 4.7 Comparison between XRD data of unaged specimen and specimen aged at 350°F, 3000 psi and 40% CO <sub>2</sub> (Omosebi et al., 2015).....	103
Table 5.1 Constants in permeability-porosity correlation .....	171
Table 5.2 Initial components in Ca(OH) <sub>2</sub> -SiO <sub>2</sub> -CO <sub>2</sub> -NaCl-H <sub>2</sub> O chemical system.....	174
Table 5.3 Constants in Antoine equation .....	179
Table 5.4 Components in CO <sub>2</sub> -NaCl-H <sub>2</sub> O chemical system .....	180
Table 5.5 Quantity of hydrates after hydration of cement.....	191
Table 5.6 Composition of chemical compounds after curing.....	192

Table 5.7 Concentration of species in the pore water of cement and the amount of minerals .....	196
Table 5.8 Effect of temperature and the presence of silica in the pH of pore water ....	197
Table 5.9 Model prediction for the fugacity of water vapor, CO <sub>2</sub> gas, and CH <sub>4</sub> gas ...	197
Table 5.10 Concentration of aqueous species in the bulk fluid.....	200

## List of Figures

Figure 1.1 (a) Challenges confronting operators of HPHT resources; (b) Knowledge gaps in the development of HPHT resources.....	2
Figure 1.2 Carbon Capture, Utilization and Storage (CCUS) Cycle.....	4
Figure 1.3 Potential leakage pathways through casing-cement-rock system.....	5
Figure 1.4 Workflow for analysis of cement integrity after exposure to CO <sub>2</sub> – brine fluid under HPHT conditions.....	10
Figure 2.1 Strength development at different compositions of C <sub>3</sub> S (Horkoss and Lteif, 2011).....	19
Figure 2.2 Effect of salt concentration on compressive strength (Nelson, 1990) .....	22
Figure 2.3 Experimental solid phase calcium profile of pure cement sample (Haga et al., 2005).....	27
Figure 2.4 Penetration depth versus time after exposure of cement to CO <sub>2</sub> -containing fluid (Kutchko et al., 2008).....	30
Figure 2.5 Optical images of Class H cement exposed to CO <sub>2</sub> fluids (Kutchko et al. 2011) .....	32
Figure 3.1 Individual degrees of hydration of clinker compounds generated using Lothenbach et al. (2008) and Parrot and Killoh (1989) model.....	51
Figure 3.2 Effect of shrinkage on cement seal .....	52
Figure 3.3 Charts for the transformation of amorphous CSH to crystalline phases (Omosebi et al., 2015; Adopted from Taylor, 1964 and 1997) .....	54
Figure 3.4 Effect of leaching and decalcification on cement exposed to deionized water .....	58



Figure 3.5 Interaction between cement degradation mechanisms .....	63
Figure 3.6 Reaction fronts due to CO <sub>2</sub> attack on well cement .....	64
Figure 3.7 Carbon dioxide pressure-temperature phase diagram .....	65
Figure 3.8 Temperature effect on CO <sub>2</sub> solubility in 1m NaCl solution at different pressures (Data source: Duan and Sun, 2003).....	66
Figure 3.9 Pressure effect on CO <sub>2</sub> solubility in 1m NaCl solution at different temperatures (Data source: Duan and Sun, 2003).....	67
Figure 3.10 Effect of CO <sub>2</sub> gas composition on: (a) concentration of species; (b) pH of solution .....	68
Figure 3.11 Effect of NaCl concentration on CO <sub>2</sub> solubility at: (a) different pressures; (b) different temperatures (Data source: Duan and Sun, 2003) .....	69
Figure 4.1. (a) Consist-o-meter reading; (b) Rheological reading (Omosebi et al., 2015; GS and HS refer to Class G and Class H with 35% silica respectively) .....	73
Figure 4.2 Specimen aging system comprising HPHT autoclave and gas injection and storage system: (a) schematic (Omosebi et al., 2015); (b) photo .....	76
Figure 4.3 Phase condition of CO <sub>2</sub> under the test conditions in Table 4.4.....	78
Figure 4.4 Typical color of fluid samples: (a) before and; (b) after end-point of titration .....	79
Figure 4.5 Compressive strength testing apparatus (a) schematic; (b) photo (Omosebi et al., 2015).....	81
Figure 4.6 (a) stresses exerted on specimen during compression tests; (b) typical stress-strain plot .....	83

Figure 4.7 (a) Specimens before compression test; (b) Specimens after compression test .....	83
Figure 4.8 SEM images showing penetrated and unpenetrated zones in (a) Class G; (b) Class H cements (Omosebi et al., 2015).....	87
Figure 4.9 (a) SEM images showing formation of hydrate in the unpenetrated zone of Class H cement; (b) composition of elements obtained from EDX spot analysis of (a); (c) SEM image showing formation of calcium carbonate in penetrated zone of Class H cement at 3000 psi; (d) SEM image showing formation of calcium carbonate at 9000 psi; (e) composition of elements obtained from EDX spot analysis of (d).....	88
Figure 4.10 (a) SEM image showing formation of calcium silicate carbonate in penetrated zone at 3000 psi; (b) composition of elements obtained from EDX analysis .....	89
Figure 4.11 Three selected zones in degraded specimens used for FTIR analysis: inner (red), middle (blue) and outer (yellow) zones (show only top and cut sections) .....	89
Figure 4.12 Comparison of FTIR spectra of unaged and aged specimens of Class H cement.....	90
Figure 4.13 XRD data for unaged Class H specimen cured for 5 days at 200°F (a) XRD spectra; (b) contribution of minerals in wt. % (Omosebi et al., 2015).....	94
Figure 4.14 XRD spectra of the degraded zones of Class H specimen aged for 14 days in 2% NaCl solution at 225°F, 6000 psi, 100% CO <sub>2</sub> : (a) inner zone; (b) middle zone; (c) outer zone (Omosebi et al., 2015) .....	98
Figure 4.15 Contribution of chemical phases in Class H cement aged for 14 days at 225°F, 6000 psi, 100% CO <sub>2</sub> in 2% NaCl solution (Omosebi et al., 2015).....	99

Figure 4.16 XRD spectra of the degraded zones of Class H specimen aged for 14 days in 2% NaCl solution at 350°F, 3000 psi, 40% CO <sub>2</sub> : (a) inner zone; (b) middle zone; (c) outer zone (Omosebi et al., 2015).....	102
Figure 4.17 Contribution of chemical phases in Class H cement aged for 14 days at 350°F, 3000 psi, 40% CO <sub>2</sub> in 2% NaCl solution (Omosebi et al., 2015).....	103
Figure 4.18 (a) Effect of CO <sub>2</sub> partial pressure on bulk fluid calcium concentration; (b) Effect of CO <sub>2</sub> partial pressure on bulk fluid pH.....	104
Figure 4.19 Effect of temperature at 100% CO <sub>2</sub> gas composition on the normalized absorbance peaks extracted from FTIR spectra of degraded zones of Class H cement: (a) 3000 psi; (b) 6000 psi; and (c) 9000 psi (Omosebi et al., 2015) .....	107
Figure 4.20 Effects of temperature at 100% CO <sub>2</sub> gas composition and different test pressures on the compressive strength, porosity, and permeability of: (a) Class G; (b) Class H (Omosebi et al., 2015).....	111
Figure 4.21 Visual degradation of Class G cement due to variation in temperature at 100% CO <sub>2</sub> gas composition and: (a) 3000 psi; (b) 6000 psi; (c) 9000 psi (Omosebi et al., 2015) .....	112
Figure 4.22 Visual degradation of Class H cement due to variation in temperature at 100% CO <sub>2</sub> gas composition and: (a) 3000 psi; (b) 6000 psi; (c) 9000 psi .....	112
Figure 4.23 Effect of temperature at 6000 psi on the normalized absorbance peaks extracted from FTIR spectra of degraded zones of Class H cement: (a) 10% CO <sub>2</sub> ; (b) 40% CO <sub>2</sub> ; and (c) 100% CO <sub>2</sub> (Omosebi et al., 2015).....	114

Figure 4.24 Effects of temperature at 6000 and different CO <sub>2</sub> gas compositions on the compressive strength, porosity, and permeability of: (a) Class G; (b) Class H (Omosebi et al., 2015).....	117
Figure 4.25 Visual degradation of Class G cement due to variation in temperature at 6000 psi and CO <sub>2</sub> gas composition of: (a) 10%; (b) 40%; (c) 100% (Omosebi et al., 2015)	118
Figure 4.26 Visual degradation of Class H cement due to variation in temperature at 6000 psi and CO <sub>2</sub> gas composition of: (a) 10%; (b) 40%; (c) 100% .....	119
Figure 4.27 Effect of CO <sub>2</sub> gas composition at 100°F on the normalized absorbance peaks extracted from FTIR spectra of degraded zones of Class H cement (Omosebi et al., 2015b) .....	120
Figure 4.28 Effect of CO <sub>2</sub> gas composition at 100°F and 6000 psi on the compressive strength, porosity, and permeability of Classes G and H cement (Omosebi et al., 2015) .....	121
Figure 4.29 Visual degradation due to variation in CO <sub>2</sub> gas composition at 100°F and 6000 psi: (a) Class G; (b) Class H (Omosebi et al., 2015) .....	124
Figure 4.30 Effect of CO <sub>2</sub> gas composition at 225°F on the normalized absorbance peaks extracted from FTIR spectra of degraded zones of Class H cement: (a) 3000 psi; (b) 6000 psi; and (c) 9000 psi .....	126
Figure 4.31 Effects of CO <sub>2</sub> gas composition at 225°F and different test pressures on the compressive strength, porosity, and permeability of: (a) Class G; (b) Class H .....	129
Figure 4.32 Visual degradation of Class G cement due to variation in CO <sub>2</sub> gas composition at 225°F and: (a) 3000 psi; (b) 6000 psi; (c) 9000 psi .....	131

Figure 4.33 Visual degradation of Class H cement due to variation in CO <sub>2</sub> gas composition at 225°F and: (a) 3000 psi; (b) 6000 psi; (c) 9000 psi .....	131
Figure 4.34 Effect of CO <sub>2</sub> gas composition at 350°F on the normalized absorbance peaks extracted from FTIR spectra of degraded zones of Class H cement: (a) 3000 psi; (b) 6000 psi; and (c) 9000 psi .....	132
Figure 4.35 Effects of CO <sub>2</sub> gas composition at 350°F and different test pressures on the compressive strength, porosity, and permeability of: (a) Class G; (b) Class H .....	134
Figure 4.36 Visual degradation of Class G cement due to variation in CO <sub>2</sub> gas composition at 350°F and: (a) 3000 psi; (b) 6000 psi; (c) 9000 psi .....	137
Figure 4.37 Visual degradation of Class H cement due to variation in CO <sub>2</sub> gas composition at 350°F and: (a) 3000 psi; (b) 6000 psi; (c) 9000 psi .....	138
Figure 4.38 Effect of CO <sub>2</sub> gas composition at 430°F and 6000 psi on the normalized absorbance peaks extracted from FTIR spectra of degraded zones of Class H cement	139
Figure 4.39 Effect of CO <sub>2</sub> gas composition at 430°F and 6000 psi on the compressive strength, porosity, and permeability of Classes G and H cement.....	140
Figure 4.40 Effect of total test pressure at 225°F and different CO <sub>2</sub> gas composition on the compressive strength, porosity, and permeability of: (a) Class G; (b) Class H .....	143
Figure 4.41 Effect of total test pressure at 350°F and different CO <sub>2</sub> gas composition on the compressive strength, porosity, and permeability of: (a) Class G; (b) Class H .....	147
Figure 4.42 Effect of test pressure at 430°F and 100% CO <sub>2</sub> on the normalized absorbance peaks extracted from the FTIR spectra of the degraded zones of Class H cement .....	148
Figure 4.43 Effect of test pressure at 430°F and 100% CO <sub>2</sub> on the compressive strength, porosity, and permeability of Classes G and H cement.....	149

Figure 4.44 Effect of aging time at 350°F, 6000 psi and 10% CO <sub>2</sub> on the compressive strength, porosity, and permeability of Classes G and H cement.....	151
Figure 4.45 Visual degradation due to variation in exposure time at 350°F, 6000 psi, and 10% CO <sub>2</sub> gas composition: (a) Class G; (b) Class H .....	151
Figure 5.1 Bulk and pore fluid chemistry resulting in chemical degradation of cement .....	159
Figure 5.2 Modeling Workflow .....	160
Figure 5.3 (a) Typical profile of the solid-phase calcium in half section of the exposed specimen with bi-carbonated and leached zone distinct from the fully carbonated zone; (b) typical profile of the solid-phase calcium in half section of the exposed specimen with bi-carbonated and leached zone masked by the fully carbonated zone; (c) physical model of the degraded zone.....	185
Figure 5.4 Typical distribution of solid minerals in cement exposed to carbonic acid	188
Figure 5.5 Model predictions for the degrees of hydration and chemical shrinkage of cement: (a) with clinker compositions in Table 4.1; (b) with clinker composition of Class H the same as Class G .....	190
Figure 5.6 Validation of hydration model with experimental data .....	191
Figure 5.7 Validation of transport properties model with experimental data: (a) porosity; (b) permeability .....	193
Figure 5.8 Comparison between: (a) model prediction and experimental data from previous study (Voigt and Shah, 2003); (b) model predictions for Classes G and H cement .....	193

Figure 5.9 Comparison between model prediction and experimental data from this study .....	194
Figure 5.10 Comparison of the mutual solubility of CO <sub>2</sub> and CH <sub>4</sub> gases in 2% NaCl solution .....	198
Figure 5.11 Fluid pH and solubility of CO <sub>2</sub> gas (m <sub>CO2</sub> ) in 2% NaCl solution: (a) effect of temperature at 6000 psi; (b) effect of pressure at 350°F .....	199
Figure 5.12 (a) Cut section of exposed specimen; and typical concentration of aqueous species (mol/m <sup>3</sup> ) after solute transport between the bulk and the pore fluids: (b) H <sup>+</sup> ; (c) HCO <sub>3</sub> <sup>-</sup> ; (d) Ca <sup>2+</sup> .....	201
Figure 5.13 (a) comparison between the solid-phase calcium profiles of Classes G and H cement at 6000 psi, 350°F, and 10% CO <sub>2</sub> ; (b) CO <sub>2</sub> gas composition effect on the solid-phase calcium profile of Class G cement at 6000 psi and 350°F; (c) temperature effect on the solid-phase calcium profile of class G cement at 6000 psi and 40% CO <sub>2</sub> .....	202
Figure 5.14 (a) model prediction of the solid-phase calcium from the residual cement hydrates and calcium carbonate after cement is exposed to carbonated-brine; (b) model prediction of the evolution of porosity after cement is exposed to carbonated-brine ..	203
Figure 5.15 Comparison between model predictions and experimental measurements for Class G cement: (a) pressure effect at 10% CO <sub>2</sub> and 350°F; and (b) CO <sub>2</sub> effect at 6000 psi and 350°F .....	205
Figure 5.16 Comparison between model predictions and experimental measurements for Classes G and H cement: (a) pressure effect at 100% CO <sub>2</sub> and 430°F; and (b) CO <sub>2</sub> effect at 6000 psi and 430°F .....	205

## Abstract

Cement exposed to brine saturated with CO<sub>2</sub> gas undergoes combination of chemical processes leading to mechanical degradation after placement behind the casing. These processes are influenced by downhole conditions such as temperature, pressure, and the composition of CO<sub>2</sub> gas. The objectives of this study are to understand the mechanisms governing the degradation of well cement and to quantify the rate of deterioration using experimental and modeling techniques.

Experiments were conducted by exposing Classes G and H cement to CO<sub>2</sub>-saturated brine solution under HPHT conditions. Temperature was varied between 100°F and 430°F while pressure was varied between 3,000 psi and 9,000 psi. To generate aggressive fluid around the cement, the composition of CO<sub>2</sub> gas was varied by injecting a mixture of gases, containing varying compositions of carbon dioxide and methane, into the HPHT autoclave. Compressive strength was measured before and after exposure to determine the alteration in mechanical integrity due to chemical attack. In addition, fluid samples were collected after the test and chemical analysis was conducted to quantify pH and calcium content. These are supported with porosity, permeability, FTIR, XRD, EDX, SEM, and visual inspection of the degraded specimens. Besides, a methodology for coupling the governing mechanisms involved in cement degradation is proposed and a fully-coupled model is developed.

In both classes of cement, overall mechanical behavior shows improvement, although the specimens were chemically degraded. Three mechanisms of degradation were identified as the driver of the degradation process. Structural transformation of calcium silicates at elevated temperature leads to slight retrogression in strength.



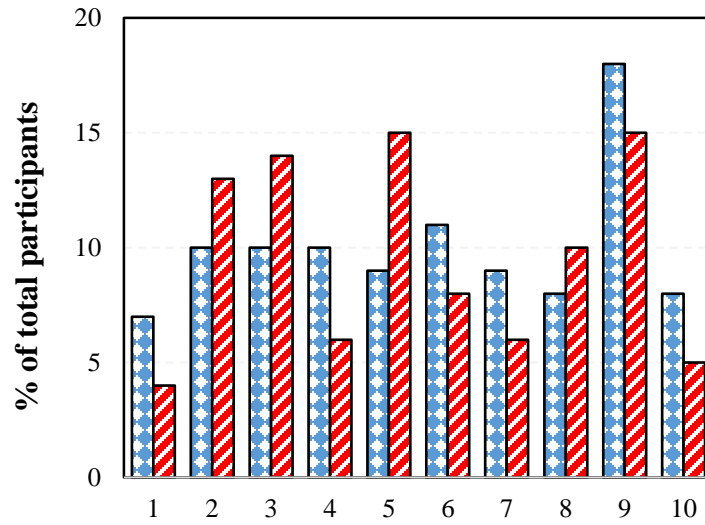
Carbonation reaction improves mechanical strength but reduces porosity and permeability. Bicarbonation and leaching reactions increase porosity and permeability leading to the loss of mechanical strength. These mechanisms are interrelated; the overriding process governs the rate of degradation. Within the experimental time scale adopted in this study, carbonation is the rate-controlling process because overall mechanical integrity is improved. Parametric studies of the effects of downhole parameter on mechanical behavior show that cement degradation is sensitive to temperature, pressure, and CO<sub>2</sub> gas composition. Relative to CO<sub>2</sub> gas composition and pressure, temperature is identified as the most critical downhole parameter for cement design in HPHT carbonic acid environment. Comparison between experimental data and the model developed in this study shows good agreement.

Very limited studies have been conducted to evaluate cement performance in HPHT acidic environment. In previous investigations, alterations in the mechanical strength of well cement in hostile environments have not been thoroughly examined. This study provides understanding on how the mechanical integrity of commonly used well cement is affected by aggressive and harsh downhole conditions. The outcome of this study lays the ground work for engineering CO<sub>2</sub>-resistant cement that would ensure well integrity for long-term CO<sub>2</sub> storage and containment.

# Chapter 1 Introduction

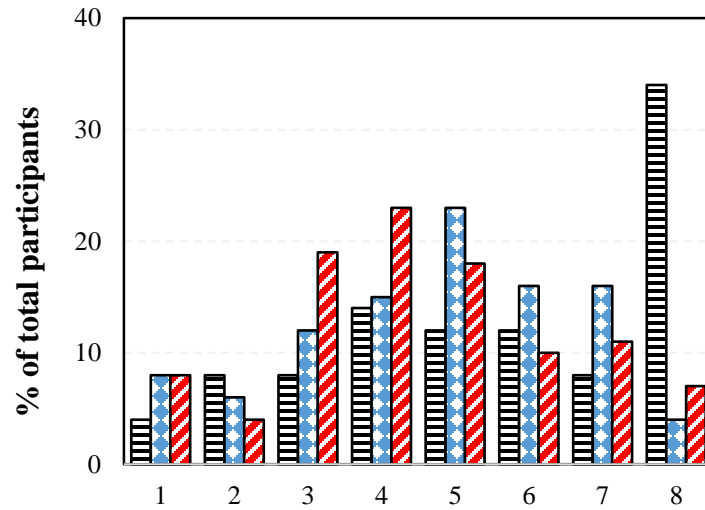
## 1.1 Overview of Cement Degradation

High pressure and high temperature (HPHT) energy resources, such as geothermal resources, are increasingly used for energy production (e.g. electricity generation). Development of these resources poses unique challenges. **Figure 1.1a** is the result of a survey conducted at HPHT Wells Summits (2013, 2015) where well design, completions and well control & intervention were reported to account for 38% of the biggest challenges the industry faces with the development of HPHT assets in 2013 and 2015. In 2010 (**Figure 1.1b**), this industry-led poll revealed that casing, cement design, and seals and testing make up 34% of the existing knowledge gaps limiting the use of HPHT resources. By years 2012, 2013 and 2015, this number has increased by almost 60%, 55% and 65%, respectively. In addition, extreme downhole conditions of pressure and temperature are frequently encountered in deepwater drilling. Lessons learnt from previous environmental disasters in this terrain (e.g. Motara blowout, Macondo oil spills, etc.) have consistently pin point good cementing practice as critical step towards averting these catastrophes. To understand the unique challenges with cementing HPHT wells, studies (Salim and Amani, 2013; Ravi et al. 1999; Shado and Joel, 2011; Frittella and Babbo, 2009; Adamson et al., 1998; Lehr and Collins, 2015) have been conducted to highlight the current state of the arts in cementing technology.



- 1 – Geographical location
- 2 – Material issues
- 3 – Personnel & workforce issues
- 4 – Electronic issue
- 5 – Well design
- 6 – Completions
- 7 – Data logging
- 8 – Equipment selection
- 9 – Well control & intervention
- 10 – Corrosion understanding

(a)



- 1 – Casing
- 2 – Tubulars
- 3 – Polymer & metallurgy
- 4 – Cement design & formation
- 5 – Seals
- 6 – Safety measures
- 7 – Testing
- 8 – Other

(b)



**Figure 1.1 (a) Challenges confronting operators of HPHT resources; (b) Knowledge gaps in the development of HPHT resources**

Besides, the petroleum industry is presently seeking additional reserves in unconventional hydrocarbon resources such as sour gas reservoirs. In recent times, exploration and production of oil and gas from these resources have increased steadily. A significant amount of residual proven gas reserves are believed to contain substantial quantity of carbon dioxide (CO<sub>2</sub>). CO<sub>2</sub> is either produced as associated gas (e.g. deep sour gas condensate and volatile oil fields) or injected in reservoirs during carbon capture, utilization and storage (e.g. geological carbon storage, CO<sub>2</sub> enhance oil recovery, etc.). **Figure 1.2** illustrates CO<sub>2</sub> capture, utilization and storage cycle. In producing oil and gas fields, CO<sub>2</sub> concentration can be between 5-65% (e.g. Greater Gorgon Fields, Snohvit field, Salah Oil field, Sleipner West field, LaBarge field) (MIT, 2015). Moreover, injection of CO<sub>2</sub> into underground rocks takes place under two major instances. In the first instance, CO<sub>2</sub> is injected into petroleum reservoirs to drive the recovery of oil when the primary source of reservoir energy is not sufficient to move reservoir fluid to the surface. This method of oil recovery is called CO<sub>2</sub> enhanced oil recovery (EOR). In the second case, CO<sub>2</sub> is injected into depleted petroleum reservoirs or deep saline aquifers for permanent underground storage. This is necessitated by the impact of carbon emission on global climate change. A recent Carbon Capture and Storage (CCS) Database by National Energy Technology Laboratory (NETL) documents 274 CCS projects worldwide (NETL, 2015). Some of these projects are in the planning and development stage while others are actively capturing and injecting CO<sub>2</sub> into underground formations. In active carbon capture projects, CO<sub>2</sub> concentration could be as high as 98% (e.g. Port Arthur Project, Wasatch Plateau) (MIT, 2015).

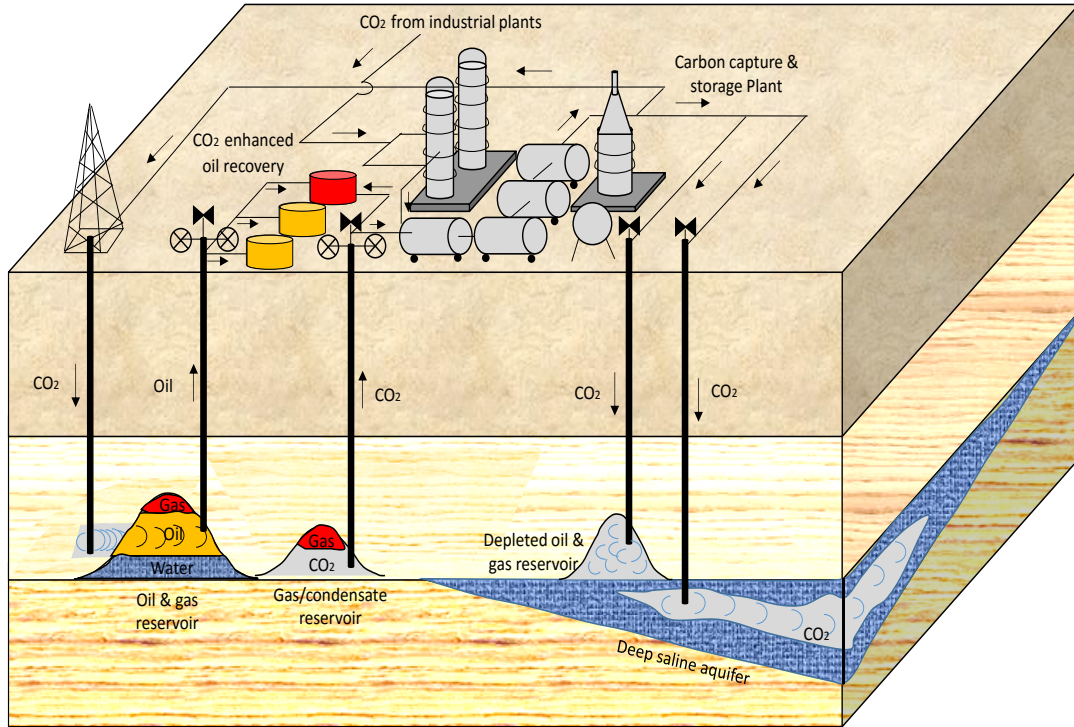


**Figure 1.2 Carbon Capture, Utilization and Storage (CCUS) Cycle**

In both cases of CO<sub>2</sub> injection, wells are drilled up to thousands of feet of depth. At these depths, extreme downhole conditions exist (i.e. high temperature and high pressure). The injection wells are often completed with well barriers comprising multiple strings of metallic steel pipes (also known as casings) which are cemented to the host rock. Cement is the primary means of protecting these casings from corrosive fluids and isolating storage zones from overlying fresh water aquifers. Cement slurry is pumped behind the casing during drilling operations to seal off casing-formation annulus, provide mechanical support for the casing, protect the casing from acidic fluids, and isolate productive zones thereby ensuring long-term reliability of the well. Over the life of the well, injected and/or formation fluids (i.e., CO<sub>2</sub>, formation brine, hydrocarbons etc.) create aggressive environment around the cement sheath. The presence of CO<sub>2</sub> under HPHT conditions complicates well construction design and if appropriate steps are not

taken to mitigate inherent risks during well planning stage, loss of well integrity can occur with huge remedial or abandonment cost.

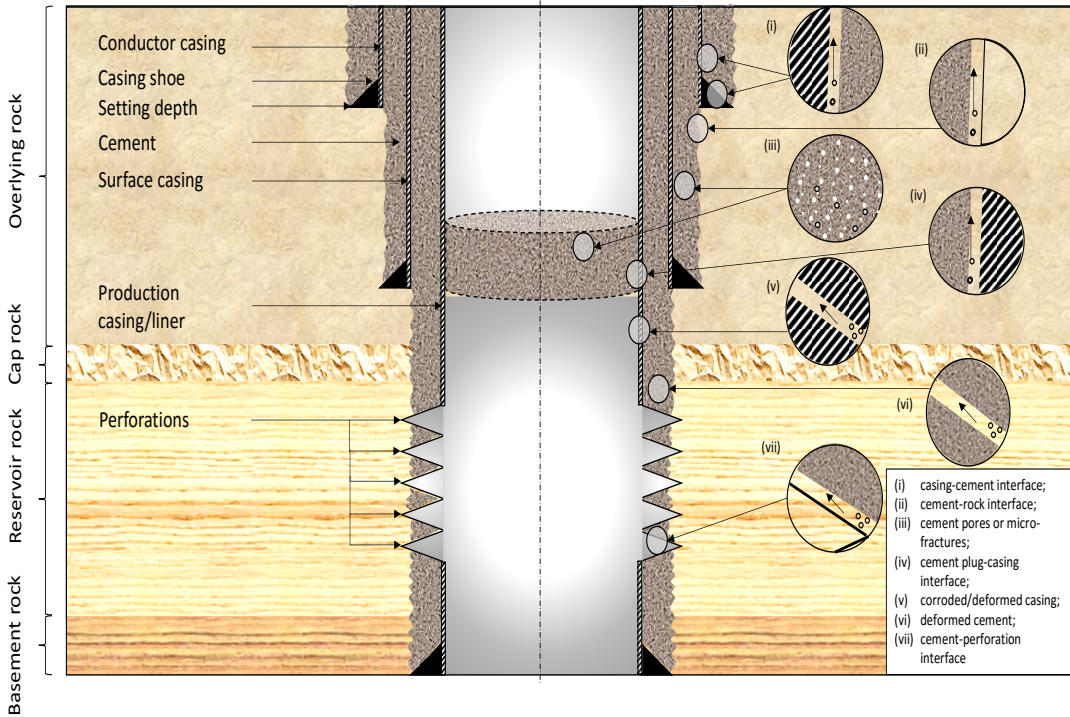


**Figure 1.3 Potential leakage pathways through casing-cement-rock system**

Extreme downhole condition degrades cement quality thereby undermining its ability to perform effectively during the operational life of the well. Interaction of wellbore materials with hostile fluids in HPHT environment opens up pathways for fluid flow (**Figure 1.3**). This could lead to the loss of zonal isolation, weakening of the hardened cement, and ultimate failure of the cement sheath, potentially leading to microannulus. Once this occurs, formation fluid leaks through cement-rock and casing-cement interfaces thereby contaminating fresh domestic water in overlaying rock strata. If the leak problem is not mitigated, it poses serious well integrity issues that could affect the safety of lives, the environment, and oil and gas installations. Therefore, oil well cement must be formulated and placed to perform its function throughout the productive life of the well even after plugging and abandonment. Wellbore materials used to construct these

wells required careful selection to minimize environmental footprint due to energy production from these resources.

## **1.2 Statement of Problem**

Cement is the first and possibly the most important downhole barrier against uncontrolled flow of formation fluid after drilling operation. In carbonic acid and HPHT environment, the risk of cement sheath failure is high. If failure occurs, CO<sub>2</sub> would leak to overlying fresh water aquifers and possibly to the surface causing unimaginable environmental disasters. Long-term integrity of wells completed in HPHT carbonic acid environment is a subject of great concern for operators and regulators. The outcome of investigations (BOEMRE 2011; USCG 2011) on the reasons for the major environmental tragedies in recent history, have stressed the urgent need to improve well cementing practices. Although good cement placement is important for efficient zonal isolation, however it is not a guarantee that the well will continue to perform its function efficiently for tens to hundreds and even thousands of years. Significant knowledge gap still exists on how to improve well cementing practices. A number of CO<sub>2</sub>-resistant cement formulations have been developed and commercialized as high-alumina CO<sub>2</sub>-resistant cement (e.g. ThermaLock™, and EverCRETE™). However, limited data exist in the public domain on how these formulations compare to standard baseline cement slurry. Furthermore, previous studies mostly investigated the effect of CO<sub>2</sub>-brine system on cement degradation under low pressure and low temperature. Nonetheless, effect of extreme environmental conditions of temperature, CO<sub>2</sub> concentration, and pressure on cement degradation is not well understood. In addition, reliable database on alteration in mechanical strength due to variation in these critical parameters is scarce. This underlines

the need for more aggressive research aimed at improving understanding of the integrity of cements used to complete wells that were drilled in HPHT carbonic acid environment. Scientific understanding on how hardened cement deteriorate upon exposure to CO<sub>2</sub>-containing fluid under HPHT conditions forms the basis of engineering the appropriate CO<sub>2</sub>-resistant cement formulations.

Besides, the genesis of cement degradation in HPHT carbonic acid environment can be due to mechanical or chemical process or both. Chemical degradation is initiated when cured cement is exposed to a fluid medium containing solute species that are not in chemical thermodynamic equilibrium with the solute species in the pore fluid of the hardened cement. In carbonic acid environment, cement minerals react with aqueous carbonic species to form other minerals. This alters its original mechanical properties leading to mechanical degradation. The performance of this degraded cement throughout its service life is determined by the composition of the cement slurry and the temperature, CO<sub>2</sub> concentration and pressure to which it is exposed. Mathematical modeling of the interaction between cement materials and corrosive fluids is very complex. This is due to the complex nature of the interaction between the governing processes. Limited mathematical models exist but they are over simplified. Majority of these models do not fully capture the critical mechanisms that govern cement degradation in HPHT carbonic acid environment. In view of this, a fully-coupled cement degradation model that predicts cement mechanical behavior is a valuable contribution to existing knowledge base.



### **1.3 Research Objectives**

The general objective of this study is to understand how extreme borehole conditions alter the mechanical behavior of well cement. The specific objectives are:

1. To understand the mechanisms governing cement degradation process in HPHT carbonic acid environment.
2. To understand the effects of temperature, CO<sub>2</sub> gas composition and pressure on mechanical degradation of well cement under HPHT conditions.
3. To improve existing models relating to cement deterioration.
4. To develop new models that incorporate alteration in mechanical behavior due to the effect of CO<sub>2</sub>.
5. To couple the new and improved models for cement integrity evaluation.

### **1.4 Research Methodology**

The methodology adopted in this research is grouped into three broad categories. These include:

1. Theoretical study: Industry challenges in the area of drilling and completion technology were investigated through thorough review of technical reports, conference proceedings and technical articles. Extensive literature survey was conducted to know the state of the art in cementing technology. This was used to establish the required theoretical foundation for designing experimental program and formulating mathematical models.
2. Experimental study: The outcome of literature survey reveals the limitation in previous studies that were conducted on cement degradation. New experimental methods were designed based on industry standard testing

procedures. The experimental program in this study includes cement mixing and curing procedure, CO<sub>2</sub> aging experiment, aging fluid sampling and chemical analysis, mechanical testing procedure and mineralogy characterization.

3. **Mathematical Modeling:** The mechanisms describing cement degradation in HPHT carbonic acid environment were modeled using equation-based modeling approach. Existing models were improved and new models are formulated. These models were systematically coupled in a manner that reflects the complexity of the degradation process. To enable cross-platform application, the model was programmed in Matlab and integrated with Comsol Multiphysics, a fast and robust commercial software that uses finite element method to solve time-dependent problems in any arbitrary domain.

**Figure 1.4** is summarizes the approach used to conduct this research.

## **1.5 Scope of Study**

In this research, the experimental studies are limited by the types of well cement investigated, composition of slurry and the test conditions. Classes G and H Portland-based cement were used as baseline cement materials. The aggressive environment is a CO<sub>2</sub>-saturated brine at high pressure (up to 9,000 psi), high temperature (up to 430°F), high CO<sub>2</sub> concentration (up to 100% purity) and aging test duration (up to 28 days). During the CO<sub>2</sub> exposure tests, these parameters were varied as follows:

- Temperature: 100°F (38°C), 225°F (107°C), 350°F (177°C) and 430°F (221°C),
- CO<sub>2</sub> gas composition: 0%, 10%, 40% and 100%,

- Pressure: 3000 psi (21 MPa), 6000 psi (42 MPa) and 9000 psi (62 MPa)
- Test duration: 6 days, 14 days and 28 days.

These aging conditions were carefully and systematically selected to simulate practical downhole conditions and to concurrently investigate the effects of variation in temperature, CO<sub>2</sub> gas composition and pressure without duplicating experiments.

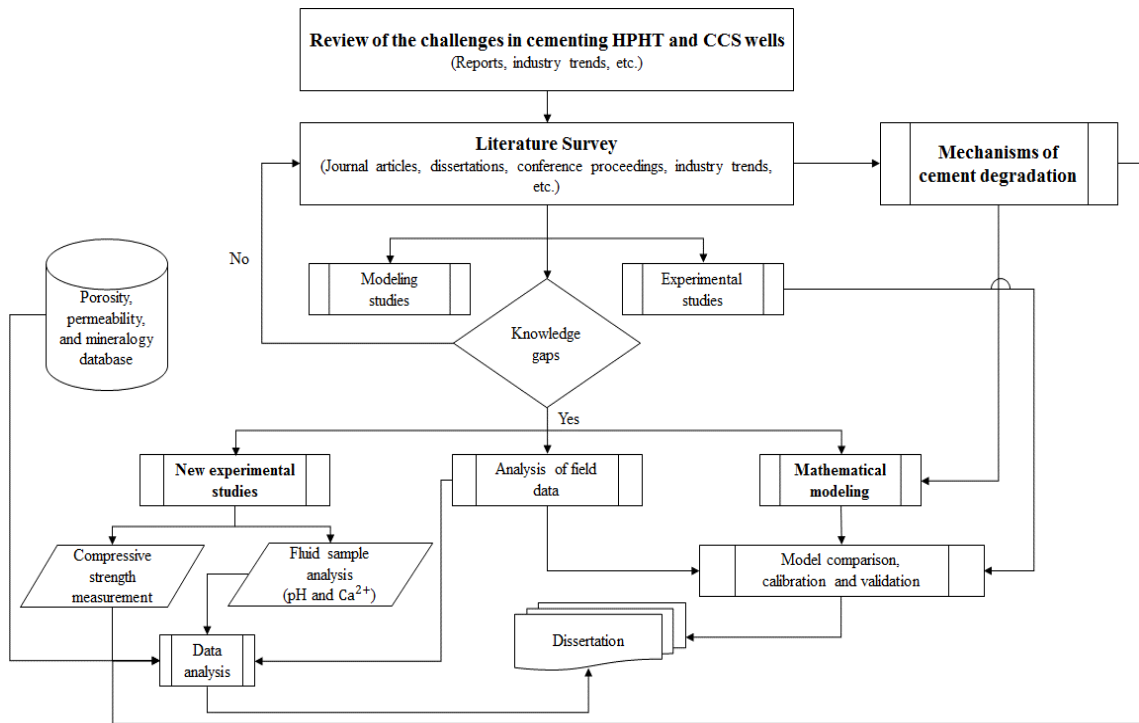


**Figure 1.4 Workflow for analysis of cement integrity after exposure to CO<sub>2</sub> – brine fluid under HPHT conditions**

## Chapter 2 Background Study

### 2.1 Overview

A number of studies have been conducted to understand the effect of acidic fluids on oil well cement and the role of slurry composition, temperature, pressure, and brine concentration. These investigations can be broadly categorized into experimental studies and theoretical modeling. To systematically review these previous studies, each category is sub-divided into two groups. The first group comprises investigations on cement degradation in the absence of acidic fluids while the second group includes studies that were conducted in the presence of aggressive fluids. The abundant information on cement corrosion science is reviewed in this chapter. To start with, cement chemistry before and after exposure to carbonic acid environment is revised.

### 2.2 Cement Chemistry

#### 2.2.1 Hydration of Clinker Compounds

Cement is generally classified as non-Portland-based or Portland-based cement. Non-Portland-based cement comprises calcium aluminate cement (CAC), resin cement, etc. According to API standard (Bourgoyne et al. 1986), conventional Portland-based oil well cements are grouped into three types based on their sulfate resistance. These include Ordinary (O), Medium Sulfate Resistant (MSR) and High Sulfate Resistant (HSR) cement. These cement types are further divided into eight (8) classes (Classes A through H) based on temperatures, applicable depth and use with additives. **Table 2.1** summarizes the conditions under which each class of cement is applicable.

Classes G and H cement are most commonly used in the petroleum industry as baseline cement because they are applicable over wide range of temperatures and depth and are well-suited for use with additives (Bourgoyne et al., 1986). Class H cement is the standard cement used for cementing oil and gas wells along the US Gulf coast, in the Midcontinent, and in the Permian basin. Class G cement is used primarily in the western US, Canada, and most other parts of the world (Smith, 1991). The main differences between these API cements are the standard quantity of mixing water required per sack of cement (i.e. 94 pounds in oilfield standard) and particle fineness (Bourgoyne Jr., 1986; API SPEC 10A 1995; Bensted and Barnes, 2002; Hewlett 2004). Different mixing water is required to attain the same slurry consistency and to ensure uniformity of testing. **Table 2.2** shows the typical Blaine fineness and API recommended water-to-cement (w/c) ratio for each class of cement. To control batch to batch variability during slurry preparation, these Classes of oil well cements are formulated with strict setting time requirements (Bensted and Barnes, 2002). They are prepared by mixing the cement in powdery form with water and other additives are added to control the slurry rheological properties required under the most extreme downhole conditions.

**Table 2.1 API cement classification (Bourgoyne et al. 1986)**

<b>API</b>	<b>Classification based on sulfate resistance</b>	<b>Applicability</b>
Class A	O	Shallow depth (up to 6000 ft)
Class B	MSR and HSR	Shallow depth (up to 6000 ft)
Class C	O, MSR and HSR	High early strength at shallow depth (up to 6000 ft)
Class D	MSR and HSR	Moderately high temperature and pressures (depths between 6000 and 10000 ft)
Class E	MSR and HSR	HPHT Wells (depths between 10000 and 14000 ft)
Class F	MSR and HSR	Extreme HPHT wells (depths between 10000 and 16000 ft)

Class G	MSR and HSR	Various depths (up to 8000 ft) and temperature. Can be used with various accelerators and retarders
Class H	MSR	Various depths (up to 8000 ft) and temperature. Can be used with various accelerators and retarders

**Table 2.2 Fineness and water-to-cement ratio of Classes G and H cement (Hewlett 2004)**

API Classes	Blaine fineness (cm <sup>2</sup> / gm)	Water-to-Cement (w/c) ratio
<b>G</b>	2700-3500	0.44
<b>H</b>	2200-3000	0.38

Dry Portland cement contains calcium oxide or lime (CaO), silicon oxide or silica (SiO<sub>2</sub>), aluminium oxide or alumina (Al<sub>2</sub>O<sub>3</sub>), iron oxide (Fe<sub>2</sub>O<sub>3</sub>) and sulfur trioxide (SO<sub>3</sub>). These components are present in cement as crystalline phases which comprises tricalcium silicate or alite, (Ca<sub>3</sub>SiO<sub>5</sub> or C<sub>3</sub>S), dicalcium silicate or belite (Ca<sub>2</sub>SiO<sub>4</sub> or C<sub>2</sub>S), tricalcium aluminate (Ca<sub>3</sub>Al<sub>2</sub>O<sub>6</sub> or C<sub>3</sub>A) and tetracalcium aluminoferrite (Ca<sub>4</sub>Al<sub>2</sub>Fe<sub>2</sub>O<sub>10</sub> or C<sub>4</sub>AF) and calcium sulfate or gypsum (CaSO<sub>4</sub>). The crystalline phases (sometimes called clinker compounds) constitute the major part of the cement in its dry form. Relative quantities of these compounds are determined from oxide analysis (otherwise called Bogue analysis). API recommends the following equations for estimating the weight percent of each compound from the weight percent of the oxides present (Bouroyne et al. 1986):

$$C_3S = 4.07 * CaO - 7.6 * SiO_2 - 6.72 * Al_2O_3 - 1.43 * Fe_2O_3 - 2.85 * SO_3 \dots\dots\dots (2.1)$$

$$C_2S = 2.87 * SiO_2 - 0.754 * C_3S \dots\dots\dots (2.2)$$

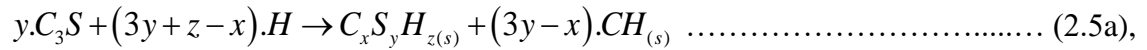
$$C_A A = 2.65 * Al_2O_3 - 1.69 * Fe_2O_3 \dots\dots\dots (2.3)$$

$$C_A AF = 3.04 * Fe_2O_3 \dots\dots\dots (2.4)$$

These equations are valid only when  $Al_2O_3 / Fe_2O_3 > 0.64$ .

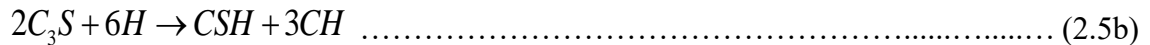
The clinker compounds hydrate independently upon mixing with water to form different cement hydrates. The reactions involved in the hydration process are summarized below (Bensted and Barnes, 2002; Hewlett 2004).

(i) Hydration of Alite ( $C_3S$ )



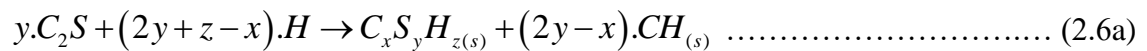
where  $x$ ,  $y$ , and  $z$  are the number of molecules of  $CaO$ ,  $SiO_2$ , and  $H_2O$  that are chemically bond together to form the structure of CSH.

When  $x = 3$ ,  $y = 2$ , and  $z = 3$  (afwillite), equation 2.5a becomes:



The reaction stages, chemical processes and overall kinetic behavior involved in  $C_3S$  hydration are well-documented by Bensted and Barnes (2002). Three stages are mainly involved: a short period of rapid chemical dissolution, a middle stage in which ions transport to and fro the surfaces of anhydrous cement particles through gradually growing layers of hydration products and a late period in which free water permeates through the hydration products making further reactions possible. The products of hydration are amorphous calcium silicate hydrate (CSH) and calcium hydroxide or portlandite ( $Ca(OH)_2$  or CH), both of which aid early strength development.

(ii) Hydration of Belite ( $C_2S$ )



When  $x = 3$ ,  $y = 2$ , and  $z = 3$ , equation 2.5a becomes:



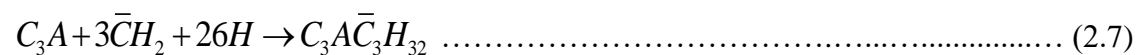
Hydration of belite is a relatively slow process when compared to the hydration of alite. Therefore,  $C_3S$  is believed to be the principal component that controls setting and early strength development. Belite, on the other hand, contributes to long-term strength development due to its slow rate of hydration. The products of hydration of alite and belite are the same except that belite consumes less water and produces less amount of CH (Equation 2.6). CSH and CH produced from hydration of these chemical compounds constitute approximately 70-85% of the composition by weight of all products of hydration. Hence, these cement hydrates are the predominant constituents in cement after curing and hardening.

(iii) Hydration of tricalcium aluminate ( $C_3A$ )

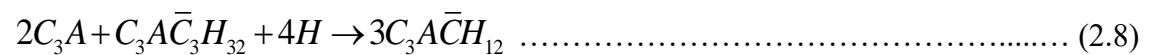
Hydration of  $C_3A$  is more complicated than those of alite and belite. Equations 2.7-2.10 summarize the reaction steps that are involved.

(a) Presence of gypsum

Step 1: Formation of Ettringite

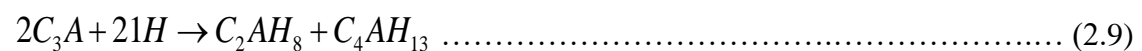


Step 2: Formation of calcium monosulfoaluminate



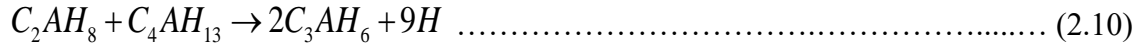
(b) Absence of Gypsum

Step 1: Formation of metastable calcium aluminate hydrates



Step 2: Conversion of metastable calcium aluminate hydrates to cubic hydrate (i.e., hydrogarnet group e.g. katoite)





(iv) Hydration of Tricalcium Aluminoferrite (C<sub>4</sub>AF)

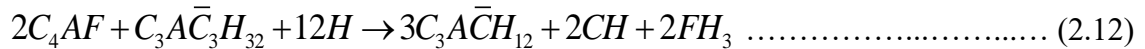
C<sub>4</sub>AF hydrates in similar manner as C<sub>3</sub>A. However, its rate of hydration is relatively slower. The chemical reaction steps involved are summarized by equations 2.11-2.13.

(a) Presence of Gypsum

Step 1: Formation of Ettringite

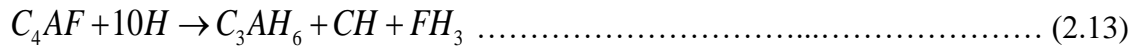


Step 2: Formation of calcium monosulfoaluminate



(b) Absence of Gypsum

Formation of cubic hydrate (hydrogarnet group)



The abbreviated group terms used in equations 2.5-2.13 (i.e. C,  $\bar{C}$ , S, H, A, and F) are all defined in the nomenclature. The products of hydration described above (i.e. calcium silicate hydrate, calcium hydroxide, ettringite, calcium monosulfoaluminate and hydrogarnet group) exhibit unique properties, which are distinct from the unhydrated clinker compounds.

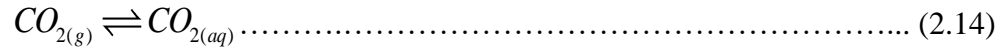
### 2.2.2 Reaction between Cement and Carbonic Acid

Exposure of hydrated cement to CO<sub>2</sub>-containing fluid initiates reactions between cement hydrates and the aggressive fluid. Although gaseous CO<sub>2</sub> is not very reactive with the hydrates, in combination with water it dissolves to form carbonic acid.

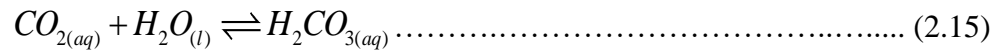
This acidic environment leads to chemical attack. Under HPHT condition, acid attack severely alters the mechanical properties of the hardened cement and degrades its quality after prolonged exposure. The following chemical reactions occur during this process:

(i) Dissolution of CO<sub>2</sub> in water or brine solution

(a) Carbon dioxide gas enters water through equilibrium with the atmosphere



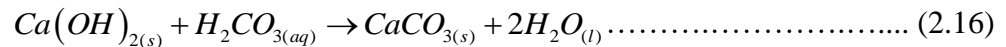
(b) Aqueous CO<sub>2</sub> reacts with water to form carbonic acid



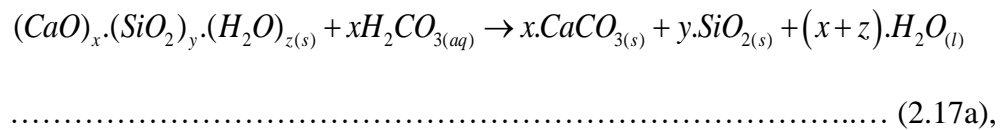
(ii) Commencement of cement degradation process

(a) Carbonation of cement hydrates

- Carbonation of portlandite



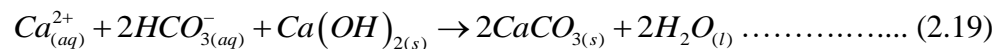
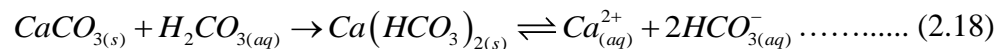
- Carbonation of calcium silicate hydrate



When  $x = 3$ ,  $y = 2$ , and  $z = 3$ , equation 2.17a becomes:



(b) Leaching out and deposition of calcium carbonates



## 2.3 Experimental Studies

### 2.3.1 Experimental Studies in the Absence of CO<sub>2</sub>

Previous studies have investigated the effects of cement composition (clinker compounds and additives), salt concentration, temperature, and pressure on cement performance in the absence of an acid.

Tricalcium silicate (C<sub>3</sub>S) is the most important constituent of cement because it controls setting and early strength development (Bensted and Barnes 2002; Bouroyne et al. 1986). When hydrated, it produces amorphous calcium silicate hydrate which readily transforms to different crystalline phases depending on temperature and CaO/SiO<sub>2</sub> (C/S) ratio. Differential thermal analysis (DTA), thermal gravimetric analysis (TGA), Nuclear Magnetic Resonance (NMR) spectroscopy, X-Ray Diffraction (XRD) and Scanning Electron Microscopy (SEM) techniques were used by Méducin et al. (2002) to study the structure and morphology of minerals formed after hydration of C<sub>3</sub>S at high temperature (392°F) and pressure (6530 psi). Crystalline phases such as portlandite and hillebrandite were detected in the study. Horkoss and Lteif (2011) investigated the influence of clinker composition on early hydration of Portland cement. In their study, thirteen formulations of neat cement were obtained from cement factory with different compositions of CaO, SiO<sub>2</sub>, Al<sub>2</sub>O<sub>3</sub>, Fe<sub>2</sub>O<sub>3</sub> and SO<sub>3</sub>. **Figure 2.1** shows how compressive strength of four out of the thirteen formulations varies with time. Although it is difficult and almost impossible to isolate the effect of a particular clinker material since the composition of these materials were simultaneously varied in the study, it can be inferred that the development of compressive strength during the curing period is sensitive to the composition of clinker materials present. The incremental gain in strength during the first

25 days of curing is due to the rapid dissolution of the clinker materials to form cement hydrates. Similar experiments were conducted by Sahmaran et al. (2007) and Cao et al. (1997) and their findings agree with this observation. Furthermore, observation from an experimentally-calibrated model studies indicates that change in clinker composition during hydration does not have significant effect on elastic constants (Young's and Shear modulus) of Class G cement (Ghabezloo, 2011).

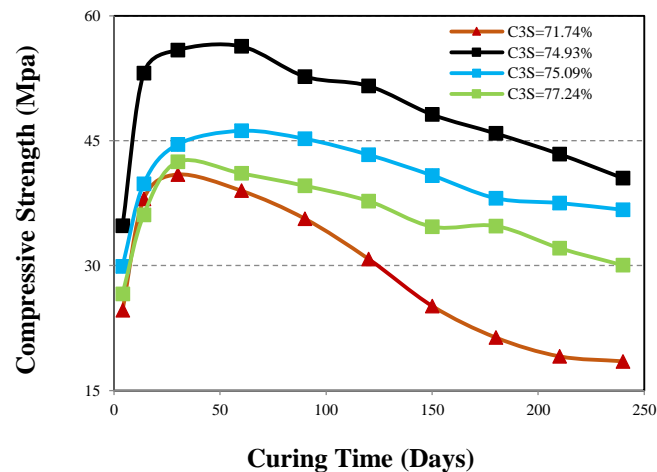


**Figure 2.1 Strength development at different compositions of C<sub>3</sub>S (Horkoss and Lteif, 2011)**

Additives are commonly added to baseline (neat) cement to control slurry rheological properties thereby allowing modification of baseline cement performance. There are tens (if not hundreds) of chemical additives currently used to improve cement performance. Selection of these additives depends on the property to be improved and the environmental conditions to which cement is subjected. Effect of expanding additives, such as magnesium oxide (MgO), on compressive strength of Class G cement was investigated by Rubiandini (2000). High sulfate resistant (HSR) Class G cement (with and without 35% silica flour) containing 0 to 10% of MgO expanding additive was used for the test which last for 24 hours. Exposure conditions range between 212°F and 392°F. A 5% optimum concentration of MgO was recommended to minimize loss of mechanical

strength at high temperature and pressure. Usually, 35-40% by weight of cement (BWOC) silica is added to the base slurry to prevent strength retrogression at elevated temperature (Bruckdorfer, 1986; Bensted and Barnes, 2002). However, Foster et al. (2011) formulated thermally resistant cement for steam injection wells with 60% BWOC silica flour. Furthermore, Heinold et al. (2002) investigated the effects of several additives on compressive strength of Class G cement. The outcome of their study shows that the addition of polyvinyl alcohol (PVA), silica fume, metakaolin, wollastonite, hydroxyethyl cellulose, and sodium metasilicate to neat Class G cement slightly improves its mechanical strength up to 200°F. However, loss of mechanical integrity was observed at higher temperature. Baumgarte et al. (1999) demonstrated how expanding cements can be used to prevent the formation of micro annulus. Slurry of Class G Portland cement, dry-blended with 10% BWOC calcium oxide-based expanding agent, was prepared and cured at 170°F. Compression and annular expansion mold tests were conducted on specimens from the hardened cement. Compressive strength of 5950 psi was measured and maximum linear expansion of about 3% was recorded after two weeks. Root and Calvert (1971) compared the expansion characteristics of different expanding cement systems. The specimens used in the analysis were initially cured at 80°F and 0 psi after which curing was conducted at 100°F and 0 psi, 100°F and 1000 psi, 150°F and 0 psi, and 150°F and 1000 psi. Compressive strength, permeability and linear expansion of the specimens were measured before and after the second stage of the curing process. Measured strength of the expansive cement systems were found to be lower than the strength of Portland cement subjected to the same test conditions. Besides, permeability of these specially-formulated cements is equivalent to the permeability of conventional

Portland-based cement but measured linear expansion is about four times the expansion of Portland cement. The swelling characteristics of calcium oxide (CaO) and magnesium oxide (MgO) were investigated by Ghofrani and Plack (1993). Compressive strength of Class G cement (with and without 35% silica flour) was measured after 7 days of curing at 302°F and 248°F. This was then compared to the strength of CaO and MgO-swelling cements. At 302°F curing temperature, Class G cement with 35% silica flour shows higher improved strength than both CaO and MgO-swelling cements. At 248°F curing temperature, however, the trend is reversed.

Effect of salt concentration on strength development has been examined previously. Cement cured in calcium chloride (CaCl<sub>2</sub>) solution develops strength rapidly during the first few days after placement (Nelson, 1990). The rate of strength development depends on the curing temperature and CaCl<sub>2</sub> concentration. **Figure 2.2** shows the effect of sodium chloride concentration on compressive strength after 1 day of curing at different temperatures (Nelson 1990). At temperatures below 160°F, strength increases with NaCl concentration with maximum strength at 10% by weight of mix water (BWOW) approximately. At higher curing temperature, maximum strength occurs at lower NaCl concentration (about 5%). Above these NaCl concentrations, strength loss is very significant. This implies that the peak strength of cement under compressive loading is determined by the concentration of NaCl and curing temperature. Besides, Lecolier et al. (2007) used brine as aging fluid and then investigated the effects of fluid circulation and replacement on mechanical strength. The results of their investigations show that fluid renewal and the presence of salt result in significant loss of strength (about 50%). However, cement specimens that were aged in static water shows lower loss in

mechanical strength (about 20%). Eiler et al. (1980) studied the effect of the presence and flowing condition of formation fluids on the properties of the crystalline phases of calcium silicate hydrate. In their study, xonotlite demonstrated the best performance after exposure to static brine solution.

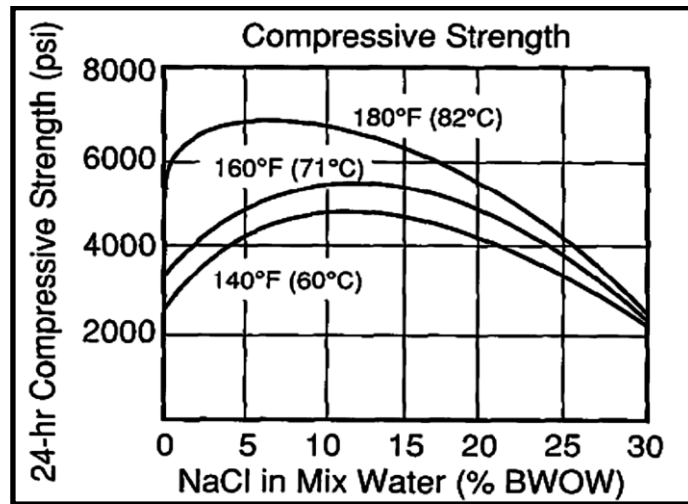


Figure 2.2 Effect of salt concentration on compressive strength (Nelson, 1990)

Temperature affects early strength development of cement by accelerating the growth of principal products of hydration. Craft et al. (1935) were one of the earliest investigators that studied the effects of temperature, pressure and water-cement ratio on the strength of neat Portland cement. The outcome of their studies shows that substantial strength retrogression when cement is subjected to high temperature. On the contrary, strength increased with curing pressure up to 4000 psi. In addition, they observed that compressive strength decreases as the composition of mixed water increases. Experimental data that were published by Rahmani et al. (2012) and Alawode and Idowu (2011) supports the existence of inverse relationship between compressive strength and the composition of mixed water used to prepare cement slurry. The work done by Deschner et al. (2013) shows that elevated curing temperature is helpful to early strength

development of ordinary Portland cement (OPC). After the early periods of hydration, specimens containing fly ash also demonstrated good improvement in strength at elevated temperature. In addition, Stiles (2006) evaluated mechanical behavior of cement systems after exposure to extremely high temperature (645°F). Cement systems investigated include conventional 15.4 lbm/gal Class G cement (containing 40% BWOC silica flour, 4.3% BWOC gypsum, fluid-loss-control additive, and CaCl<sub>2</sub> accelerator), 14.5 lbm/gal thixotropic cement (containing 92% Class cement, 8% BWOC gypsum with 40% by weight of blend silica flour, fluid-loss-control additive, and CaCl<sub>2</sub> accelerator), 11.65 lbm/gal foamed cement (containing Class G cement, 40% BWOC silica flour, and surfactant to generate 26% gas by volume of the foamed cement), 11.65 lbm/gal high-strength cement (containing hollow ceramic microspheres, >40% BWOC silica flour, fluid-loss-control additive, and CaCl<sub>2</sub> accelerator), and 12.5 lbm/gal flexible and expanding cement (containing 50% by volume of blend solid flexible particles, and MgO-based expander). These cement formulations were exposed for duration ranging from 0 up to two years and the mechanical properties were measured afterwards. Compressive strength of conventional Class G cement formulation was the highest (>8000 psi) after the test period. This was attributed to the formation of crystalline phases at high temperature. However, strength loss becomes noticeable with time. The conventional and foamed cement formulations exhibited higher brittleness when compared to other cement systems. Furthermore, James and Boukhelifa (2008) presented techniques for evaluating the mechanical properties of hardened cement. Cement properties investigated include unconfined compressive strength (UCS), Young's modulus, Poisson's ratio, and tensile strength. Four cement systems, including 17.02 lbm/gal Class G cement with 35% silica



flour, were cured at 392°F and 482°F. The conventional Class G cement formulation (cured at 392°F) was aged from 1 to 26 weeks (6 months). After aging, UCS in the range 8700-11600 psi was measured. These values are comparable to the measurement obtained by Stiles (2006). However, some disparities in measurements arise from the compositions of each cement system, aging temperature and test period. Teodoriu et al. (2012) and Teodoriu et al. (2013) studied the effect of curing temperature on compressive strength development of neat Class G cement. After mixing, the slurry was cured in rectangular molds at room condition and at 149°F and 212°F for duration lasting up to 55 days. After measurement, it was observed that strength increased with temperature. The maximum compressive strength (about 9400 psi) was attained after 30 days of curing at 149°F. Saunders and Walker (1954) investigated the effect of temperature on mechanical strength of well cement. ASTM types I, II and III cements were used to study the effect of extreme curing conditions on mechanical integrity. Slurries containing various blends of additives were prepared from these cements and cured at 3000 psi and temperatures ranging from 200°F to 320°F for 1, 3 and 7 days. Values of compressive strength measured after curing shows strength retrogression at elevated temperature. However, addition of retarders and pozzolans to some of the cement formulations minimized this strength deterioration. Eilers et al. (1983) and Nelson and Eilers (1985) investigated the effect of high temperature curing on integrity of Classes G and H cement. In their study, compressive strength and water permeability were measured after curing these classes of cement for 24 month at 446°F. After 1 month, the compressive strength of both cement decreased from its initial values and water permeability increased significantly. To control this loss of integrity, standard formulations of these classes of cement were

stabilized with 35% silica leading to considerable improvement in cement properties. Many other investigators (e.g. Mirza et al., 1991; Scherer et al., 2011; Richardson, 2008) arrived at the same conclusion that the strength of hardened cement deteriorates as temperature increases but addition of silica helps to stabilize the cement by minimizing strength retrogression. Noik and Rivereau (1999) measured the compressive strength and water permeability of Class G cement containing 35-40% silica sand after the specimens were aged at 248°F, 284°F, and 356°F for time period between 3 months and 2 years. They observed an initial decrease in strength at early duration followed by strength stabilization and then decrease in strength. Microstructural analysis of the aged specimens, using NMR and discontinuous DRX techniques, confirms the formation of CSH and quartz at 248°F, CSH, quartz, and xonotlite at 284°F, and quartz and xonotlite at 356°F. The formation of these minerals account for the observation in mechanical and transport properties. Le Saoût et al. (2006a, 2006b) immersed Class G cement containing sand and silica fume in brine solution for one year under two test conditions (68°F, 14.5 psi and 176°F, 1015 psi). After the test, the microstructure and mineralogy of the specimens were characterized by Si, Al NMR and XRD techniques. Unhydrated clinker materials ( $C_3S$ ,  $C_2S$ ,  $C_3A$  and  $C_4AF$ ), silica fume, quartz, portlandite,  $AF_t$  (calcium sulfoaluminate hydrates e.g. ettringite,  $AF_m$  (calcium aluminate hydrates), and crystalline phases of CSH were detected after 30 days of curing at 68°F and 14.5 psi. By six month of exposure at this test condition, pozzolanic reactions between portlandite and silica fume results in the complete consumption of portlandite. For the specimens cured at 176°F and 1015 psi, portlandite and silica reacted to form tobermorite (a crystalline form of CSH) but  $AF_t$  was not detected.

Increase in curing pressure is believed to accelerate the rate of hydration. However, comprehensive studies are still required for better understanding (Bensted and Barnes 2002; Kutcko et al. 2007). Nonetheless, available hydration model (Lin and Meyer) and experimental data (Bresson et al., 2002) show that the degree of hydration increases with pressure. Experimental data indicates an early stage strength development as pressure increases at high temperature (Kutcko et al. 2007; Bearden 1959). At low temperature (176°F), increase in fluid pressure weakens Portland cement (Liteanu et al. 2009) but the presence of CO<sub>2</sub> minimizes strength loss due to the effect of carbonation.

After cement has hardened, exposure to deionized fluid results in leaching of calcium from the solid matrix. The effect of exposing cement to non-acidic but deionized solution has been investigated (Carde and Francois, 1999; Haga et al., 2005; Gérard, et al., 2002). Generally, calcium leaching and decalcification are identified as the major drivers of the degradation process. This process is initiated by the calcium ion concentration gradient that is established between the pore solution of the cement and the bulk fluid medium in which cement is immersed. This concentration gradient leads to the diffusion of calcium ions from the pore solution to the bulk (deionized) solution. Subsequently, dissolution of calcium-bearing compounds in the solid matrix of the cement is triggered. As leaching progresses, solid-phase calcium present in the cement matrix depends on cement chemistry and the condition under which it has been exposed. **Figure 2.3** shows typical solid phase calcium profiles obtained from microprobe analysis on cement samples after leaching test (Haga et al. 2005). Initially, calcium concentration in the solid phase was constant throughout the specimen. However, increased exposure time leads to the progressive reduction in calcium content from the center of the specimen

towards the surface. This is due to calcium leaching. This alteration in solid phase calcium will result in increase in porosity, permeability and loss of mechanical strength.

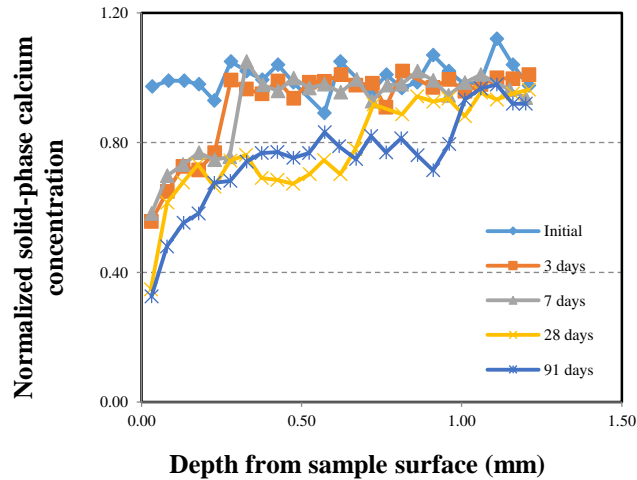


Figure 2.3 Experimental solid phase calcium profile of pure cement sample (Haga et al., 2005)

### 2.3.2 Experimental Studies in the Presence of CO<sub>2</sub>

Barlèt-Gouédard et al. (2006) investigated the degradation of well cement caused by exposure to wet supercritical CO<sub>2</sub> and CO<sub>2</sub>-saturated water. The formulated slurry comprises of Class G Portland cement, an antifoam agent, a dispersant and a retarder. The specimens used in the experiment were first cured for 3 days, at 3000 psi and 194°F, and subsequently exposed to static wet CO<sub>2</sub> at 4061 psi and 194°F for 3 months. The carbonation depth, compressive strength, weight and volume change of the cores, density and porosity, and pH of fluid were measured to quantify the degree of degradation. Carbonation depth increased steadily as time progresses but stabilizes quicker in CO<sub>2</sub>-saturated water than in wet supercritical CO<sub>2</sub>. However, strength reduction was more severe for specimens that were aged in wet supercritical CO<sub>2</sub>. Back-scattered electron images show that portlandite and calcium silicate hydrate were carbonated to form carbonates (calcite, aragonite and vaterite) and amorphous silica gel.

The results also show evidence of progressive densification as time progresses. In a similar study, Barlèt-Gouédard et al. (2009) assessed the CO<sub>2</sub>-resistance of conventional Portland cement. The specimens were first cured for 72 hours at 194°F or 104°F and 1450 psi. Then, CO<sub>2</sub> experiments were conducted at 194°F and 4060 psi or 104°F and 1450 psi. Compressive strength and porosity were measured after the test. Results show an early rapid decrease in strength which then stabilizes as time progresses.

Duguid (2009) estimated the time it would take to completely degrade Class H cement in carbonic acid environment. Exposure tests were conducted at 68°F and 122°F under atmospheric pressure using 0.5 M NaCl solution saturated with CO<sub>2</sub>. Analysis of cement specimens after exposure shows that diffusion of chemical species through the hardened cement is the major cause of deterioration. It was estimated that it would take between 30,000 and 700,000 years to completely degrade a 1 inch thick cement. In HPHT environment, however, reactions between cement materials and carbonic acid will facilitate the rate of attack.

In carbonic acid environment, combined effect of temperature and pressure can result in extensive damage to the mechanical and transport properties of cement. Kutchko et al. (2007) investigated cement degradation in CO<sub>2</sub> environment. Cylindrical cores of Class H cement were cured for 28 days in 1% NaCl solution at different conditions; 72°F and 14.5 psi, 72°F and 4400 psi, 122°F and 14.5 psi, and 122°F and 4400 psi. Exposure of cured samples to CO<sub>2</sub>/brine solution was performed at 122°F and 4400 psi for 9 days. Sample analysis was conducted by scanning electron microscopy (SEM), energy dispersive spectroscopy (EDS), DTA/TGA, XRD analysis and Vickers hardness test. Results show that the degree of hydration is high at high pressure and high

temperature which favors the resistance of CO<sub>2</sub> to carbonic acid attack. In addition, it was observed that the depth of carbonic acid penetration is determined by the initial curing pressure. Compared to curing at ambient conditions (14.5 psi and 72°F), less penetration was observed at high curing pressure (4400 psi) and temperature (122°F). This decrease in degradation depth was attributed to both increase in hydration and change in the microstructure of portlandite since permeability decreases with higher degree of hydration thereby improving resistance to acid attack. Also, a well-defined band of calcite was observed indicating less penetration. Ingress of carbonated water into the cement pores leads to zonal partitioning of the exposed specimen with each zone exhibiting different transport and mechanical properties. In a related study by Kutchko et al. (2008), the rate of acid attack on Class H cement was evaluated. The specimens were cured for 28 days in 1% NaCl solution at 122°F and 4400 psi. Exposure test was conducted by submerging a portion of the specimens in CO<sub>2</sub>-saturated brine and exposing the other portion to supercritical CO<sub>2</sub> at 122°F and 4400 psi for duration up to 1 year. Analysis of the specimens by BSE-SEM, EDS, and XRD shows that the carbonated depth versus square root of time plot (**Figure 2.4**) is linear for the portion of the cement that was exposed to supercritical CO<sub>2</sub> while cement exposed to CO<sub>2</sub>-saturated brine exhibits non-linear behavior. This indicates that the degradation of cement exposed to supercritical CO<sub>2</sub> is governed by diffusion. However, the diffusion of aqueous species through cement exposed to CO<sub>2</sub>-saturated brine is limited by reaction. Carbonation depth of cement exposed to CO<sub>2</sub>-saturated brine was found to be substantially greater than the carbonation depth of specimens that were exposed to supercritical CO<sub>2</sub>. Besides, Figures 2.4 shows

that the rate of deterioration is initially highest at early durations of exposure but decreases as time progresses.

Condor and Asghari (2009) measured compressive strength and permeability of Class G cement after exposure to a mixture of brine and supercritical CO<sub>2</sub> at 2200 psi and 131°F for 3 months. At early period of exposure, strength and permeability decreased initially and then increase possibly due to initial shrinkage. Subsequently, strength decreases while permeability increases, which indicates that the specimens were subjected to leaching. Similar investigations on Class G cement (Tarco and Asghari, 2010) suggests that the peak of carbonation is reached within first few months of exposure after which leaching becomes a dominating degradation mechanism due to the effect of long-term exposure.

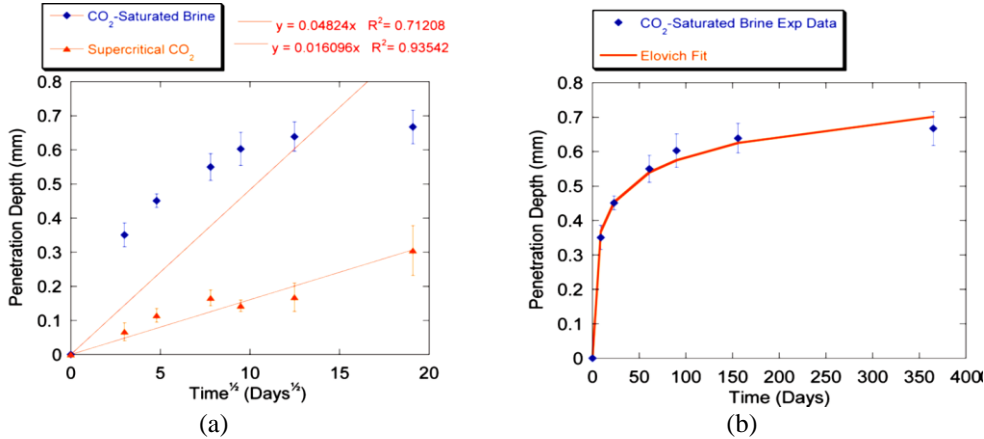


**Figure 2.4 Penetration depth versus time after exposure of cement to CO<sub>2</sub>-containing fluid (Kutchko et al., 2008)**

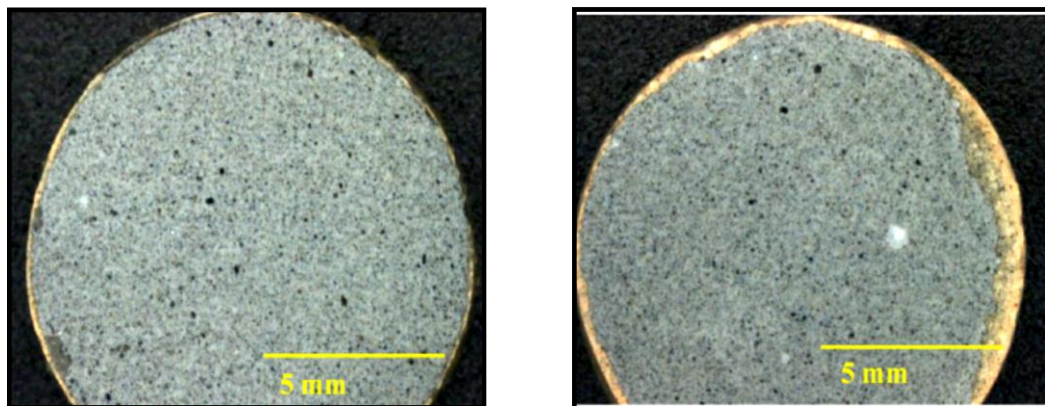
Brandl et al. (2011) measured the mechanical properties and mineral content of cement after exposure to CO<sub>2</sub>-containing fluid. Slurries of Class G cement with 35% BWOC silica flour were prepared and cured for 96 hours at 3000 psi and 300°F after which the specimens were treated with CO<sub>2</sub>-containing water for test period up to 6 months at 3000 psi and 300°F. Strength developed quickly during the first month of

exposure but stabilizes thereafter. Quantitative analysis of mineralogy indicates the formation of calcium carbonate which helps to improve mechanical strength. In a closely-related study, Ilesanmi et al. (2013) designed expanding cement and investigated its long-term performance in CO<sub>2</sub> environment. The cement was cured at 3000 psi and 250°F for 4 days and subsequently exposed to CO<sub>2</sub>-saturated liquid at 3000 psi and 250°F for 6 months. Strength of the cement system increased after exposure due to further hydration and minor carbonation. However, water permeability increased slightly but was below the acceptable value (0.1mD).

Bruckdorfer (1986) examined the effect of wet CO<sub>2</sub> on oil well cement by exposing Class H cement containing 35% silica flour to carbon dioxide at 3000 psi and 175°F for 6 weeks. Before the experiment, the specimens were first cured at 3000 psi and 175°F for 3 days. Carbonation depth and compressive strength were measured after the exposure test. Outcome of this study indicates that cement undergoes a steady decrease in compressive strength and show marked visual deterioration in the presence of wet carbon dioxide after six weeks of exposure. These measurements shows an initial decrease in strength and an observable depth of acid penetration. As the density of the slurry was varied, however, no significant change in compressive strength was observed but carbonation depth shows that less carbon dioxide penetrates as cement density is increased. The work done by Barlèt-Gouédard et al. (2006) and Kutchko et al. (2007, 2008) support the observation of visual degradation. However, similar outcome from Brandl et al. (2011) shows slightly different observation; strength and water permeability increased, though there was evidence of significant carbonation.



Compared to CO<sub>2</sub>-saturated brine (wet CO<sub>2</sub>), the rate of strength loss in cement exposed to supercritical CO<sub>2</sub> is lower (Sauki and Irawan 2010; Barlèt-Gouédard et al. 2009; Kutchko et al. 2008; Carey et al. 2007). **Figure 2.5** shows optical images of Class H neat cement obtained by Kutchko et al. (2011) after exposure to supercritical CO<sub>2</sub> and CO<sub>2</sub>-saturated brine for 28 days at 252°F and 2175 psi. These images illustrate the deeper penetration caused by CO<sub>2</sub>-saturated brine than supercritical CO<sub>2</sub>. The orange rims are characteristic of cement exposed to CO<sub>2</sub>-containing fluid (Barlèt-Gouédard et al., 2006; Carey et al., 2007; Duguid et al., 2006; Kutchko et al., 2007, 2008, 2011).



Pure CO<sub>2</sub> gas in the headspace

CO<sub>2</sub>-saturated in 1% NaCl solution

**Figure 2.5** Optical images of Class H cement exposed to CO<sub>2</sub> fluids (Kutchko et al. 2011)

Deshpande et al. (2015) and Aiex et al. (2015) evaluated the alteration in cement properties after exposure to aqueous CO<sub>2</sub> environment. Neat cement slurry (containing Class G cement, viscosifier, fluid-loss additive, elastometer, expansion additive and defoamer) was used in the study. The specimens were cured and exposed to carbonic acid for duration between 15 days and 365 days at 165°F and 2000 psi. Fluid chemistry and cement properties were measured and cement mineralogy was characterized. Initially, cement properties were improved but cement performance

declined as time progresses. This was attributed to the occurrence of carbonation and leaching.

Santra et al. (2009) conducted an experiment to study how CO<sub>2</sub> reacts with Portland cement at borehole conditions. The specimens were first cured in water at 200°F and 2000 psi for 15 days. Subsequently, the samples were subjected to CO<sub>2</sub> treatment at 200°F and 2000 psi for 15 days (first batch) and 90 days (second batch). Thermal gravimetric analysis (TGA), Brinell hardness and X-ray diffraction were used to assess the scale of deterioration caused by this exposure. In the penetrated zone, estimated amount of portlandite was found to decrease after 15 days. However, Brinell hardness index indicates that this zone is harder than the unpenetrated portion. For the specimens that were exposed for 90 days, depths of penetration were higher than the penetration depths of specimen exposed for 15 days. Sweatman et al. (2009) conducted similar experiment to study the effect of CO<sub>2</sub> on cement degradation. Neat Class G and a CO<sub>2</sub>-resistant formulation were used in the study. The specimens were exposed to CO<sub>2</sub> (CO<sub>2</sub>-saturated water and supercritical CO<sub>2</sub>) at 2000 psi and 140°F for 15 days (batch 1) and 90 days (batch 2) after curing at 2000 psi and 140°F for 28 days. Both cement system showed evidence of chemical degradation but it is more significant in neat Class G cement because it produces more portlandite and calcium carbonate during hydration and carbonation respectively.

Bois et al. (2013) studied the mechanisms of mechanical degradation of Class G cement exposed to CO<sub>2</sub>-saturated water under three test programs: carbonation test at 194°F and 1160 psi, carbonation test at 284°F and 1160 psi, and coupled chemo-mechanical (dynamic) test. In the dynamic test, typical downhole condition was simulated

by mechanically-loading the specimen under triaxial loading conditions while simultaneously exposing it to CO<sub>2</sub>-saturated water. Test duration varied from one week to 3 months. Degradation caused by these exposure tests was determined using techniques such as X-Ray tomography, SEM, XRD, etc. The specimen that was exposed to carbonic acid during triaxial compression shows less penetration than the specimen without mechanical loading.

Laudet et al. (2011) and Garnier et al. (2012) investigated the kinetics of chemical degradation of cement after exposure to CO<sub>2</sub>-rich fluids. Two test programs (static and dynamic tests) were employed and two cement materials were tested: neat Class G cement and Class G cement with 35% BWOC silica flour. The neat Class G cement was tested (i.e. curing and CO<sub>2</sub>-exposure) at 194°F and at atmospheric pressure while Class G cement with 35% BWOC silica flour was tested at 284°F and 3000 psi. CO<sub>2</sub> pressure was maintained at 1160 psi throughout the tests. X-Ray tomography images indicate the formation of carbonation front which progresses from the surface of the specimen towards its center. The rate of propagation of this front was determined to be faster in the specimens aged at high temperature (284°F) which indicates more carbonation and or leaching. However, chemical analysis of the aging fluid samples (leachant) shows that more calcium is released into solution at 284°F than 194°F. Empirical relationship between the degradation depth and exposure time reveals that the degradation of neat Class G cement is mainly governed by diffusion whereas the diffusion of solutes in Class G cement with 35% BWOC silica flour is limited by reaction kinetics. Mineralogical analysis shows that the outer surface of the exposed specimens is the most carbonated; calcite and aragonite were the main minerals detected by XRD analysis.

Carey et al. (2007) evaluated cement samples that were recovered from a well in SACROC unit, West Texas. The well was exposed to CO<sub>2</sub> for 30 years. Assessment of air permeability of the specimen indicates that the cement still has capacity to minimize fluid flow after several years of interacting with carbonated fluid. In addition, it was observed that the thickness of carbonated portion of the cement was greater at the cement-rock interface than at the casing-cement interface. Besides, XRD analysis of the retrieved specimen shows the presence of calcite, aragonite, vaterite, katoite, quartz and residual uncarbonated portlandite.

Neuville et al. (2012) characterized Class G cement after exposure to carbonated brine. Cement slurry was cured for 1 month at 176°F and curing pressures of 1015 psi and 2900 psi. After curing, degradation tests was performed by aging the cured specimens in constantly-renewed carbonated brine at 176°F/14.5 psi, 176°F/1015 psi and 176°F/2900 psi for 1 month. At the end of the test, Mercury Intrusion Porosimetry (MIP), SEM, XRD, TGA/TDA and Si/Al NMR techniques were used to characterize the degraded specimens. Three zones (inner, middle and outer) were identified in the specimens. At 176°F and 14.5 psi, the inner zone was mainly composed of portlandite, calcium silicate hydrate, katoite and AF<sub>m</sub>. At 176°F and 1015 psi, the amount of portlandite detected in this zone is lower and a small amount of calcium carbonate was detected. At 176°F and 2900 psi, the amount of portlandite decreased further. The middle zone is very thin and SEM indicates high porosity which arises from the leaching of calcium from portlandite. However, the outer zone is mainly composed of calcium carbonate. The detection of calcite, aragonite and katoite agrees with field observation by Carey et al. (2007).

Sauki and Irawan (2010) conducted experiments to study the effects of temperature and pressure on cement degradation in the presence of supercritical CO<sub>2</sub>. Class G cement was used for the experiment. The specimens were initially cured before exposure to CO<sub>2</sub> environment. Curing and CO<sub>2</sub> exposure tests were carried out under two conditions. In the first condition, the tests were conducted at two temperatures (104°F and 248°F) and a constant pressure of 2031 psi. In the second condition, the tests were conducted at two pressures (1523 psi and 2031 psi) and a constant temperature of 104°F. Curing duration is 8 hours while CO<sub>2</sub> exposure tests were performed for 1, 3 and 5 days. After the test, compressive strength was measured. In addition, the microstructure, mineralogy and morphology of the specimens were characterized by XRD, EDX, and back-scattered electron (BSE)-SEM. Reduction of strength was more severe at high temperature. Unhydrated cement compounds were detected but the amount of these clinker materials is low at high temperature. Also, formation of calcium carbonate and amorphous silica was observed.

Lesti and Planck (2013) compared the performance of different cement systems to API Class G cement. The specimens were first cured for two weeks in synthetic reservoir fluids at atmospheric conditions and then for 28 days at 5800 psi and 194°F. CO<sub>2</sub> exposure experiment was also conducted at 5800 psi and 194°F. Compressive strength of the cement systems reduced after exposure but the residual strength is still sufficient for casing support. Results of the measurement of porosity and permeability agrees with strength measurement and the formation of calcium carbonate was observed.

Mason et al. (2013) investigated the alterations caused by exposing cement to CO<sub>2</sub>-rich brine. Class G cement was used in the experiment. The slurry was cured at 2176 psi and 122°F for more than 28 days. Exposure test was carried out at CO<sub>2</sub> pressure of 435 psi and 140°F for 8 days. Analysis of mineralogy by NMR and SEM reveals the formation of portlandite, calcium silicate hydrate, ettringite, aragonite and calcite, in addition to the unhydrated cement compounds. Besides, uniquely degraded zones were observed. Precipitation of carbonate was observed in the carbonate layer while dissolution of carbonates was observed in the amorphous layer. As a result of this alteration in mineralogy, Young's modulus of elasticity decreased across all degraded zones.

Newell and Carey conducted experiment to study the leakage pathway along cement-formation interface. Class H cement, containing fly ash and bentonite, was used for the experiment. The cement was cured for 1 week at 149°F and held at room temperature for 1 year. A composite core of the cement and rock was prepared and exposed to supercritical CO<sub>2</sub>-brine system at 1450 psi and 140°F after which the permeability of the core was measured. Results show a significant reduction in permeability after exposure. Although electron microscopy indicates that the core was leached, the drop in permeability was not attributed to carbonation but on migration and formation of other minerals.

Milestone et al. (1986) studied the effect of silica on Portland cement after exposure to CO<sub>2</sub> for 14 days at 302°F. After investigating different compositions of silica, it was found that the presence of excess silica results in pozzolanic reaction with portlandite, which leads to reduction in the amount of portlandite. Therefore, 15% BWOC

silica was recommended for portlandite retention instead of the conventional 35-40% BWOC.

### **2.3.3 Summary**

**Table 2.3** is a summary of some of the previous studies. Overall assessment of these previous investigations reveals three major limitations to the existing state of the art in corrosion of well cement by CO<sub>2</sub>-containing fluids.

Firstly, most of the previous studies are limited to low pressure and low temperature investigations. However, the current trends in the petroleum industry indicate that operators are now seeking additional oil and natural gas from unconventional HPHT resources. In addition, exploratory activities have recently increased in geothermal environment.

Secondly, the effects of variation in downhole parameters has not been investigated. **Table 2.4** shows the operational pressure, temperature and CO<sub>2</sub> concentration for some of the notable carbon capture, utilization and storage (CCUS) projects. Extreme variation in these downhole parameters will have significant effect on the reliability of the cement used to complete the wells.

Thirdly, although aging tests of cement in CO<sub>2</sub> environment have been investigated over long duration (Deshpande et al. 2015; Barlèt-Gouédard et al. 2006; Santra et al. 2009; Kutchko et al. 2008; Matteo and Scherer 2012), the outcome of these studies, especially the work done by Barlèt-Gouédard et al. 2006, Kutchko et al. 2008 and Matteo and Scherer 2012 clearly shows that the rate of deterioration is initially highest at early durations of exposure but decreases as time progresses. The effect of this early exposure to carbonated brine has not been thoroughly investigated.

After qualitatively describing the outcome of chemical analyses conducted on cement samples that were retrieved from a 19-year-old well at Teapot Dome in Wyoming, Scherer et al. (2011) recommended additional cement retrieval and further experimental and theoretical modeling studies on cement degradation. Understanding how well cement is corroded during the early period of contact with CO<sub>2</sub>-rich brine in HPHT environment is not only vital for long-term deliverability of well, but it is extremely critical for the safety of lives and the environment.

**Table 2.3 Summary of experimental studies on oil well cement degradation**

Reference	Cement type	Maximum exposure condition			
		Press. (psi)	Temp. (°F)	Fluid system	Time
Sauki et al. (2010)	Class G	2031	248	CO <sub>2</sub> + 0.01m NaCl (brine) solution	120 hours
Barlèt-Gouedard et al. (2006)	Class G	4061	194	Wet supercritical CO <sub>2</sub> and CO <sub>2</sub> – saturated water	85 days
Barlèt-Gouedard et al. (2007)	Class G	4061	194	CO <sub>2</sub> -saturated water and wet supercritical CO <sub>2</sub>	83 days
Bruckdorfer (1986)	Classes A, C and H	3000	175	CO <sub>2</sub> -saturated water	6 weeks
Brandl et al. (2010)	Class G	3000	300	CO <sub>2</sub> environment	90 days
Condor and Asghari (2009)	Class G	2200	131	Mixture of supercritical CO <sub>2</sub> and brine	12 months
Ilesanmi et al. (2013)		3000	250	CO <sub>2</sub> -saturated brine.	6 months
Kutchko et al. (2007)	Class H.	4395	122	Supercritical CO <sub>2</sub> and CO <sub>2</sub> + 1% NaCl solution	9 days



Kutchko et al. (2008)	Class H	4395	122	Supercritical CO <sub>2</sub> and CO <sub>2</sub> + 1% NaCl solution	1 year
Lecolier et al. (2007)	Class G	1015	176	Water, brine, and crude oil	355 days
Neuville et al. (2012)	Class G	2900	176	Carbonated brine	1 month
Noik and Rivereau (1999)	Class G	1015	356	Deionised water	600 days
Stiles et al. (2006)	Class G	2133	645		24 months
Santra et al. (2009)	Class F	2000	200	Supercritical CO <sub>2</sub> + fresh water	90 days
Santra et al. (2011)		2000	140	Supercritical CO <sub>2</sub> + fresh water	1 year

**Table 2.4 Operational conditions of CCUS projects**

CCUS projects	Well classification (Injecting or producing?)	Operational conditions			Source
		Pressure (psi)	Temperature (°F)	CO <sub>2</sub> composition (%)	
Snohvit	Injecting	4,350-10,160	75-205	99	Einken et al. (2011); Ringrose et al. (2011); Alnes et al. (2011)
In Salah	Injecting	2,900-7,250	130-215	5.5* 98-99.5**	*MIT (2015) CCS project database;**Einken et al. (2011)
Sleipner	Injecting	1,015-1,450	85-125	98	Einken et al. (2011); Ringrose et al. (2011); Alnes et al. (2011)
Greater Gorgon Fields	Injecting	***	***	14	MIT (2015) CCS project database
LaBarge field	Producing/Injecting	***	***	40	MIT (2015) CCS project database
Port Arthur Project	Injecting	***	***	97	MIT (2015) CCS project database
Wasatch Plateau	Injecting	***	***	98	MIT (2015) CCS project database

\*\*\*Information was not available at the time this study was conducted

## 2.4 Theoretical Modeling Studies

### 2.4.1 Modeling Studies without CO<sub>2</sub> Effect

The amount of hydrates formed after curing of cement and the mechanical and transport properties developed are directly related to the degree of hydration of clinker compounds. Empirical models are available to estimate degree of cement hydration (Cervera et al. 1999; Cervera et al. 2002) but their use is limited to experimental conditions under which they were developed. Most of these empirical models were developed for low temperature applications and effects of curing pressure are neglected. In wellbore scenario involving pressure and temperature cycles, these models may not be sufficient to capture the chemical reaction and thermodynamic processes occurring at microscopic level; hence, a huge set back in their application for HPHT degradation modeling.

The individual degrees of hydration of clinker compounds was described by Lothenbach et al. (2008) following the work done by Parrot and Killoh (1989). The hydration model was based on three stages during hydration process. Equations 2.20, 2.21, and 2.22 were used to describe the rate of hydration ( $R_t$ ) during each stage:

Stage 1: Nucleation and growth

$$R_t = \frac{K_1}{N_1} (1 - \alpha_t) \{-\ln(1 - \alpha_t)\}^{(1-N_1)} \dots\dots\dots (2.20)$$

Stage 2: Diffusion

$$R_t = \frac{K_2 (1 - \alpha_t)^{\frac{2}{3}}}{1 - (1 - \alpha_t)^{\frac{1}{3}}} \dots\dots\dots (2.21)$$

Stage 3: Formation of hydration shell

$$R_t = K_3 (1 - \alpha_t)^{N_3} \dots\dots\dots (2.22),$$

where the terms  $K_1$ ,  $K_2$ ,  $K_3$ ,  $N_1$ , and  $N_3$  are properties of each clinker phase.

$R_t$  is computed at each time step and the stage corresponding to the least value is considered to be the rate-controlling process.

The rate of hydration of cement is influenced by temperature and pressure. A hydration model, which is based on the reactive porous media theory, was developed by Lin and Meyer (2009). Predictions from this model reasonably matched experimental data acquired at high pressure (up to 12,000 psi) and moderately high temperature (up to 195°F). Clinker composition, cement fineness, water-cement ratio, curing temperature, and applied pressure are input variables accepted by the model. Model assumption is built around three stages of hydration; an early chemical dissolution stage otherwise called pre-induction, transport quiescent stage which starts when ions move in and out of surfaces of anhydrous cement particles slowly developing layers of hydrated product, which lasts for few days, and a diffusion-controlled late stage which is the longest and most dominant. Other investigators (Zhang and Ye, 2012; Dabić et al., 2012) have developed models for the degree of hydration.

Calcium leaching in cementitious materials has been modeled by many investigators (Mainguy et al. 2000; Mainguy and Coussy 2000; Gérard et al. 2002; Carde et al. 1996; Carde and Francois, 1999; Haga et al., 2005; Nakarai et al. 2006). This phenomenon is often modeled as a diffusion process, which is governed by Fick’s law of diffusion. Equation 2.23 is generally adopted as the governing 1-D partial differential equation for calcium leaching in a static deionized fluid.

$$\frac{\partial}{\partial x} \left( D_{Ca^{2+}} \frac{\partial C_{Ca^{2+}}}{\partial x} \right) - R_{Ca^{2+}} = \frac{\partial (\phi C_{Ca^{2+}})}{\partial x} \dots\dots\dots (2.23),$$

where,

$D_{Ca^{2+}}$  = effective diffusion coefficient of  $Ca^{2+}$  ion

$C_{Ca^{2+}}$  = concentration of  $Ca^{2+}$  ion in the pore solution (liquid phase)

$R_{Ca^{2+}} = \frac{\partial C_s}{\partial t}$  = rate of dissolution of calcium-bearing minerals (i.e. CH and CSH)

$C_s$  = concentration of calcium in the solid phase (i.e. CH and CSH)

$\phi$  = matrix porosity

Mainguy and Coussy (2000) developed an analytic solution (equation 2.24) for predicting the leached depth, subject to the condition that the deionized water is constantly renewed at the surface of the specimen (i.e. the concentration of calcium at the surface of the specimen is always zero). This solution is useful in predicting location of the dissolution front once it propagates. Numerical solution was also obtained by the authors using finite volume technique.

$$x_d = 2\xi_d \sqrt{Dt} \dots\dots\dots (2.24)$$

$\xi_d$  is obtained by solving equation 2.25.

$$\varepsilon e^{-\xi_d^2} = \sqrt{\pi} \xi_d \operatorname{erf}(\xi_d) \dots\dots\dots (2.25)$$

where,

$$\varepsilon = \frac{\phi C_{Ca^{2+}}^{eq}}{C_s^o}$$

$C_{Ca^{2+}}^{eq}$  = concentration of  $Ca^{2+}$  at equilibrium

$C_s^o$  = Initial total concentration of calcium in the solid matrix before leaching commences

For diffusion-controlled processes, a linear relationship exist between the leached depth and square root of exposure time (Mainguy at al. 2000; Mainguy and Coussy 2000; Gérard et al. 2002; Carde et al. 1996; Fabbri et al. 2012).

In the absence of CO<sub>2</sub>, the decrease in solid-phase calcium concentration is believed to be the major factor governing both the decrease in mechanical strength and the increase in porosity (Carde et al. 1996; Carde and Francois 1997; Carde and Francois 1999). This loss in calcium arises from the dissolution of portlandite and the progressive decalcification of calcium silicate hydrate (a major strength component); hence the loss of strength and increase in porosity. Carde and Francois (1999) proposed a simple model for predicting relative loss of strength after calcium leaching. The underlying assumption in the development of this model is that stress distribution in leached zone is similar to calcium distribution in the solid phase of the cement, since loss of calcium is assumed to be solely responsible for mechanical degradation. The mathematical model was developed for two cases of blended cement samples; pure Portland cement paste and Portland cement paste containing silica fume.

For pure Portland cement paste, equation 2.26 was proposed for the degraded strength ratio.

$$\frac{\Delta\sigma}{\sigma} = 1 - \frac{1}{r^2} \left\{ \left( 1 - \frac{R_c R_p}{12} - \frac{11R_p}{12} \right) x_d^2 + \left( \frac{3rR_p}{2} + \frac{rR_c R_p}{2} - 2r \right) x_d + r^2 \right\} \dots\dots\dots (2.26)$$

For Portland cement paste with silica fume, equation 2.27 was proposed.

$$\frac{\Delta\sigma}{\sigma} = 1 - \frac{1}{r^2} \left\{ \left( \frac{1 - R_c}{3} \right) x_d^2 + r(R_c - 1)x_d + r^2 \right\} \dots\dots\dots (2.27),$$

where,

$\sigma$  = compressive strength of the control (unleached) specimen

$\Delta\sigma$  = loss in compressive strength after leaching

$x_d$  = leached depth

$r$  = radius of the specimen

Parameters  $R_c$ ,  $R_p$ , and  $x_d$  are estimated from the solid-phase calcium profile.

The degraded depth ( $x_d$ ) can be estimated using Mainguy and Coussy (2000) model, although this may not provide good estimate due to the boundary condition assumed in the derivation of the analytical solution.

#### **2.4.2 Modeling Studies with CO<sub>2</sub> Effect**

When brine solution is laden with CO<sub>2</sub> gas, aqueous speciation takes place until a reasonable state of equilibrium is attained. The molality of the solute species in solution is of great interest because these species are responsible for chemical activities with the solute species in the pore solution of cement. Duan and Sun (2003), Duan et al. (2007) and Millero et al. (2002, 2007) have worked extensively on modeling the phase equilibria of binary, ternary and multi-component systems involving the dissolution of CO<sub>2</sub>. Under HPHT conditions, some of these models provide good prediction of the solubility of aqueous species within acceptable experimental errors.

Acid attack of cement by carbonic acid leads to mineral precipitation and dissolution as described by equations 2.14 to 2.19. At any given time, cement minerals (solids) may or may not exist in equilibrium with the aqueous phase, but equilibrium is often reached as time progresses. A common modeling approach is to assume that minerals (e.g. calcite) will dissolve if the aqueous phase is under-saturated with respect to the solid phase thereby increasing the concentration of its products in aqueous phase

(Ceyhan et al. 2011; Raouf et al. 2012). On the contrary, an oversaturated aqueous phase results in mineral precipitation, thereby decreasing the concentration of aqueous species. This dissolution/precipitation hypothesis implies the aqueous phase as the only medium of interaction between the solid minerals and dissolved CO<sub>2</sub> thereby neglecting any direct interaction. This assumption is reasonable since CO<sub>2</sub> is not corrosive by itself but dissociates in aqueous solution to form carbonic acid. For CO<sub>2</sub>-saturated brine, the aqueous solution is often a bulk fluid with significant volume whereas the aqueous solution for cement exposed to supercritical CO<sub>2</sub> is the fluid in its pores. In addition, since the objective interest is to model alterations in mechanical strength of cement when exposed to acidic environment, overall effect of mineral dissolution/precipitation determines this residual mechanical strength.

Generally, a one-dimensional Fick's law similar to equation 2.23 is often used to mathematically represent the diffusion of all aqueous species and many authors have been consistent with this approach (Glasser et al. 2008; Haga et al. 2005; Crank 1975). The reaction term (positive for mineral precipitation and negative for mineral dissolution) is typically expressed by a rate kinetic law. Scherer and Huet (2009) developed analytical solution for cement that is exposed to time-independent reservoir of carbonated brine in a cylindrical wellbore. Equation 2.28 was presented for estimating the carbonated depth:

$$x_c = r_o \left\{ 1 - \sqrt{1 - \frac{C_o}{\pi C_{Ca}} \left(1 - \frac{z}{L}\right) \sum_{n=1}^7 a_n \left(\frac{Dt}{r_o^2}\right)^{\frac{n}{2}}} \right\} \dots\dots\dots (2.28)$$

where,

$r_o$  = radius of cement

$C_o$  = concentration of acid at the reservoir interface

$C_{Ca}$  = concentration of calcium

Using the transport equation proposed by Crank (1975), Matteo and Scherer (2012) published analytical models for the degraded depth that includes the effect of acid penetration. These models are analogous to the model proposed by Mainguy (2000); the major difference arises from the reaction term included in the partial differential equation and imposed boundary conditions.

Unlike diffusion-controlled models, the relationship between the degraded depth and square root of exposure time is not linear but strongly influenced by temperature and solution pH due to reaction between aqueous species (Raouf et al. 2012; Matteo and Scherer 2012). Hence, the mechanism of degradation is reaction-controlled but diffusion-limited.

The major demerit with these analytical models is their representativeness, especially in wellbore condition where calcium concentration at the external boundary of the cement (i.e. cement-formation interface) varies due to mineral dissolution/precipitation. Therefore, they should be applied with caution in cement degradation modeling.

Besides, diffusion of carbonic acid through cement matrix in a casing-cement-rock system, is best modeled as a radial problem since cement is always placed in the annular area between casing and rock formation. Therefore, the one-dimensional approach is only appropriate for linear penetration as may be the case in cement plugs used for well abandonment purposes. Furthermore, the assumption that diffusion is the sole transport mechanism that governs the supply of dissolved CO<sub>2</sub> to the pore fluid may



not be completely representative. Although this supposition may be valid for a perfectly-cemented annulus (one in which micro-annulus does not exist between the casing-cement and cement-rock interfaces) where carbonic acid is relatively static, it does not account for fluid movement as would be expected in sections of the well close to the perforations and behind casing for poorly cemented casing strings.

### **2.4.3 Summary**

Cement exposed to brine saturated with CO<sub>2</sub> undergoes combination of hydration, carbonation and leaching processes, which are controlled by slurry composition, temperature, pressure, and CO<sub>2</sub> partial pressure. This makes the modeling of cement deterioration very challenging. The approach used by previous investigators is to isolate these processes and model them separately. This is an oversimplification of the problem because, in reality, these processes interact in a very complex manner which would require mathematical coupling. Besides, the analytic models proposed by these investigators were developed under exposure conditions that are not representative of practical wellbore scenario. Thus, applications of these model are very limited.

## **Chapter 3 Mechanisms of Cement Degradation in HPHT Carbonic Acid Environment**

### **3.1 Overview**

Well cement is very susceptible to chemical attack in the presence of reactive fluids such as carbonic acid, sulfuric acid, hydrochloric acid, etc. Real world scenarios involving practical exposure of well cement to these aggressive fluids include CO<sub>2</sub>-EOR, carbon capture and storage, CO<sub>2</sub>/H<sub>2</sub>S co-sequestration and matrix acidizing. Literature survey presented in Chapter 2 reveals that the origin of cement degradation can be due to physical, chemical or mechanical processes or combination of these. Physical degradation occurs when cement is exposed to reactive fluids which leads to physical discoloration. This mode of degradation also takes place when cement shrinks during hydration which may result in loss of hydraulic and shear bonding. Chemical degradation occurs when cement reacts with aggressive fluids to form minerals that are easily leachable or susceptible to further reaction. Mechanical degradation occurs when cement is subjected to expansion and thermally-induced pressurization which leads to the formation of cracks thereby increasing permeability. This mode of degradation arises when cement is exposed to extreme loading conditions resulting from drilling, reservoir depletion and geological processes. Cement exposed to brine saturated with CO<sub>2</sub> undergoes combination of processes which includes hydration and chemical shrinkage, expansion and thermally-induced pressurization, structural transformation of calcium silicates, decalcification, carbonation, bi-carbonation and mineral leaching. The degree of occurrence of these processes are controlled by temperature, CO<sub>2</sub> gas composition, pressure, slurry

compositions, and brine concentration. This chapter describes the mechanisms involved in the degradation of well cement in HPHT carbonic acid environment.

### **3.2 Hydration and Chemical Shrinkage**

Cement degradation due to hydration results from interrelated chemical processes which are affected by particle fineness and size distribution, clinker composition, blended additives, water-to-cement ratio and curing conditions (temperature, pressure and brine concentration). The chemical reactions involved were presented in Chapter 2.  $C_3S$  is the principal component that controls setting and early strength development because it hydrates faster than  $C_2S$ . However, slow hydration of  $C_2S$  contributes to long-term development of strength. In field operations, most of the  $C_3S$  and  $C_2S$  components are hydrated during “wait on cement” period, through a curing process, thereby producing amorphous calcium silicate hydrate (CSH) and calcium hydroxide or portlandite, both of which aid early strength development. Correspondingly, hydration of  $C_3A$  is more rapid than the hydration of  $C_4AF$ . However, these has no effect on strength development but on rheology of the slurry and the expansion characteristics, especially  $C_3A$ , after setting (Carter et al., 1966; Moran et al., 1991). Conversely, the formation of large-size crystals of ettringite in the presence of gypsum (equations 2.7 and 2.11 in Chapter 2) leads to expansion and might result in the development of cracks.

$C_3S$ ,  $C_2S$ ,  $C_3A$  and  $C_4AF$  hydrate simultaneous upon mixing with water to produce cement hydrates (equations 2.5 through 2.13 in Chapter 2); hence, there is overlapping of hydration of these components. Therefore, the overall degree of hydration is usually different from individual degrees of hydration. **Figure 3.1** shows the prediction of the individual degrees of hydration of the clinker compounds using the model proposed

by Lothenbach et al. (2008). This parameter determines the amount of cement hydrates formed (i.e. CH, CSH,  $C_3AH_6$ ,  $C_3A\bar{C}_3H_{32}$ ,  $C_3A\bar{C}H_{12}$ , and  $FH_3$ ) and the transport properties (porosity and permeability) of the cured cement. As hydration progresses, stresses can be induced from the growth of CSH gel which is caused by absorption of pore fluid during hydration process. With high growth rate, these stresses may generate micro-fractures that permit fluid flow after the cement hardens. Although compressive strength in the range 100-500 psi and water permeability of 0.1 mD are generally sufficient to proceed with drilling after cement is set behind the casing (Bouroyne et al. 1986; Stiles 1997, Nelson et al. 1981), further hydration occur throughout the productive life of the well and after it has been abandoned.

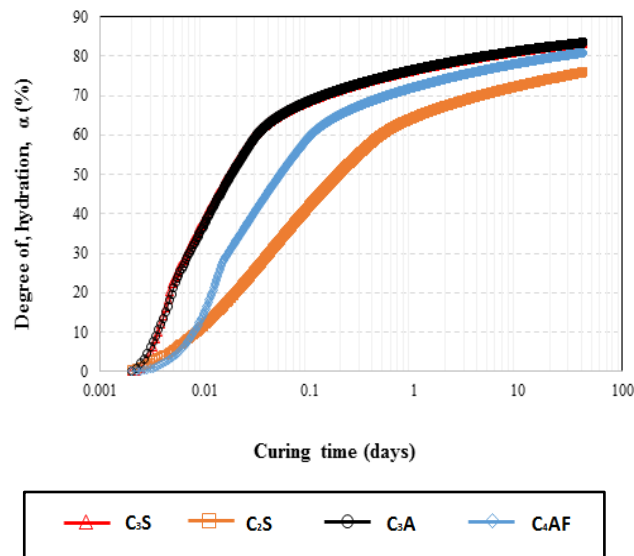


**Figure 3.1 Individual degrees of hydration of clinker compounds generated using Lothenbach et al. (2008) and Parrot and Killoh (1989) model**

Chemical shrinkage is a phenomenon that occurs when the volume of cement reduces during setting of cement slurry. This process has been observed by many investigators (Beirute and Tragesser, 1973; Backe et al., 1998; Backe et al., 1999; Holt, 2005; Justnes, et al., 1995; Chenevert and Shrestha, 1991; Parcevaux and Sault, 1984;

Reddy et al., 2009). Chemical shrinkage results in the development of internal porosity which are often filled with vapors; thus, decreasing the pore pressure. This decrease in pore pressure increases the effective stress on cement (Terzaghi effect), which results in capillary-related internal stresses. This can lead to the formation of cracks in the cement and the debonding of cement from the casing or rock. Cement shrinkage also reduces the hydrostatic pressure of the slurry column in wells, thus creating a well stability problem during wait-on-cement period. In the lateral section of horizontal wells, shrinkage of cement may also result in the formation of free water (**Figure 3.2**). Shrinkage of cement is affected by temperature, pressure, and salt concentration. Generally, cement shrinkage increases with temperature and pressure but decreases with salt concentration.

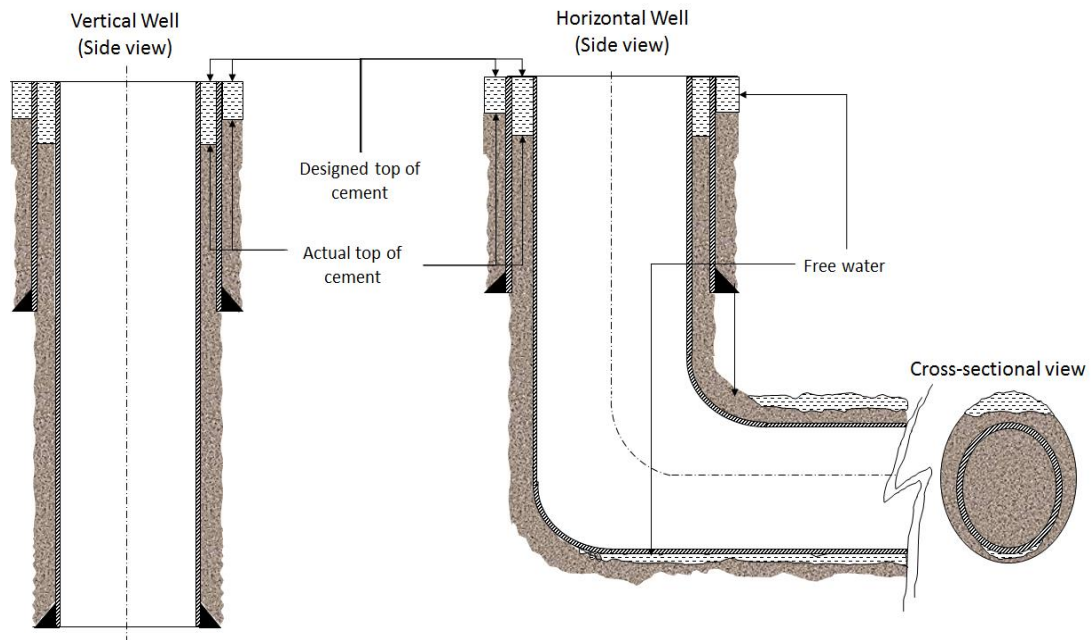


**Figure 3.2** Effect of shrinkage on cement seal

### **3.3 Structural Transformation of Amorphous CSH**

This refers to the conversion of amorphous calcium silicate hydrate (CSH) gel (or normal tobermorite gel), formed at ambient temperature, to one or more crystalline phases at elevated temperatures. The generalized chemical formula for these crystalline

compounds is  $(\text{CaO})_x \cdot (\text{SiO}_2)_y \cdot (\text{H}_2\text{O})_z$  but they are collectively designated as C-S-H. **Table 3.1** shows the mole numbers of lime (x), silica (y), and water (z) in some known crystalline phases of calcium silicate hydrate. Cement degradation due to CSH structural transformation is a phenomenon that occurs predominantly during cement curing at elevated temperature and has been reported extensively in literatures (Richardson, 2008; Eilers et al., 1983; Nelson et al., 1981; Nelson, 1990; Taylor, 1964 and 1997).

**Table 3.1 Mole numbers of lime, silica, and water in some crystalline C-S-H phases**

Crystalline C-S-H	Chemical formula	x	y	z
Afwillite	$(\text{CaO})_3 \cdot (\text{SiO}_2)_2 \cdot (\text{H}_2\text{O})_3$	3	2	3
Wollastonite	$(\text{CaO})_1 \cdot (\text{SiO}_2)_1 \cdot (\text{H}_2\text{O})_0$	1	1	0
Hillebrandite	$(\text{CaO})_2 \cdot (\text{SiO}_2)_1 \cdot (\text{H}_2\text{O})_{1.17}$	2	1	1.17
Gyrolite	$(\text{CaO})_2 \cdot (\text{SiO}_2)_3 \cdot (\text{H}_2\text{O})_{2.5}$	2	3	2.5
Foshagite	$(\text{CaO})_4 \cdot (\text{SiO}_2)_3 \cdot (\text{H}_2\text{O})_6$	4	3	6
Tobermorite 9Å	$(\text{CaO})_5 \cdot (\text{SiO}_2)_6 \cdot (\text{H}_2\text{O})_{1-3}$	5	6	1 to 3
Tobermorite 11Å	$(\text{CaO})_{4-5} \cdot (\text{SiO}_2)_6 \cdot (\text{H}_2\text{O})_{5-6}$	4 to 5	6	5 to 6
Tobermorite 14Å	$(\text{CaO})_5 \cdot (\text{SiO}_2)_6 \cdot (\text{H}_2\text{O})_{7-10.5}$	5	6	7 to 10.5
Xonotlite	$(\text{CaO})_6 \cdot (\text{SiO}_2)_6 \cdot (\text{H}_2\text{O})_1$	6	6	1

Temperature affects early strength development of cement by accelerating the growth of principal products of hydration such as CSH, which is principally responsible for strength development. At curing temperatures exceeding 230°F, CSH gel is no longer stable and will transform to its crystalline polymorphs. Since  $\text{C}_3\text{S}$  is the most important strength component, its hydration is considered as the most influential mechanism for early strength development. Once hydrated,  $\text{C}_3\text{S}$  and  $\text{C}_2\text{S}$  produce calcium silicate hydrate gel which transforms to its crystalline polymorphs at high temperature with possibility of loss of cement integrity. There are several polymorphs of CSH. **Figure 3.3** shows the combination of temperature and C/S ratio that could lead to the formation of some crystalline polymorphs of CSH.

The transformation of amorphous CSH to its structural polymorphs can alter the mechanical and transport properties of the set slurry. Up to 230°F, strength increases with temperature (Calvert 1990) but severe loss is possible at higher temperatures. To minimize strength retrogression at elevated temperature, a common oilfield practice is to add 35-40% BWOC silica flour to the base cement so as to maintain C/S ratio close to 1 (Table 3.2). At C/S ratio of about 1, Figure 3.3 shows that increasing curing temperature will likely transform CSH to tobermorite gel or xonotlite both of which have acceptable mechanical and transport properties.

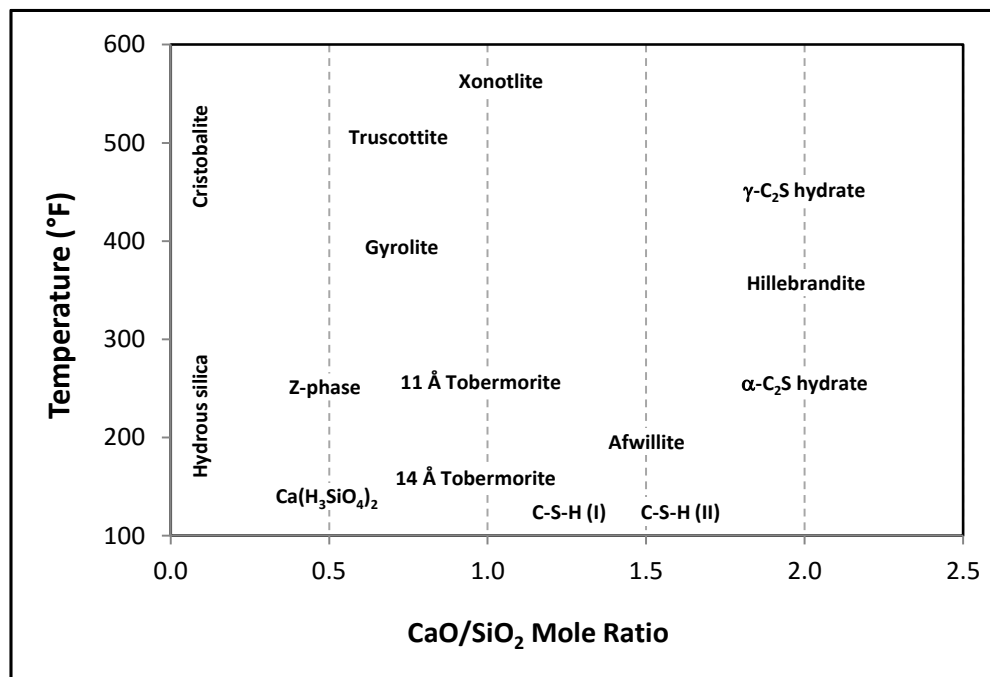


Figure 3.3 Charts for the transformation of amorphous CSH to crystalline phases (Omosebi et al., 2015; Adopted from Taylor, 1964 and 1997)

Table 3.2 Effect of 35% BWOC silica flour on C/S ratio in C-S-H

	No added silica	35% BWOC silica added
	CaO/SiO <sub>2</sub>	CaO/SiO <sub>2</sub>
C <sub>3</sub> S	2.80	1.20
C <sub>2</sub> S	1.87	0.93

Compared to tobermorite gel, xonotlite ( $C_6S_6H$ ) exhibits slightly lower strength (about 5000 psi for 16 lbm/gal neat Class G cement) and high permeability (about 4-5 times more) (Eiler et al. 1980). Several forms of tobermorite have been reported which include 9Å tobermorite (e.g. riversideite), 10Å tobermorite (e.g. oyelite), 11Å tobermorite or normal tobermorite ( $Ca_{5-x}Si_6O_{17-2x}(OH)_{2x}.5H_2O$ ) and 14Å tobermorite (e.g. plombierite) (Hara et al., 1978; Nelson et al., 1981; Henmi and Kusachi, 1992; Merlino et al., 2001; Matsushita et al., 2004; Richardson, 2008; Churakov, 2009). Below 230°F, tobermorite gel (a CSH gel) is the predominant phase with good binding properties, high compressive strength and low permeability. This temperature has been recommended as optimum curing temperature to prevent strength retrogression during early curing stage. Above 302°F, a moderately permeable but strong xonotlite is formed. In hot CO<sub>2</sub>-brine system, carbonic acid attack transforms xonotlite to carbonates and silica with possibility of strength loss due to recrystallization of large grains which reduces bonding area (Eiler et al., 1980; Nelson, 1979; DOE Report, 1980; Gallus et al., 1979). Truscottite, formed at about 419-599°F, is a weaker but less permeable form of tobermorite and may transform to xonotlite in its stable form. Trace amounts of scawtite, usually formed at about 284-572°F when carbonates are present in Portland cement, are common in geothermal and high temperature oil well cements. In this quantity, it enhances the compressive strength thereby producing more competent cement (Eiler et al. 1980). Formation of other polymorphs (e.g. pectolite, gyrolite, afwillite, wollastonite, etc.) takes place at different temperature and C/S ratio. The structure, mineralogy and relative weights of these polymorphs are characterized using FTIR, SEM, XRD, and NMR techniques (Le Saoût et al. 2004, 2005).



### **3.4 Matrix Expansion and Thermally-Induced Pressurization**

Another phenomenon that leads to mechanical deterioration of oil well cement is uncontrolled matrix expansion. This phenomenon can be intentionally designed into engineered cement materials through the use of expanding additives. As noted in Chapter 2, formation of ettringite leads to the expansion of cement matrix. While matrix expansion is important to ensure sealing integrity of the annular area between casing and rock, excessive expansion of the matrix can lead to severe damage of the cement sheath. Since well cements are confined between casing and rock formation, expansion-induced stresses can build and, if not moderate, might result in the development of cracks that serves as conductive pathway for fluid flow. As time progresses, severe loading conditions degrade cement quality thereby compromising wellbore integrity.

Furthermore, increase in temperature causes matrix expansion and pore fluid pressurization. The thermal-induced pressurization felt by the cement arises from net effect of thermal expansion coefficients of the pore fluid and of the pore volume. Pore pressure increase reduces effective mean stress, which may lead to shear failure or hydraulic fracturing. Thermally-induced pressurization phenomenon occurs when the reservoir rock and well cement lining undergo sudden temperature changes which is common in heavy oil extraction by steam injection. This rapid temperature increase could damage cement integrity leading to the loss of zonal isolation (Ghabezloo et al. 2009). Geomechanical issues, such as cracks or shear strain arising from cycles of pressure and temperature fluctuations and geologically-induced formation stresses, can occur. This results in increased permeability, severe mechanical damage, and ultimate failure of the cement sheath, potentially leading to the formation of micro-annulus that allows fluid

leakage through the cement, cement-casing or cement-rock interfaces. This fluid leakage can lead to the contamination of freshwater aquifers. With good elastic properties, cement can effectively respond to the fluctuating temperatures. In some applications, effective response of cement to these fluctuations can be achieved if its thermal coefficient is designed as close as possible to the thermal coefficient of the casing/rock.

### **3.5 Dissolution of CH and Decalcification of CSH**

Generally, there are two types of leaching: calcium leaching in the absence of  $\text{CO}_2$  and mineral dissolution (or carbonate leaching) in the presence of  $\text{CO}_2$ . The former simulates the dissolution of portlandite (CH) in the absence of an acid while the latter accounts for the effect of  $\text{CO}_2$  on the progress of dissolution front through the cement (discussed in Section 3.7). When cement comes in contact with deionized water (i.e. water of zero calcium ion concentration), diffusion of calcium ions out of cement pore fluid toward the fresh water can take place due to concentration gradient. This leads to the reduction of calcium ion concentration in the pore solution. To restore equilibrium between the calcium concentration in the pore fluid and the solid matrix, calcium-bearing hydrates in the cement matrix dissolve by releasing calcium ( $\text{Ca}^{2+}$ ) ions into pore solution. The release of  $\text{Ca}^{2+}$  ions by CH is termed leaching because the CH completely dissolves in solution thereby releasing  $\text{Ca}^{2+}$  and  $\text{OH}^-$  ions in the process. However, the release of  $\text{Ca}^{2+}$  ions by CSH is termed decalcification because amorphous silica is left behind as a by-product. The dissolution of CH is more rapid than the decalcification of CSH because the solubility of CH is higher. However, the solubility of CH decreases with temperature. Crystalline phases of calcium silicate hydrate (C-S-H), which were discussed in Section 3.3, often decalcify incongruently (Berner, 1988 and 1992; Reardon, 1992; Clodic and

Meike, 1997; Kulik and Kersten, 2001; Soler, 2007; Kulik, 2011). Equations 3.1 and 3.2 describe the dissolution of portlandite and decalcification of C-S-H in pore solution.

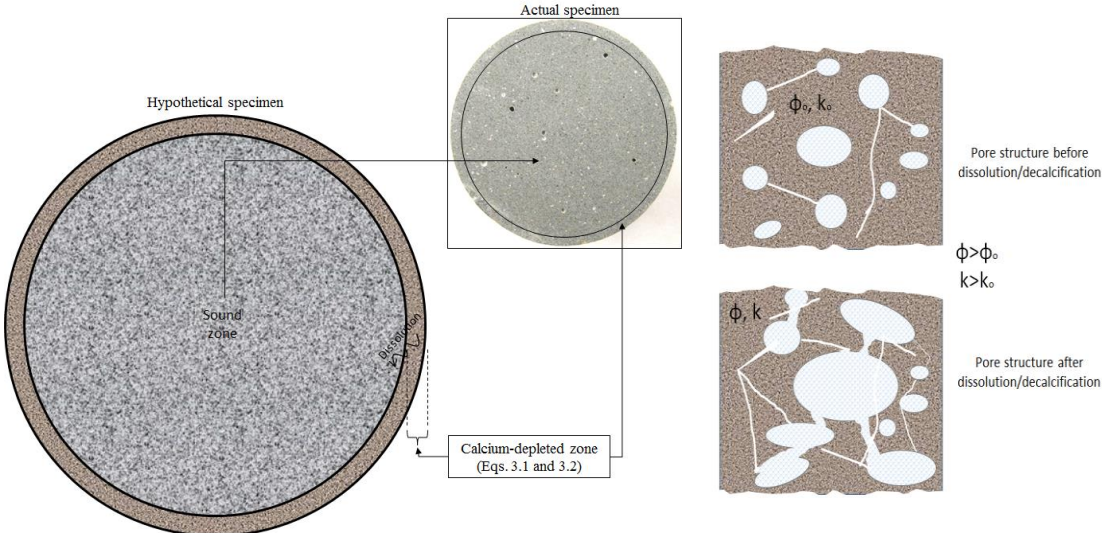
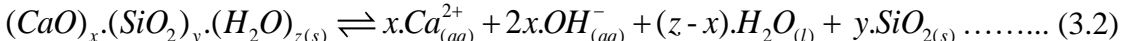
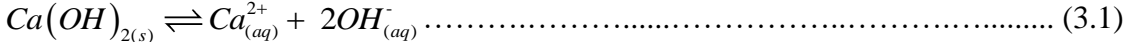


**Figure 3.4 Effect of leaching and decalcification on cement exposed to deionized water**

Since the exchange of ions and subsequent dissolution of solid matrix occur in a non-acidic bulk fluid, this mode of degradation is called calcium leaching or decalcification and it often result in loss of mechanical strength. The decrease in calcium content of the solid matrix is believed to be the major driver of both the loss in mechanical strength and the corresponding increase in porosity and permeability (Carde et al., 1996; Carde and Francois, 1997 and 1999). Reduction of solid phase calcium arises from the consumption of portlandite, which is the first hydrate to dissolve completely, and the progressive decalcification of calcium silicate hydrate (a major strength component); hence, the loss of strength and increase in porosity and permeability (illustrated in **Figure 3.4**). Under this mode of leaching, the degraded depth can be estimated using the model proposed by Mainguy and Coussy (2000), if the hardened cement is exposed to a static

but constantly renewed bulk fluid. However, a numerical solution of the governing equation (equation 2.20 in Chapter 2) is appropriate, if the bulk fluid is neither static nor renewed.

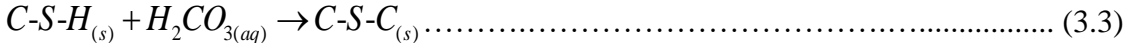
### **3.6 Carbonation**

Cement in contact with carbonic acid undergoes chemical degradation governed by the chemical reactions summarized in equations 2.14-2.19 (Chapter 2). Two modes of carbonation are possible when cement hydrates react with carbonic acid.

In the first mode, cement hydrates (CH and C-S-H) react with carbonic acid to form calcium carbonate (equation 2.16 and 2.17 in Chapter 2). This mode of carbonation is referred to as complete carbonation. Complete carbonation reduces porosity and reinforces cement matrix thereby improving the aggregate strength. Depending on the prevailing temperature and pressure, calcium carbonate ( $\text{CaCO}_3$ ) exists in different forms. These include calcite, aragonite, vaterite and ikaite. However, calcite is the most thermodynamically stable at low temperature and is the most expected polymorph of  $\text{CaCO}_3$ . Conversely, other metastable polymorphs (i.e. aragonite, vaterite and ikaite) are often formed at elevated temperature and pressure.

In the second mode, reaction progress of the carbonation of calcium silicate hydrate (C-S-H) is incomplete due to the formation of calcium silicate carbonate or C-S-C (equation 3.3). Examples of C-S-C are scawtite ( $\text{Ca}_7(\text{Si}_6\text{O}_{18})(\text{CO}_3)\cdot 2\text{H}_2\text{O}$ ), fukalite ( $\text{Ca}_4\text{Si}_2\text{O}_6(\text{OH})_2\text{CO}_3$ ), spurrite ( $\text{Ca}_5(\text{SiO}_4)_2\text{CO}_3$ ), tilleyite ( $\text{Ca}_5(\text{Si}_2\text{O}_7)(\text{CO}_3)_2$ ) and galuskinite ( $\text{Ca}_7(\text{SiO}_4)_3\text{CO}_3$ ) (Glasser, 1973; Bolio-Arceo and Glasser, 1990; Zhang et al., 2013). Formation of scawtite has been observed in cement exposed to  $\text{CO}_2$  (Eilers et al., 1983). Incomplete carbonation mostly takes place at elevated temperatures when

structural polymorphs of C-S-H are incompletely carbonated. Unlike complete carbonation, aggregate strength of incompletely carbonated cement may or may not be improved, even if porosity and permeability reduces. Scawtite, for instance, improves the strength of carbonated cement if it is formed in trace quantity, but excessive formation weakens cement (Eiler et al. 1980).



The rate of carbonation is controlled by several parameters such as temperature, pressure, cement formulation, CO<sub>2</sub> partial pressure and brine concentration. Moderate carbonation can be beneficial for cement porosity and permeability, since it forms CaCO<sub>3</sub> that plugs the pores of the cement and acts as a protective layer that limits further ingress of dissolved CO<sub>2</sub>. However, extensive carbonation can result in the loss of structural integrity. Although incomplete carbonation limits the degree of leaching since C-S-Cs are inconvertible to water-soluble calcium bicarbonate that results in mineral leaching, excessive formation of C-S-Cs may result in loss of mechanical strength even if porosity and permeability reduces.

**3.7 Bi-Carbonation and Leaching**

Cement bi-carbonation is the process that occurs when precipitated calcium carbonate (CaCO<sub>3</sub>), which is formed during complete carbonation of cement hydrates, further reacts with carbonic acid to produce water-soluble calcium bicarbonate (equation 2.18 in Chapter 2). The dissolution of calcium bicarbonate in to pore solution initiates reaction of its dissolved species with the residual portlandite in the cement matrix (equation 2.19 in Chapter 2) to produce additional CaCO<sub>3</sub>, which again reacts with carbonic acid. This establishes a cycle of precipitation and dissolution of CaCO<sub>3</sub> in which

portlandite is continuously consumed in the process. This reaction step is called mineral leaching. Unlike calcium carbonate, calcium silicate carbonates (C-S-Cs) are inconvertible to water-soluble calcium bicarbonate; hence not vulnerable to mineral leaching except when favorable condition exists that allows the incomplete carbonation reaction to progress to completion. The consumption of portlandite and dissolution of calcium carbonate leads to loss of strength and increase in matrix porosity and permeability. Increased rate of acid attack favors both consumption of portlandite and leaching of calcium carbonate with the penetrated portion of the cement matrix reduced to amorphous and porous silica, which leads to loss of structural integrity. This trend continues as long as the supply of carbonic acid is not interrupted until the cement is completely leached resulting in structurally-weak silica and eventual loss of casing protection and zonal isolation. Generally, portlandite is the first to be completely leached out before complete decalcification of C-S-H since it becomes unstable at higher pH and is more soluble than C-S-H (Brandl et al. 2011; Santra et al. 2009; Le Saout et al. 2005; Le Saout et al. 2006a, 2006b). Field results of cement samples that were retrieved from three wells (55-year old well with 30 years of CO<sub>2</sub> injection, 19- and 15-year old sour gas wells) corroborate this phenomenon (Carey, 2007; Scherer et al., 2011; Krilov, 2000). Although carbonated cement is susceptible to leaching through bi-carbonation reaction, diffusion-controlled calcium leaching occurs as discussed in Section 3.5. Like carbonation, cement leaching due to bi-carbonation is reaction-controlled but limited by the diffusion of solute species between the pore and bulk solutions.

### **3.8 Interactions between Mechanisms and Propagation of Reaction Fronts**

The processes that lead to cement degradation are very complex due to vast number of influencing variables most of which are uncontrollable. In several field cases, cement samples that were retrieved from wells with CO<sub>2</sub> history have consistently showed that many processes interact to degrade oil well cement (Carey et al. 2007; Scherer et al. 2011; Krilov et al. 2000). For instance, while mechanical processes such as uncontrolled matrix expansion, thermally-induced pressurization or stress perturbations might result in induced fractures in the cement matrix, experimental studies have shown that precipitation of calcite (i.e. a carbonation process) result in healing of these fractures under high pressure high temperature down-hole conditions (IEA Report, 2009; Huerta et al. 2009; Lecolier et al. 2008). The mechanisms of cement degradation described in the preceding sections involve interactions between aqueous species and solid minerals. **Figure 3.5** illustrates how these mechanisms interact to deteriorate oil well cement in carbonic acid environment. Detailed understanding of these interactions is important in developing a representative model for long-term prediction of cement integrity. These interactions are very complicated and accurate prediction of the extent of mechanical deterioration requires constructing models that account for all influencing mechanisms. Such theoretical modeling must honor the strong coupling between the governing processes. A coupled thermo-chemo-mechanical model for cement degradation is presented in Chapter 5.

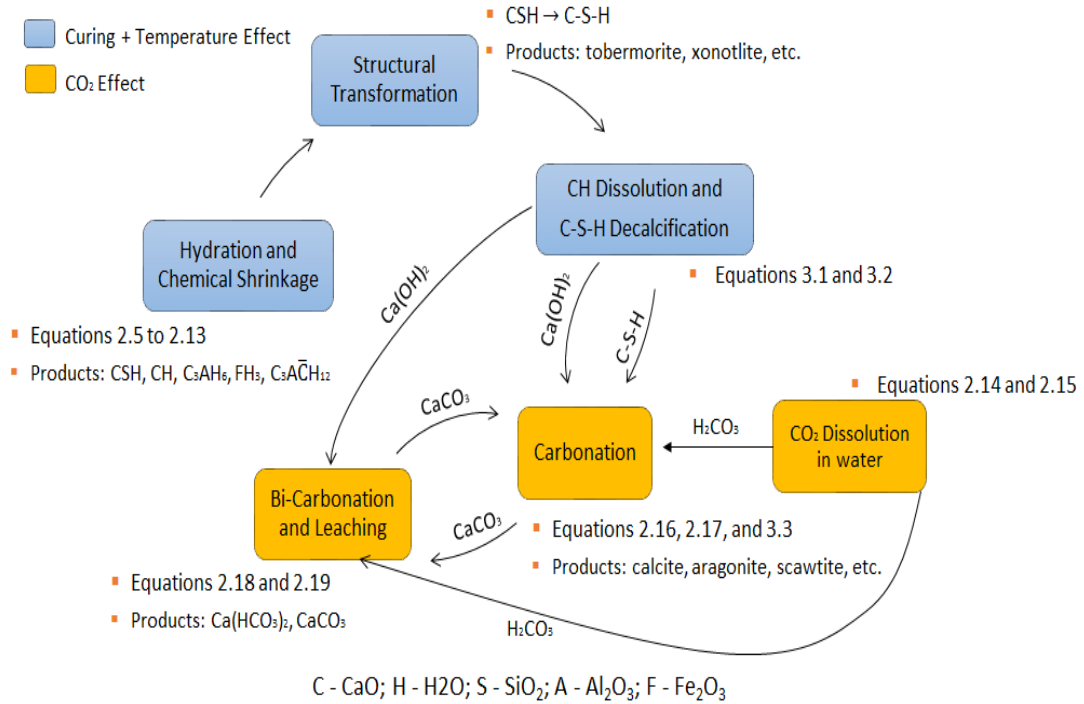


**Figure 3.5 Interaction between cement degradation mechanisms**

**Figure 3.6** shows the typical reaction fronts and the degraded zones for cement that has been exposed to CO<sub>2</sub>-containing fluid. Four zones can be identified, each with unique mineralogical compositions and distinct mechanical and transport properties. First is the inner “sound zone” which is unpenetrated. The mechanical and transport properties in this zone are mostly dictated by the degree of hydration. This zone is trailed by the front-end “dissolution zone” where calcium is leached from portlandite and CSH. High porosity, high permeability and low mechanical strength are typical properties of the minerals formed in this zone. Next is the “carbonation zone” where calcium carbonate and/or calcium silicate carbonate is formed after dissolved CO<sub>2</sub> penetrates cement matrix. In this zone, porosity and permeability are low while strength is high. Behind the carbonation zone is the “leaching zone”, where the precipitated calcium carbonate reacts with carbonic acid to form water-soluble calcium bi-carbonate resulting in severe loss of



strength and increase in porosity/permeability. As time progresses, this multi-zone partitioning acts as a protective layer, which limits the further ingress of fresh acid from the bulk fluid to the unpenetrated zone, since each zone exhibit distinct transport properties. Therefore, the rates of reaction, between carbonic acid and the primary minerals (i.e. CH and C-S-H) in the sound zone and carbonic acid and the secondary minerals in the penetrated zone, slow down. Besides, the mechanical strength after exposure is the aggregate strength of all minerals post-degradation.

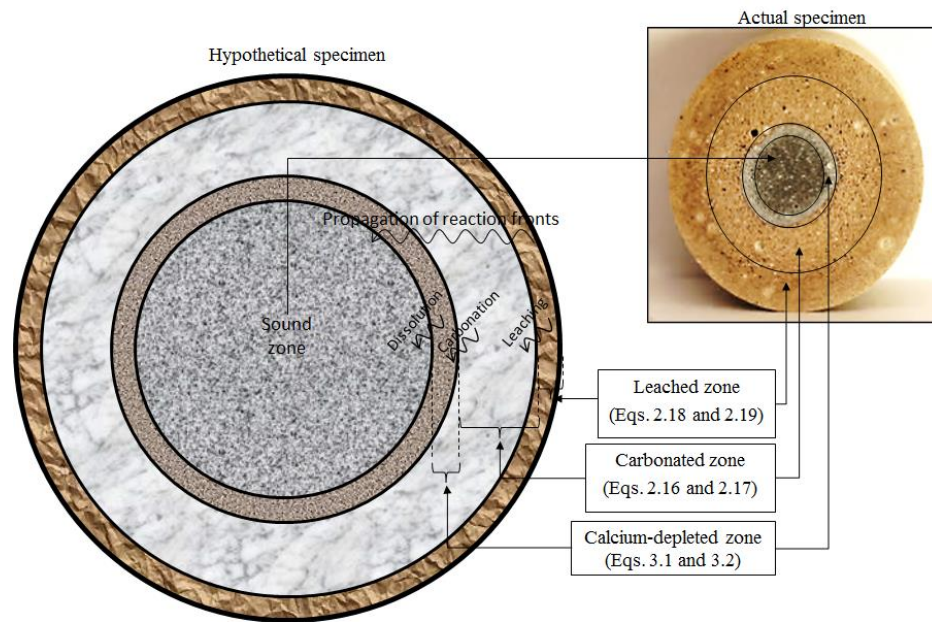


Figure 3.6 Reaction fronts due to CO<sub>2</sub> attack on well cement

### 3.9 Effects of Downhole Parameters on the Mechanisms of Cement Degradation

The mechanisms described in the preceding sections are influenced by temperature, CO<sub>2</sub> gas composition, pressure, and salt concentration. Re-writing equation 2.18 gives equation 3.4, which is the overall reaction that leads to chemical degradation of well cement. High temperature and pressure enhance the rate of attack by increasing

solubility of CO<sub>2</sub> gas in brine solution, which favors precipitation of calcite (i.e. carbonation) and subsequent dissolution of calcium bicarbonate (i.e. leaching).



**3.9.1 Effect of Temperature**

Temperature affects the mechanisms of cement degradation in three ways. In the first case, variation in temperature affects the degree of hydration of clinker materials and chemical shrinkage, structural transformation of calcium silicate hydrate, thermal expansion of cement matrix, and dissolution of CH and decalcification of C-S-H. This is discussed in Sections 3.2, 3.3, 3.4, and 3.5 respectively.

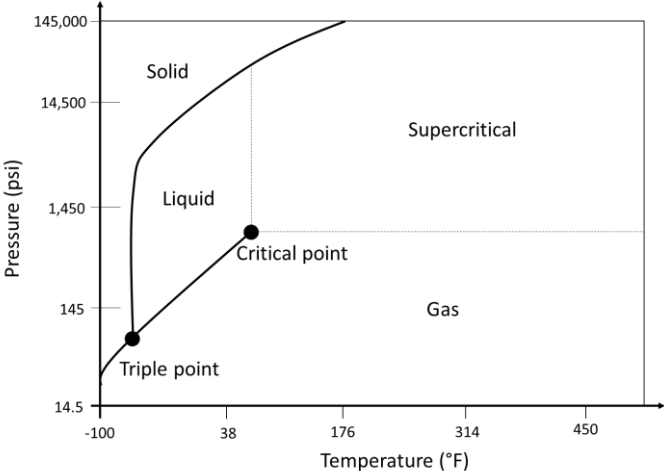


**Figure 3.7 Carbon dioxide pressure-temperature phase diagram**

In the second scenario, increasing temperature alters CO<sub>2</sub> phase behavior and its solubility in the bulk solution. Depending on temperature and pressure, CO<sub>2</sub> can exist in supercritical, gaseous, liquid or solid state as illustrated in **Figure 3.7**.

**Figure 3.8** shows the effect of temperature variation at different pressures on CO<sub>2</sub> solubility in 1 M NaCl solution. At low pressure (below 1450 psi in Figure 3.8), less CO<sub>2</sub> dissolves in brine as temperature increases. At higher pressures, however,

temperature effect on CO<sub>2</sub> solubility shows a mixed trend. As temperature increases up to 200-250°F, CO<sub>2</sub> solubility decreases. Therefore, the equilibrium position of equation 2.15 (Chapter 2) shifts to the left (Le Châtelier's Principle) thereby producing less carbonic acid. In response to this shift in equilibrium, the equilibrium position of equation 3.4 shifts to the left thereby allowing more CaCO<sub>3</sub> to precipitate, since less Ca(HCO<sub>3</sub>)<sub>2</sub> would be formed. Above 200-250°F, CO<sub>2</sub> solubility increases with temperature thereby shifting the equilibrium positions of equations 2.15 and 3.4 to the right. These equilibrium shifts enhance the formation of calcium bi-carbonate that results in leaching.

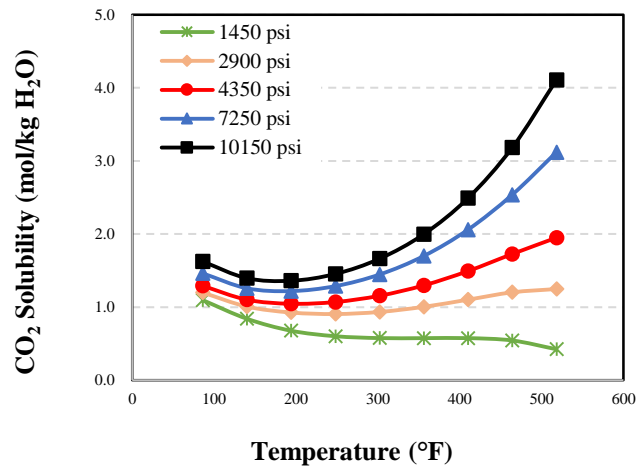


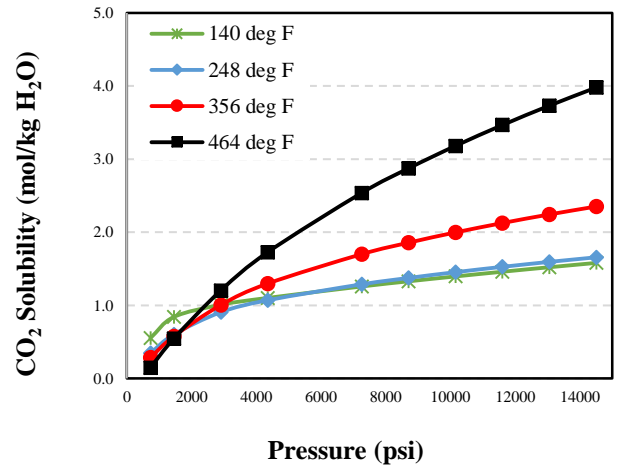
**Figure 3.8 Temperature effect on CO<sub>2</sub> solubility in 1m NaCl solution at different pressures (Data source: Duan and Sun, 2003)**

In the third case, temperature determines the stable form of calcium carbonate that would precipitate out of solution. Typical polymorphs of calcium carbonate are calcite, aragonite, vaterite, and ikaite.

### 3.9.2 Effect of Pressure

As noted in Section 2.3.1 of Chapter 2, effect of pressure on cement hydration and structural transformation of calcium silicate hydrate is not well understood. However, variation in pressure alters the phase behavior of CO<sub>2</sub> and its solubility in NaCl solution.

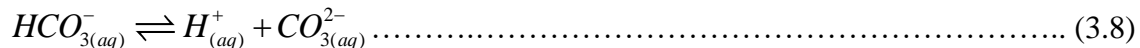
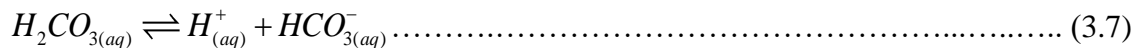
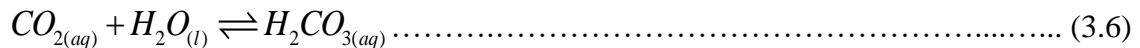
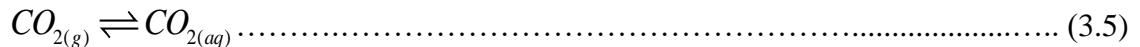
**Figure 3.9** shows the effect of pressure variation at different temperatures on CO<sub>2</sub> solubility in 1 M NaCl solution. As pressure increases, more CO<sub>2</sub> dissolves in brine. Therefore, the equilibrium position of equation 2.15 shifts to the right thereby increasing production of carbonic acid. As this occurs, chemical reaction in equation 3.4 shifts to the right thereby triggering the formation of Ca(HCO<sub>3</sub>)<sub>2</sub> which leads to leaching.



**Figure 3.9 Pressure effect on CO<sub>2</sub> solubility in 1m NaCl solution at different temperatures (Data source: Duan and Sun, 2003)**

### 3.9.3 Effect of CO<sub>2</sub> Gas Composition

When CO<sub>2</sub> is dissolved in brine, the carbonic acid formed results in chemical degradation of oil well cement and subsequent corrosion of casing. Equations 3.5-3.8 describe the basic aqueous phase speciation in CO<sub>2</sub>-saturated water.



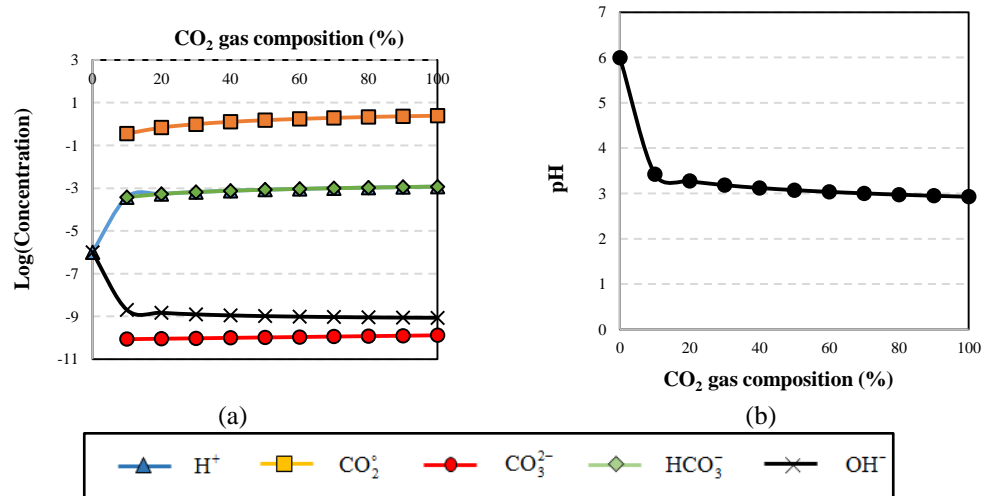


Figure 3.10 Effect of CO<sub>2</sub> gas composition on: (a) concentration of species; (b) pH of solution

Variation in CO<sub>2</sub> concentration leads to alteration in the concentration of aqueous species. **Figure 3.10** shows the typical behavior of the concentration of aqueous species in CO<sub>2</sub>-NaCl-H<sub>2</sub>O equilibrium system when CO<sub>2</sub> partial pressure is varied. Clearly increase in CO<sub>2</sub> partial pressure increases its solubility (i.e. CO<sub>2</sub><sup>0</sup> in Figure 3.10a) in brine, thus increasing the concentration of the bi-carbonate ion (HCO<sub>3</sub><sup>-</sup>) that is principally responsible for the carbonation of cement. As expected, pH of the solution decreases with increase in CO<sub>2</sub> partial pressure (Figure 3.10b), which makes the fluid more acidic. As the concentration of HCO<sub>3</sub><sup>-</sup> rises in the bulk fluid, it diffuses into the pore fluid, due to concentration gradient, and then reacts with Ca<sup>2+</sup> ion from calcium leaching (equations 3.1 and 3.2) to form calcium carbonate. In the presence of additional HCO<sub>3</sub><sup>-</sup> ion, calcium carbonate is leached thereby releasing Ca<sup>2+</sup> ion into the pore solution. This Ca<sup>2+</sup> ion then diffuses out of the pore solution into the bulk solution due to concentration gradient. Alternatively, increase in CO<sub>2</sub> partial pressure increases the production of H<sub>2</sub>CO<sub>3</sub><sup>\*</sup> which increases the dissolution of CaCO<sub>3</sub> since the equilibrium position of equation 3.4 shifts to the right. Therefore, increase in CO<sub>2</sub> partial pressure would lead to

the dissolution of  $\text{CaCO}_3$  while precipitation occurs as  $\text{CO}_2$  partial pressure decreases. With continuous supply of  $\text{CO}_2$ , the leaching of precipitated calcium carbonate leads to loss of cement integrity.

### 3.9.4 Effect of NaCl Concentration

Figure 3.11 shows the effect of NaCl concentration on  $\text{CO}_2$  solubility at different pressures (Figure 3.11a) and different temperatures (Figure 3.11b). In both cases,  $\text{CO}_2$  solubility decreases as the concentration of NaCl increases. This decrease in solubility is steeper at high pressure and high temperature. As a result of the decrease in  $\text{CO}_2$  solubility, the equilibrium position of equation 2.15 moves to the left to produce less carbonic acid. As this shift occurs, equilibrium position of equation 3.4 responds by shifting to the left thus producing less  $\text{Ca}(\text{HCO}_3)_2$ . Consequently, more carbonation takes place than leaching.

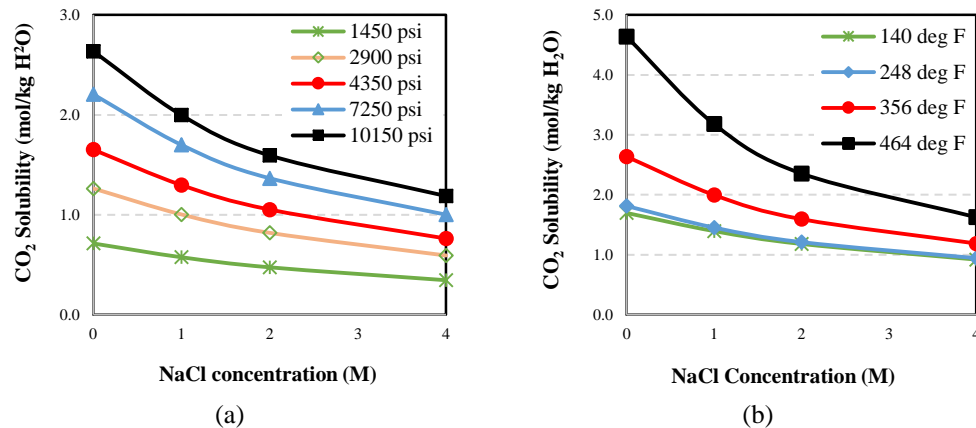


Figure 3.11 Effect of NaCl concentration on  $\text{CO}_2$  solubility at: (a) different pressures; (b) different temperatures (Data source: Duan and Sun, 2003)

### 3.10 Summary

The mechanisms governing cement degradation in HPHT carbonic acid environment are hydration and chemical shrinkage, matrix expansion and thermally-induced pressurization, structural transformation of calcium silicates, dissolution of CH,

decalcification of C-S-H, carbonation, and bi-carbonation and leaching. Cement hydration and chemical shrinkage result in the development of initial compressive strength and transport properties (porosity and permeability). In the oilfield, extreme chemical shrinkage causes reduction in slurry hydrostatic column; thus, creating condition for the well to kick (if not controlled) during primary cementing operations. This phenomenon can also lead to free water in the lateral section of horizontal wells. Excessive matrix expansion and thermally-induced pressurization of cement leads to the development of micro-fractures thereby increasing matrix permeability. Structural transformation of calcium silicates leads to strength retrogression and increase in permeability. Dissolution of CH and progressive decalcification of CSH reduce aggregate strength and makes cement susceptible to fluid flow through its matrix. Carbonation of cement momentarily improves its structural integrity while subsequent bi-carbonation and leaching results in the loss of mechanical integrity. In HPHT carbonic acid environment, these mechanisms interact in complex manner; thus, the overall effect on cement performance is determined by the dominant mechanism and downhole conditions. Generally, high temperature, high pressure and high CO<sub>2</sub> concentration favor mineral leaching while the exposure of hardened cement to high salinity fluid enhances its carbonation.

## Chapter 4 Experimental Studies

### 4.1 Materials

#### 4.1.1 Slurry Materials

High sulfate resistant Class G and medium sulfate resistant Class H API cements are used in this study. Table 4.1 presents information on the manufacturer and the compositions of clinker compounds.

**Table 4.1 Manufacturer, density and clinker composition of Classes G and H cement**

API Class	Manufacturer	Specific Gravity	C <sub>3</sub> S	C <sub>2</sub> S	C <sub>3</sub> A	C <sub>4</sub> AF	SO <sub>3</sub>
G	Mountain Cement Company	3.15	58.00	18.00	6.00	11.00	2.97
H	Buzzi Unicem USA	3.15	58.71	20.25	0.42	16.46	0.64

API recommends that the composition of clinker materials should satisfy the following criteria:

1. Maximum and minimum C<sub>3</sub>S composition = 0.58 and 0.48 respectively
2. Maximum C<sub>3</sub>A composition = 0.03
3. Maximum (C<sub>4</sub>AF composition + 2\*C<sub>3</sub>A composition) = 0.24

The data in Table 4.1 satisfy these conditions.

#### 4.1.2 Slurry Formulation and Preparation

**Table 4.2** presents the quantity of baseline cement, water and additives mixed in each slurry formulation. Cement slurries were prepared according to API RP 10B (1997) procedure. In order to prepare the baseline cement slurries, standard API cement formulation for high-temperature application was used. Accordingly, slurries containing cement, water, silica flour, antifoam Agent and hydroxyethyl cellulose (HEC) were



prepared. According to API specification, the water requirement for Class H cement is 38% BWOC. For Class G cement, the composition of mix water is 44% BWOC. 35% BWOC of silica flour was added to minimize strength retrogression at elevated temperature by maintaining the C/S (CaO/SiO<sub>2</sub>) ratio close to 1 (Table 3.2 in Chapter 3). 0.1% HEC, a natural polymer, was added during preparation of slurry to prevent free water and settling. Antifoam agent in the amount of 0.1 gallon/sack of cement was added to prevent the formation of foam during blending of cement slurry. This helps to prevent air entrainment within the cement, thereby maintaining slurry density within the desired range. The API procedure requires using a special high-speed mixer with 4,000 and 12,000 rpm preset speeds. API standard blender (Grace Model M3080 Variable Speed Mixer) was used to prepare cement slurries. The blender allows automatic mixing sequences, which are exactly configured to meet the API speed requirements for cement slurries.

**Table 4.2 Compositions of cement, water and additives**

Materials	Composition	
	Class G	Class H
Cement	100% BWOC*	100% BWOC*
Water for Cement	44% BWOC*	38% BWOC*
Silica Flour	35% BWOSF*	35% BWOSF*
HEC	0.1% of water for Silica	0.1% of water for Silica
Anti-Foaming Agent	0.1 gal/sack of cement	0.1 gal/sack of cement

\*BWOC = by weight of cement; \*\*BWOSF = by weight of silica flour

### 4.1.3 Slurry Properties

Density, rheology, filtration loss and thickening time were measured after preparation of cement slurries. CTE Model 200 atmospheric consist-o-meter was used to measure consistency and thickening time of the slurries at 135°F. This is reported at API

Bearden units of consistency ( $B_c$ ) value of 100. Above 100, the slurry becomes thick and cannot be pumped. **Figure 4.1** presents the consist-o-meter readings and the rheological measurements for both Class G and H slurries.

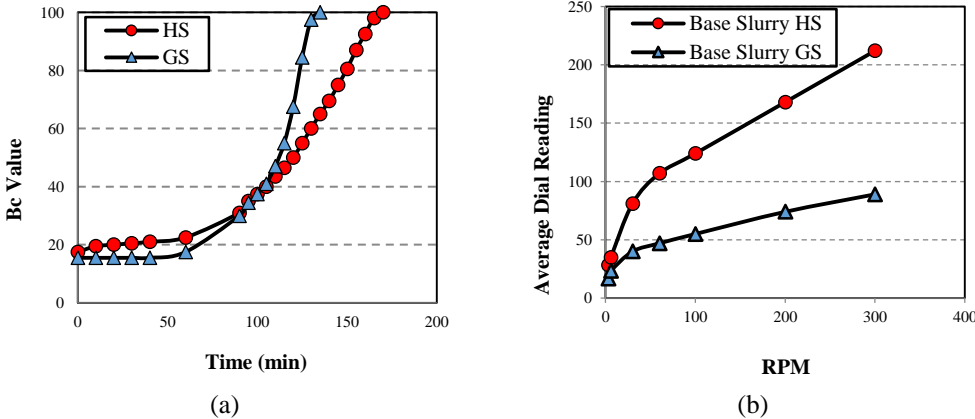


**Figure 4.1.** (a) Consist-o-meter reading; (b) Rheological reading (Omosabi et al., 2015; GS and HS refer to Class G and Class H with 35% silica respectively)

**Table 4.3. Slurry properties (Omosabi et al., 2015)**

Parameter	Class G	Class H
Theoretical density, lbm/gal	15.51	15.96
Measured density, lbm/gal	15.45	16.20
API fluid loss, mL	240	200
Rheological properties	Power law fluid $n = 0.34$ $K = 10.5 \text{ lbf-sec}^{0.34}/100\text{ft}^2$	Power law fluid $n = 0.43$ $K = 14.4 \text{ lbf-sec}^{0.43}/100\text{ft}^2$
API thickening time, min	135	170

Rheological properties were measured using OFITE Model 900 viscometer. The measurements were obtained as per the API standards (R1B1 bob and spindle geometry with spring factor of 1). Tests were performed under ambient room temperature, varying the rotor speed from 3 to 300 RPM. Industry standard low-pressure filter press (OFITE Model 142-53) was used to measure filtration loss at 100 psi and ambient temperature. The press has a cell body to hold slurry sample, a pressure inlet for

pressurization, a base cap with screen and filter paper to simulate permeable formation, CO<sub>2</sub> charger to pressurize the sample and pressure regulator to accurately control the cell pressure. Slurry density was measured using oilfield standard atmospheric OFITE mud balance. A good match was obtained when measurement was compared to theoretical computation and these were within practical range used in the field. These properties are presented in (Table 4.3).

## **4.2 Methods**

### **4.2.1 Curing Procedure and Specimen Preparation**

To prepare specimens for experiment and testing, cement slurry was poured into rectangular rubber molds and completely immersed in 2% sodium chloride (NaCl) solution inside a pressure cooker. The pressure cooker was sealed and kept in an oven maintained at 200°F for 5 days (120 hrs.) to allow curing and hardening of the slurry. Before curing, expected degree of hydration was predicted using Lin and Meyer (2009) model. The predictions suggest initial rapid hydration of approximately 65% (for Class G) and 50% (for Class H) after 4 days of curing at 200°F. According to the model, the hydration stabilizes after 4 days. Hence, 5-day curing was selected as optimal duration to achieve substantial hydration with reasonable time. The specimens were allowed to cure at the vapor pressure of water corresponding to 200°F (about 12 psi). After curing, the cement blocks were taken out of the molds and thirty cylindrical cores (15 Class G and 15 Class H), each measuring approximately 1.5 inch in length and 1 inch in diameter, were cut. The cores were ground and polished to the exact dimensions. Ten of the cylindrical specimens (5 Class G and 5 Class H) were kept in 2% NaCl solution for 14 days at ambient conditions. These specimens were labelled as ‘unaged’ specimens and

were used to observe the initial alteration in cement properties after curing. The remaining twenty cylindrical cores (10 Class G and 10 Class H) were kept for 14 days in an HPHT autoclave filled with 2% NaCl solution at various experimental conditions of temperatures, pressures and CO<sub>2</sub> concentrations.

## **4.2.2 CO<sub>2</sub> Exposure Tests under HPHT Conditions**

### **4.2.2.1 Test Setup**

**Figure 4.2** shows the schematic and photograph of the specimen aging system. The system contains the following components:

- (i) An HPHT autoclave, with 3 liter capacity, which is used to simulate downhole conditions. It is filled up to 80% capacity (gas/liquid volume ratio is 0.25) with 2% NaCl solution,
- (ii) Three gas cylinders filled with test gases (CO<sub>2</sub> and methane) and nitrogen,
- (iii) Gas injection cylinder (250 mL capacity), which is used to accurately control the compositions of the gases in the headspace of the aging cell, and
- (iv) Data acquisition (DAQ) system.

### **4.2.2.2 Test Procedure**

In each batch of experiment, twenty cylindrical cores comprising 10 Class G and 10 Class H cements were aged for 14 days in HPHT autoclave (Figure 4.2). However, some specimens were exposed for shorter duration (6 days) and longer duration (28 days). As noted in Chapter 2, the rate of deterioration is initially highest at early durations of exposure but decreases as time progresses; hence the choice of 6, 14, and 28 days of exposure.



utilization and storage (Table 2.4 in Chapter 2) and HPHT wells. The test matrix provides the complete dataset required to investigate the effects of variation in exposure time, temperature, CO<sub>2</sub> gas composition and pressure. As shown in **Figure 4.3**, CO<sub>2</sub> is in the supercritical state under these test conditions.

**Table 4.4 Test matrix for aging experiment**

<b>Exp. No.</b>	<b>Temperature (°F)</b>	<b>Total test pressure (psi)</b>	<b>CO<sub>2</sub> (%)</b>	<b>CH<sub>4</sub> (%)</b>	<b>Exposure time (days)</b>
1	100	6,000	10	90	14
2	100	6,000	40	60	14
3	100	6,000	100	0	14
4	225	3,000	10	90	14
5	225	3,000	40	60	14
6	225	3,000	100	0	14
7	225	6,000	10	90	14
8	225	6,000	40	60	14
9	225	6,000	100	0	14
10	225	9,000	10	90	14
11	225	9,000	40	60	14
12	225	9,000	100	0	14
13	350	3,000	10	90	14
14	350	3,000	40	60	14
15	350	3,000	100	0	14
16	350	6,000	10	90	6
17	350	6,000	10	90	14
18	350	6,000	10	90	28
19	350	6,000	40	60	14
20	350	6,000	100	0	14
21	350	9,000	10	90	14
22	350	9,000	40	60	14
23	350	9,000	100	0	14
24	430	3,000	100	0	14
25	430	6,000	10	90	14
26	430	6,000	40	60	14

27	430	6,000	100	0	14
28	430	9,000	100	0	14

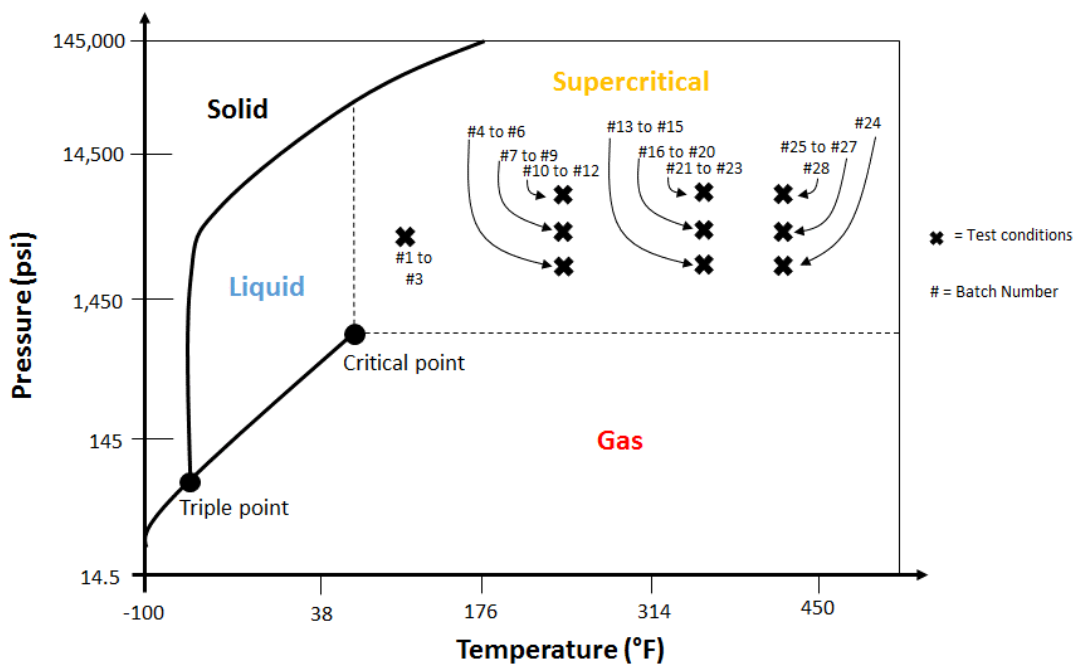


Figure 4.3 Phase condition of CO<sub>2</sub> under the test conditions in Table 4.4

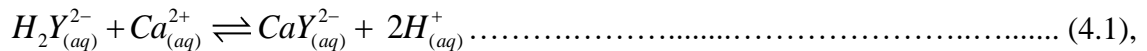
## 4.2.3 Chemical Analysis of Fluid Samples

### 4.2.3.1 Measurement of Fluid pH

Fluid samples were collected from the aging cell after each batch of experiment to test for pH and calcium content. Initially, possible range of pH value of the fluid sample was determined using color-marked pH papers. Afterwards, OAKTON pH/mV/°C pH 11 series pH meter was used to determine the actual pH value. To ensure the accuracy of measurement, the equipment was first calibrated using color-coded buffers of fixed pH (4, 7 and 10 standards). Then, the meter electrode is slowly immersed in the fluid sample until it is fully submerged and the pH is recorded at a room temperature of approximately 72°F.

### 4.2.3.2 Measurement of Fluid Calcium Content

Water hardness (calcium concentration) of fluid samples was determined using Ethylenediaminetetraacetic acid (EDTA) titration procedure. The mixing flask was first rinsed with distilled water. Subsequently, 20 mL of fluid sample (i.e.  $V_{fluid}$ ) was collected in the flask. Drops of Eriochrome Black T in Methoxyethanol color indicator were added to the fluid sample. After the addition of color indicator, the colorless fluid changes to rosy pink color which indicates that the fluid has some degree of hardness. Then, 0.01M (0.02N) EDTA (i.e.  $C_{EDTA}$ ) acid was added as titrant to the fluid sample until color changes from rosy pink to blue. This marks the end point of titration. After the addition of drops of Eriochrome Black T to the fluid samples, **Figure 4.4** shows the typical colors before and after EDTA titration. The reaction that takes place at end-point is presented in equation 4.1.



where  $H_2Y_{(aq)}^{2-}$  is used to represent EDTA.

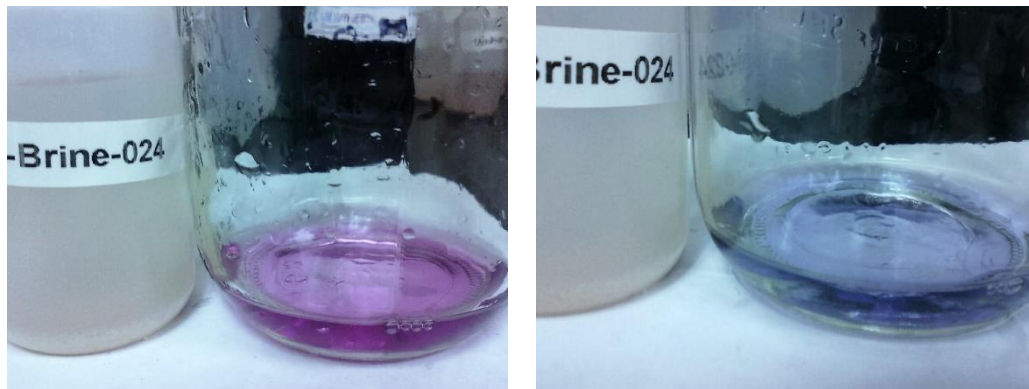


**Figure 4.4 Typical color of fluid samples: (a) before and; (b) after end-point of titration**



The volume of titrant required to reach the end point was measured and recorded as  $V_{EDTA}$ . Equation 4.2 is then formulated from the reaction stoichiometry (equation 4.1) and is used to estimate the amount of calcium in the fluid sample.

$$C_{Ca^{2+}_{(aq)}} = \frac{40080C_{EDTA}V_{EDTA}}{V_{fluid}} \quad (\text{ppm}) \dots\dots\dots (4.2)$$

## 4.2.4 Triaxial Compression Test

### 4.2.4.1 Test Setup

Mechanical properties, such as compressive strength, are very important parameters used to evaluate cement performance. **Figure 4.5** shows schematic of the compressive strength testing apparatus with pressure regulator and cut-off valves. The test setup consists of:

- (i) Confining cell,
- (ii) Power cylinders to apply compression force on the specimens,
- (iii) Air-operating hydraulic pump to develop the confining pressure,
- (iv) Syringe-operated pump to supply hydraulic power to the power cylinders, and
- (v) Data acquisition (DAQ) system.

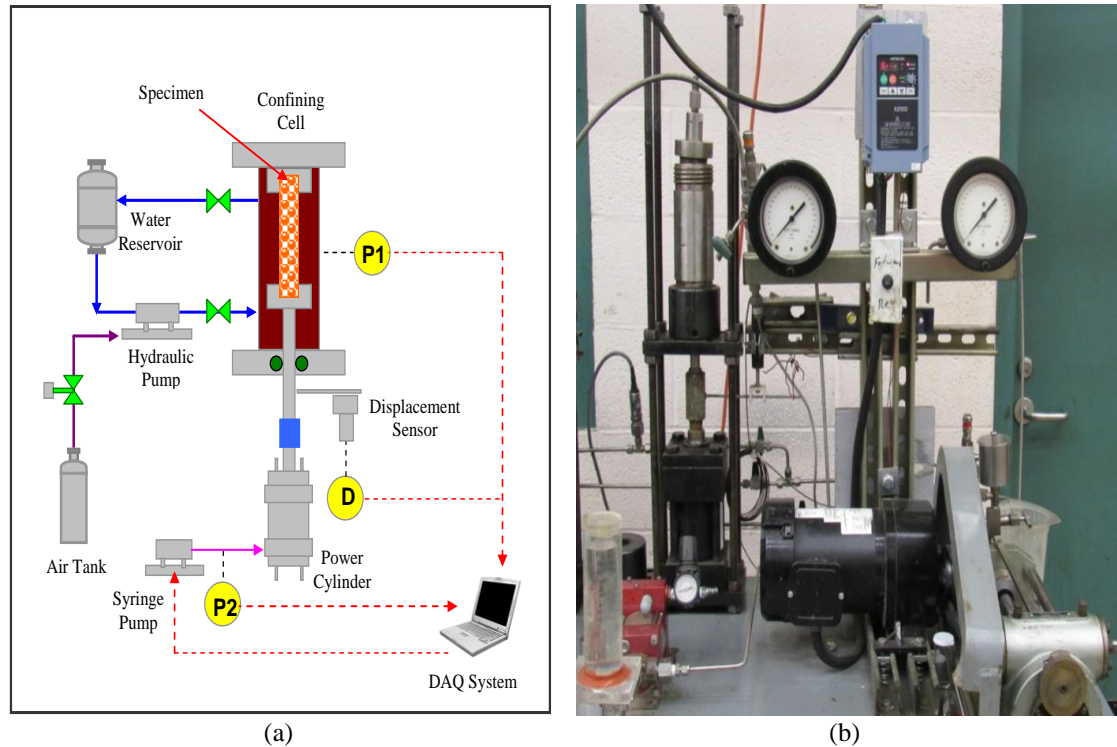


**Figure 4.5 Compressive strength testing apparatus (a) schematic; (b) photo (Omosebi et al., 2015)**

#### 4.2.4.2 Test Procedure

Compressive strength was measured according to ASTM C39/C39M (2012) standard procedure. Cylindrical cement specimen is placed in Hassler rubber sleeve, mounted on the plunger attached to the power cylinder shaft, and confined in a cell. The Hassler sleeve is used to isolate the specimen from confining fluid (i.e., water). The confining pressure was maintained at a constant level ( $\sigma_3 = 1000$  psi) using an air-driven hydraulic pump. Air pressure regulator controls the pump output pressure. Oil is pumped at the desired rate, using a syringe pump with flow controller, to hydraulically power a plunger mounted on a power cylinder. This hydraulic pressure results in vertical movement of the plunger thereby exerting axial force and stress on the specimen. The specimen is compressed and deformed until complete mechanical failure occurs. The pump speed is regulated using a computer program to maintain standard stress loading

rate in the final stage of the test in the range of 28 to 42 psi/second as required by ASTM standard C39-C39M-12. The mechanical testing equipment is equipped with high precision elevation sensors. These sensors record the change in elevation of the bottom plunger as the specimen compresses. During the test, the DAQ system displays and records all the measurements. The elevation data was used to compute axial strain on the specimens. This, in addition to the axial stress ( $\sigma_1$ ) data, was then used to generate stress-strain curves from which Young's modulus was inferred. The measured values of compressive strength were adjusted according to ASTM C39/C39M-12 guideline (**Table 4.5**) since length to diameter ratio (L/D) of the cores was a little less than the standard (2.00). **Figure 4.6** shows an illustration of the stresses exerted on the specimen during compression tests and typical stress-strain curve generated for an unaged specimen.

Previous studies (Stiles, 2006; Sauki and Irawan, 2010; Lesti et al., 2013) on compressive strength showed significant scattering in measurements. In order to minimize scattering and establish a reasonable trend, the values of compressive strength for each class of cement were averaged (three for unaged specimens and six for aged specimens). **Figure 4.7** shows photos of some specimens before and after compression test.

**Table 4.5 Correction factor for compressive strength measurements.**

L/D ratio	Correction Factor
1.75	0.98
1.50	0.96
1.25	0.93
1.00	0.87

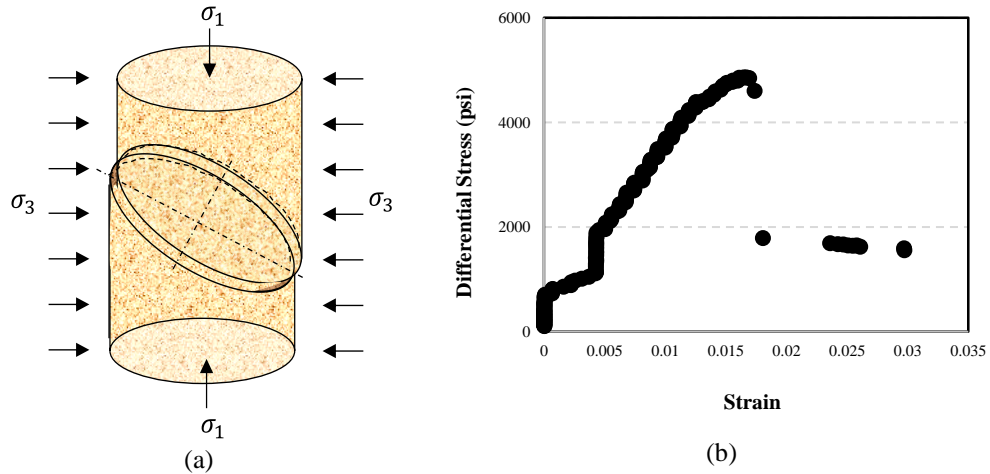


Figure 4.6 (a) stresses exerted on specimen during compression tests; (b) typical stress-strain plot

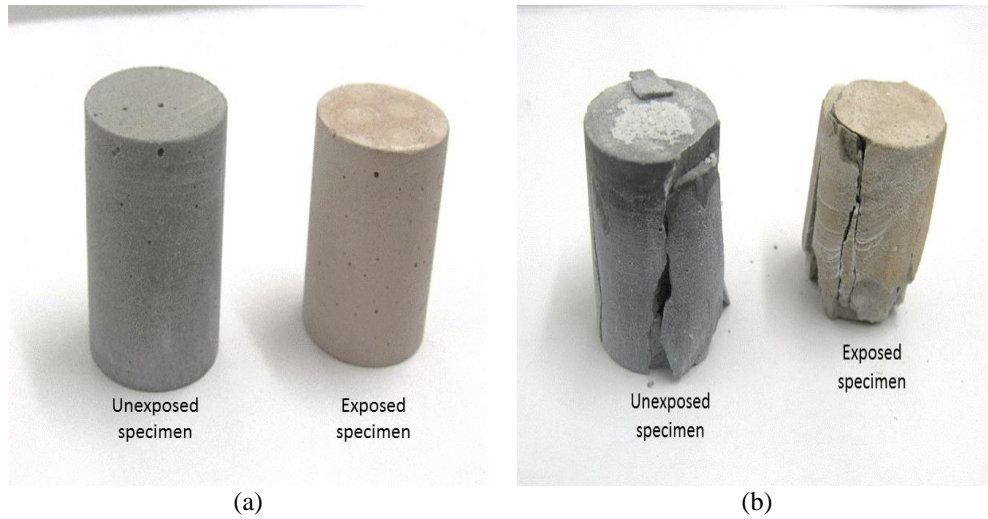


Figure 4.7 (a) Specimens before compression test; (b) Specimens after compression test

## 4.2.5 Transport Properties and Mineralogy

The remaining specimen from each class of cement (two unaged and four aged) were dried and used by Maheshwari (2014) to measure porosity, permeability and mineralogy. Cut sections from these specimens (Class H) were also used to conduct back-scattered scanning electron microscopy (BSE-SEM), Fourier transform infrared (FTIR), X-Ray Diffraction (XRD) and Energy-Dispersive X-Ray (EDX) spectroscopy analyses. Only Class H cement was selected for further analysis with BSE-SEM, FTIR, XRD, and

EDX because the combined results from compressive strength, porosity and permeability show that it demonstrates improved performance than Class G cement.

BSE-SEM and EDX spectroscopy were obtained, using FEI equipment equipped with back-scattered electron imaging, to ascertain and examine different degraded regions, identify the interface between them, and to estimate elemental composition of minerals in these zones.

XRD runs were carried out on a RIGAKU MiniFlex 600 outfitted with a Cu X-ray tube, a six-position sample changer, a NaI scintillation counter, and a diffracted-beam monochromator. Powdered samples were pressed into standard 1-inch (25-mm) round holders and run from 4-65 degrees two-theta in step-mode, with two seconds/step counting time. A Class H reference cement was also run. Sample mineralogy was quantified using Rietveld refinement; for this, RIQAS software from MDI Inc. was used. The amorphous component was quantified by adding an internal standard (alpha-alumina) at a loading of 15 weight percent and rerunning the powders. Modeling was then carried out with no amorphous component, thus yielding an over-determination of the alumina content (e.g. 25%). Normalization to the known content then allowed for estimation of the general amorphous content.

The porosity, permeability, SEM, FTIR, XRD and EDX measurements have been presented elsewhere (Maheshwari, 2014), but they are referenced and re-analyzed in this study to support observations from mechanical test.

### **4.3 Results and Discussion**

Effects of temperature, CO<sub>2</sub> gas composition and total test pressure on cement degradation are presented in this section. Evidence of alteration in mineralogy,

microstructure, and morphology after exposure to CO<sub>2</sub>-saturated brine is first presented using BSE-SEM, EDX, FTIR, XRD, and fluid chemistry measurements. Afterwards, the effects of variation in temperature, CO<sub>2</sub> gas composition and total test pressure on FTIR mineralogy, compressive strength, porosity, permeability and physical degradation is discussed.

### **4.3.1 Characterization of Mineralogy, Morphology and Microstructure**

#### **4.3.1.1 SEM Images and EDX Elemental Composition**

**Figure 4.8** presents two different resolutions of the back-scattered SEM images of Classes G and H specimens that were aged at 225°F, 6000 psi and 40% CO<sub>2</sub>. These pictures show the interface between the CO<sub>2</sub> penetrated zone (usually carbonated) and the unpenetrated zone (uncarbonated). The back-scattered electron images show zones consisting of three color-coded sections: white, light grey and dark grey. Kutchko et al. (2007) deduced from BSE image that unhydrated cement compounds are usually the brightest while calcium hydroxide (CH) is less bright and calcium silicate hydrate (C-S-H) is darker. Therefore, the white spots in the unpenetrated region refer to the unhydrated clinker materials (i.e. C<sub>3</sub>S, C<sub>2</sub>S, C<sub>3</sub>A and C<sub>4</sub>AF). The light grey corresponds to CH while the dark grey signifies C-S-H. A location was selected in this unpenetrated zone and enlarged SEM images were obtained at two different resolutions (**Figure 4.9a**). Typically, CH and CSH are the primary compounds expected to be present in this zone, both being cement hydrates that are produced after hydration of clinker compounds. To confirm the elemental composition of the hydrate present, EDX analysis (**Figure 4.9b**) was conducted at the location of the image. The elements detected by EDX are typical

elements in calcium hydroxide and calcium silicate hydrate. Using this information together with the FTIR and XRD mineralogy (presented in Sections 4.3.1.2 and 4.3.1.3), the presence of CH and CSH is inferred. Although dissolved CO<sub>2</sub> has not penetrated this zone, calcium leaching can occur due to the difference between calcium ion concentration in solid CH and calcium ion concentration in the pore solution. This concentration difference establishes a gradient that leads to the diffusion of calcium ions into the pore fluid, which would result in the dissolution of solid CH.

**Figure 4.9c** shows the SEM image at a location in the penetrated zone of a specimen that was aged at 3000 psi. The pore at this location is packed with CaCO<sub>3</sub>, which arises from carbonation of cement hydrates. **Figure 4.9d** displays the SEM image at a location in the penetrated zone of a specimen that was prepared, cured and aged under the same conditions of temperature and CO<sub>2</sub> concentration with the exception of total test pressure (9000 psi). This image shows additional grain packing in the pores, which suggests high degree of carbonation at this pressure. EDX data (**Figure 4.9e**) shows that the penetrated zone is composed of carbonates, especially calcium carbonate (CaCO<sub>3</sub>). Subsequently, CaCO<sub>3</sub> is leached after exposure to additional carbonated brine. The leaching front (i.e. dissolution of CaCO<sub>3</sub>) occurs behind the carbonation front. In the leached zone, structurally weak amorphous silica is the expected by-product of cement degradation.

**Figure 4.10a** shows the SEM image at a location in the degraded zone of another specimen that was aged at 3000 psi. At this location, the pore would normally be filled with carbonates, which arises from carbonation of CH and C-S-H. The specific type of carbonate was investigated by EDX analysis (**Figure 4.10b**). EDX detected

elements that are typically found in  $\text{CaCO}_3$  and calcium silicate carbonate (C-S-C). So, the presence of  $\text{CaCO}_3$  and C-S-C is inferred from this data. Several forms of C-S-H exist including  $9\text{\AA}$  tobermorite or riversideite,  $10\text{\AA}$  tobermorite or oyelite,  $11\text{\AA}$  tobermorite or normal tobermorite,  $14\text{\AA}$  tobermorite or plombierite, xonotlite, truscottite, pectolite etc. (Eilers et al., 1983; Méducin et al., 2002; Le Saout et al., 2004, 2006a, and 2006b; Brandl et al., 2011; Noik and Rivereau, 1999). Similarly, scawtite, spurrite, fukalite, tilleyite and galuskinite are known forms of C-S-C. XRD analysis was conducted to precisely determine the form of C-S-H and C-S-C present post-degradation. The result of this analysis is presented in Section 4.3.1.3.

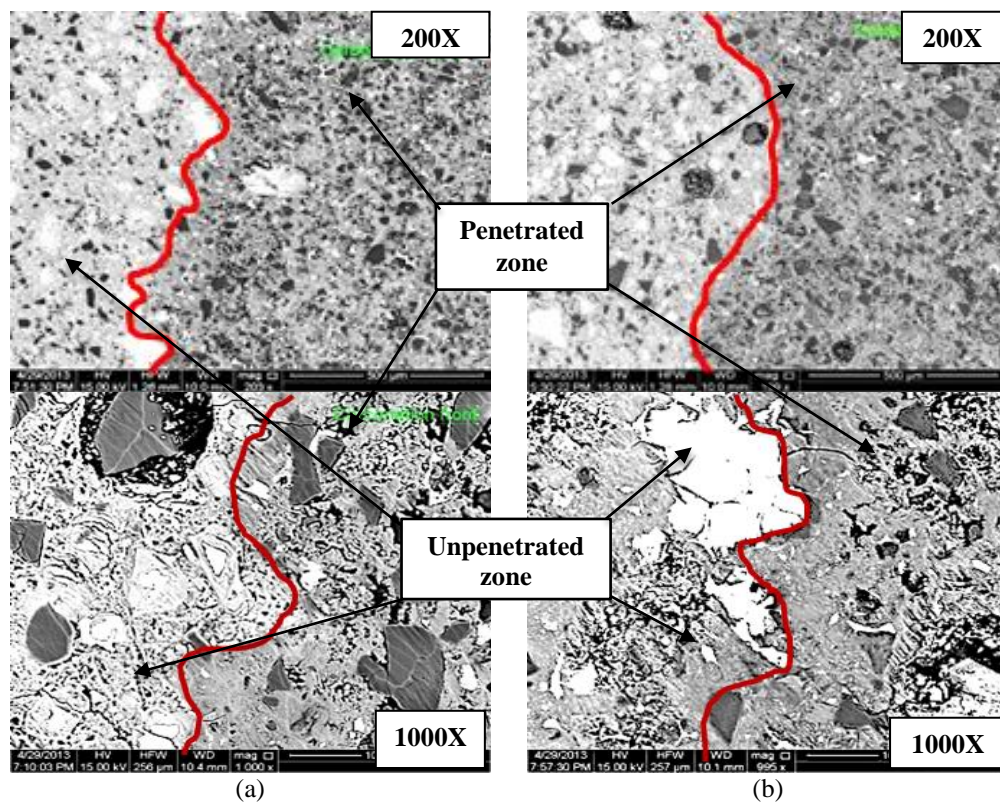


**Figure 4.8 SEM images showing penetrated and unpenetrated zones in (a) Class G; (b) Class H cements (Omosibi et al., 2015)**



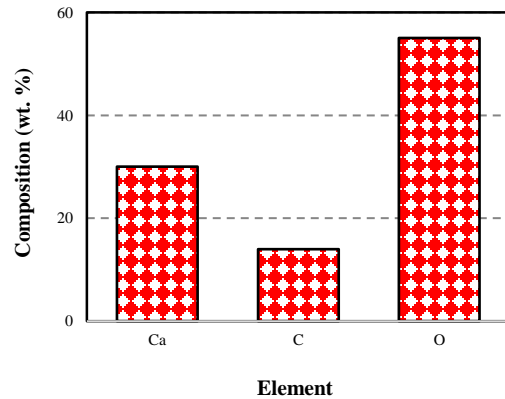
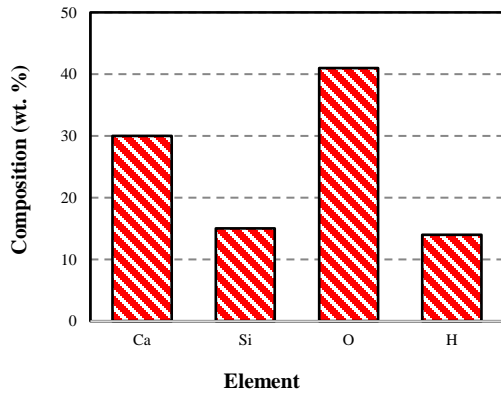
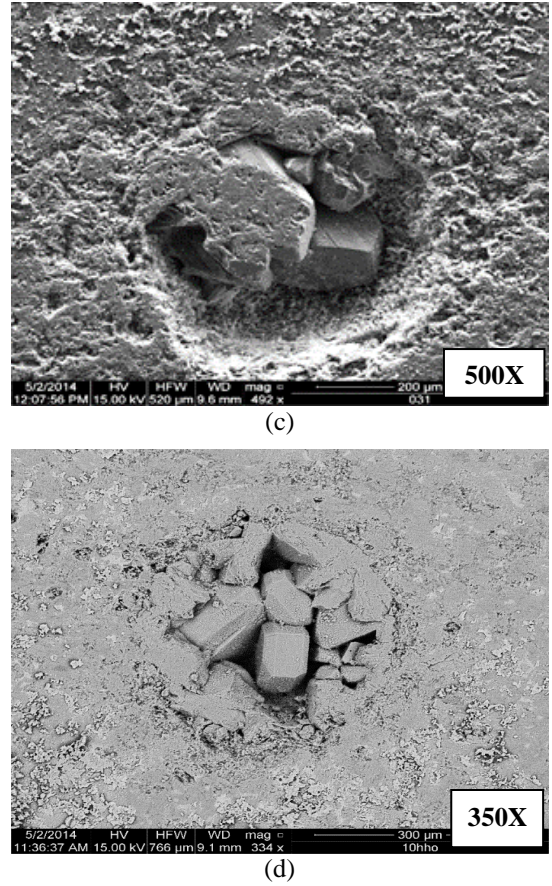
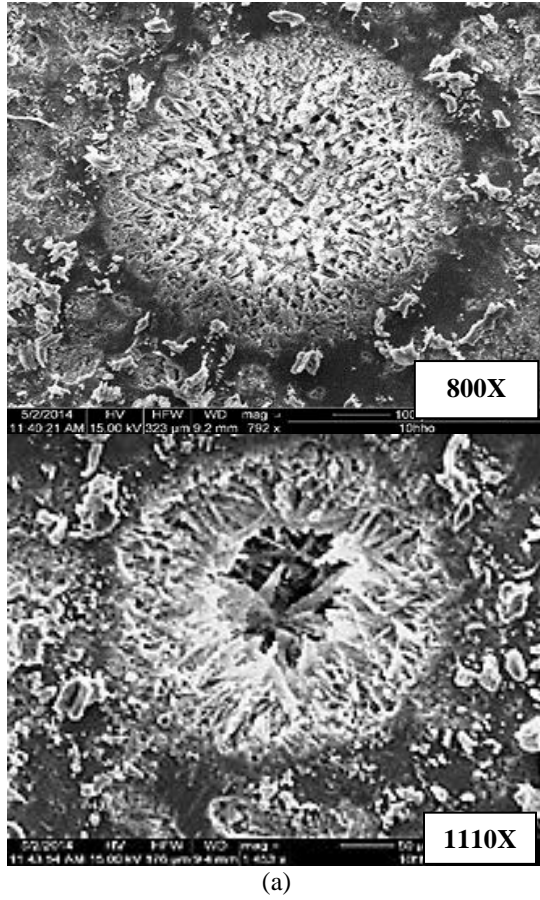


**Figure 4.9 (a) SEM images showing formation of hydrate in the unpenetrated zone of Class H cement; (b) composition of elements obtained from EDX spot analysis of (a); (c) SEM image showing formation of calcium carbonate in penetrated zone of Class H cement at 3000 psi; (d) SEM image showing formation of calcium carbonate at 9000 psi; (e) composition of elements obtained from EDX spot analysis of (d)**

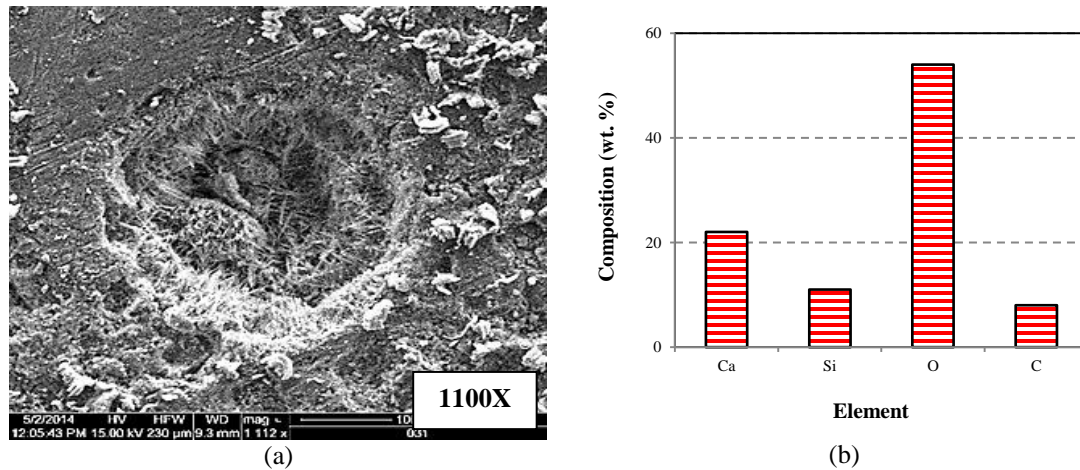


Figure 4.10 (a) SEM image showing formation of calcium silicate carbonate in penetrated zone at 3000 psi; (b) composition of elements obtained from EDX analysis

### 4.3.1.2 Fourier Transform Infra-Red (FTIR) Analysis

FTIR Spectra Analysis. FTIR-based mineralogy analysis was conducted to characterize the minerals present in the degraded specimens and to assess the degree of degradation and alteration due to chemical attack. In this analysis, three points were selected to collect FTIR samples, one from each of the outer, middle and inner zones of Class H specimens (Figure 4.11).

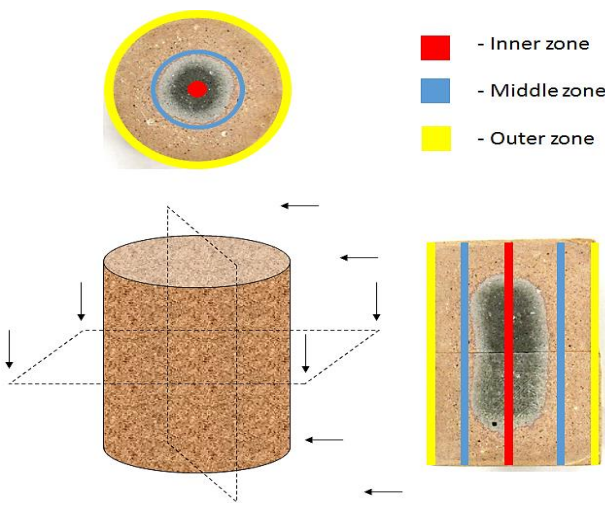
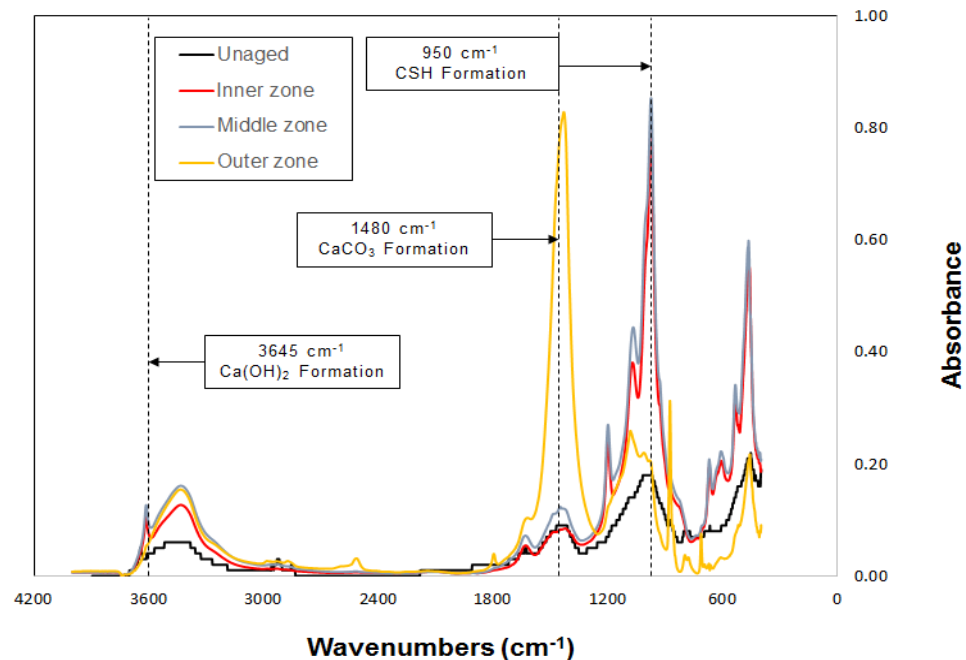


Figure 4.11 Three selected zones in degraded specimens used for FTIR analysis: inner (red), middle (blue) and outer (yellow) zones (show only top and cut sections)

Absorbance peaks of FTIR spectrum at wavenumbers specific to a mineral can be used to identify the presence of the mineral. The intensity (i.e. height) of this peak is directly related to the amount of the mineral present. For instance, qualitative assessment of carbonation and leaching can be conducted using FTIR absorbance peaks. Ylmén et al. (2013) applied this technique successfully to monitor the formation of carbonates in cement. Each peak of absorbance at a certain wavenumber in the FTIR spectra denotes a specific mineral. The distinct absorbance peaks of binding components of cement (CH and C-S-H) and expected degradation products were used to identify the minerals present. Calcium silicate hydrate, calcium carbonate and calcium hydroxide are the major minerals expected after exposure, each exhibiting approximate peaks of 950, 1480 and 3645  $\text{cm}^{-1}$ , respectively (Rutt and Nicola 1974; Frech et al. 1980; Xyla and Koutsoukos 1989; Matsuda and Tsukada, 1995; Vagenas et al. 2003; Gunasekaran et al. 2006; Zaki et al., 2006; Baciu and Simitzis, 2007; Ylmén et al. 2009, 2013).



**Figure 4.12 Comparison of FTIR spectra of unaged and aged specimens of Class H cement**

**Figure 4.12** compares FTIR spectra of unaged and aged specimens. At wave number  $3645\text{ cm}^{-1}$ , the unaged specimen and inner/middle zones of the aged specimen, show CH absorbance peak. This implies that CH has been consumed in the outer zone through carbonation and/or leaching reactions. At  $950\text{ cm}^{-1}$ , similar observation occurs in the inner and middle zones of the aged specimen as well as the unaged specimen. This indicates that C-S-H is preserved in these zones. In the outer zone, absorbance peak of  $\text{CaCO}_3$  occurs at  $1480\text{ cm}^{-1}$  due to the consumption of CH and C-S-H in this zone. In the inner and middle zones, weak absorbance peaks of  $\text{CaCO}_3$  indicate limited penetration of carbonic acid. This mineralogical proof substantiates the existence of maximum carbonation in the outer zone of the aged sample, which arises from direct exposure of this zone to carbonated brine. To investigate the effects of temperature,  $\text{CO}_2$  gas composition and total test pressure on chemical degradation, FTIR absorbance peaks of calcium hydroxide (CH), calcium silicate hydrate (C-S-H), and carbonates were retrieved and normalized. These are presented in Sections 4.3.2, 4.3.3, and 4.3.4.

Although FTIR spectra analysis is able to identify CH, CSH and carbonates ( $\text{CaCO}_3$  and C-S-C) in the exposed and unexposed specimens, it does not fully characterize the minerals present for the following reasons. Firstly, calcium silicate hydrate exhibits structural polymorphs depending on temperature and C/S ratio. Characterization of these polymorphs requires a more sophisticated technique. Secondly, FTIR uses carbonate bond ( $\text{CO}_3^{2-}$ ) to identify the presence of carbonates. When cement is exposed to carbonated brine, several types of carbonates could be formed, depending on the cement hydrates being carbonated and environmental conditions of temperature and pressure. These include calcite, aragonite, vaterite, ikaite, scawtite, fukalite, spurrite,

tilleyite and galuskinite. FTIR is not able to detect the specific carbonate formed under the aging conditions. Thirdly, cement clinker compounds hydrate at different rates. Unhydrated clinker materials are not easily detected and/or quantified by FTIR. For these reasons, additional mineralogy technique is required to ascertain and quantify minerals that are not easily characterized by FTIR analysis. XRD analysis is a useful means of obtaining this information.

### **4.3.1.3 X-Ray Diffraction (XRD) Analysis**

#### **4.3.1.3.1 Unaged Specimen**

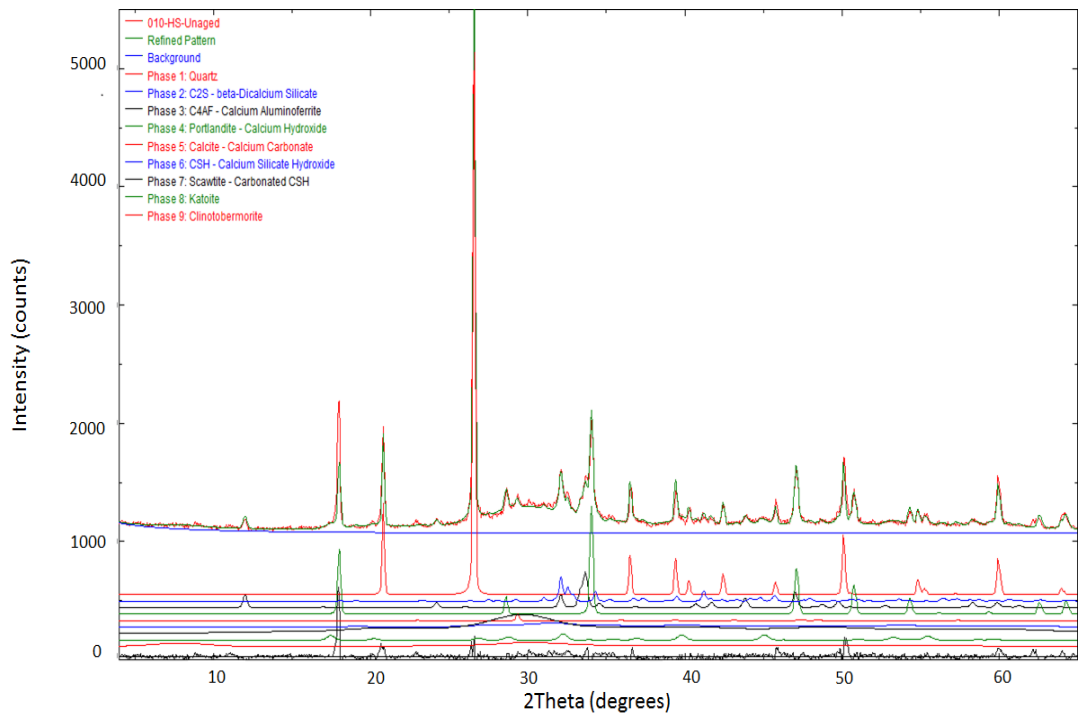
X-Ray diffraction patterns of unaged Class H specimen after 5 days of curing at 200°F is shown in **Figure 4.13a**. A high degree of crystallinity is resonated in the narrow peaks. **Figure 4.13b** shows the composition of all chemical compounds present. C<sub>2</sub>S and C<sub>4</sub>AF hydrate slowly but all the C<sub>3</sub>S and C<sub>3</sub>A were rapidly hydrated to produce portlandite, amorphous calcium silicate hydrate, and katoite (i.e., tricalcium aluminate hexahydrate, C<sub>3</sub>AH<sub>6</sub>). Compared to C<sub>2</sub>S and C<sub>4</sub>AF, rates of hydration of C<sub>3</sub>S and C<sub>3</sub>A are higher. Since the slurry was cured at 200°F, it is likely that pozzolanic reaction occurs between silica flour and portlandite. Occurrence of this reaction will reduce the amount of portlandite but increase the amount of calcium silicate hydrate.

Normally, a sulfate phase is necessary in well cement, not only to retard the aluminate, but also to act as a source for Ca<sup>2+</sup> ions. However, primary ettringite (formed in the presence of a sulfate phase) was not detected by XRD. Instead, metastable calcium aluminate hydrate (from hydration of C<sub>3</sub>A) is formed which is subsequently converted to cubic hydrate (i.e., katoite hydrogarnet). Moreover, formation of clinotobermorite (a crystalline polymorph of CSH) is likely due to the structural transformation of a fraction

of the amorphous CSH at curing temperature of 200°F. This crystalline phase of CSH is structurally related to 11Å tobermorite (Henmi and Kusachi, 1992), which is typically formed at temperatures near and above 200°F (Figure 3.3 in Chapter 3).

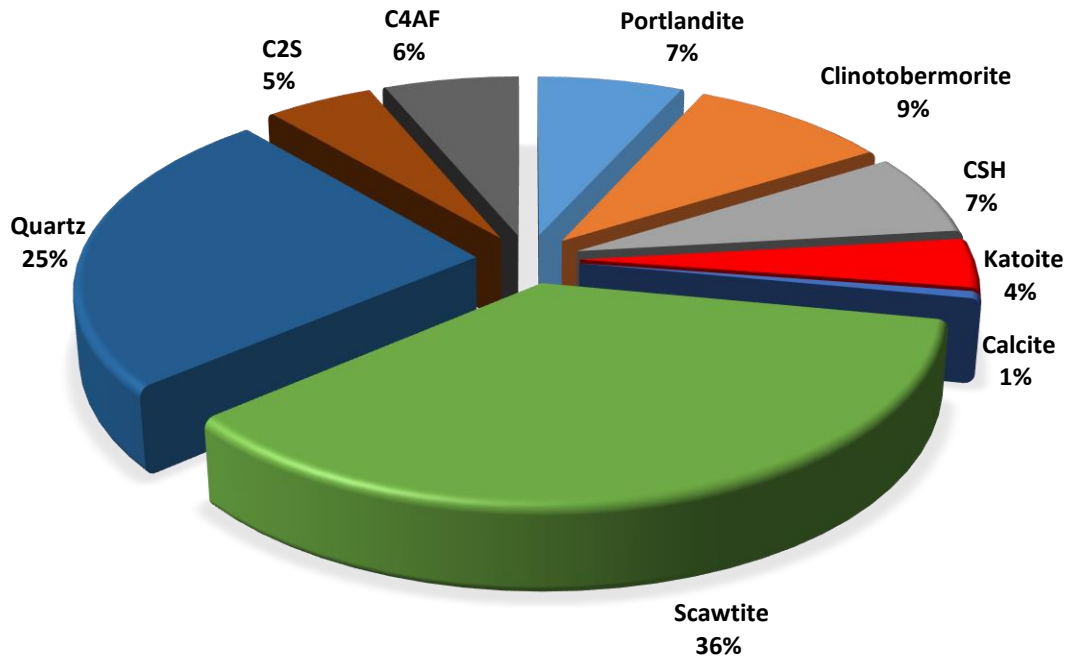
In the presence of atmospheric CO<sub>2</sub>, which dissolves in water during slurry mixing to form low concentration of carbonic acid, portlandite reacts to form calcite while reaction of calcium silicate hydrate account for the scawtite detected. Calcite-aragonite phase diagram (Mulder and Hassan, 2011) shows that aragonite is typically formed at high pressure. So, the absence of aragonite could be due to low curing pressure.

Over one-third of the cured cement is composed of scawtite while quartz occupies one-quarter after hydration (Figure 4.13b). Quartz may have been formed at 93°C from the added silica that has not undergone pozzolanic reaction with calcium hydroxide.



(a)





(b)

**Figure 4.13 XRD data for unaged Class H specimen cured for 5 days at 200°F (a) XRD spectra; (b) contribution of minerals in wt. % (Omosebi et al., 2015)**

44% BWOC water was used to prepare Class G cement slurry while 38% BWOC water was used to prepare Class H cement. The difference in mixing water content is expected to affect the performance of these classes of cement. It is not exactly clear the amount of water required to completely hydrate clinker materials. While some investigations reported 38% BWOC as the minimum amount of water required to chemically transform all cement clinker compounds to cement hydrates and that extra water merely fill the pores (Taylor 1997), former and recent data show a departure from this conclusion. In the work done by Danielson (1962), for instance, only 70% and 80% of cement was hydrated with water-to-cement (w/c) ratio of 40% and 50% respectively after 42 days of curing. Similarly, Bentz (2006) obtained 70% and 80% of hydrated cement with w/c ratio of 35% and 45% respectively, after the same curing period. It is worth mentioning that the composition of clinker materials and Blaine fineness also

control the overall degree of hydration ( $\alpha$ ). In both classes of cement, the compositions of clinker phases (Table 4.1) are comparable especially the calcium silicate phases both of which control development of mechanical strength. Lin and Meyer (2009) presented a comprehensive model for predicting overall degree of hydration with curing temperature, pressure, w/c ratio, clinker composition and Blaine fineness as input variables. This model was used to estimate  $\alpha$  under the mixing and curing conditions adopted in this study. For Class G cement,  $\alpha$  was approximately equal to 65%, while  $\alpha$  is equal to 60% for Class H cement. As reported by Lin and Meyer (2009), the value of  $\alpha$  for Class H cement is close to the experimental value for a cement system with  $\alpha = 60\%$  (Danielson 1962), whose w/c ratio, Blaine fineness and clinker composition are similar to the typical values for Class H cement that was presented in Table 4.1. Figure 4.14 shows that the clinker compounds were not completely reacted after mixing Class H cement with 38% BWOC mixing water.  $C_3S$  and  $C_3A$  are completely reacted because they hydrate faster while  $C_2S$  and  $C_4AF$  are incompletely reacted due to low rate of hydration. Therefore, it is not conclusive that 38% BWOC water would chemically transform all cement clinker materials to cement hydrates.

#### **4.3.1.3.2 Specimen Aged at 225°F, 6000 psi and 100% CO<sub>2</sub>**

X-Ray diffraction patterns of this specimen is presented in **Figure 4.14** and composition of minerals is presented in **Table 4.6** alongside the XRD data for the unaged specimen.

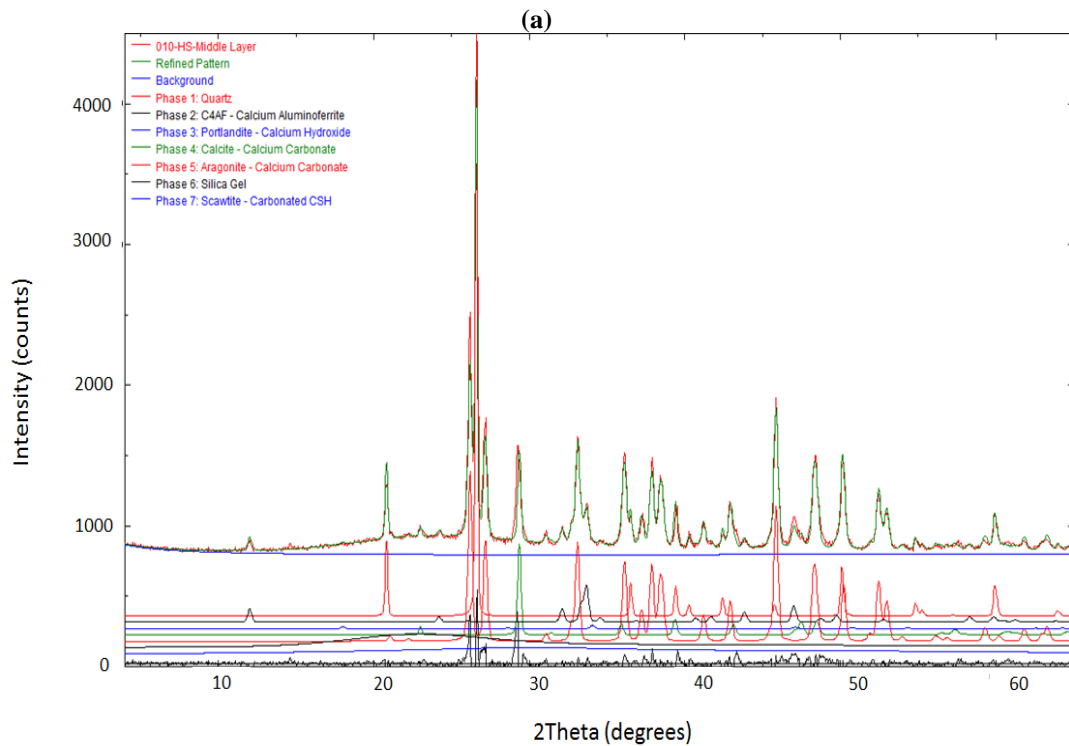
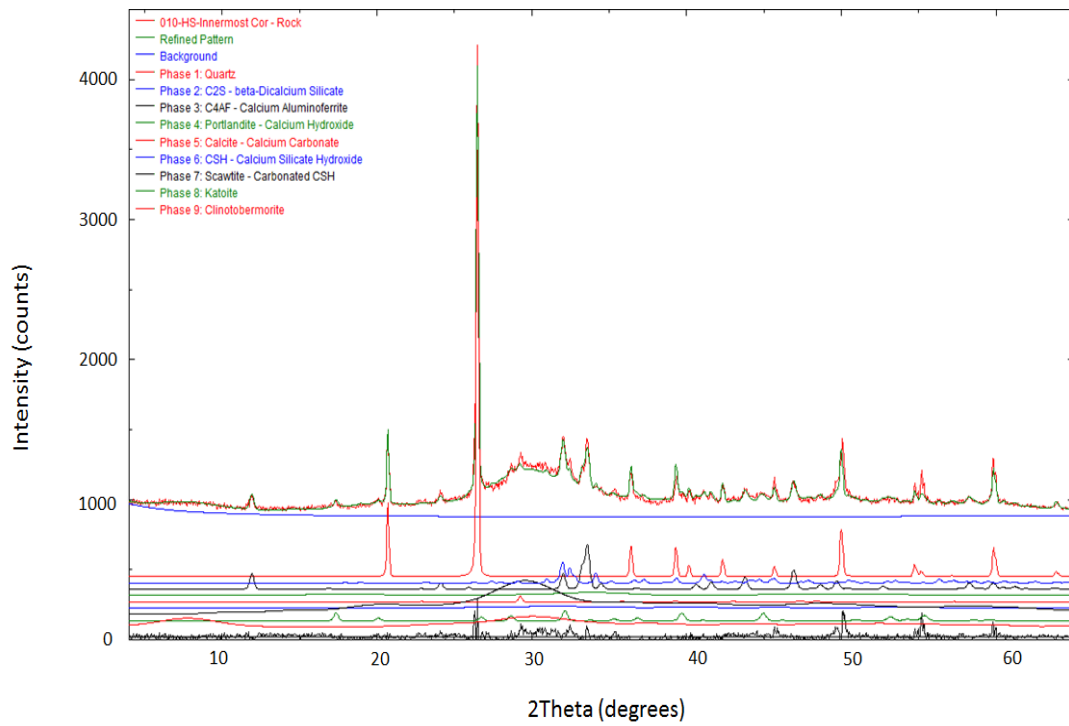
Compared to the unaged specimen,  $C_2S$  in the middle and outer zones of the aged specimen is completely reacted to form CH and CSH while further hydration of this slow-hydrating clinker compound may have occurred in the inner zone. Likewise,  $C_3A$

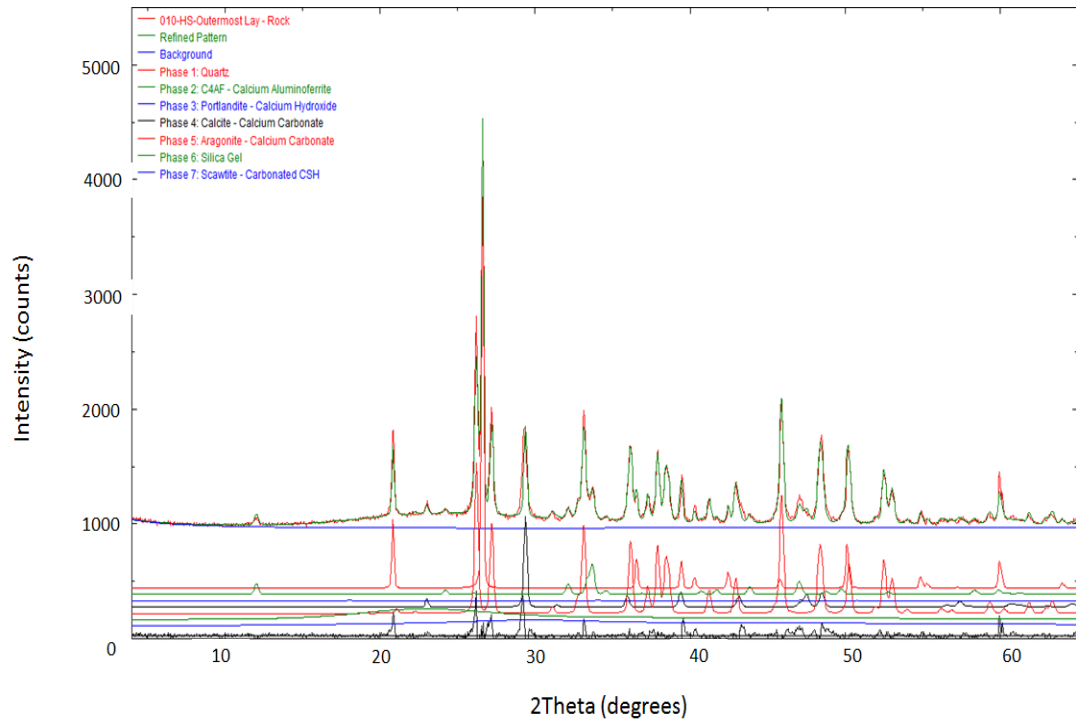


and  $C_4AF$  hydrate to produce katoite. Besides, the composition of  $C_4AF$  across all zones is roughly the same when compared to its composition in the unaged specimen. This suggests that  $C_4AF$  has low reactivity with carbonic acid. In addition,  $C_4AF$ , like  $C_2S$ , is a slow-hydrating compound. Formation of clinotobermorite in the inner zone is due to structural transformation of uncarbonated portion of CSH.

CH and CSH were consumed, especially in the outer and middle zones. Clearly, these zones are the most degraded due to increased exposure to acidic environment. In these zones, the reacted hydrates were carbonated to form calcite, aragonite and scawtite. The detection of calcite, aragonite and katoite agrees with field results of cement samples recovered from a well in West Texas with 30 years of  $CO_2$  flooding (Carey et al., 2007). Carbonation of CH was always complete leading to the formation of  $CaCO_3$ . However, carbonation of CSH was in some cases incomplete depending on the concentration of  $CO_2$  and temperature. Complete carbonation of CSH forms  $CaCO_3$  (calcite and aragonite) while incomplete carbonation forms C-S-Cs (e.g. scawtite). The XRD data shows higher amount of scawtite in the inner zone compared to the middle and outer zones. This is because of carbonic acid concentration variation in the specimen. Diffusion of dissolved  $CO_2$  from the bulk fluid to the pore fluid is limited by its reaction with cement hydrates; hence, the lowest acid concentration is expected in the inner zone. This low  $CO_2$  concentration favors dense formation of scawtite (Eilers et al., 1983). However, other calcium silicate carbonates (i.e., fukalite, spurrite, tilleyite and galuskinite) were not detected. In the middle and outer zones, however,  $CO_2$  concentration was relatively higher thereby minimizing the amount of scawtite formed in these zones. Formation of these carbonates in cement pores reduces transport properties

(i.e., porosity and permeability) and improves mechanical strength through matrix reinforcement.





(c)

**Figure 4.14 XRD spectra of the degraded zones of Class H specimen aged for 14 days in 2% NaCl solution at 225°F, 6000 psi, 100% CO<sub>2</sub>: (a) inner zone; (b) middle zone; (c) outer zone (Omosebi et al., 2015)**

**Table 4.6 Comparison between XRD data of unaged specimen and specimen aged at 225°F, 6000 psi and 100% CO<sub>2</sub> (Omosebi et al., 2015)**

Mineral	Composition (wt. %)			
	Aged			Unaged
	Inner Zone	Middle Zone	Outer Zone	
Calcium hydroxide	3.3	0.2	0.1	6.8
Calcium silicate hydrate	2.8	0.0	0.0	7.0
Clinotobermorite	18.9	0.0	0.0	9.4
Calcite	0.3	5.3	6.4	0.6
Aragonite	0.0	34.9	34.7	0.0
Scawtite	46.6	16.4	16.5	35.9
Quartz	15.1	17.0	17.5	24.9
Silica gel	0.0	21.1	19.7	0.0
Katoite	2.9	0.0	0.0	4.2
Tricalcium silicate	0.0	0.0	0.0	0.0
Dicalcium silicate	3.9	0.0	0.0	5.0
Tricalcium aluminate	0.0	0.0	0.0	0.0
Tetracalcium aluminoferrite	6.2	5.1	5.0	6.3

The formation of carbonates, in addition to the structural transformation of CSH, aids the retention of compressive strength. Silica gel is formed in the middle and outer zones due to bi-carbonation and leaching of  $\text{CaCO}_3$  which was formed from complete carbonation of C-S-H. Thus, in addition to quartz, silica gel constitutes the by-products of leaching, which are structurally weak. Compared to the strength-reinforcing carbonates, the amount of these materials is low (**Figure 4.15**). Consequently, carbonates are the dominant minerals governing mechanical behavior. This suggests that carbonation is the overriding mechanism of degradation. Therefore, the performance of well cement after exposure to carbonic acid under HPHT conditions is governed by chemical processes. The prevailing process dictates the mechanical performance of cement.

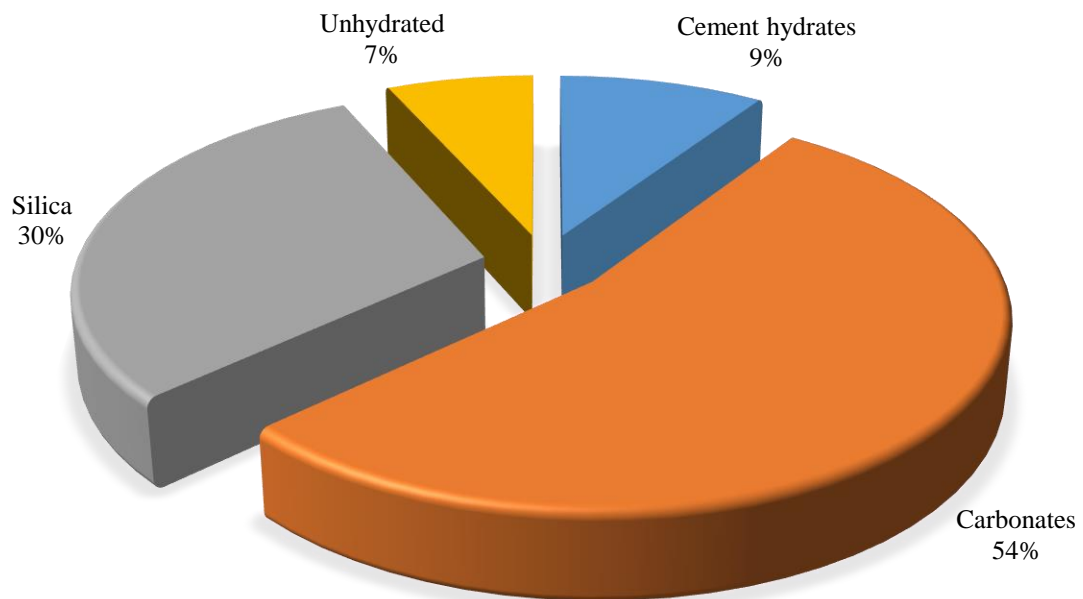


**Figure 4.15 Contribution of chemical phases in Class H cement aged for 14 days at 225°F, 6000 psi, 100%  $\text{CO}_2$  in 2% NaCl solution (Omosebi et al., 2015)**

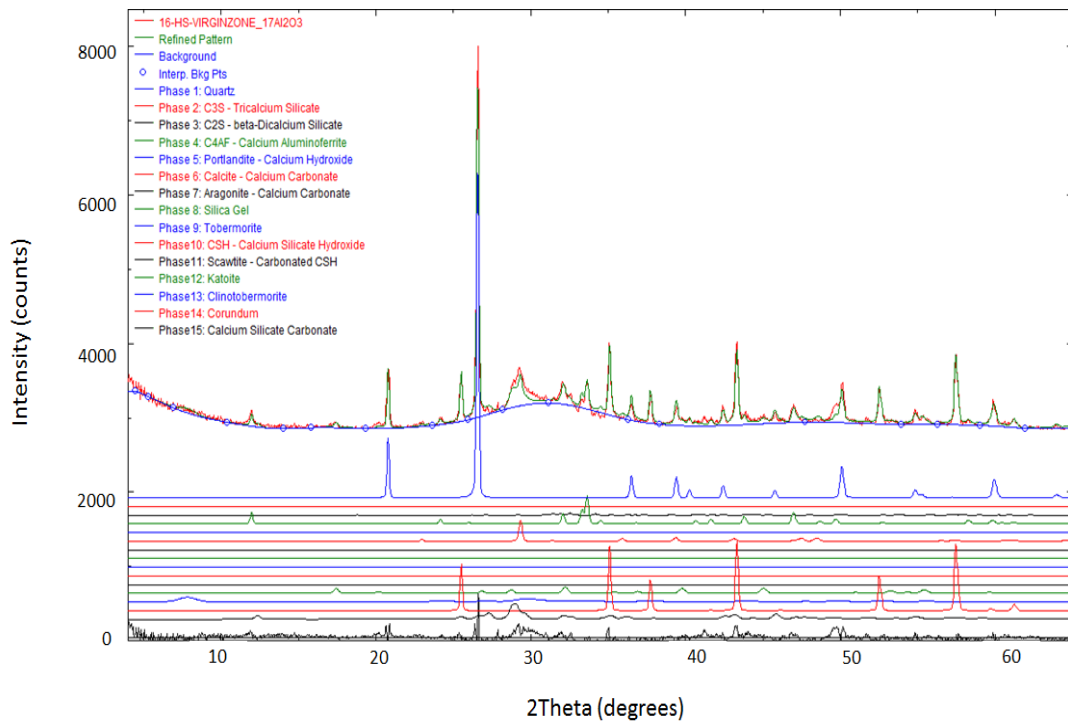
#### 4.3.1.3.3 Specimen Aged at 350°F, 3000 psi and 40% CO<sub>2</sub>

X-Ray diffraction patterns of the three degraded zones of this specimen is presented in **Figure 4.16** and composition of minerals is presented in **Table 4.7** alongside the XRD data for the unaged specimen.

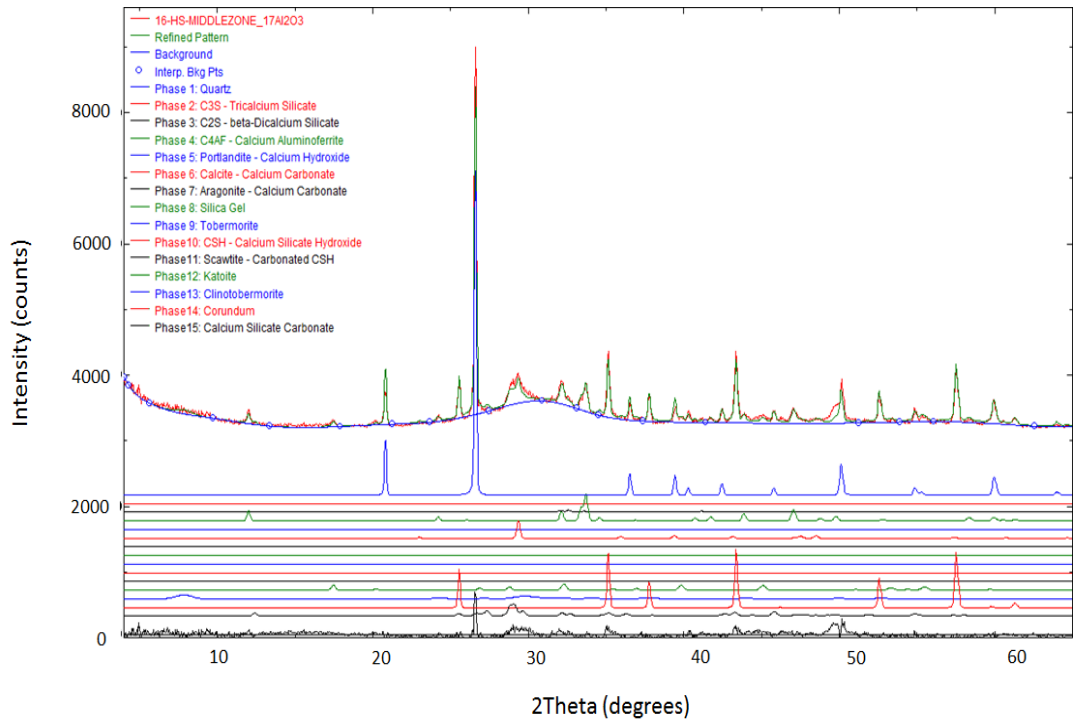
Compared to the unexposed specimen, all the C<sub>3</sub>S and C<sub>3</sub>A has been hydrated to produce portlandite, clinotobermorite and katoite while C<sub>2</sub>S and C<sub>4</sub>AF are not completely hydrated. Therefore, C<sub>3</sub>S is the major clinker component responsible for short-term strength development. Also, this indicates that C<sub>3</sub>S and C<sub>3</sub>A hydrate faster than C<sub>2</sub>S and C<sub>4</sub>AF. In the event of strength loss due to leaching, slow hydration of residual C<sub>2</sub>S can provide additional portlandite and calcium silicate hydrate required for long-term structural integrity. Besides, further hydration of C<sub>4</sub>AF is insignificant but reduction in the residual amount of C<sub>2</sub>S after exposure indicates further hydration. In addition, the composition of katoite across all zones is roughly the same after exposure, which implies that this mineral has low reactivity with carbonic acid.

Comparison of the mineral compositions in the unaged specimen with the composition of minerals across the degraded zones of the aged specimen (Table 4.7) confirms that calcium hydroxide is completely reacted to form and precipitate CaCO<sub>3</sub> (calcite and aragonite) while only a proportion of amorphous CSH is carbonated to form CaCO<sub>3</sub> or C-S-C. As stated previously, pozzolanic reaction between silica flour and portlandite might have reduced the amount of portlandite being carbonated. The compositions of calcite, aragonite and calcium silicate carbonate are highest in the outer zone. Evidently, this zone is the most degraded followed by the middle zone because it is exposed for the longest duration as dissolved CO<sub>2</sub> diffuses radially through the pore

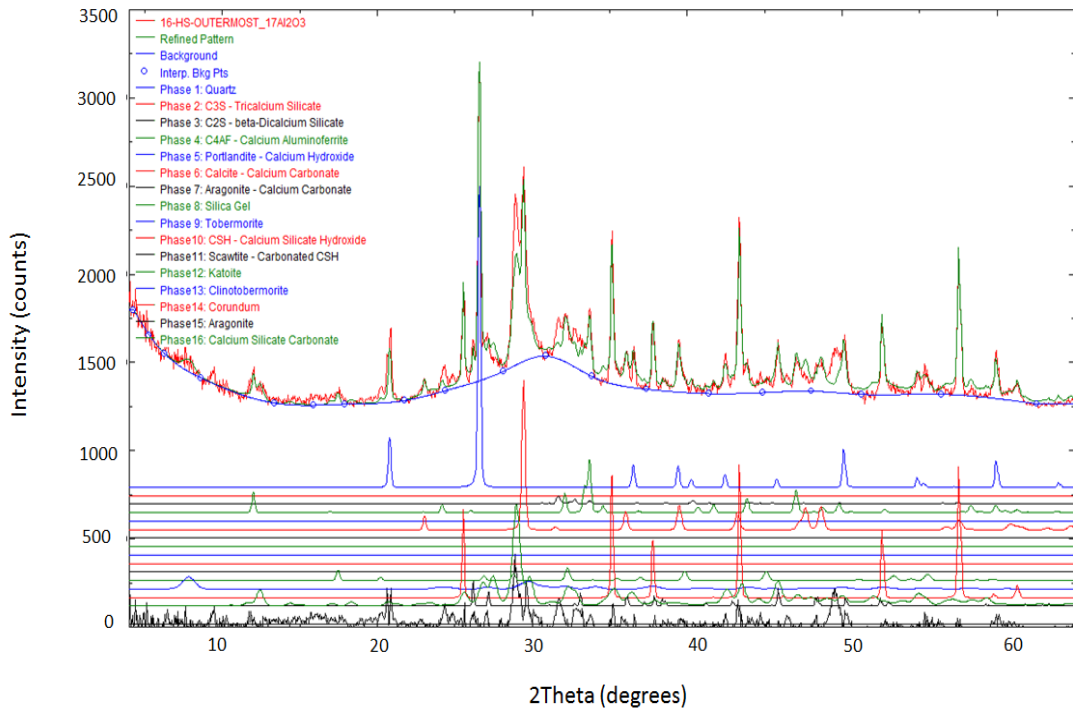
solution. The residual carbonate is mainly C-S-C which could be scawtite, fukalite, spurrite, tilleyite or galuskinite. However, XRD data does not indicate the exact type of C-S-C present. This incomplete carbonation limits the degree of leaching since the calcium silicate carbonates are inconvertible to water-soluble calcium bicarbonate that results in leaching. The uncarbonated portion of the amorphous CSH is transformed to crystalline clinotobermorite ( $\text{Ca}_5\text{Si}_6\text{O}_{14}(\text{OH})_4 \cdot 5\text{H}_2\text{O}$ ), a monoclinic polymorph of tobermorite which has similar microstructure as 11Å tobermorite (Henmi and Kusachi, 1992) with good transport and mechanical properties. Like CSH, clinotobermorite can also be carbonated when exposed to  $\text{CO}_2$ -containing fluid. The presence of these carbonates and clinotobermorite will contribute to the development of mechanical strength.



(a)



(b)



(c)

**Figure 4.16 XRD spectra of the degraded zones of Class H specimen aged for 14 days in 2% NaCl solution at 350°F, 3000 psi, 40% CO<sub>2</sub>: (a) inner zone; (b) middle zone; (c) outer zone (Omozebi et al., 2015)**

**Table 4.7 Comparison between XRD data of unaged specimen and specimen aged at 350°F, 3000 psi and 40% CO<sub>2</sub> (Omosebi et al., 2015)**

Mineral	Composition (%)			
	Aged			Unaged
	Inner Zone	Middle Zone	Outer Zone	
Calcium hydroxide	0.0	0.0	0.0	7.0
Clinotobermorite	5.6	6.2	6.3	9.0
Calcite	2.3	2.5	9.8	1.0
Quartz	22.9	24.4	13.8	25.0
Katoite	3.8	4.2	3.5	4.0
Dicalcium silicate	1.0	1.0	1.6	5.0
Tetra calcium aluminoferrite	5.6	7.2	6.3	6.0
Aragonite	0.0	0.0	2.5	0.0
Calcium silicate carbonate	10.4	8.6	33.5	0.0
Amorphous phases	48.4	45.9	22.8	0.0
Calcium silicate hydrate	0.0	0.0	0.0	7.0

Amorphous silica is the by-product of bi-carbonation and leaching of calcium carbonate due to incessant exposure to carbonic acid. **Figure 4.17** shows the overall contribution of the major materials after degradation. The composition of silica phases, a structurally-weak mineral, indicates a severely leached specimen.

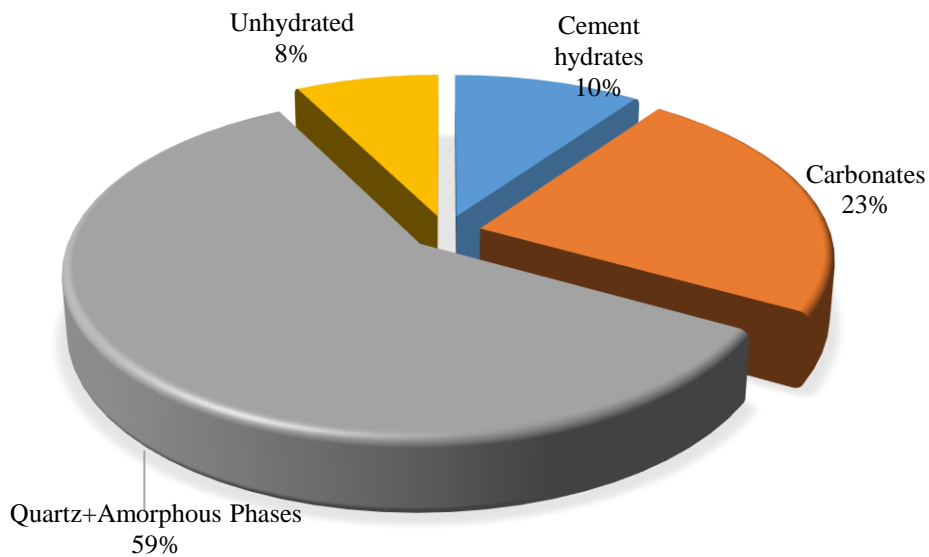


**Figure 4.17 Contribution of chemical phases in Class H cement aged for 14 days at 350°F, 3000 psi, 40% CO<sub>2</sub> in 2% NaCl solution (Omosebi et al., 2015)**



### 4.3.2 Bulk Fluid Chemistry

The effects of variation in CO<sub>2</sub> partial pressure at different temperatures on bulk fluid calcium concentration and pH are presented in **Figure 4.18**. As noted previously, concentration of HCO<sub>3</sub><sup>-</sup> increases with CO<sub>2</sub> partial pressure (Figure 3.10a in Chapter 3). This leads to the diffusion of HCO<sub>3</sub><sup>-</sup> into the pore fluid due to concentration gradient. The diffused HCO<sub>3</sub><sup>-</sup> then interacts with Ca<sup>2+</sup> ion from the speciation of Ca(OH)<sub>2</sub> and CSH in pore solution to form calcium carbonate. The calcium carbonate is further leached in the presence of additional HCO<sub>3</sub><sup>-</sup> ion thereby releasing Ca<sup>2+</sup> ion, which subsequently diffuses from the pore fluid into the bulk fluid. The diffusion of this Ca<sup>2+</sup> ion, in addition to the back and forth transport of other aqueous species, alters the pH of the bulk fluid.

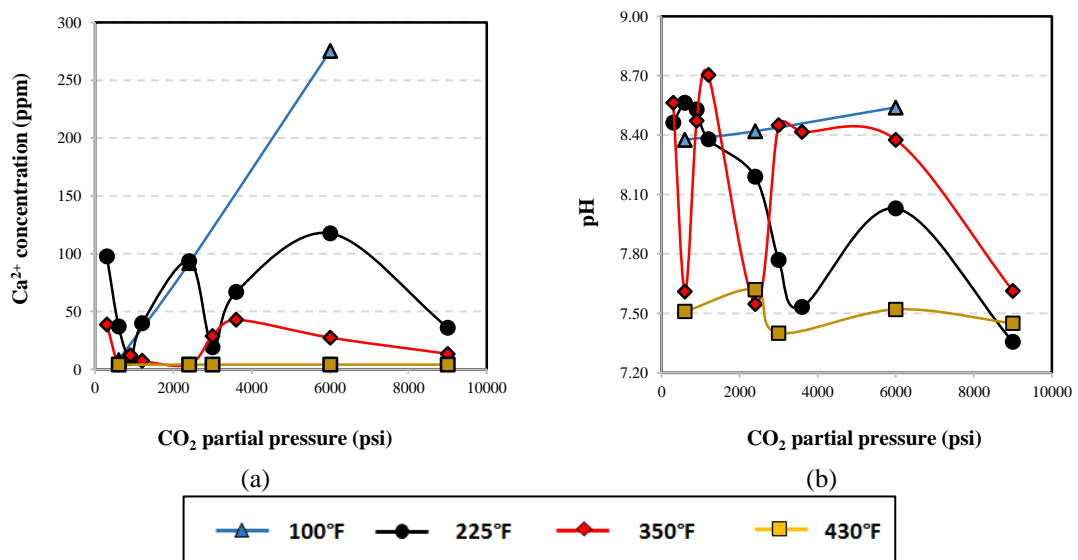


**Figure 4.18 (a) Effect of CO<sub>2</sub> partial pressure on bulk fluid calcium concentration; (b) Effect of CO<sub>2</sub> partial pressure on bulk fluid pH**

At 100°F, pH of the bulk fluid increases as the composition of CO<sub>2</sub> gas is increased. This arises from the consumption of HCO<sub>3</sub><sup>-</sup> ion during carbonation reaction and the release of OH<sup>-</sup> (from the dissolution of calcium hydroxide) into the bulk solution;

thus, increasing the alkalinity of the bulk fluid. The corresponding increase in  $\text{Ca}^{2+}$  ion concentration indicates that the specimen is progressively leached. At this relatively low temperature, the solubility of cement hydrates, especially calcium hydroxide, are high. Well-defined linear trends for calcium content and pH imply less reactivity between cement and carbonated-brine. Thus, the dissolution and/or decalcification of cement hydrates account for the trend observed.

At 225°F, fluid pH generally decreases with  $\text{CO}_2$  partial pressure; hence the overall condition of the bulk fluid is acidic. However, the calcium content interchanges between high and low values, but shows the same behavior as pH between 2400 psi and 9000 psi partial pressures. This could mean that the chemical reactions leading to cement degradation as approached equilibrium, when the net change in mechanical and transport properties is almost constant. Below 2400 psi  $\text{CO}_2$  partial pressure, pH cannot be correlated with calcium content because the rate of carbonation and leaching reactions have not reached equilibrium. At total test pressure of 3000 psi, for instance, variation in  $\text{CO}_2$  concentration corresponds to 300 psi, 1200 psi and 3000 psi  $\text{CO}_2$  partial pressures. Thus, calcium ion concentration decreases with  $\text{CO}_2$  gas composition at this total test pressure. This indicates that leaching is suppressed compared to carbonation. Experimental measurements of mechanical and transport properties of the specimens aged in this fluid are presented in Section 4.3.4.2.2. Analysis of the results shows that the specimens were dominated by carbonation and not leaching. At high test pressures, however, calcium ion concentration generally increases with  $\text{CO}_2$  gas composition, which indicates that leaching is more effective than carbonation. However, the magnitude of

change in bulk fluid calcium content suggests a gradual leaching of the specimens. Similar behavior occurs at 350°F and 430°F.

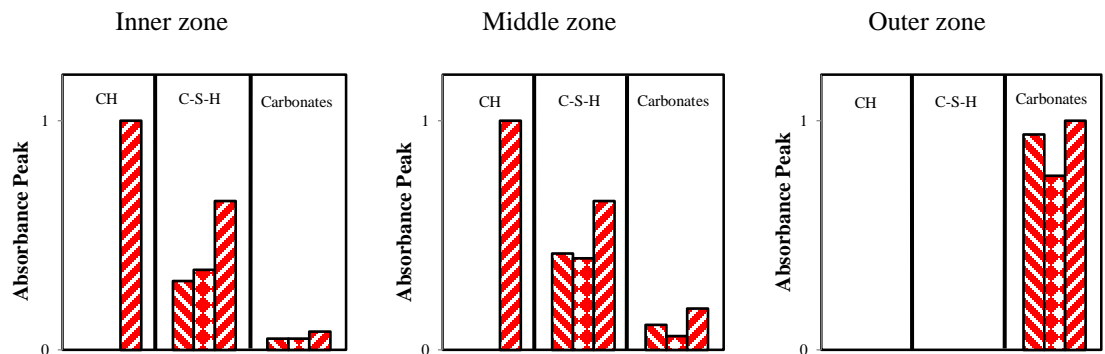
Generally, the amount of calcium in the bulk fluid decreases as temperature increases. As noted previously, this is due to the reduction in the solubility of cement hydrates as temperature increases.

### 4.3.3 Effect of Temperature on Cement Integrity

Two case studies of temperature effects are investigated. In the first case, temperature was varied at 100% CO<sub>2</sub> concentration and pressures of 3000 psi, 6000 psi and 9000 psi. In the second case, temperature was varied at 6000 psi and CO<sub>2</sub> concentrations of 10%, 40% and 100%. Compressive strength data are analyzed and supported with porosity, permeability, XRD, FTIR, and SEM measurements.

#### 4.3.3.1 Effect of Temperature at 100% CO<sub>2</sub>

In this section, CO<sub>2</sub> gas composition is kept constant at 100% and temperature was varied from 225°F to 430°F at 3000 psi, 6000 psi, and 9000 psi.



(a)

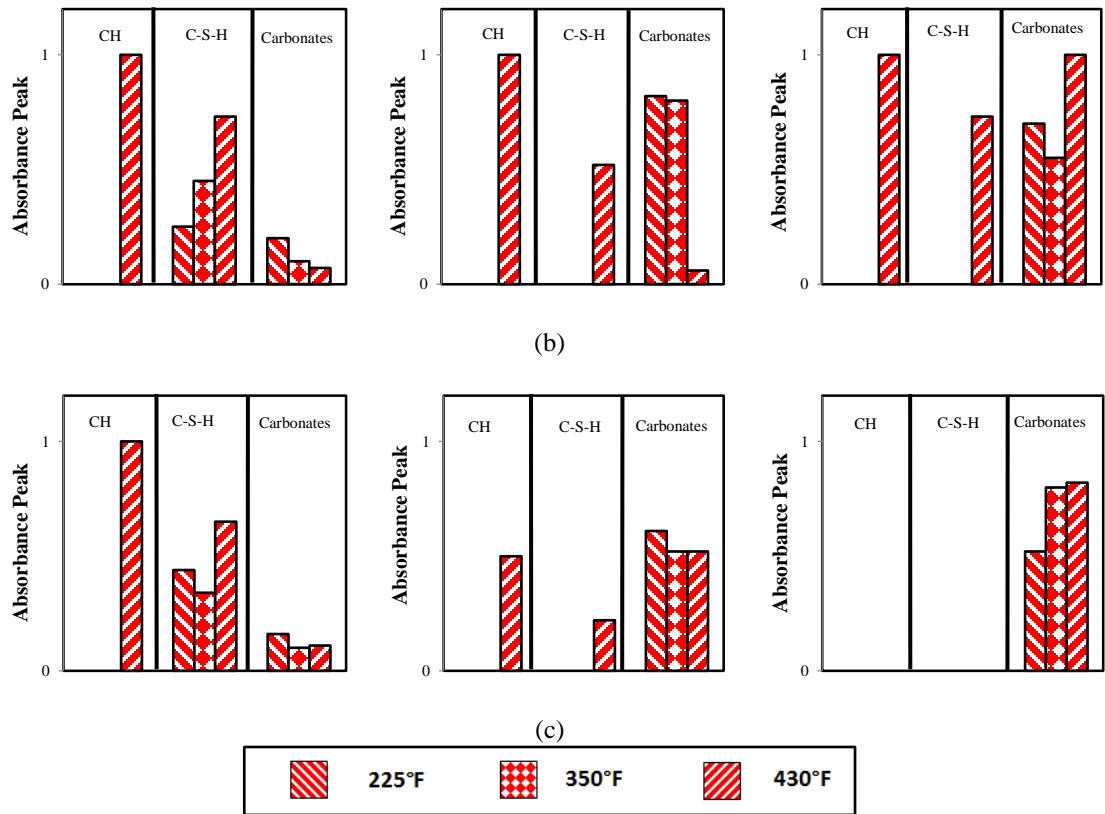


**Figure 4.19** Effect of temperature at 100% CO<sub>2</sub> gas composition on the normalized absorbance peaks extracted from FTIR spectra of degraded zones of Class H cement: (a) 3000 psi; (b) 6000 psi; and (c) 9000 psi (Omosebi et al., 2015)

#### 4.3.3.1.1 FTIR Mineralogy

**Figures 4.19** shows the peaks of calcium hydroxide, calcium silicate hydrate and carbonates (CaCO<sub>3</sub> and C-S-C) extracted from FTIR spectra of the degraded zones of Class H specimens that were aged 100%CO<sub>2</sub> concentration and 3000 psi, 6000 psi, and 9000 psi. In the inner and middle zones, C-S-H is preserved at all temperatures investigated while portlandite has been consumed across all zones except at 430°F. The retention of CH at 430°F is due to the reduction in its solubility as temperature increases (Nakarai, 2006). The rapid consumption of portlandite at 225°F and 350°F leads to the formation of CaCO<sub>3</sub> in the penetrated zones while additional incomplete carbonation of C-S-H intensified the absorbance peak of carbonates in the outer zone. At 6000 psi and

9000 psi (**Figures 4.19b and 4.19c**), deeper penetration of carbonic acid is observed since almost all the hydrates have been carbonated in the middle and outer zones to produce carbonates. The degrees of consumption of portlandite and C-S-H increases as pressure rises from 6000 psi to 9000 psi. As stated previously, the retention of portlandite and C-S-H in the inner and middle zones at 430°F implies that their solubilities are low at this high temperature.

#### **4.3.3.1.2 Mechanical Degradation**

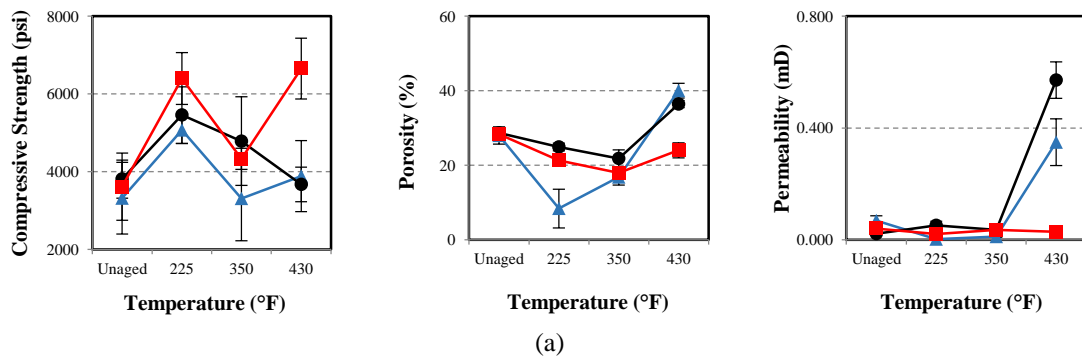
**Figure 4.20** shows the compressive strength, porosity, and permeability of Classes G and H cement, after temperature was varied at 100% CO<sub>2</sub> gas composition and different test pressures. At 3000 psi, strength initially develops in both classes of cement up to 225°F due to carbonation. Correspondingly, porosity and permeability decreases at the same temperature. Subsequently, compressive strength decreases at higher temperatures. This implies that 225°F is the maximum temperature at which carbonation controls degradation. Above this temperature, CO<sub>2</sub> solubility increases with temperature (Figure 3.8 in Chapter 3) and this shifts the equilibrium position of equation 2.15 to the right for increased H<sub>2</sub>CO<sub>3</sub> production. This rightward shift of equilibrium position promotes dissolution of calcium carbonate as equilibrium reaction in equation 3.4 responds by shifting to the right. Therefore, carbonation reaction is expected to be complete leading to the formation of CaCO<sub>3</sub>. In the presence of high CO<sub>2</sub> concentration, this carbonate could be leached subsequently thereby reducing strength and increasing porosity and permeability. XRD analysis of Class H specimen aged at 350°F, 3000 psi and 40% CO<sub>2</sub> gas composition (Fig 4.17 in Section 4.3.1.3.3) confirms a leaching-dominated chemical degradation. Although the CO<sub>2</sub> gas composition in the present

investigation is higher than 40%, the presence of higher concentration of carbonic acid will only facilitate the leaching process.

At 6000 psi, compressive strength increased up to 225°F in Class G cement due to formation of calcium silicate carbonate and/or calcite over its dissolution. Porosity and permeability decreased consistently. Above 225°F, strength decreases while transport properties increase signifying a chemical degradation controlled by leaching. The same trend is observed in Class H cement but strength development persisted up to 350°F possibly due to its improved CO<sub>2</sub> resistance than Class G cement. This also accounts for the corresponding reduction in porosity and permeability of the cement up to 350°F, with self-healing (i.e., precipitation, dissolution and further precipitation of carbonates) of cracks also playing major role in the mixed trends observed in these transport properties. XRD analysis indicates that the degradation of Class H specimen aged at 225°F, 6000 psi and 100% CO<sub>2</sub> gas composition (Figure 4.15 in Section 4.3.1.3.2) is controlled by carbonation. This explains the trend observed in Class H cement at 225°F. At extremely high temperature (i.e., 430°F), commencement of leaching-dominated reaction is noticeable but residual strength, porosity and permeability are adequate for casing support and zonal isolation.

At 9000 psi, measurements show mixed trend in compressive strength, porosity and permeability. Strength development persisted up to 225°F in Class G cement primarily due to the precipitation of carbonates which is expected as the dominant mechanism at this temperature. Beyond 225°F, a switch to leaching-dominated reaction is observed and this is consistent with data that were presented previously. At 430°F, strength is further developed in this class of cement. Slight increase in porosity at this

temperature indicates that a degradation mechanism, other than carbonation, controls the overall mechanical behavior. At high temperature, solubility of portlandite decreases. In addition to  $\text{CaCO}_3$  formed in the pores, the retention of portlandite preserves matrix strength thereby improving further strength development. Under this temperature condition, strength retrogression of uncarbonated CSH would be minimized owing to the presence of 35% BWOC silica flour. At best, CSH would be transformed to xonotlite, according to the phase transformation chart presented in Chapter 3. This crystalline phase of CSH has acceptable mechanical and transport properties required for casing support and good zonal isolation. Similar trend is demonstrated by Class H cement but with superior performance over Class G cement because it is more  $\text{CO}_2$  resistant (Bruckdorfer, 1986) and hence carbonation dominates up to  $350^\circ\text{F}$ . Measurement of compressive strength and water permeability of Classes G and H cement by Nelson and Eilers (1985) also shows that Class H cement is stronger and less permeable than Class G cement at elevated temperature. Overall trend in compressive strength shows a progressive increase in strength as total test pressure increases.



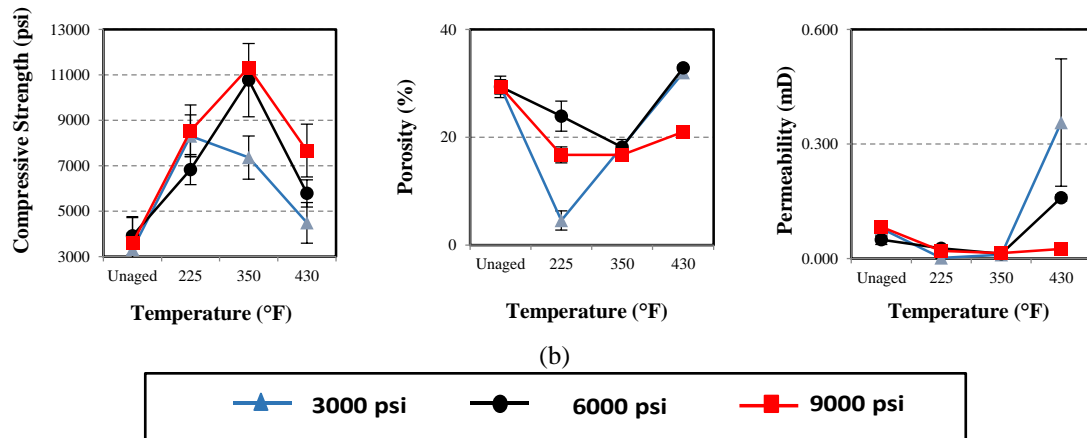
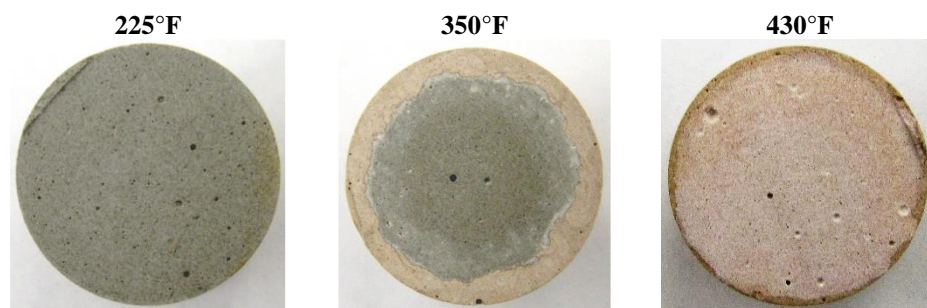


Figure 4.20 Effects of temperature at 100% CO<sub>2</sub> gas composition and different test pressures on the compressive strength, porosity, and permeability of: (a) Class G; (b) Class H (Omosebi et al., 2015)

### 4.3.3.1.3 Visual Degradation

Figures 4.21 and 4.22 show visual degradation of the degraded cores of Classes G and H specimens. In each figure, temperature is varied from left to right while pressure is varied from top to bottom. In both cements, visual inspection shows that the degree of cement degradation increases with temperature. At 430°F, complete penetration occurs in both cement. In both classes of cement, variation in pressure increases the depth of penetration of carbonic acid. In Class G specimens, however, increase in temperature creates uneven pattern of penetration fronts. As discussed in Chapter 3 of this study, this is attributed to inconsistency in the effects of temperature on the transformation of CSH microstructure and the reactivity of CH and CSH with carbonic acid.



(a)



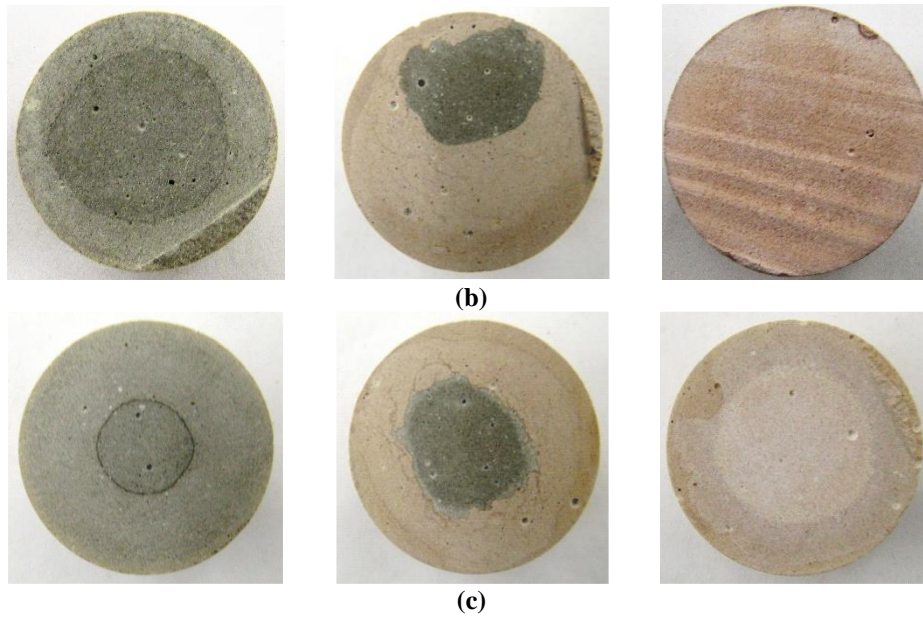


**Figure 4.21 Visual degradation of Class G cement due to variation in temperature at 100% CO<sub>2</sub> gas composition and: (a) 3000 psi; (b) 6000 psi; (c) 9000 psi (Omosebi et al., 2015)**

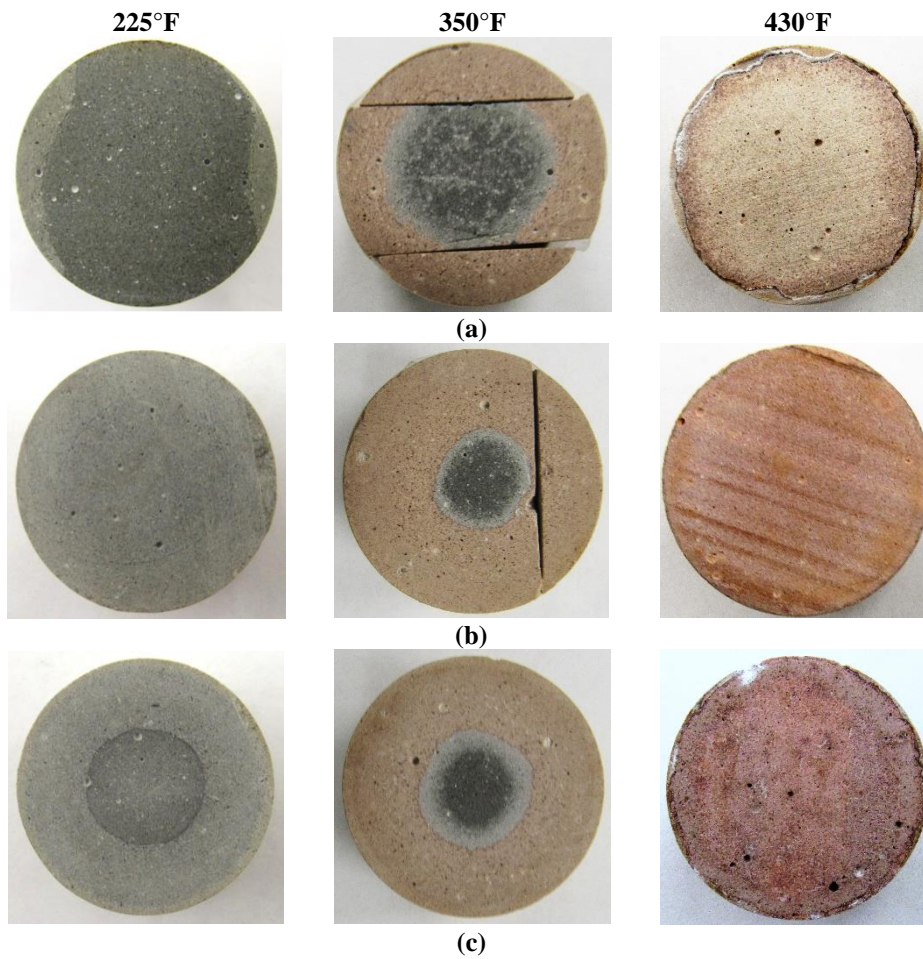


**Figure 4.22 Visual degradation of Class H cement due to variation in temperature at 100% CO<sub>2</sub> gas composition and: (a) 3000 psi; (b) 6000 psi; (c) 9000 psi**

### 4.3.3.2 Effect of Temperature at 6000 psi

This section presents the results of temperature variation from 100°F to 430°F at 10%, 40%, and 100% CO<sub>2</sub> gas compositions. Total test pressure is kept constant at 6000 psi.

#### 4.3.3.2.1 FTIR Mineralogy

**Figures 4.23** shows the FTIR data of the degraded zones of Class H specimens aged at 6000 psi. At 10% CO<sub>2</sub> gas composition (Figure 4.23a), complete consumption of portlandite at 225°F across all zones indicates that the degradation of specimens is maximum at this temperature. In addition to carbonated CH, carbonation of C-S-H in the outer zone results in the precipitation of carbonates which compensate for loss in structural integrity. Retention of C-S-H, especially in the inner and middle zones, also preserves mechanical strength. At 40% CO<sub>2</sub> gas composition (Figure 4.23b), portlandite is completely consumed across all zones at 225°F but it is preserved at very low temperature (i.e., 100°F) and elevated temperatures (i.e., 350°F and 430°F). Also, the outer zone of the samples is the most carbonated with increasing temperature and carbonation of C-S-H results in the increased absorbance peak of precipitated carbonates. In the inner and middle zones, C-S-H is preserved which significantly contributes to strength retention after aging. However, C-S-H is consumed in the middle zone at 225°F due to the deeper penetration of carbonic acid. The carbonation of C-S-H at this temperature leads to the increased absorbance peak of carbonates. In addition, this FTIR data suggests that the retention of cement hydrates at elevated temperature (i.e., 430°F) is due to the reduction in solubility of the hydrates which result in strengthening of the matrix. At 100% CO<sub>2</sub> gas composition (Figure 4.23c) and temperatures of 225°F and

350°F, CH is completely consumed in the inner and middle zones while C-S-H is consumed in the middle zone but retained in the inner zone. The consumption of C-S-H in the middle zone leads to the increase in absorbance peak of carbonates at these temperatures. Therefore, maximum degradation occurs at 225°F and 350°F.

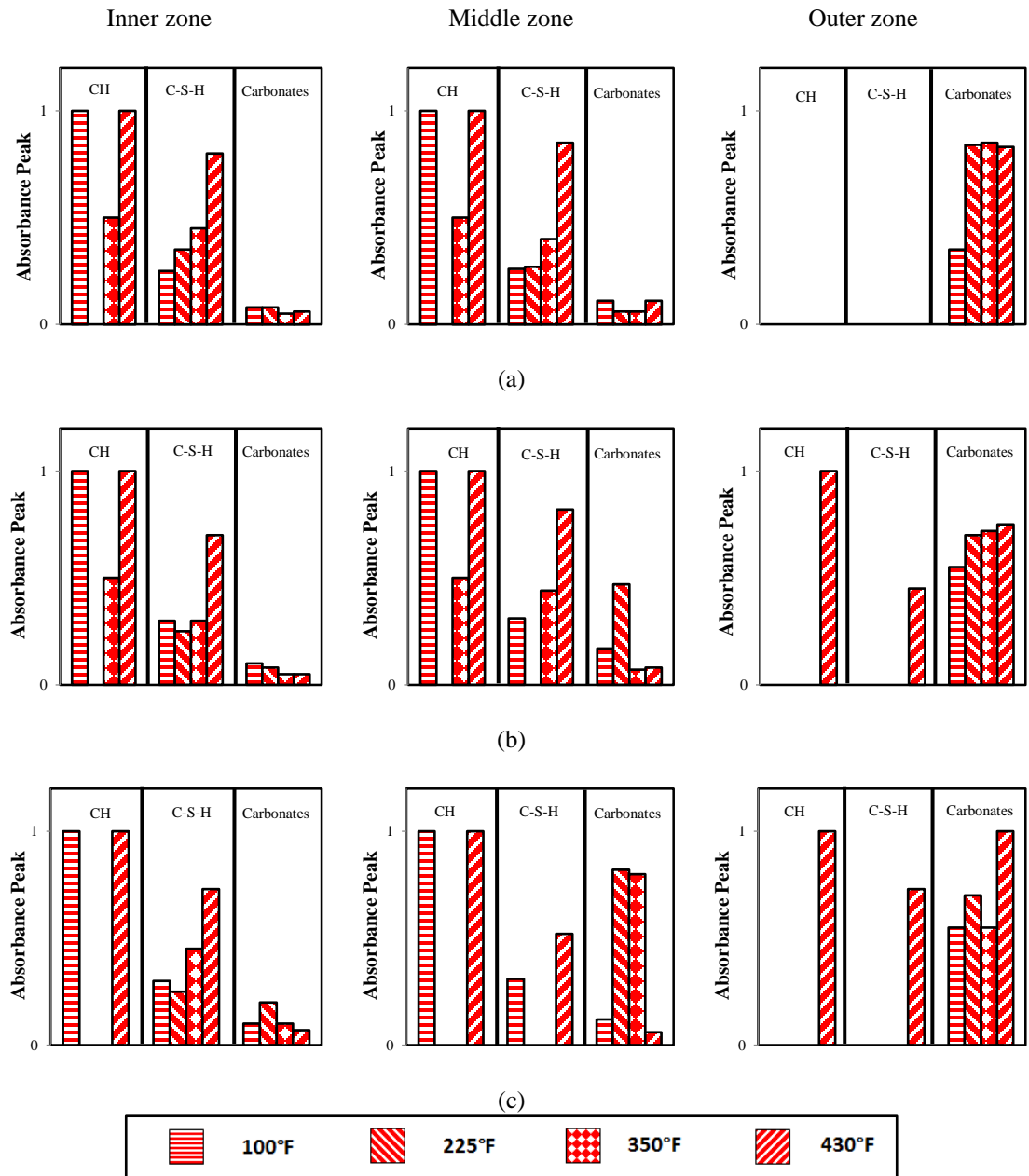


Figure 4.23 Effect of temperature at 6000 psi on the normalized absorbance peaks extracted from FTIR spectra of degraded zones of Class H cement: (a) 10% CO<sub>2</sub>; (b) 40% CO<sub>2</sub>; and (c) 100% CO<sub>2</sub> (Omosebi et al., 2015)

#### 4.3.3.2.2 Mechanical Degradation

The effects of temperature at 6000 and different CO<sub>2</sub> gas compositions on the compressive strength, porosity, and permeability of Classes G and H cement are shown in **Figure 4.24** show the evolution of compressive strength, porosity and permeability after immersion of the samples in 2% NaCl brine solution and exposure to different aging temperatures for 14 days.

At 10% and 40% CO<sub>2</sub> gas compositions, initial strength gain in Class G cement peaks at 100°F due to the overriding effect of carbonation since transport properties decrease correspondingly. The produced carbonates fill the pores of the cement, reducing porosity and permeability. At 350°F, decline in mechanical strength is observed which signifies that leaching is more prevalent since transport properties also increases slightly. However, increase in compressive strength and transport properties at 430°F underscores the combined effects of reduction in portlandite solubility, carbonation, leaching, and structural transformation of C-S-H to xonotlite (possibly). Using phase transformation chart (Figure 3.3 in Chapter 3), it is likely that amorphous CSH transforms to 11Å tobermorite or clinotobermorite at 225°F and xonotlite (C<sub>6</sub>S<sub>6</sub>H) at 350°F and 430°F. Tobermorite is the strongest and least permeable crystalline phase of CSH (Nelson, 1990; Smith, 1991) while xonotlite is relatively weaker and more permeable, but its mechanical and transport properties are still acceptable for casing support and protection against corrosive fluids. Xonotlite has been detected previously from discontinuous DRX and NMR analyses of Class G cement that had been stabilized with 40-35% silica sand and exposed to elevated curing temperature (Noik and Rivereau, 1999).

In Class H cement, initial strength development persists up to 225°F and is more significant than strength developed by Class G cement. Porosity and permeability decreases correspondingly. As temperature increases above 225°F, CO<sub>2</sub> solubility also increases which shifts the equilibrium positions of equations 2.15 (Chapter 2) and 3.4 (Chapter 3) to the right. This increases the formation of water-soluble calcium bicarbonate which is subsequently leached. Leaching of this mineral leads to the loss of compressive strength and parallel increase in transport properties, especially porosity. Uneven trend in permeability could be due to the development of micro-cracks during depressurization of the aging cell.

At 100% CO<sub>2</sub> gas composition, the trends in both API cements are consistent with trends at 10% and 40% CO<sub>2</sub> gas compositions. However, excess supply of CO<sub>2</sub> gas aids further carbonation of the specimens. This leads to strength development up to 225°F (in Class G cement) and up to 350°F (in Class H cement) with porosity and permeability decreasing correspondingly. Above these temperatures, leaching is the prevailing mechanism of degradation because strength decreases in both API cements while transport parameters increase simultaneously.

Effect of CO<sub>2</sub> gas composition on overall mechanical behavior shows slightly mixed trend in both classes of cement. In Class G cement, increase in CO<sub>2</sub> gas composition generally improves mechanical strength. However, overall mechanical strength in Class H cement initially decreases when CO<sub>2</sub> gas composition increases from 10% to 40%. Nevertheless, gain in strength is restored at 100% CO<sub>2</sub>. Extensive study of the effects of variation in CO<sub>2</sub> gas composition is discussed in Section 4.3.3.

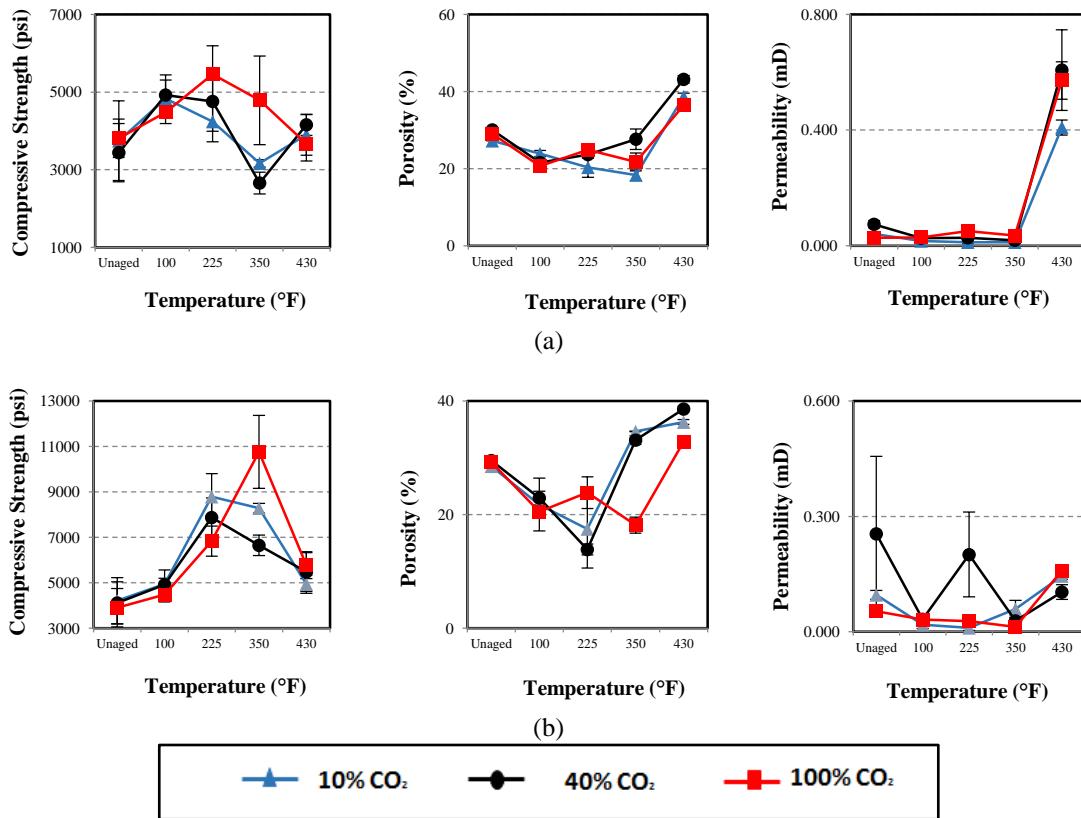


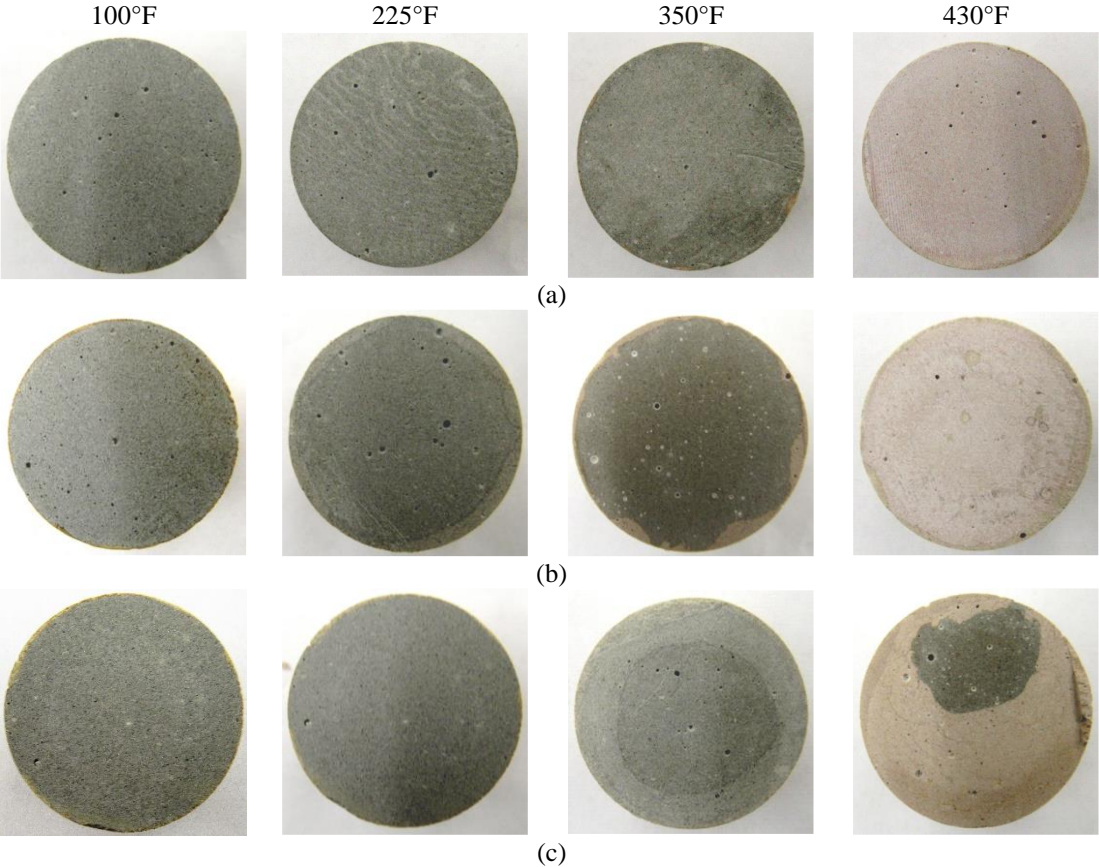
Figure 4.24 Effects of temperature at 6000 and different CO<sub>2</sub> gas compositions on the compressive strength, porosity, and permeability of: (a) Class G; (b) Class H (Omosebi et al., 2015)

#### 4.3.3.2.3 Visual Degradation

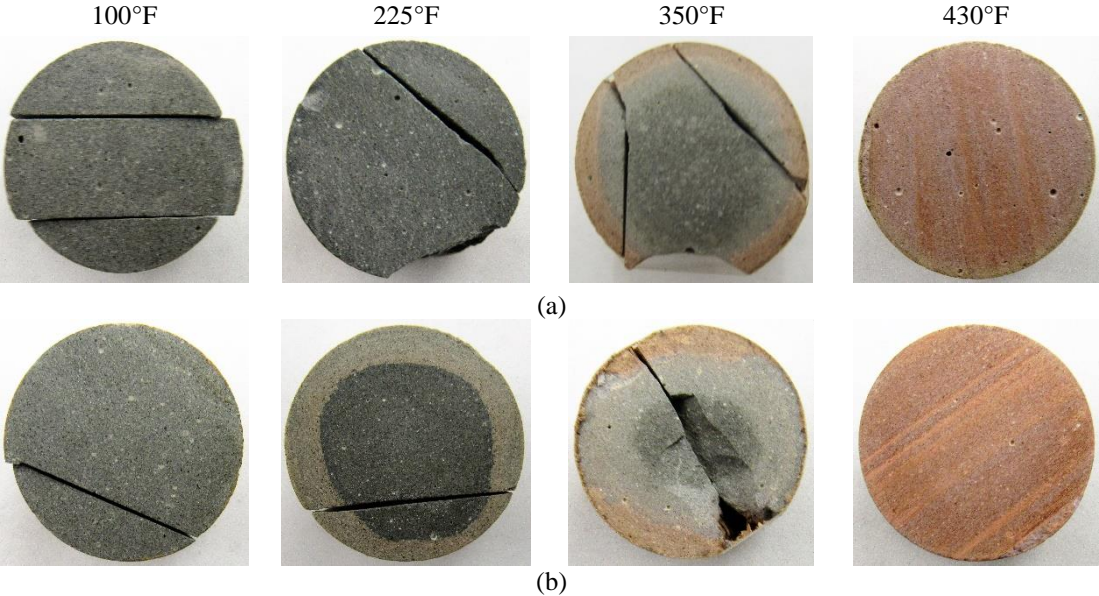
Figures 4.25 and 4.26 show visual degradation of the degraded cores of Classes G and H specimens. Temperature is varied from left to right while CO<sub>2</sub> gas composition is varied from top to bottom. Visual examination indicates that temperature facilitates the rate of acid attack since the degree of visual degradation increases with temperature. In Class G specimens, variation in CO<sub>2</sub> gas composition leads to progressive discoloration of the exposed specimens while increase in temperature, as previously noted, determines the progress of reaction fronts through the cement cores. Specifically, reaction fronts through Class G cement is irregular while the fronts are more regularly-patterned in Class H cement. However, the penetration fronts are deeper in Class H than



Class G cement, indicating that the degree of carbonation is higher in Class H. This further explains why Class H cement shows improved performance than Class G cement.



**Figure 4.25 Visual degradation of Class G cement due to variation in temperature at 6000 psi and CO<sub>2</sub> gas composition of: (a) 10%; (b) 40%; (c) 100% (Omosebi et al., 2015)**



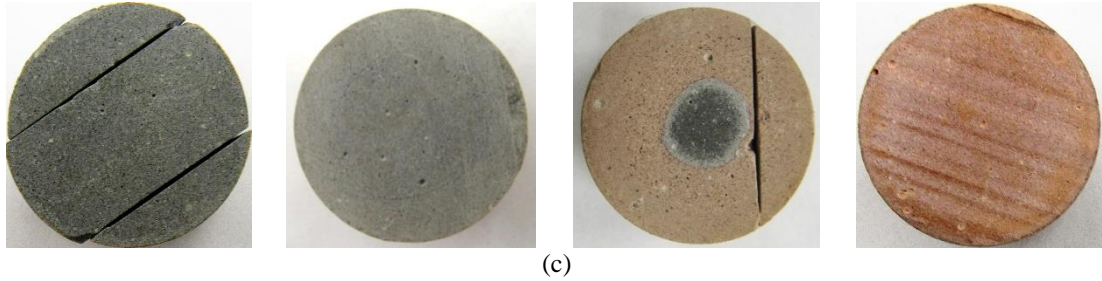


Figure 4.26 Visual degradation of Class H cement due to variation in temperature at 6000 psi and CO<sub>2</sub> gas composition of: (a) 10%; (b) 40%; (c) 100%

### 4.3.3.3 Summary

In addition to the microstructural, morphological, and mineralogical evidence, the compressive strength, porosity, and permeability measurements show that maximum degree of carbonation occurs between 225°F and 430°F. At 430°F, Class G cement appears to be less susceptible to mechanical degradation, possibly due to the reduction in the dissolution rate of cement hydrates. Visual inspection of the degraded cores confirms that the degree of cement degradation increases with temperature. Class H cement demonstrated better improvement in performance than Class G cement, even though it shows evidence of leaching at 430°F.

### 4.3.4 Effect of CO<sub>2</sub> Gas Composition on Cement Integrity

#### 4.3.4.1 Effect of CO<sub>2</sub> Gas Composition at 100°F

##### 4.3.4.1.1 FTIR Mineralogy

Figure 4.27 presents the effect of CO<sub>2</sub> gas composition on FTIR mineralogy of the three degraded zones at 100°F and 6000 psi. This data shows that CH and CSH were completely consumed in the outer zone through reaction with carbonated brine. The by-products of this reaction are carbonates (i.e. CaCO<sub>3</sub> and/or C-S-Cs). The exact type of carbonate would normally depend on the extent of carbonation (complete or incomplete).

Carbonation is deemed complete in this case because the outer zone is exposed



to fresh acid for the most duration than the middle and inner zones and C-S-Cs are typically formed at temperatures above 100°F. In addition, leaching may have also occurred, although at a small scale. Slight reduction of the FTIR absorbance peak in the outer zone at 10% CO<sub>2</sub> composition could be due to leaching. Therefore, the outer zone is the most carbonated as CO<sub>2</sub> concentration increases. In the inner and middle zones, CH and CSH were preserved due to slow propagation of reaction fronts at low temperature. In addition, the carbonates produced in the outer zone form a protective layer which limits further ingress of dissolved CO<sub>2</sub>, thereby preserving CH and CSH in these zones. This also explains why the absorbance peaks of carbonates in these zones are lower than the absorbance peaks of carbonates in the outer zone.

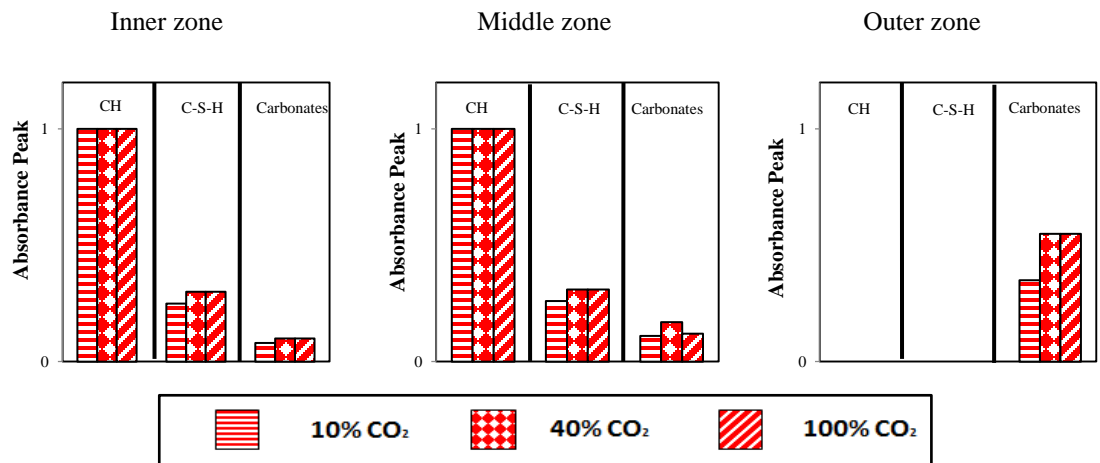
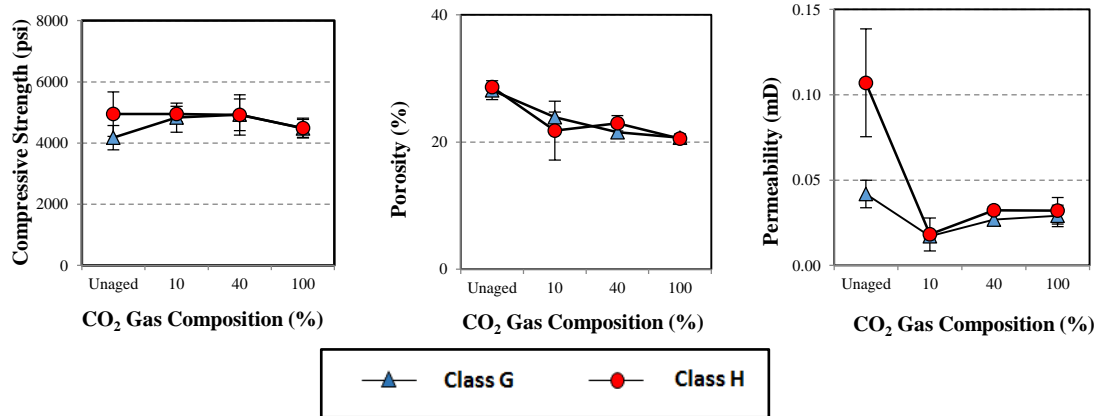


Figure 4.27 Effect of CO<sub>2</sub> gas composition at 100°F on the normalized absorbance peaks extracted from FTIR spectra of degraded zones of Class H cement (Omosebi et al., 2015b)

#### 4.3.4.1.2 Mechanical Degradation

Figure 4.28 shows the compressive strength, porosity and permeability of degraded classes G and H cement after immersion in 2% NaCl solution and exposure to varied CO<sub>2</sub> gas composition for 14 days at 100°F and 6000 psi. In both classes of cement, strength is preserved as CO<sub>2</sub> concentration increases. Similarly, porosity decreases slightly while permeability decreases initially after aging at 10% CO<sub>2</sub> concentration, but

increases marginally as CO<sub>2</sub> concentration increases. These observations can be attributed to the dissolution of portlandite, slow decalcification of C-S-H and chemical reactions leading to chemical degradation.



**Figure 4.28** Effect of CO<sub>2</sub> gas composition at 100°F and 6000 psi on the compressive strength, porosity, and permeability of Classes G and H cement (Omosebi et al., 2015)

The amount of CH and CSH produced in each class of cement and the corresponding porosity ( $\phi$ ) and permeability ( $k$ ) are directly related to the degree of hydration. As discussed previously in Section 4.3.1.3.1, the Class G cement material used in this study is expected to achieve a slightly higher degree of hydration than Class H cement. So, typically Class G cement will produce a little higher amount of cement hydrates and higher  $\phi$  than Class H cement. Hence, from theoretical point of view Class G cement will undergo slightly higher degree of carbonation than Class H cement because it constitutes higher amount of reactants and would allow more diffusion of carbon-bearing aqueous species (slightly higher transport properties). Coincidentally, lower water-to-cement slurries (e.g. Class H cement) were reported as CO<sub>2</sub>-resistant (Bruckdorfer 1986). Visual inspection of specimens exposed at 100°F (presented in Section 4.3.3.1.4) supports this explanation. However, a reversal of this trend is possible at higher temperatures.

Solubility of portlandite (CH) increases as temperature decreases (Nakarai et al., 2006). This is especially true in the unexposed specimen and in the unpenetrated zone of the exposed specimen. In these unreacted zones, the dissolution of portlandite is purely driven by concentration gradient. As this gradient evolves, portlandite aims at establishing equilibrium with the pore fluid species thereby triggering its dissolution. Technically, this high rate of dissolution releases  $\text{Ca}^{2+}$  ions into the pore fluid (i.e. calcium leaching) and this would have far-reaching consequences on mechanical behavior. As discussed in Chapter 3, incongruent decalcification of C-S-H would have similar effect on mechanical strength. Fluid pH and calcium ion concentration (presented in Section 4.3.2) shows an increased rate of dissolution. In the penetrated zone, however, this mode of degradation is compensated by carbonation of cement hydrates which is known to reduce porosity and reinforce cement matrix due to formation of calcium carbonates in the pores. Continuous exposure to carbonic acid results in the leaching of these carbonates. Since the slurry was cured at 200°F, it is likely that pozzolanic reaction occurs between silica flour and cement hydrates, especially portlandite which would have reduced the amount of portlandite being carbonated. The by-product of the pozzolanic reaction would increase the amount of calcium silicates.

While the dissolution of CH and slow decalcification of C-S-H take place in the unpenetrated zone, the penetrated zone is subjected to carbonation and leaching reactions. These reactions occur in the front-end and back-end of the reaction fronts respectively. Hence, these mechanisms of cement degradation are expected to occur simultaneously. However, the dominant process dictates overall effect on cement integrity. The trends in both Classes of cements suggest an even effect since aggregate

strength is approximately constant. However, the slight reduction in porosity underscores the impact of carbonation. Although leaching might have taken place, as discussed under FTIR spectra analysis in the outer zone of the exposed specimen, but the decrease in porosity indicates that carbonation maintains a slight edge over leaching as CO<sub>2</sub> concentration increases. The slight increase in permeability could be due to the development of micro-cracks, which were observed during visual inspection of the degraded specimens. It is possible that these cracks were developed when the specimens were dried at 110°F (Maheshwari, 2014). Furthermore, the progress of reaction fronts is expected to be slow at low temperature, thereby minimizing the loss of mechanical strength. As discussed in Section 4.3.2, the fluid pH and calcium content indicates less reactivity between cement and carbonated-brine. Besides, strength retrogression, due to structural transformation of calcium silicate hydrate (CSH), is not expected at 100°F since sufficient amount (i.e. 35% BWOC) of silica flour was added to the baseline cement. This mechanical deterioration normally occurs at elevated temperature (above 200°F, approximately). At best, the added silica would undergoes pozzolanic reactions with the cement hydrates.

#### **4.3.4.1.3 Visual Degradation**

Photographs of the degraded samples are shown in **Figure 4.29**. In both Classes of cement, CO<sub>2</sub> concentration is varied from left to right. Class H specimens shown in this figure were cut deliberately to gain access to the degraded zones that were used to collect FTIR data. Class G cement shows more discoloration than Class H cement through progressive degradation as CO<sub>2</sub> concentration increases. As discussed previously, this is due to carbonation of cement hydrates (CH and CSH). Discoloration

in Class H cement is not visually noticeable, which explains the trends in mechanical strength. However, the absence of observable discoloration does not indicate absence of chemical degradation. Obviously, the FTIR data (Figure 4.27) confirms that these Class H specimens were chemically degraded.

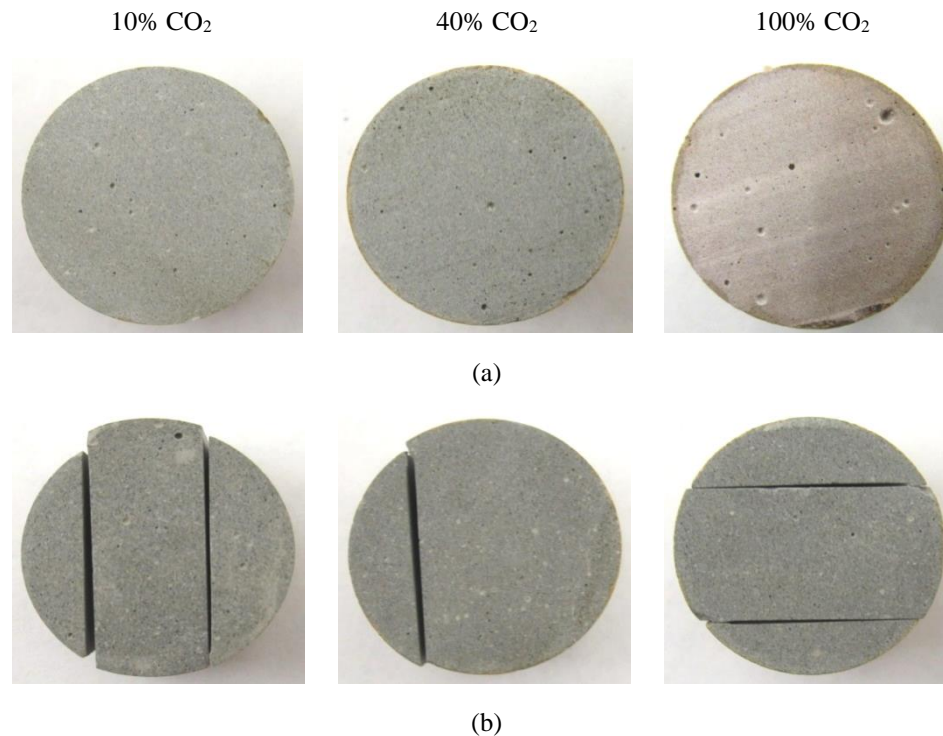


**Figure 4.29** Visual degradation due to variation in CO<sub>2</sub> gas composition at 100°F and 6000 psi: (a) Class G; (b) Class H (Omosebi et al., 2015)

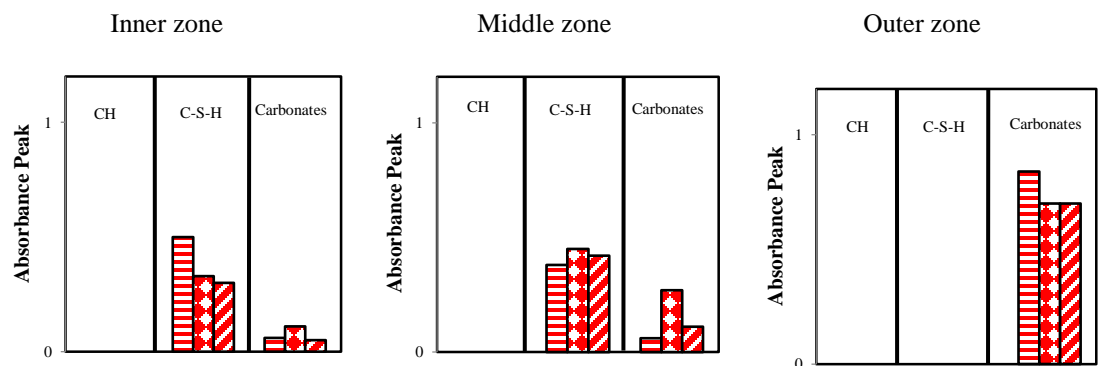
#### **4.3.4.2 Effect of CO<sub>2</sub> Gas Composition at 225°F**

In this section, CO<sub>2</sub> concentration was varied at 225°F and total system pressures of 3000 psi, 6000 psi and 9000 psi. The effects of this variation on bulk fluid chemistry, FTIR mineralogy, compressive strength, porosity, permeability and visual degradation are discussed.

##### **4.3.4.2.1 FTIR Mineralogy**

Effect of CO<sub>2</sub> gas composition on FTIR mineralogy is presented in **Figure 4.30**. At 225°F and 3000 psi (Figure 4.30a), increase in CO<sub>2</sub> concentration leads to the

consumption of CH across all degraded zones while C-S-H was preserved, except in the outer zone. This is due to increased reactivity of CH as CO<sub>2</sub> concentration was increased. Complete consumption of CH leads to the formation of CaCO<sub>3</sub> in all zones. In addition to the carbonation of CH, carbonation of C-S-H (complete or incomplete) also occurred in the outer zone, which leads to higher absorbance peak for the carbonates. At 225°F and 6000 psi (Figure 4.30b), FTIR data indicates complete consumption of CH in all zones at all CO<sub>2</sub> concentrations while C-S-H was retained mostly in the inner core. This observation is comparable to previous result at a lower pressure (3000 psi). However, consumption of CH and C-S-H to form higher amount of carbonates in the middle zone suggests deeper penetration of reaction fronts when compared to mineralogy at 3000 psi. This confirms that higher pressure increases cement carbonation due to high CO<sub>2</sub> solubility which permits fresh acid to penetrate deeper into cement matrix. At 225°F and 9000 psi (Figure 4.30c), CH was consumed across all zones while C-S-H was retained in the inner and middle zones, except at high CO<sub>2</sub> concentration. Like the previous result, CO<sub>2</sub> penetrates deeper at high pressure.



(a)

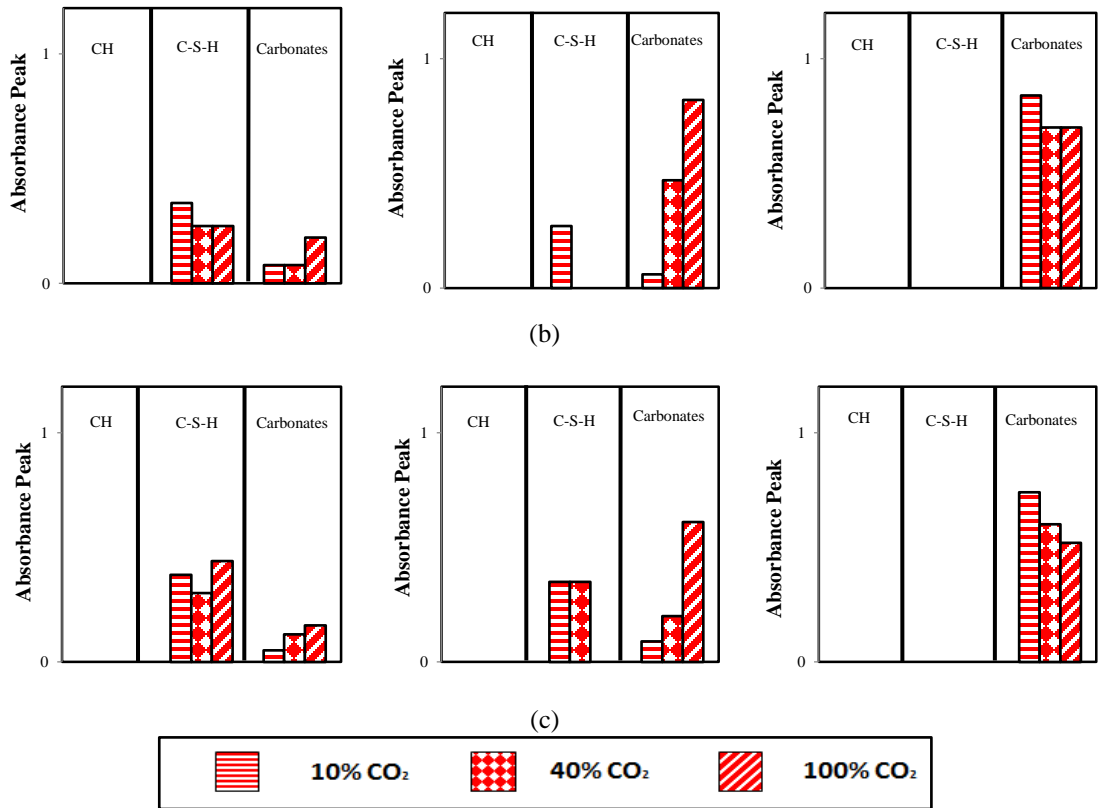


**Figure 4.30** Effect of CO<sub>2</sub> gas composition at 225°F on the normalized absorbance peaks extracted from FTIR spectra of degraded zones of Class H cement: (a) 3000 psi; (b) 6000 psi; and (c) 9000 psi

#### 4.3.4.2.2 Mechanical Degradation

The effect of CO<sub>2</sub> gas composition on mechanical integrity of Classes G and H cement is investigated at 225°F and the results are presented in **Figure 4.31**.

As the concentration of CO<sub>2</sub> increases at 225°F and 3000 psi, compressive strength of both well cement increases while porosity and permeability generally decreases relative to the unaged specimen. This is due to acid attack of cement hydrates to produce carbonates. As discussed in Chapter 3, structural transformation, carbonation and leaching are the principal mechanisms that lead to the degradation of well cement in HPHT carbonic acid environment. Of these mechanisms, carbonation of cement hydrates and subsequent leaching (i.e. dissolution) are major controlling processes. After carbonation, calcium carbonate precipitate and fill cement pores thereby reducing

porosity and permeability but improving mechanical strength. However, in presence of excess carbonic acid, calcium carbonate converts to water-soluble calcium bicarbonate according to equation 2.18. Then, calcium bicarbonate further reacts with portlandite (equation 2.19) thereby opening up pathways for fluid movement (i.e. increase in porosity and permeability) and facilitating leaching process. Mechanical strength is lost through the bicarbonation-induced leaching process. Although supplementary  $\text{CaCO}_3$  precipitates through a “self-healing cycle” but the consumption of additional portlandite further weakens the matrix. Carbonation and leaching occurs simultaneously. However, the dominant process will dictate overall structural integrity of the cement. Results clearly show that carbonation is the dominant process during the first 14 days of acid attack, especially at  $\text{CO}_2$  composition up to 40%. Above this  $\text{CO}_2$  gas composition, strength data shows leaching of calcium-bearing minerals reduce the effect of carbonation. This leaching effect is expected to be more distinct with prolonged exposure.

At 6000 psi, compressive strength of Class G cement exhibits similar behavior as the trend at 3000 psi, with slight increase at 100%  $\text{CO}_2$  composition. However, porosity and permeability of this cement increased consistently with  $\text{CO}_2$  concentration after exposure. This could be due to combined impacts of several processes. Since porosity and permeability increased as strength increased, it is not likely that carbonation solely controls the degradation process. One possible reason for strength retention is the transformation of CSH to  $11\text{\AA}$  tobermorite or clinotobermorite, which is a strong cement material. The increase in porosity and permeability could be due to increase in  $\text{CO}_2$  solubility, which arises from high pressure. This increases the concentration of carbonic acid thereby enhancing the leaching of  $\text{CaCO}_3$ . Compared to the unaged specimen,



strength peaks at 10% CO<sub>2</sub> concentration in Class H cement primarily due to carbonation since porosity and permeability decreased correspondingly. As CO<sub>2</sub> concentration was increased further, the onset of leaching followed because strength decreased while porosity increased, even though the residual strength was still sufficient for casing support. Compared to its behavior at 3000 psi, Class H cement is subjected to leaching as composition of CO<sub>2</sub> gas exceed 10%, unlike Class G cement which shows further carbonation. So, high pressure (6000 psi) has more effect on leaching of Class H cement than its carbonation at 225°F and high gas CO<sub>2</sub> composition. This is because of the increase in CO<sub>2</sub> solubility which arises from pressure increase. Permeability shows mixed trend due to uneven precipitation and dissolution of carbonates (i.e. self-healing). Another possible reason for the increase in porosity and permeability is the development of micro-cracks during depressurization of the aging cell.

At 9000 psi, compressive strength of both classes of cements increases consistently with CO<sub>2</sub> concentration due to dominant influence of carbonation over leaching. At this high pressure, CO<sub>2</sub> solubility is enhanced with CO<sub>2</sub> gas content, thereby increasing the degree of carbonation. Initially, porosity and permeability decreased after aging at 10% CO<sub>2</sub> concentration. Although the specimens are slightly more porous and permeable as CO<sub>2</sub> concentration increases, the general trend shows a cumulative effect of carbonation when compared to the unaged specimen. At this system pressure, cement properties shows improvement over the values at 3000 psi and 6000 psi.

Furthermore, structural transformation of uncarbonated CSH may have contributed to the trend observed. Although pressure effect on CSH transformation is not well-understood, temperature effect has been documented. The phase transformation

chart (Figure 3.3 in Chapter 3) indicates that amorphous CSH would be transformed to 11Å tobermorite at 225°F and CaO/SiO<sub>2</sub> (C/S) of 1. This crystalline phase of CSH has similar structure as clinotobermorite. Of the CSH phases, 11Å tobermorite is the strongest and least permeable. Therefore, its presence would reinforce cement matrix for additional structural integrity. XRD analysis, which was presented previously, confirms the formation of clinotobermorite.

Generally, Class H cement demonstrates improved integrity for casing support than Class G cement because it is stronger after exposure to varying concentrations of CO<sub>2</sub>.

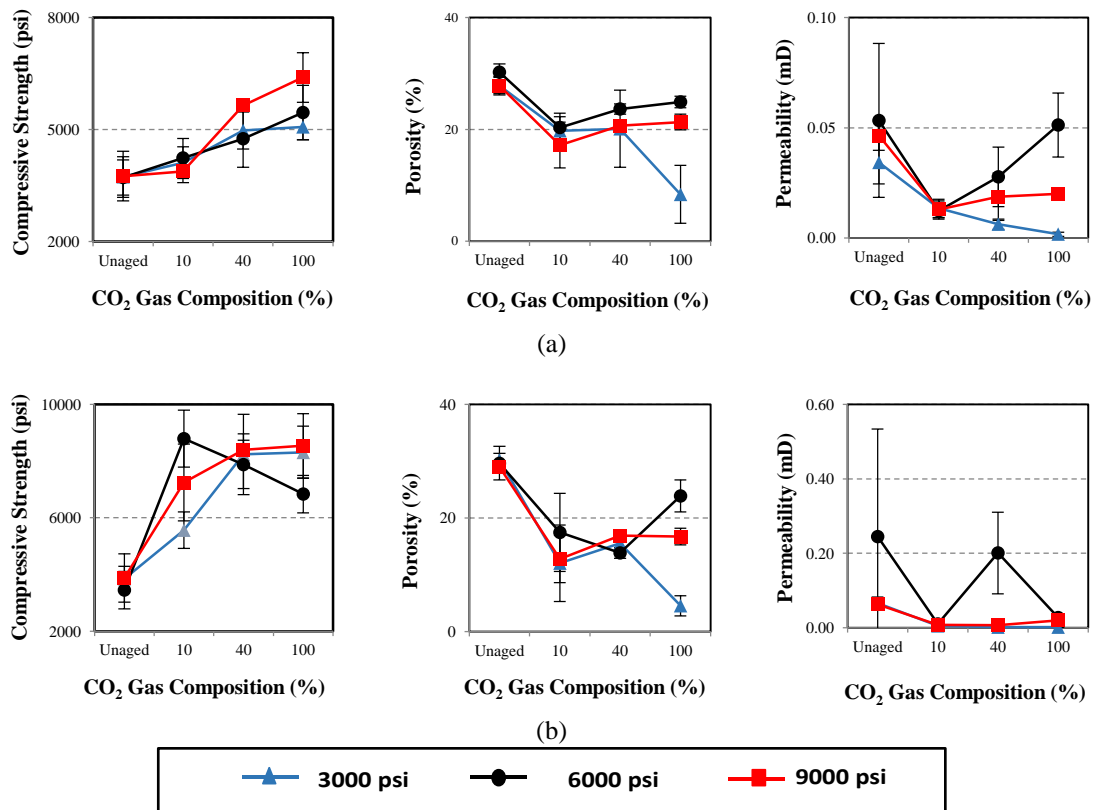
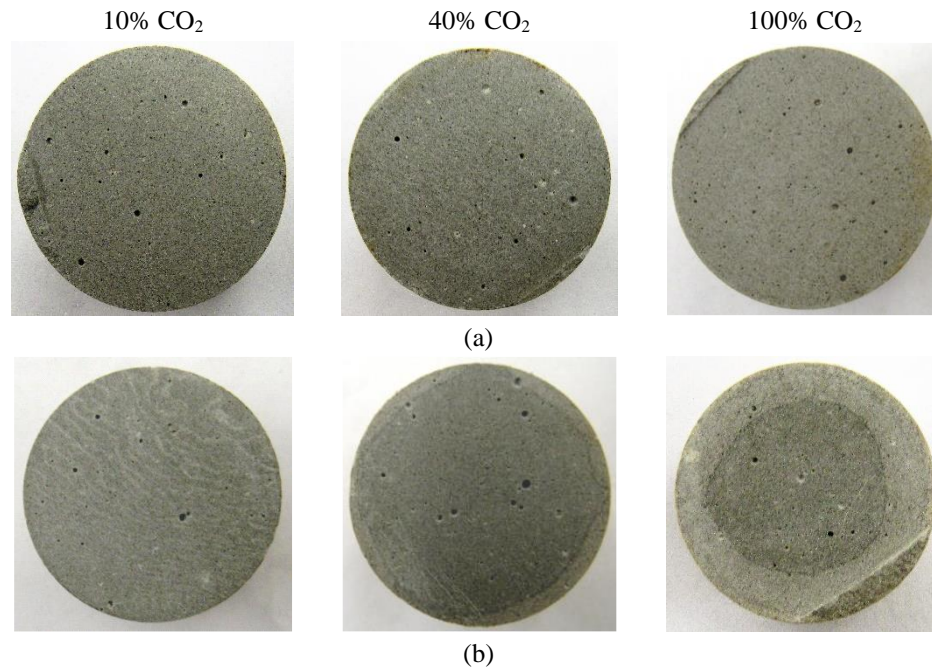


Figure 4.31 Effects of CO<sub>2</sub> gas composition at 225°F and different test pressures on the compressive strength, porosity, and permeability of: (a) Class G; (b) Class H

### 4.3.4.2.3 Visual Degradation

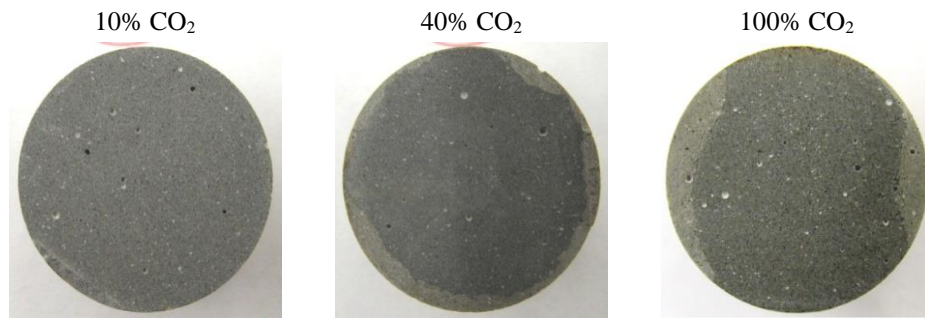
A complete set of photos of specimens that were exposed at 225°F are shown in **Figures 4.32 and 4.33**. In these figures, CO<sub>2</sub> concentration is varied from left to right and total test pressure from top to bottom. For Class H cement, the cut specimens were used for FTIR analysis (presented in Section 4.3.4.2.1). Visual discoloration indicates chemical degradation of cement. Depth of discoloration vary with CO<sub>2</sub> gas composition. As the composition of CO<sub>2</sub> gas increases, the specimens show progressive discoloration and increasing depth of penetration. As discussed previously, this is due to carbonation of cement hydrates (CH and CSH). The degree of carbonation is more conspicuous at high test pressure due to high solubility of CO<sub>2</sub> gas in the aging fluid. Compared to visual degradation due to temperature variation (Sections 4.3.3.1.3 and 4.3.3.2.3), the reaction fronts in Class G cement are well-defined.





(c)

**Figure 4.32 Visual degradation of Class G cement due to variation in CO<sub>2</sub> gas composition at 225°F and: (a) 3000 psi; (b) 6000 psi; (c) 9000 psi**



(a)



(b)



(c)

**Figure 4.33 Visual degradation of Class H cement due to variation in CO<sub>2</sub> gas composition at 225°F and: (a) 3000 psi; (b) 6000 psi; (c) 9000 psi**

### 4.3.4.3

### 4.3.4.4 Effect of CO<sub>2</sub> Gas Composition at 350°F

#### 4.3.4.4.1 FTIR Mineralogy

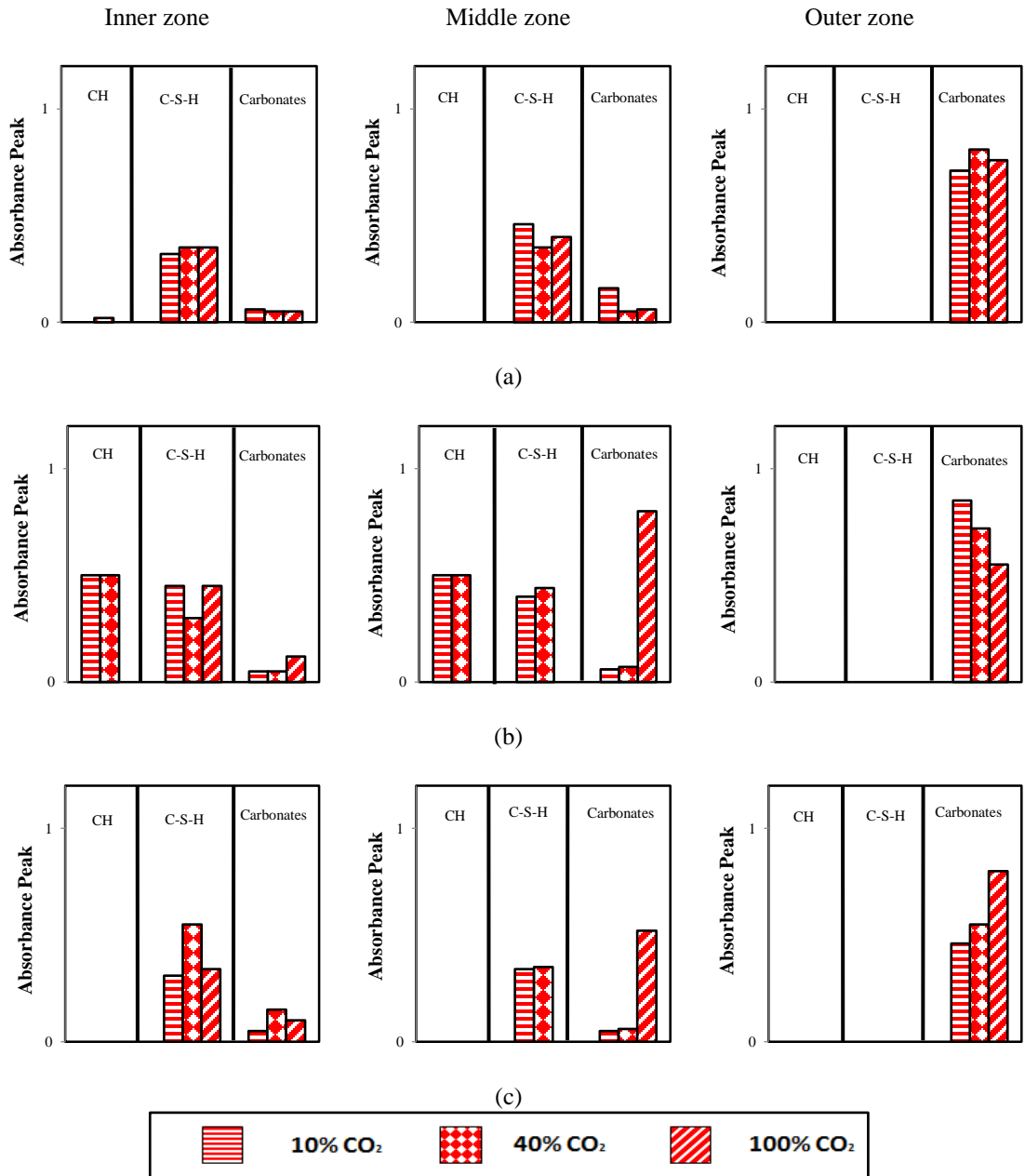


Figure 4.34 Effect of CO<sub>2</sub> gas composition at 350°F on the normalized absorbance peaks extracted from FTIR spectra of degraded zones of Class H cement: (a) 3000 psi; (b) 6000 psi; and (c) 9000 psi

At 350°F, the effect of CO<sub>2</sub> concentration on FTIR mineralogy is presented in

**Figure 4.34.** CO<sub>2</sub> concentration effect at 3000 psi (Figure 4.34a) confirms formation and

precipitation of carbonates, which resulted from the reaction of cement hydrates, especially portlandite. In addition to partial carbonation of C-S-H in the outer zone, retention of C-S-H preserved mechanical strength. Moreover, less diffusion of dissolved CO<sub>2</sub> into the matrix, due to the formation of protective layer of CaCO<sub>3</sub>, limits degree of reaction thereby protecting the matrix while the carbonated portion improves mechanical strength. At 6000 psi (Figure 4.34b), both portlandite and C-S-H were retained in the inner and middle zones, especially with 10% and 40% CO<sub>2</sub> concentrations. At 100% CO<sub>2</sub> concentration, calcium silicate hydrate was preserved in the inner region but calcium hydroxide was completely consumed across all zones because it is more reactive than C-S-H. In the outer zone, calcium-bearing hydrates were completely converted to carbonates (i.e. CaCO<sub>3</sub> and C-S-C) regardless of CO<sub>2</sub> concentration. In this zone, the progressive reduction in the peak of carbonates implies that the carbonates are leached as CO<sub>2</sub> gas composition increases. Therefore, carbonation of the outer zone is likely to be complete. At 9000 psi (Figure 4.34c), FTIR results suggest total consumption of CH across all zones but C-S-H was retained in the inner and middle regions.

#### **4.3.4.4.2 Mechanical Degradation**

**Figure 4.35** shows the effect of variation in CO<sub>2</sub> gas composition on compressive strength, porosity and permeability. Strength of Class H cement increased while porosity and permeability generally decreased as CO<sub>2</sub> gas composition was increased at 3000 psi. This can be attributed to chemical degradation dominated by carbonation reaction and transformation of crystalline cement hydrates at elevated temperature. Both XRD and FTIR data confirms the occurrence of carbonation. At 100% CO<sub>2</sub> gas composition, the increase in porosity could be due to leaching of specimen.

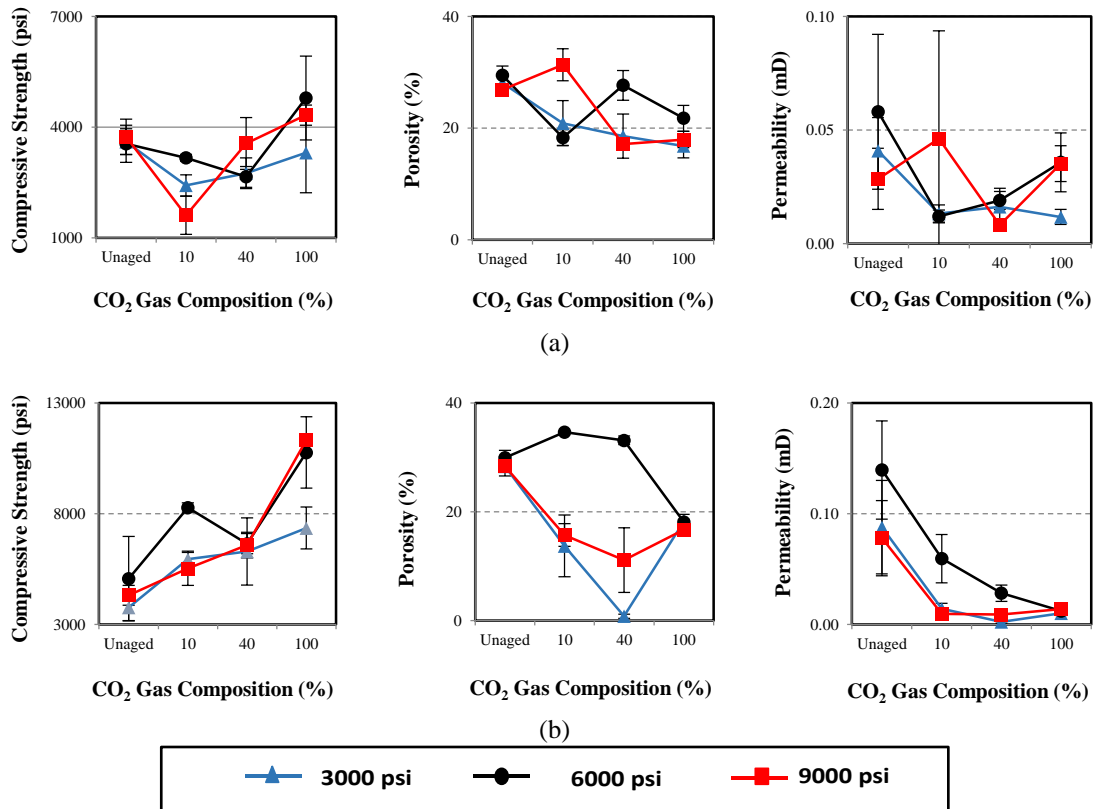


**Figure 4.35** Effects of CO<sub>2</sub> gas composition at 350°F and different test pressures on the compressive strength, porosity, and permeability of: (a) Class G; (b) Class H

Similarly, mechanical strength increased slightly in Class G cement as CO<sub>2</sub> gas composition is increased. Corresponding reduction in porosity and permeability implies that the effect of carbonation overrides leaching of carbonates. Furthermore, addition of 35% silica flour minimizes strength retrogression at elevated temperature (i.e. 350°F) but does not hinder structural transformation of amorphous CSH to its crystalline phases (i.e. C-S-H). Addition of silica to the neat cement reduces the C/S (or CaO/SiO<sub>2</sub>) ratio from 3 to 1, approximately (Table 3.2 in Chapter 3). According to the C-S-H phase diagram (Figure 3.3 in Chapter 3), calcium silicate hydrate produced during curing transforms to xonotlite or clinotobermorite (11Å tobermorite) at aging temperature of 350°F and C/S of 1, approximately. As presented in Section 4.3.1.3.3, XRD analysis of specimen that was aged at 350°F, 3000 psi and 40% CO<sub>2</sub> confirms the transformation of

amorphous CSH to crystalline clinotobermorite. This crystalline phase of CSH is believed to have adequate mechanical and transport properties required for good zonal isolation.

At 6000 psi, measurements show slightly different trend. At low CO<sub>2</sub> concentration (10%), aging improved the strength of Class H cement while strength of Class G cement was essentially constant. This suggests that mechanical performance was dominated by carbonation since availability of CO<sub>2</sub> is limited; hence preventing further leaching. This observation is verified by FTIR mineralogy, especially in the outer zone of the specimen. Correspondingly, permeability decreased in both cements while porosity increased in Class H suggesting the occurrence of diffusion-controlled leaching of portlandite in the pores while induced fractures were healed by reaction-controlled precipitation of carbonates. This phenomenon was observed in cement samples retrieved after 30 years of CO<sub>2</sub> exposure in the SACROC unit, West Texas (Carey et al., 2007). At higher CO<sub>2</sub> concentration, rate of precipitation of carbonates is faster than the rate at which water-soluble calcium bicarbonate is leached out. This leads to further strength development due to carbonation and reduction in the solubility of portlandite at high temperature (Nakarai et al., 2006), which preserves matrix strength. Additionally, severe strength retrogression at elevated temperature is not expected, since sufficient amount of silica flour was added to the neat cement. It is deduced from the C-S-H phase diagram that clinotobermorite is the most likely crystalline phase present in the aged specimens.

At 9000 psi, the overall mechanical behavior is similar to the trends observed at lower pressures. That is, the specimens of both cements are progressively carbonated as CO<sub>2</sub> gas composition increases. However, strength improvement in Class H cement is more significant than strength development in Class G cement. FTIR mineralogy shows



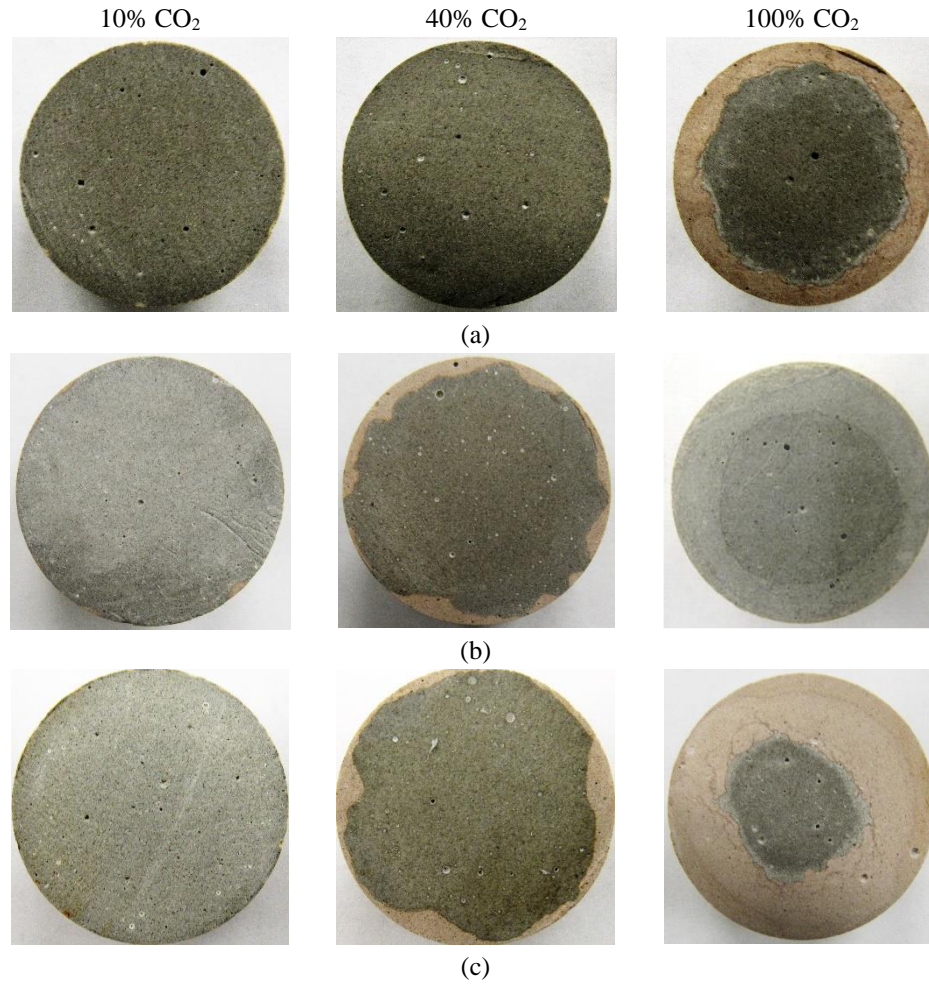
that Class H cement is increasingly carbonated as CO<sub>2</sub> gas composition increases. In this cement, further hydration and structural transformation at elevated temperature may have contributed to additional compressive strength development. The degree of carbonation in both API cements is lesser at low CO<sub>2</sub> partial pressure than at high partial pressure.

Therefore, evolution of mechanical and transport properties of well cement in the event of exposure to varying composition of CO<sub>2</sub> gas under high-temperature and high-pressure condition is direct consequence of interrelated chemical processes. The dominant chemical process will dictate the mechanical behavior of cement.

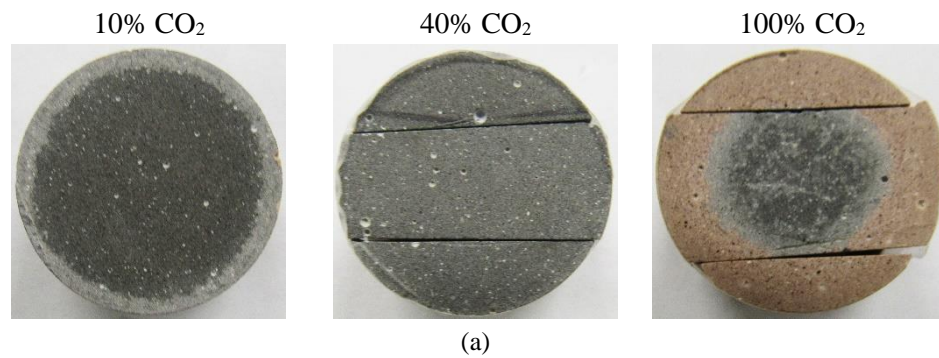
#### **4.3.4.4.3 Visual Degradation**

Pictures of degraded specimens are shown in **Figures 4.36 and 4.37**. The cracked pieces in Class H are not due to aging but the specimens were deliberately broken in order to conduct FTIR studies. In both Classes of cement, CO<sub>2</sub> concentration is varied from left to right while total test pressure is varied from top to bottom. At 40% CO<sub>2</sub> gas composition, Class G cement shows uneven visual degradation (discoloration) than Class H cement, although the later suggests deeper CO<sub>2</sub> penetration than the former. As noted previously, the deeper penetration of dissolved CO<sub>2</sub> through Class H cement subjects it to more carbonation; hence, it shows better improvement in strength than Class G cement. Evidently, increase in CO<sub>2</sub> concentration and total test pressure leads to further chemical attack. However, variation in CO<sub>2</sub> partial pressure has more impact than variation in total test pressure. This is expected because methane has low solubility in brine, which means that CO<sub>2</sub> solubility governs the degradation process. As discussed previously, this dissolution leads to carbonation of cement hydrates (CH and C-S-H). Therefore, it can be inferred from visual inspection that the degree of cement degradation increases with CO<sub>2</sub>

concentration.



**Figure 4.36 Visual degradation of Class G cement due to variation in CO<sub>2</sub> gas composition at 350°F and: (a) 3000 psi; (b) 6000 psi; (c) 9000 psi**



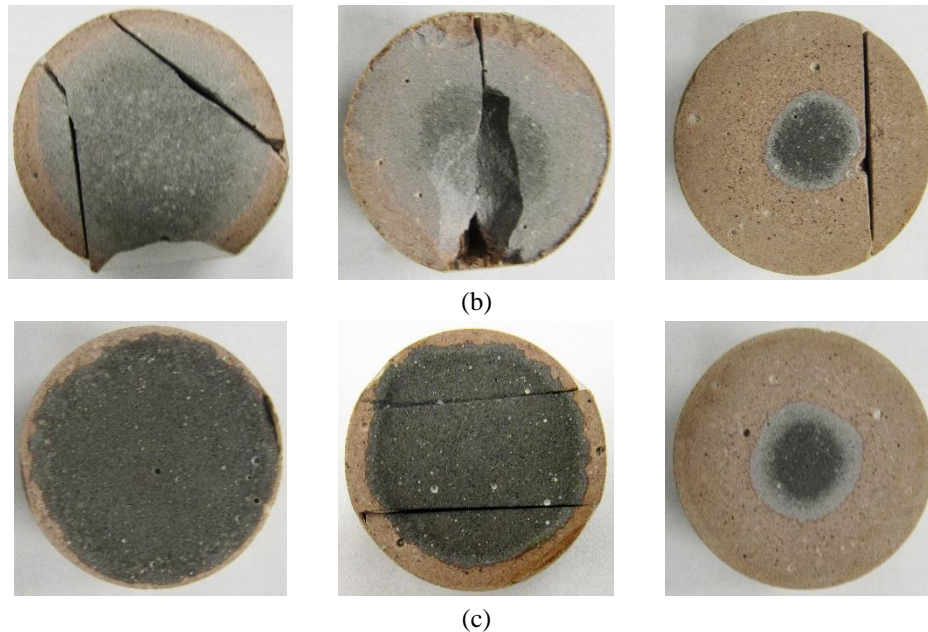


**Figure 4.37** Visual degradation of Class H cement due to variation in CO<sub>2</sub> gas composition at 350°F and: (a) 3000 psi; (b) 6000 psi; (c) 9000 psi

#### **4.3.4.5 Effect of CO<sub>2</sub> Gas Composition at 430°F**

##### **4.3.4.5.1 FTIR Mineralogy**

**Figure 4.38** shows the effect of variation in CO<sub>2</sub> gas composition at 430°F and 6000 psi on FTIR mineralogy. In the inner and middle zones, the peak of CH is constant, indicating that the reactivity of CH with CO<sub>2</sub>-rich brine is minimized. As noted previously, the solubility of cement hydrates (especially CH) reduces as temperature increases. Thus, the concentration of Ca<sup>2+</sup> ions released into pore solution by these hydrates is insufficient for rapid carbonation of the specimens. In the outer zone, CH and C-S-H are completely consumed at 10% CO<sub>2</sub> gas composition but only C-S-H reacts with carbonic acid at higher CO<sub>2</sub> gas composition. Compared to the inner and middle zones, the quantity of carbonates in the outer zone is higher. This implies that the outer zone is the most carbonated because the concentration of acid in this zone is higher than the inner and middle zones. Also, this zone is in contact with fresh acid for the longest duration. Overall, C-S-H shows more reactivity with carbonated brine than CH. This could be due to the effect of high temperature on structural transformation of amorphous calcium

silicate hydrate and its subsequent decalcification into pore solution. However, CH and C-S-H are generally preserved across all zones after 14 days of exposure. Thus, the formation of carbonates is expected to aid compressive strength development.

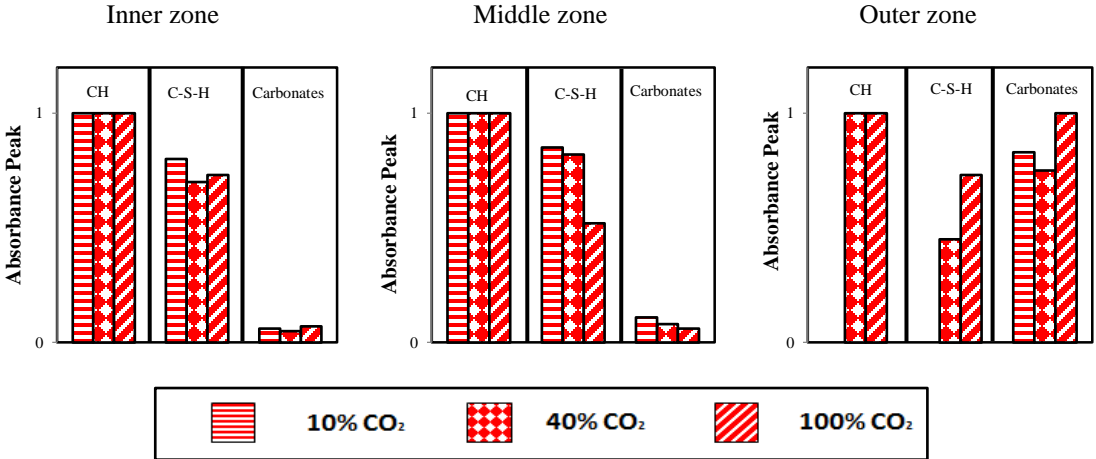


Figure 4.38 Effect of CO<sub>2</sub> gas composition at 430°F and 6000 psi on the normalized absorbance peaks extracted from FTIR spectra of degraded zones of Class H cement

**4.3.4.5.2 Mechanical Degradation**

Figure 4.39 presents the effect of CO<sub>2</sub> gas composition at 430°F and 6000 psi on mechanical degradation. In both Classes of cement, compressive strength increased with CO<sub>2</sub> gas composition while transport properties initially increased, but then decreases at high CO<sub>2</sub> gas composition. As noted from the FTIR mineralogy data, the carbonation of the specimens was limited due to the reduction in the solubility of hydrated clinker compounds; thus, preserving CH and C-S-H. However, the transformation of amorphous CSH to its crystalline phases is expected due to the elevated temperature condition. At 430°F and C/S ratio of 1, transformation of amorphous CSH to xonotlite is expected (Figure 3.3 in Chapter 3). Strength of this crystalline phase of CSH is acceptable but its transport properties are high. Xonotlite has been identified previously in Class G cement (with 40-35% silica sand) after the cement was cured at high temperature (Noik and Rivereau, 1999). Furthermore, the specimen may have expanded due to the high

temperature (430°F). This expansion can result in the development of micro-cracks that paves the pathway for fluid movement.

Therefore, the increase in compressive strength is likely due to the combined effects of carbonation, structural transformation of amorphous CSH, and the retention of cement hydrates while the initial increase in transport parameters could be due to the presence of micro-cracks and xonotlite. It is possible, however, that increased formation of carbonates at very high CO<sub>2</sub> concentration (100%) is able to heal the cracks; thus, decreasing transport properties while the development compressive strength is sustained. Comparison of the two classes of cement shows that Class H cement demonstrates improved performance over Class G cement because it is stronger, less porous and less permeable after exposure to CO<sub>2</sub>-containing fluid.

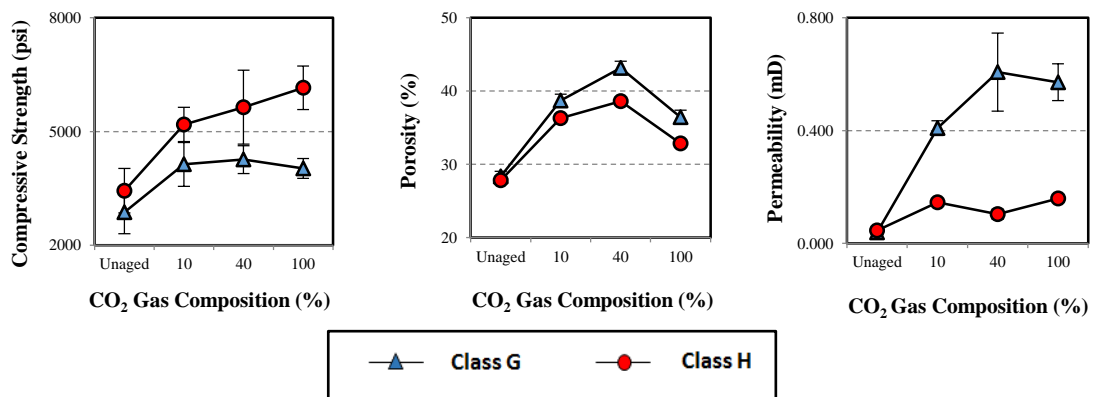


Figure 4.39 Effect of CO<sub>2</sub> gas composition at 430°F and 6000 psi on the compressive strength, porosity, and permeability of Classes G and H cement

#### 4.3.4.5.3 Visual Degradation

Effect of variation in CO<sub>2</sub> gas composition at 430°F and 6000 psi is shown in Figures 4.25 and 4.26 (presented previously in Section 4.3.3.2.3). Both classes of cement were completely degraded at all CO<sub>2</sub> concentrations, except Class G cement with uneven reaction front at 100% CO<sub>2</sub> gas composition. Compared to visual degradations at 100°F,

225°F, and 350°F, extremely high temperature (430°F) facilitates the rate of acid attack on well cement.

#### **4.3.4.6 Summary**

Generally, compressive strength of Class G and H cement increases while transport properties decrease with CO<sub>2</sub> gas composition. The controlling mechanism is the carbonation of cement hydrates. At high CO<sub>2</sub> gas composition, the effect of carbonation is counteracted by leaching due to the presence of additional dissolved CO<sub>2</sub>. However, overall mechanical strength shows that carbonation is still dominant. FTIR mineralogy and visual inspection are consistent with this observation. The retention of uncarbonated hydrates, especially in the unpenetrated portion of the specimens, also contribute to strength development. Comparison of the performance of the two classes of cement shows that Class H cement demonstrates improved performance over Class G cement.

### **4.3.5 Effect of Pressure on Cement Integrity**

#### **4.3.5.1 Effect of Pressure at 225°F**

##### **4.3.5.1.1 FTIR Mineralogy**

Effects of pressure at 225°F on FTIR mineralogy is investigated using Figure 4.30. CH is completely reacted across all zones and at all test pressures leading to the formation of carbonates. C-S-H is preserved in the inner zone but partially consumed in the middle and outer zones, especially at 6000 psi. Carbonates are also formed when C-S-H reacts with carbonic acid. In the middle zone, the amount of carbonates increases with test pressure, especially as the composition of CO<sub>2</sub> gas increases. In the outer zone,

however, slight reduction in the absorbance peak of carbonates could indicate the commencement of leaching.

#### **4.3.5.1.2 Mechanical Degradation**

Theoretically, pressure variation alters CO<sub>2</sub> phase behavior and its solubility in NaCl solution. As noted in Chapter 3 (Section 3.9.2), increase in total system pressure promotes leaching of calcium carbonate. **Figure 4.40** shows the effect of increasing pressure on mechanical and transport properties of Classes G and H cement.

In Class G cement, alteration in compressive strength is insignificant at 10% CO<sub>2</sub> gas composition. Transport parameters show similar behavior. This is likely due to the limited occurrence of chemical degradation reactions, which arises from the low amount of CO<sub>2</sub> gas injected into the HPHT autoclave. At 40% CO<sub>2</sub> gas composition, however, strength decreased slightly while porosity and permeability increases. This initial behavior signifies the effect of leaching-dominated reactions. At higher test pressure (9000 psi), increase in strength and corresponding reduction in transport properties indicates that carbonation is prevalent. Similar behavior is exhibited at 100% CO<sub>2</sub> gas composition. However, performance of this cement generally improves as the composition of CO<sub>2</sub> gas increases. This is due to less chemical interaction at low pressure (relatively small variations in strength at 3000 psi), but increased chemical interaction between cementitious materials and carbonic acid as pressure increases.

In Class H cement, the trend is somewhat similar to Class G cement, except that it is reversed at 6000 psi. FTIR mineralogy shows that specimens were carbonated as pressure increases especially at 6000 psi where C-S-H is consumed in addition to CH. At this pressure, strength decreased as CO<sub>2</sub> gas composition increases. Correspondingly,

transport properties generally increases; thus, indicating that the chemical degradation reactions were dominated by leaching. In addition, it is likely that the formation of micro-cracks during depressurization of the aging system contribute to the mixed trends in compressive strength and transport parameters.

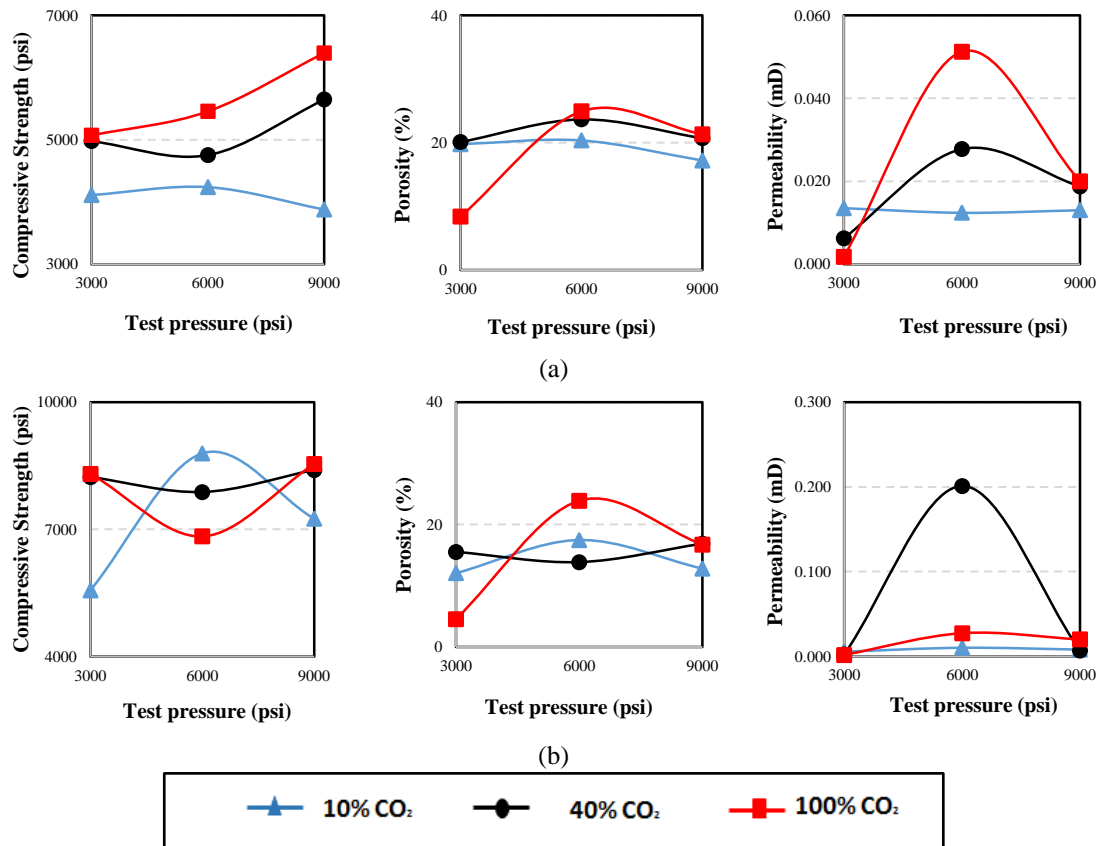


Figure 4.40 Effect of total test pressure at 225°F and different CO<sub>2</sub> gas composition on the compressive strength, porosity, and permeability of: (a) Class G; (b) Class H

#### 4.3.5.1.3 Visual Degradation

The effect of variation in test pressure at 225°F on visual degradation is presented in Figures 4.32 and 4.33. At 10% CO<sub>2</sub> gas composition, visual discoloration is not conspicuous in both classes of cement. At 40% and 100% CO<sub>2</sub> gas compositions, however, the depth of acid penetration increases with test pressure. This would lead to carbonation of the specimens. As discussed in the preceding section, the behavior of



mechanical and transport properties indicates that carbonation is the influencing mechanism of degradation.

### **4.3.5.2 Effect of Pressure at 350°F**

#### **4.3.5.2.1 FTIR Mineralogy**

Figure 4.34 is used to study the effect of pressure at 350°F on FTIR mineralogy. In the inner zone, CH is completely consumed, except at 6000 psi while C-S-H is mostly preserved at all pressures. The trend is similar in the middle zone but C-S-H is partially reacted, which indicates deeper penetration acid. However, CH and C-S-H are completely consumed in the outer zone to form carbonates. These carbonates, in addition to the preserved CH and C-S-H, contributes to mechanical integrity.

#### **4.3.5.2.2 Mechanical Degradation**

The effects of total test pressure at 10%, 40% and 100% CO<sub>2</sub> concentration are presented in **Figure 4.41**. At 10% CO<sub>2</sub> composition, increase in compressive strength is observed in Class G cement as pressure increased to 6000 psi. This results from complete carbonation of a portion of the portlandite, which precipitates calcite and its possible polymorphs (i.e. aragonite, vaterite and/or ikaite), thereby reducing porosity and permeability. However, strength decreases at extremely high pressure (9000 psi) while porosity and permeability increases. This is likely due to leaching of the fully-carbonated portion of the cement. Although carbonation and leaching may have occurred, the residual compressive strength is still sufficient for casing support. Furthermore, experimental data suggests that Class G cement is more susceptible to carbonation than leaching at low aging pressures (less than 6000 psi). However, the degree of calcium bicarbonation and subsequent leaching is higher at high pressures (greater than 6000 psi).

At moderately high CO<sub>2</sub> concentration (i.e. 40%), the trend differs from result at low CO<sub>2</sub> concentration. Strength development takes place as pressure increases due to increased rate of carbonation. This result suggests that Class G cement is carbonated faster than it is leached. Furthermore, effect of pressure on compressive strength was investigated at 100% CO<sub>2</sub> concentration. Result shows that Class G cement was subjected to further carbonation at high pressure, although the onset of leaching starts at extremely high pressure (i.e. 9000 psi). This implies that carbonation dominates leaching in Class G at low-pressure and extremely high CO<sub>2</sub> concentration.

At 10% CO<sub>2</sub> composition, increase in pressure (up to 6000 psi) leads to the development of mechanical strength in Class H cement due to the overriding effect of carbonation over leaching. Both CH and C-S-H are typically carbonated when cement is exposed to carbonated brine. Moreover, C-S-H is less reactive to carbonic acid than portlandite and complete carbonation requires longer time. With short duration (i.e. 14 days), incomplete carbonation of C-S-H to C-S-C may have occurred. Figure 4.34 of FTIR measurements (presented in Section 4.3.4.3.1) show that C-S-H is mostly preserved in the inner and middle zones of the degraded cement. This implies that the degree of carbonation of C-S-H is limited to the outer zone. Furthermore, FTIR shows that portlandite and C-S-H were preserved in the inner and middle zones at 6000 psi; hence, in addition to complete carbonation, the formation of C-S-C leads to strength development. However, leaching of completely carbonated cement hydrates offsets carbonation at higher pressures. This is more pronounced at low CO<sub>2</sub> concentration in which limited carbonation occurs. At high CO<sub>2</sub> concentration, increased carbonation plays a dominant role up to 9000 psi. In addition, since water requirement for Class H

cement is less than Class G, the degree of hydration of Class H is expected to be slightly lower than that of Class G. Therefore, further hydration and/or CSH phase transformation occurs at elevated temperature, which contributes to strength development. Trends in porosity and permeability are mixed and cannot be directly correlated to strength evolution possibly due to calcium leaching in unreacted portion of the cement, structural transformation and self-healing (i.e. uneven precipitation, dissolution and further precipitation of calcium carbonate). At 40% CO<sub>2</sub> composition, strength development in Class H cement is insignificant due to carbonation and leaching taking place at a comparable scale. Similarly, high CO<sub>2</sub> concentration (40%) favored additional strength development as total pressure increases because of increased rate of carbonation of cement hydrates over subsequent leaching of calcium bicarbonate. Moreover, the contribution of C-S-H phase transformation cannot be underestimated as the phase transformation diagram suggests the likelihood of xonotlite as C-S-H phase present. This CSH phase is strong but more permeable than tobermorite gel (Eilers et al., 1983; Nelson, et al., 1981).

Assessment of the overall trend in compressive strength shows relatively small variations at 3000 psi, though it increases slightly with CO<sub>2</sub> concentration. However, the deviation increases with total test pressure. This indicates more interaction between cement materials and solute species in the carbonated brine. Sudden reduction in mechanical strength at 9000 psi (for 10% CO<sub>2</sub>) could be due to the presence of micro cracks which may have developed either due to this high pressure or during depressurization of the HPHT autoclave. Interestingly, the porosity and permeability of Class G cement also increases. Pang et al. (2015) observed the development of cracks in

well cement after curing for 3 days and depressurizing at the rate of 50 psi/min. Their study shows that Class H cement is more resistant to depressurization damage than Class G cement. Class G cement specimens that were damaged by depressurization tends to have uneven fracture surfaces during splitting tension tests. This corroborates the uneven pattern of degradation fronts observed from visual inspection (presented in Figures 4.36 and 4.37). Since CO<sub>2</sub> concentration is low, it is possible that the carbonation that takes place is not sufficient to heal the cracks. On the contrary, high CO<sub>2</sub> concentration enhances carbonation thereby healing the cracks and significantly improving mechanical strength.

Overall, Class H cement demonstrates better capability to sustain mechanical strength than Class G cement because it is stronger after chemical degradation.

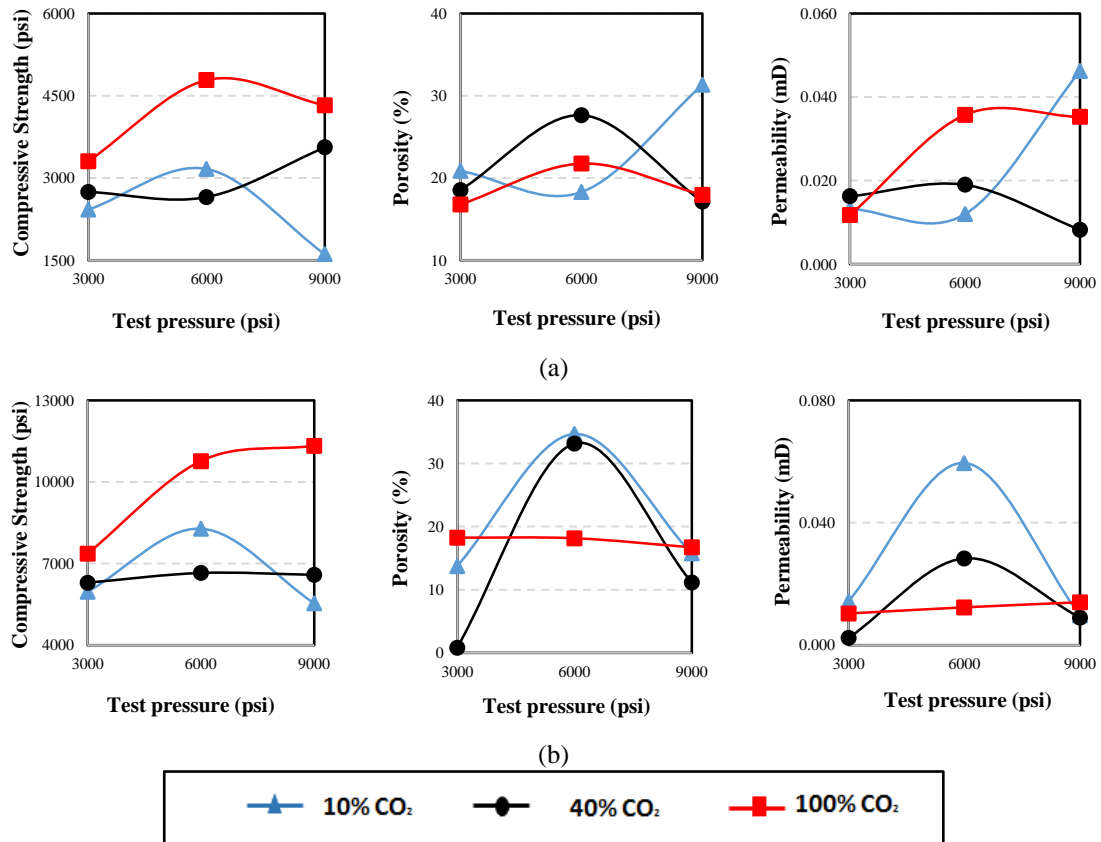


Figure 4.41 Effect of total test pressure at 350°F and different CO<sub>2</sub> gas composition on the compressive strength, porosity, and permeability of: (a) Class G; (b) Class H

### 4.3.5.2.3 Visual Degradation

Effects of pressure at 350°F on visual degradation is investigated using Figures 4.36 and 4.37. In both cement, the depth of penetration increases with test pressure. This implies that the specimens were progressively carbonated as test pressure increases. Class H cement shows deeper penetration; thus, it is stronger than Class G cement.

### 4.3.5.3 Effect of Pressure at 430°F

#### 4.3.5.3.1 FTIR Mineralogy

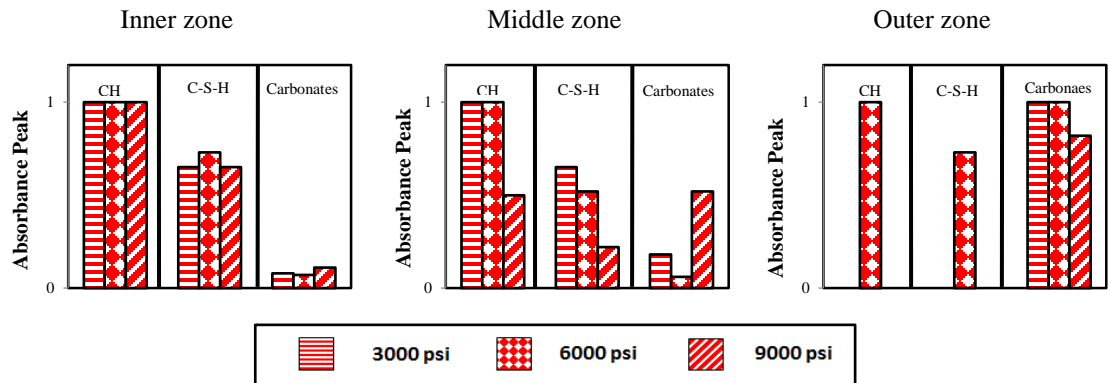


**Figure 4.42** Effect of test pressure at 430°F and 100% CO<sub>2</sub> on the normalized absorbance peaks extracted from the FTIR spectra of the degraded zones of Class H cement

Effect of pressure at 430°F and 100% CO<sub>2</sub> on FTIR mineralogy is presented in **Figure 4.42**. CH and C-S-H are mostly preserved in the inner and middle zones but are reacted in the outer zone, except at 6000 psi. As discussed previously, the retention of CH and C-S-H is likely due to lower solubility of these hydrates at high temperature (430°F) than at lower temperatures. The outer zone of the exposed specimens is the most carbonated. With deeper penetration of acid, however, partial consumption of these hydrates in the middle zone also leads to the precipitation of carbonates. These carbonates, in addition to the retained quantities of CH and C-S-H, would contribute to strength development.

### 4.3.5.3.2 Mechanical Degradation

Effect of total test pressure at 430°F and 100% CO<sub>2</sub> gas composition on mechanical degradation is shown in **Figure 4.43**. As pressure increases, compressive strength also increases in both classes of cement. Correspondingly, porosity and permeability decreases. Thus, carbonation is the prevailing mechanism of degradation. However, the presence of CSH crystalline phases (especially xonotlite) is expected to contribute to the trends observed. Although pressure effect on the structural transformation of amorphous CSH is not well understood, the presence of xonotlite is anticipated due to the temperature condition (430°F) and the amount of silica flour added to the neat cements (35% BWOC). Class H cement shows improved integrity over Class G cement because it has higher compressive strength and lower porosity and permeability.

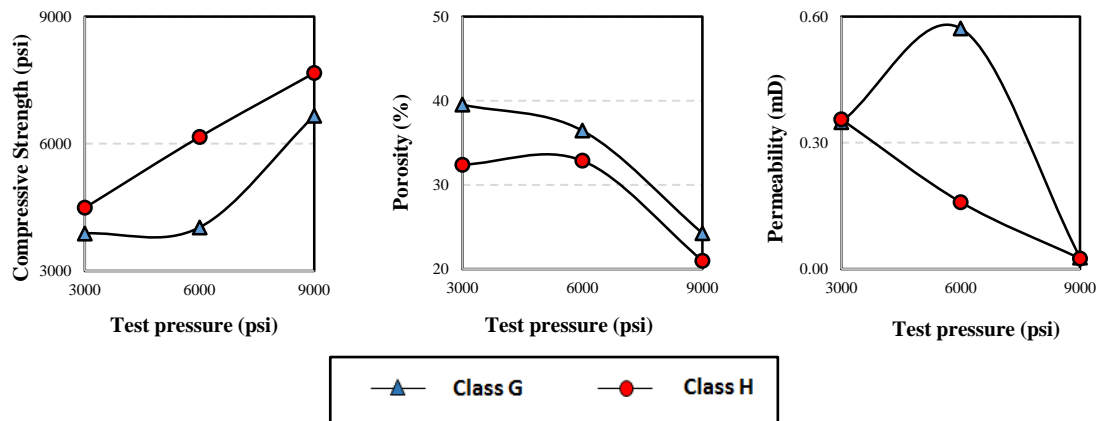


Figure 4.43 Effect of test pressure at 430°F and 100% CO<sub>2</sub> on the compressive strength, porosity, and permeability of Classes G and H cement

### 4.3.5.3.3 Visual Degradation

The influence of variation in total test pressure at 430°F and 100% CO<sub>2</sub> gas composition on visual degradation is shown in Figures 4.21 and 4.22 (presented previously in Section 4.3.3.1.3). At all test pressures, complete penetration of carbonic

acid occurs in both classes of cement, except in Class G cement with a visual reaction front at 9000 psi. Unlike visual degradations at 100°F, 225°F, and 350°F, very high temperature (430°F) aids the rate of acid attack on cement.

#### **4.3.5.4 Summary**

Compressive strength mostly increased as total test pressure increases mainly due to carbonation of cement hydrates, which results from increase in the solubility of CO<sub>2</sub> gas as pressure increases. In some cases, leaching of calcium bi-carbonate also contributes to the trends observed. Besides, the specimens show increase in penetrated depth as pressure increases. FTIR mineralogy indicates that CH and CSH are generally preserved, although increasingly consumed as pressure increases. Overall, the mechanical response of Class H cement to increase in pressure is higher than the response of Class G cement.

### **4.3.6 Effect of Exposure Time on Cement Integrity**

#### **4.3.6.1 Mechanical Degradation**

Effect of variation in exposure time is investigated at 350°F, 6000 psi and 10% CO<sub>2</sub> concentration. The result is presented in **Figure 4.44**. After the initial 6 days of exposure, changes in mechanical and transport properties of Class G cement is insignificant, indicating less reactivity with CO<sub>2</sub>. In Class H cement, strength increases considerably while porosity and permeability decreases. This indicates higher reactivity leading to carbonation reaction. As time increases, compressive strength decreases in Class G cement while transport parameters generally increase. Similar trend is observed in Class H cement, although loss in strength is more significant between 6 and 28 days.

This is due to leaching which arises from the increased period of exposure permitting more time for the carbonated brine to leach the specimens after the initial carbonation.

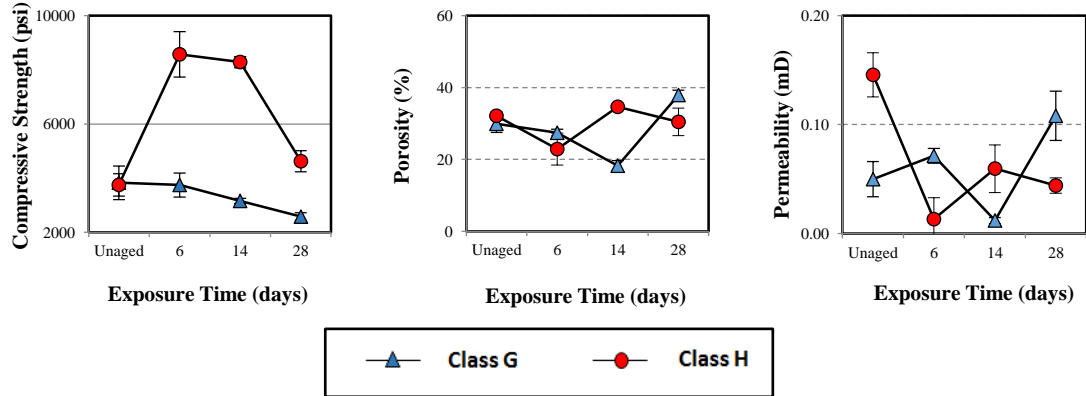


Figure 4.44 Effect of aging time at 350°F, 6000 psi and 10% CO<sub>2</sub> on the compressive strength, porosity, and permeability of Classes G and H cement

### 4.3.6.2 Visual Degradation

Figure 4.45 shows pictures of the degraded specimens. Class G cement shows uneven visual degradation than Class H cement. In both cement, the depth of penetration increases with exposure time. Evidently, increase in time leads to further chemical attack because increased time of exposure allows more reaction to take place.

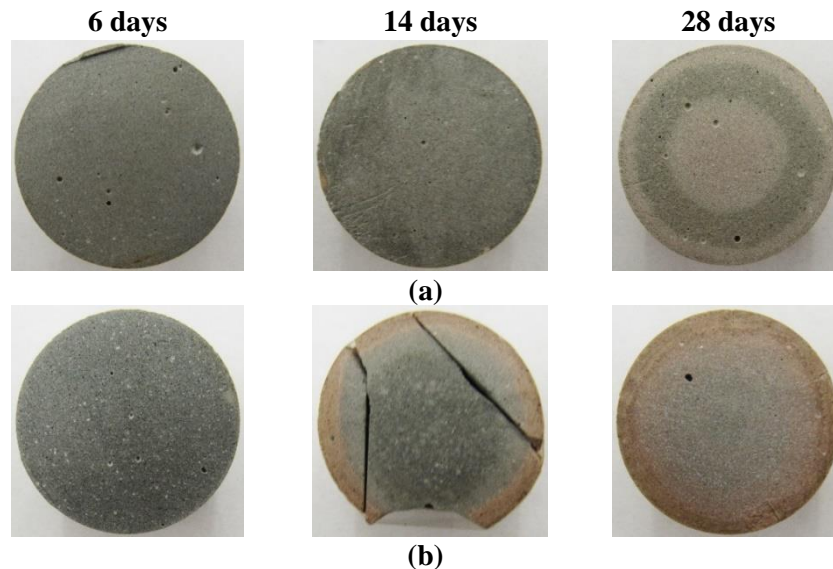


Figure 4.45 Visual degradation due to variation in exposure time at 350°F, 6000 psi, and 10% CO<sub>2</sub> gas composition: (a) Class G; (b) Class H



### **4.3.7 Summary of Experimental Studies**

In this chapter, the effects of temperature, CO<sub>2</sub> gas composition, and total test pressure on cement degradation were investigated under different conditions. The results show that the evolution of mechanical and transport properties of well cement in the event of exposure to different temperatures, CO<sub>2</sub> gas compositions, and pressures is due to interconnected chemical mechanisms. Carbonation helped to sustain mechanical strength while leaching leads to the loss of strength. The combined effect of these competing mechanisms determines the mechanical behavior of cement after exposure to CO<sub>2</sub>-containing brine. Effect of variation in temperature indicates that strength development occurs due to combined effect of carbonation, leaching, structural transformation of C-S-H, and the dissolution of cement hydrates. Furthermore, results show that carbonation is the main mechanism of degradation when CO<sub>2</sub> gas composition and pressure were varied. Comparison of the effects of the three downhole parameters suggests that pressure and CO<sub>2</sub> gas composition have fringe influence on cement degradation relative to temperature. Therefore, temperature appears to be the most critical downhole parameter that determines the mechanical integrity of well cement in HPHT acidic environment.

Overall, Class H cement demonstrates better integrity for casing support and zonal isolation than Class G cement after exposure.

## **Chapter 5 Mathematical Modeling and Simulation**

### **5.1 Overview**

The major challenge with cement degradation in acidic environment is the dissolution of hydrated products which leads to strength reduction as well as increase in porosity and permeability. As these alterations in mechanical and transport properties take place, the degradation process is intensified through further penetration of the aggressive fluid into the undamaged zone of the cement. Modeling this deterioration process is very complex due to several controlling parameters and driving mechanisms (Figure 3.5 in Chapter 3). An iteratively-coupled model accounting for all these mechanisms is required for better understanding of cement degradation. The development of this model is now discussed.

### **5.2 Model Assumptions**

1. Hydration, chemical shrinkage, carbonation, bi-carbonation, and leaching are the major mechanisms governing cement degradation.
2. Bulk fluid is under static condition, hence no advective transport of reacting species.
3. Degradation process is governed by reaction and diffusion.
4. The loss of primary minerals and the formation of secondary minerals are responsible for mechanical behavior after exposure to CO<sub>2</sub>-containing fluid.

### **5.3 Physics of the Problem and Model Formulation**

Cement degradation in CO<sub>2</sub>-brine environment under HPHT condition involves complex interaction of physical, chemical and mechanical processes. To

accurately model these complex interactions, the problem is first decomposed in order to capture the controlling mechanisms involved (i.e. the physics of the problem). There are three major physical processes leading to the mechanical and transport properties presented in Chapter 4. These are: mixing and curing, exposure to CO<sub>2</sub>-saturated brine in HPHT autoclave, and mechanical compression test. These physical processes trigger several chemical and mechanical processes leading to the performance of the specimen after exposure. The chemical and mechanical processes that occur during each physical process are discussed next.

### **5.3.1 Mixing and Curing**

The following chemical processes take place during mixing and curing:

- (i) Hydration and Chemical shrinkage,
- (ii) Pore-scale liquid-solid speciation and equilibration (pore fluid chemistry), and
- (iii) Mineral precipitation and dissolution.

Hydration and chemical shrinkage were described in Chapter 3. As hydration proceeds, clinker materials react with water to form cement hydrates. The quantity of each hydrate depends on the degree of hydration of the clinker compounds. It is clear from XRD analysis presented in Section 4.3.1.3 of Chapter 3 that these clinker materials were not completely hydrated even after exposing the specimens to CO<sub>2</sub>-containing fluid. So, prediction of the degree of hydration of the clinker materials is required. Thus, the degree of hydration can be used in reaction stoichiometry to estimate the amount of each hydrate. Furthermore, shrinkage of compounds during hydration adjusts the pore volume (porosity) and pore connectivity (permeability). By accounting for chemical shrinkage,

the initial transport properties (porosity and permeability) can be estimated from volume balance of mixing water after hydration (extra water analysis).

Pore-scale liquid-solid speciation and equilibration primarily occurs during hardening of cement. As discussed in Chapter 4, the specimens were cured at 200°F. At this curing temperature, three phenomenon can occur. First is pozzolanic reaction between calcium hydroxide (a hydrate) and silica to form calcium silicate hydrate. This reduces the amount of calcium hydroxide but increases the amount of amorphous calcium silicate hydrate. Secondly, amorphous calcium silicate hydrate transforms to its crystalline polymorph that is most stable at the curing temperature and C/S ratio. XRD analysis indicates that clinotobermorite is the crystalline CSH phase formed after partial transformation of CSH. Similarly, the residual silica transforms to its stable polymorph, which is believed to be  $\alpha$ -quartz based on XRD data and the phase diagram for silica. Thirdly, the multi-component solid matrix attempts to establish chemical equilibrium with the aqueous species in the pore fluid. This triggers dissolution and, in some cases, precipitation of minerals in the pore fluid. For instance, dissolution of atmospheric  $\text{CO}_2$  (about 0.039% of atmospheric pressure) during mixing of the slurry results in the formation of weakly-carbonated brine. This is believed to account for the formation of calcite in the cured specimen (XRD data in Section 4.3.1.3.1 of Chapter 4). Thus, the 2 wt% NaCl solution in cement pores will typically contain the following primary species in aqueous solution:  $\text{H}^+$ ,  $\text{HCO}_3^-$ ,  $\text{CO}_3^{2-}$ ,  $\text{Na}^+$ ,  $\text{OH}^-$ ,  $\text{Cl}^-$ , and  $\text{CO}_2^{\text{aq}}$ . Association between these species leads to the formation of secondary aqueous complexes such as  $\text{NaCl}^{\text{aq}}$ ,  $\text{NaOH}^{\text{aq}}$ ,  $\text{NaHCO}_3^-$ , and  $\text{NaCO}_3^-$ . When this collection of aqueous species comes into contact with cement hydrates, the state of chemical equilibrium is disturbed. The minerals

(hydrates) attempt to reestablish chemical equilibrium by dissolving ions into solution or the ions in solution interact to precipitate minerals and aqueous complexes. Complexes (e.g.  $\text{CaOH}^+$ ,  $\text{CaHCO}_3^+$ , and  $\text{CaCO}_3^{\text{aq}}$ , etc.) are typically formed. This equilibration continues until a stable assemblage of minerals is reached when no mineral precipitates or dissolves in pore solution. This is then the stable form of the specimen after curing. Prediction of this stable mineral assemblage helps to determine the porosity, permeability and compressive strength of the unaged specimen. In addition the molality of aqueous species in the pore fluid at equilibrium is the initial condition for reactive transport during exposure to carbonated brine. Therefore, the following models are required to simulate the state of the specimen after mixing and curing:

- (i) Degree of hydration/chemical shrinkage model,
- (ii) Reaction stoichiometry model,
- (iii) Transport properties model, and
- (iv) Stable mineral assemblage model.

These models are presented in Section 5.4.1.

### **5.3.2 Exposure to $\text{CO}_2$ -Saturated Brine in an HPHT Autoclave**

The following chemical processes occur during this physical process:

- (i) Gas-liquid equilibration,
- (ii) Bulk fluid speciation and equilibration (bulk fluid chemistry),
- (iii) Transport of solute species from bulk fluid to pore fluid,
- (iv) Pore-scale liquid-solid speciation and equilibration (pore fluid chemistry), and

- (v) Mineral precipitation (e.g. carbonation) and dissolution (e.g. leaching).

The corrosion of well cement by carbonated-brine leads to the precipitation of secondary minerals. Predicting the rate of precipitation of these minerals during the degradation process is a crucial step in understanding the mechanical and transport properties of cement after exposure to aggressive fluid. Some models (**refs!**) exist but their applications are very limited. The rate of mineral precipitation is controlled by the transport of dissolved  $\text{CO}_2$  into assessable pores of the cement matrix. Before commencement of the transport of ionic species to the reaction sites (i.e. pores), it is important to determine the composition of aqueous species in the bulk fluid. However, the bulk fluid chemistry depends on solubility of the injected gases ( $\text{CO}_2$  and  $\text{CH}_4$ ); hence, the gas phase equilibria of  $\text{CO}_2$ , and any mixed gas, must be determined. As described in Section 4.2.2.2 of Chapter 4, a gas mixture of carbon dioxide ( $\text{CO}_2$ ) and methane ( $\text{CH}_4$ ) is injected at different composition into the HPHT autoclave (aging cell). The cell is filled to 80% capacity, approximately. As the system is pressurized and temperature increased, water vapor will coexist with  $\text{CO}_2$ - $\text{CH}_4$  gas mixture in the headspace of the cell. This increases the number of components in the gas phase from 2 to 3 (i.e.  $\text{CO}_2$ - $\text{H}_2\text{O}$ - $\text{CH}_4$  mixture). The components in the gas phase then establishes equilibrium individually with the dissolved component in the liquid phase. That is,  $\text{CO}_2^g$  equilibrate with  $\text{CO}_2^{\text{aq}}$ ,  $\text{H}_2\text{O}^v$  equilibrate with  $\text{H}_2\text{O}^l$ , and  $\text{CH}_4^g$  equilibrate with  $\text{CH}_4^{\text{aq}}$ . The fugacity of  $\text{CO}_2^g$  is a required input for modeling bulk fluid chemistry. Thus, a gas-liquid equilibrium model is required. Furthermore, the dissolved  $\text{CO}_2$  (i.e.  $\text{CO}_2^{\text{aq}}$ ) reacts with water to form carbonic acid (i.e.  $\text{H}_2\text{CO}_3^{\text{aq}}$ ) according to equation 2.15 in Chapter 2. Subsequently,

$\text{H}_2\text{CO}_3^{\text{aq}}$  undergoes two-step dissociation in solution to form  $\text{H}^+$ ,  $\text{HCO}_3^-$ , and  $\text{CO}_3^{2-}$ . The chemistry of the reaction between dissolved  $\text{CH}_4$  (i.e.  $\text{CH}_4^{\text{aq}}$ ) with water is neglected because the solubility of methane in water (i.e. the molality of  $\text{CH}_4^{\text{aq}}$ ) is low compared to the solubility of  $\text{CO}_2$ . In addition, dissociation of 2% NaCl in bulk solution produces  $\text{Na}^+$  and  $\text{Cl}^-$ . Besides, water dissociates to form  $\text{H}^+$  and  $\text{OH}^-$ . Association between these primary species produces the following secondary aqueous complexes:  $\text{NaCl}^{\text{aq}}$ ,  $\text{NaOH}^{\text{aq}}$ ,  $\text{NaHCO}_3^-$ , and  $\text{NaCO}_3^-$ . Predicting the equilibrium concentration of these aqueous species helps to determine the boundary condition at the surface of the specimen. For the duration of  $\text{CO}_2$  exposure test, transport of ions between the bulk fluid and the pore fluid occurs which requires a reactive-transport model. In addition, the stable mineral assemblage due to pore-scale liquid-solid equilibration must be predicted to determine mineral composition and transport properties after chemical degradation of the specimen. **Figure 5.1** illustrates the dissociation reactions that occur in the bulk and pore fluids. Hence, the following models are required to simulate the state of the specimen after exposure to  $\text{CO}_2$ -saturated brine in HPHT autoclave:

- (i) Gas-liquid phase equilibration model,
- (ii) Bulk fluid speciation and equilibration model,
- (iii) Reactive-transport model,
- (iv) Stable mineral assemblage model

These models are presented in Section 5.4.2.

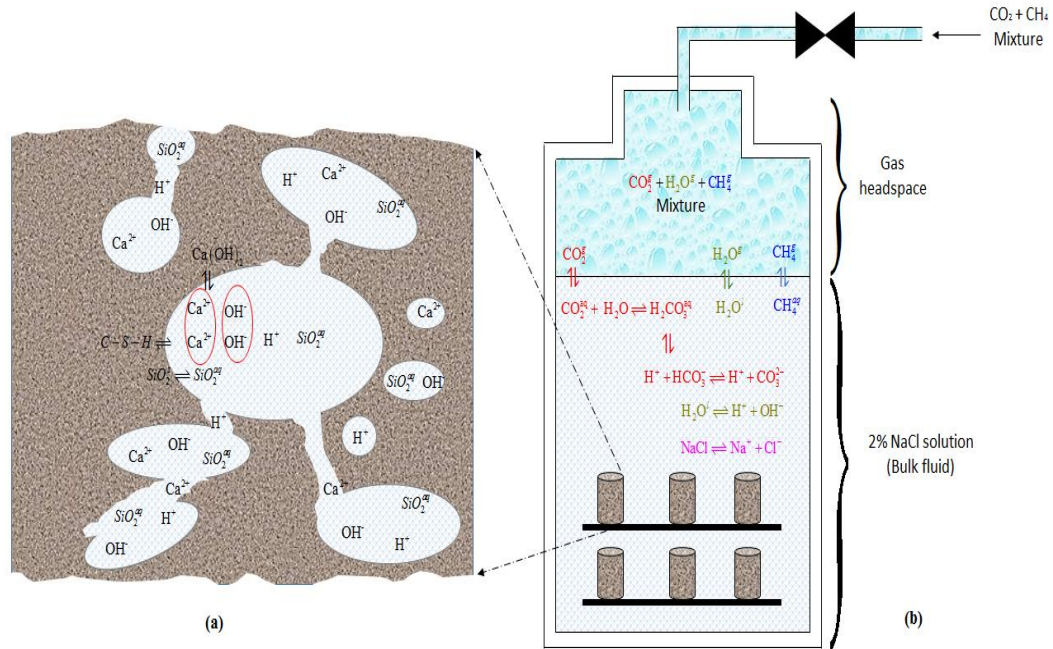


**Figure 5.1 Bulk and pore fluid chemistry resulting in chemical degradation of cement**

### 5.3.3 Mechanical Compression Test

The mechanical process that occurs during compression test is the failure of specimen. As the specimen is compressed under triaxial stress loading condition, stress builds up in the matrix. Failure occurs when stress at any point exceeds the compressive strength of the aggregate. Therefore, the development of compressive strength model is required to determine the specimen's mechanical integrity. This is presented in Section 5.4.3.

**Figure 5.2** shows a schematic for the proposed cement degradation model and the coupling between the physical, chemical, and mechanical processes. The key parameters to be predicted are degree of cement hydration, porosity and permeability before and after exposure to CO<sub>2</sub>-rich brine, concentration of aqueous species (including pH distribution in the specimen), stable mineral assemblage before and after exposure, degraded depth, and compressive strength before and after exposure.



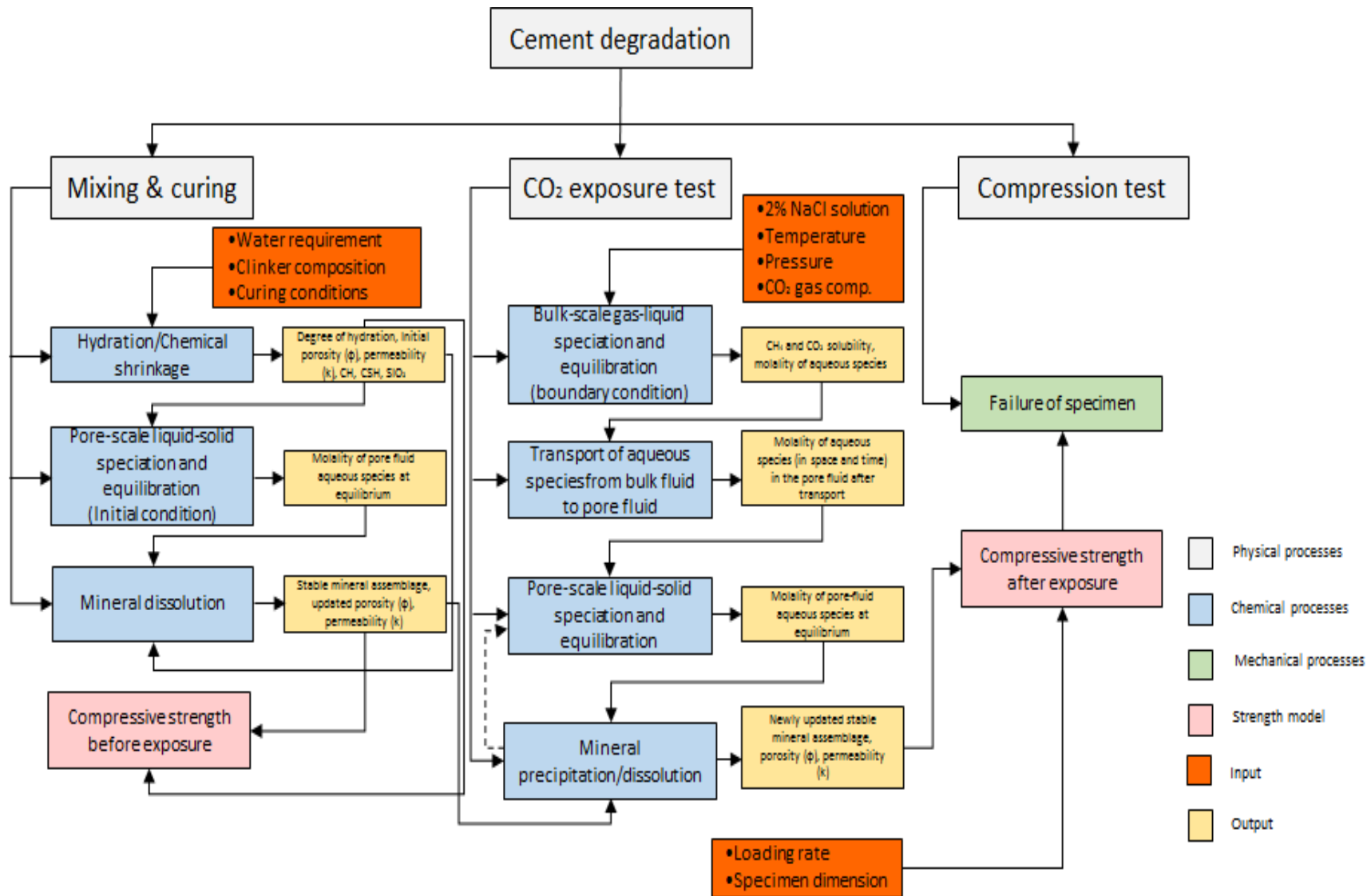


Figure 5.2 Modeling Workflow

## 5.4 Cement Degradation Modeling

### 5.4.1 Modeling Cement Mixing and Curing

#### 5.4.1.1 Modeling the Degree of Hydration and Chemical Shrinkage

The overall degree of hydration ( $\alpha$ ) and chemical shrinkage ( $v_{chsh}$ ) after curing are estimated using the model proposed by Lin and Meyer (2009). This model is selected because it accepts clinker composition, w/c ratio, Blain fineness, pressure and temperature as input variables. The following equations are required to be solved.

$$\frac{d\alpha}{dt} = A_\alpha n_\alpha e^{-\frac{E_a}{RT}} e^{\frac{E_a}{RT_0}} \dots\dots\dots (5.1)$$

$$v_{chsh} = \frac{0.0625\alpha}{0.32 + w/c} \dots\dots\dots (5.2),$$

where,

$$A_\alpha = k \left( \frac{A_o}{k\alpha_u} + \alpha \right) (\alpha_u - \alpha) e^{0.02 \left( \frac{P}{P_{atm}} - 1 \right)^{0.07} \left( \frac{\alpha}{\alpha_u} - 1.5 \left( \frac{\alpha}{\alpha_u} \right)^2 + 0.4 \right)}$$

$$n_\alpha = e^{-n_o \left( 1 + (1-\alpha)^2 \ln \left\{ \frac{350}{Blaine} \right\} \right) \left( e^{28 \cdot 10^{-6} (T-T_0)^2} \right)^{10\alpha^4} \alpha}$$

$$A_o = A'_o \left( \frac{Blaine}{350} \right)$$

$$A'_o = -0.0767C_4AF + 0.0184$$

$$k = 0.56C_3S^{-0.206} C_2S^{-0.128} C_3A^{0.161}$$

$$n_o = 10.945C_3S + 11.25C_2S - 4.10C_3A - 0.892$$

$$E_a = 22100C_3A^{0.30} C_4AF^{-0.25} Blaine^{0.35}$$

$$\alpha_{u,T}^{est} = \alpha_{u,T_o} e^{-0.00003(T-T_o)^2 \text{SGN}(T-T_o)}$$

$$\alpha_{u,T_o} = \frac{\beta_1 * w/c}{\beta_2 + w/c}$$

$$\beta_1 = \frac{1}{9.33 \left( \frac{\text{Blaine}}{100} \right)^{2.82} + 0.38}$$

$$\beta_2 = \frac{\text{Blaine} - 220}{147.78 + 1.656(\text{Blaine} - 220)}$$

$$\text{SGN}(T - T_o) = \begin{cases} 1, & \text{when } T \geq T_o \\ -1, & \text{when } T < T_o \end{cases}$$

$$\alpha_{u,T}^{th} = \frac{w/c}{0.4}$$

$$\text{If } \alpha_{u,T}^{est} \leq \alpha_{u,T}^{th}, \alpha_u = \alpha_{u,T}^{est} \text{ else } \alpha_u = \alpha_{u,T}^{th}$$

$$T_o = 293.15 \text{ K}$$

Equation 5.1 is a non-linear ordinary differential equation which requires numerical solution.

#### 5.4.1.2 Modeling Reaction Stoichiometry

The chemical reactions that take place during the hydration of Portland cement were presented in Chapter 2. The hydrates typically formed after the initial hydration of clinker materials are: calcium hydroxide (CH), calcium silicate hydrate (CSH), calcium monosulfoaluminate ( $C_3A\bar{C}H_{12}$ ), katoite ( $C_3AH_6$ ), and hydrated iron (II) oxide or rust ( $FH_3$ ). The quantity of these hydrates are determined by applying basis switching technique (Bethke, 2008; Steefel, 1992) on the balanced reaction stoichiometry of the governing chemical reactions.

Case 1: In the absence of gypsum

The governing equations 2.5, 2.6, 2.10, and 2.13 (from Chapter 2) are expressed in terms of the clinker compounds ( $C_3S$ ,  $C_2S$ ,  $C_3A$ , and  $C_4AF$ ), whose compositions are known from the information provided by the cement manufacturer.

Therefore,

$$H \rightarrow H \dots\dots\dots (5.3)$$

$$C_3S \rightarrow \frac{1}{y} C_x S_y H_{z(s)} + \frac{3y-x}{y} .CH_{(s)} - \frac{3y+z-x}{y} .H \dots\dots\dots (5.4)$$

$$C_2S \rightarrow \frac{1}{y} C_x S_y H_{z(s)} + \frac{2y-x}{y} .CH_{(s)} - \frac{2y+z-x}{y} .H \dots\dots\dots (5.5)$$

$$C_3A \rightarrow C_3AH_6 - 6H \dots\dots\dots (5.6)$$

$$C_4AF \rightarrow C_3AH_6 + CH + FH_3 - 10H \dots\dots\dots (5.7)$$

A dummy chemical reaction (equation 5.3) for H (i.e.  $H_2O$ ) is incorporated to determine the amount of water consumed in the hydration process. The components in the old basis are: H,  $C_3S$ ,  $C_2S$ ,  $C_3A$ , and  $C_4AF$  while the components in the new basis are H, CH, CSH,  $C_3AH_6$ , and  $FH_3$ . Assuming the degrees of hydration of the clinker compounds are  $\alpha_{C_3S}$ ,  $\alpha_{C_2S}$ ,  $\alpha_{C_3A}$ , and  $\alpha_{C_4AF}$ , equations 5.3 to 5.7 can be expressed in matrix form as:

$$\begin{bmatrix} H \\ C_3S \\ C_2S \\ C_3A \\ C_4AF \end{bmatrix} = \begin{bmatrix} 1 & 0 & 0 & 0 & 0 \\ -\frac{3y+z-x}{y} \alpha_{C_3S} & \frac{1}{y} \alpha_{C_3S} & \frac{3y-x}{y} \alpha_{C_3S} & 0 & 0 \\ -\frac{2y+z-x}{y} \alpha_{C_2S} & \frac{1}{y} \alpha_{C_2S} & \frac{2y-x}{y} \alpha_{C_2S} & 0 & 0 \\ -6\alpha_{C_3A} & 0 & 0 & \alpha_{C_3A} & 0 \\ -10\alpha_{C_4AF} & 0 & \alpha_{C_4AF} & \alpha_{C_4AF} & \alpha_{C_4AF} \end{bmatrix} \begin{bmatrix} H \\ CSH \\ CH \\ C_3AH_6 \\ FH_3 \end{bmatrix} \dots\dots (5.8a)$$

When  $x = 3$ ,  $y = 2$ , and  $z = 3$ , equation 2.5a becomes:

$$\begin{bmatrix} H \\ C_3S \\ C_2S \\ C_3A \\ C_4AF \end{bmatrix} = \begin{bmatrix} 1 & 0 & 0 & 0 & 0 \\ -3\alpha_{C_3S} & \frac{1}{2}\alpha_{C_3S} & \frac{3}{2}\alpha_{C_3S} & 0 & 0 \\ -2\alpha_{C_2S} & \frac{1}{2}\alpha_{C_2S} & \frac{1}{2}\alpha_{C_2S} & 0 & 0 \\ -6\alpha_{C_3A} & 0 & 0 & \alpha_{C_3A} & 0 \\ -10\alpha_{C_4AF} & 0 & \alpha_{C_4AF} & \alpha_{C_4AF} & \alpha_{C_4AF} \end{bmatrix} \begin{bmatrix} H \\ CSH \\ CH \\ C_3AH_6 \\ FH_3 \end{bmatrix} \dots\dots\dots (5.8b)$$

$$\begin{bmatrix} H \\ CSH \\ CH \\ C_3AH_6 \\ FH_3 \end{bmatrix} = \begin{bmatrix} 1 & 0 & 0 & 0 & 0 \\ 3 & -\frac{1}{\alpha_{C_3S}} & \frac{3}{\alpha_{C_2S}} & 0 & 0 \\ 1 & \frac{1}{\alpha_{C_3S}} & -\frac{1}{\alpha_{C_2S}} & 0 & 0 \\ 6 & 0 & 0 & \frac{1}{\alpha_{C_3A}} & 0 \\ 3 & -\frac{1}{\alpha_{C_3S}} & \frac{1}{\alpha_{C_2S}} & -\frac{1}{\alpha_{C_3A}} & \frac{1}{\alpha_{C_4AF}} \end{bmatrix} \begin{bmatrix} H \\ C_3S \\ C_2S \\ C_3A \\ C_4AF \end{bmatrix} \dots\dots\dots (5.9)$$

Thus, the transformation matrix is:

$$\beta = \begin{bmatrix} 1 & 0 & 0 & 0 & 0 \\ 3 & -\frac{1}{\alpha_{C_3S}} & \frac{3}{\alpha_{C_2S}} & 0 & 0 \\ 1 & \frac{1}{\alpha_{C_3S}} & -\frac{1}{\alpha_{C_2S}} & 0 & 0 \\ 6 & 0 & 0 & \frac{1}{\alpha_{C_3A}} & 0 \\ 3 & -\frac{1}{\alpha_{C_3S}} & \frac{1}{\alpha_{C_2S}} & -\frac{1}{\alpha_{C_3A}} & \frac{1}{\alpha_{C_4AF}} \end{bmatrix} \dots\dots\dots (5.10)$$

Therefore, the mole numbers of the components in the new basis are:

$$\begin{bmatrix} H \\ CSH \\ CH \\ C_3AH_6 \\ FH_3 \end{bmatrix}^{M^{new}} = (\beta^{-1})^T \begin{bmatrix} H \\ C_3S \\ C_2S \\ C_3A \\ C_4AF \end{bmatrix}^{M^{old}} = \begin{bmatrix} 1 & -3\alpha_{C_3S} & -2\alpha_{C_2S} & -6\alpha_{C_3A} & -10\alpha_{C_4AF} \\ 0 & \frac{1}{2}\alpha_{C_3S} & \frac{1}{2}\alpha_{C_2S} & 0 & 0 \\ 0 & \frac{3}{2}\alpha_{C_3S} & \frac{1}{2}\alpha_{C_2S} & 0 & \alpha_{C_4AF} \\ 0 & 0 & 0 & \alpha_{C_3A} & \alpha_{C_4AF} \\ 0 & 0 & 0 & 0 & \alpha_{C_4AF} \end{bmatrix} \begin{bmatrix} H \\ C_3S \\ C_2S \\ C_3A \\ C_4AF \end{bmatrix}^{M^{old}}$$

..... (5.11a)

In the generalized form of CSH,

$$\begin{bmatrix} H \\ C_3S \\ C_2S \\ C_3A \\ C_4AF \end{bmatrix} = \begin{bmatrix} 1 & -\frac{3y+z-x}{y}\alpha_{C_3S} & -\frac{2y+z-x}{y}\alpha_{C_2S} & -6\alpha_{C_3A} & -10\alpha_{C_4AF} \\ 0 & \frac{1}{y}\alpha_{C_3S} & \frac{1}{y}\alpha_{C_2S} & 0 & 0 \\ 0 & \frac{3y-x}{y}\alpha_{C_3S} & \frac{2y-x}{y}\alpha_{C_2S} & 0 & \alpha_{C_4AF} \\ 0 & 0 & 0 & \alpha_{C_3A} & \alpha_{C_4AF} \\ 0 & 0 & 0 & 0 & \alpha_{C_4AF} \end{bmatrix} \begin{bmatrix} H \\ CSH \\ CH \\ C_3AH_6 \\ FH_3 \end{bmatrix}$$

..... (5.11b)

Case 2: In the presence of gypsum

The governing equations 2.5, 2.6, 2.7, 2.8, 2.11, and 2.12 (from Chapter 2) are expressed in terms of the clinker compounds ( $C_3S$ ,  $C_2S$ ,  $C_3A$ ,  $C_4AF$ , and  $\bar{C}H_2$ ) whose compositions are known from the information provided by the cement manufacturer.

Therefore,

$$H \rightarrow H \dots\dots\dots (5.12)$$

$$\bar{C}H_2 \rightarrow \bar{C}H_2 \dots\dots\dots (5.13)$$

$$C_3S \rightarrow \frac{1}{y}C_xS_yH_{z(s)} + \frac{3y-x}{y}.CH_{(s)} - \frac{3y+z-x}{y}.H \dots\dots\dots (5.14)$$

$$C_2S \rightarrow \frac{1}{y} C_x S_y H_{z(s)} + \frac{2y-x}{y} \cdot CH_{(s)} - \frac{2y+z-x}{y} \cdot H \dots\dots\dots (5.15)$$

$$C_3A \rightarrow C_3A\bar{C}H_{12} - \bar{C}H_2 - 10H \dots\dots\dots (5.16)$$

$$C_4AF \rightarrow C_3A\bar{C}H_{12} + CH + FH_3 - \bar{C}H_2 - 14H \dots\dots\dots (5.17)$$

The components in the old basis are: H, C<sub>3</sub>S, C<sub>2</sub>S, C<sub>3</sub>A, C<sub>4</sub>AF, and  $\bar{C}H_2$  while the components in the new basis are H, CH, CSH, C<sub>3</sub>A $\bar{C}H_{12}$ , FH<sub>3</sub>, and  $\bar{C}H_2$  Equations 5.12 to 5.17 can be expressed in matrix form as:

$$\begin{bmatrix} H \\ C_3S \\ C_2S \\ C_3A \\ C_4AF \\ \bar{C}H_2 \end{bmatrix} = \begin{bmatrix} 1 & 0 & 0 & 0 & 0 & 0 \\ -\frac{3y+z-x}{y}\alpha_{C_3S} & \frac{1}{y}\alpha_{C_3S} & \frac{3y-x}{y}\alpha_{C_3S} & 0 & 0 & 0 \\ -\frac{2y+z-x}{y}\alpha_{C_2S} & \frac{1}{y}\alpha_{C_2S} & \frac{2y-x}{y}\alpha_{C_2S} & 0 & 0 & 0 \\ -10\alpha_{C_3A} & 0 & 0 & \alpha_{C_3A} & 0 & -\alpha_{C_3A} \\ -14\alpha_{C_4AF} & 0 & \alpha_{C_4AF} & \alpha_{C_4AF} & \alpha_{C_4AF} & -\alpha_{C_4AF} \\ 0 & 0 & 0 & 0 & 0 & 1 \end{bmatrix} \begin{bmatrix} H \\ CSH \\ CH \\ C_3A\bar{C}H_{12} \\ FH_3 \\ \bar{C}H_2 \end{bmatrix}$$

..... (5.18a)

When  $x = 3$ ,  $y = 2$ , and  $z = 3$ , equation 2.5a becomes:

$$\begin{bmatrix} H \\ C_3S \\ C_2S \\ C_3A \\ C_4AF \\ \bar{C}H_2 \end{bmatrix} = \begin{bmatrix} 1 & 0 & 0 & 0 & 0 & 0 \\ -3\alpha_{C_3S} & \frac{1}{2}\alpha_{C_3S} & \frac{3}{2}\alpha_{C_3S} & 0 & 0 & 0 \\ -2\alpha_{C_2S} & \frac{1}{2}\alpha_{C_2S} & \frac{1}{2}\alpha_{C_2S} & 0 & 0 & 0 \\ -10\alpha_{C_3A} & 0 & 0 & \alpha_{C_3A} & 0 & -\alpha_{C_3A} \\ -14\alpha_{C_4AF} & 0 & \alpha_{C_4AF} & \alpha_{C_4AF} & \alpha_{C_4AF} & -\alpha_{C_4AF} \\ 0 & 0 & 0 & 0 & 0 & 1 \end{bmatrix} \begin{bmatrix} H \\ CSH \\ CH \\ C_3A\bar{C}H_{12} \\ FH_3 \\ \bar{C}H_2 \end{bmatrix}$$

..... (5.18b)

$$\begin{bmatrix} H \\ CSH \\ CH \\ C_3A\bar{C}H_{12} \\ FH_3 \\ \bar{C}H_2 \end{bmatrix} = \begin{bmatrix} 1 & 0 & 0 & 0 & 0 & 0 \\ 3 & -\frac{1}{\alpha_{C_3S}} & \frac{3}{\alpha_{C_2S}} & 0 & 0 & 0 \\ 1 & \frac{1}{\alpha_{C_3S}} & -\frac{1}{\alpha_{C_2S}} & 0 & 0 & 0 \\ 10 & 0 & 0 & \frac{1}{\alpha_{C_3A}} & 0 & 1 \\ 3 & -\frac{1}{\alpha_{C_3S}} & \frac{1}{\alpha_{C_2S}} & -\frac{1}{\alpha_{C_3A}} & \frac{1}{\alpha_{C_4AF}} & 0 \\ 0 & 0 & 0 & 0 & 0 & 1 \end{bmatrix} \begin{bmatrix} H \\ C_3S \\ C_2S \\ C_3A \\ C_4AF \\ \bar{C}H_2 \end{bmatrix} \dots\dots\dots (5.19)$$

Thus, the transformation matrix is:

$$\beta = \begin{bmatrix} 1 & 0 & 0 & 0 & 0 & 0 \\ 3 & -\frac{1}{\alpha_{C_3S}} & \frac{3}{\alpha_{C_2S}} & 0 & 0 & 0 \\ 1 & \frac{1}{\alpha_{C_3S}} & -\frac{1}{\alpha_{C_2S}} & 0 & 0 & 0 \\ 10 & 0 & 0 & \frac{1}{\alpha_{C_3A}} & 0 & 1 \\ 3 & -\frac{1}{\alpha_{C_3S}} & \frac{1}{\alpha_{C_2S}} & -\frac{1}{\alpha_{C_3A}} & \frac{1}{\alpha_{C_4AF}} & 0 \\ 0 & 0 & 0 & 0 & 0 & 1 \end{bmatrix} \dots\dots\dots (5.20)$$

Therefore, the mole numbers of the components in the new basis are:

$$\begin{bmatrix} H \\ CSH \\ CH \\ C_3A\bar{C}H_{12} \\ FH_3 \\ \bar{C}H_2 \end{bmatrix}^{M^{new}} = (\beta^{-1})^T \begin{bmatrix} H \\ C_3S \\ C_2S \\ C_3A \\ C_4AF \\ \bar{C}H_2 \end{bmatrix}^{M^{old}} = \begin{bmatrix} 1 & -3\alpha_{C_3S} & -2\alpha_{C_2S} & -10\alpha_{C_3A} & -14\alpha_{C_4AF} & 0 \\ 0 & \frac{1}{2}\alpha_{C_3S} & \frac{1}{2}\alpha_{C_2S} & 0 & 0 & 0 \\ 0 & \frac{3}{2}\alpha_{C_3S} & \frac{1}{2}\alpha_{C_2S} & 0 & \alpha_{C_4AF} & 0 \\ 0 & 0 & 0 & \alpha_{C_3A} & \alpha_{C_4AF} & 0 \\ 0 & 0 & 0 & 0 & \alpha_{C_4AF} & 0 \\ 0 & 0 & 0 & -\alpha_{C_3A} & -\alpha_{C_4AF} & 1 \end{bmatrix} \begin{bmatrix} H \\ C_3S \\ C_2S \\ C_3A \\ C_4AF \\ \bar{C}H_2 \end{bmatrix}^{M^{old}} \dots\dots\dots (5.21a)$$

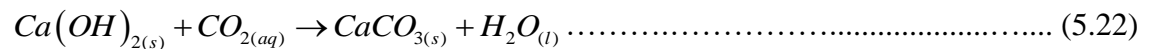


In the generalized form of CSH,

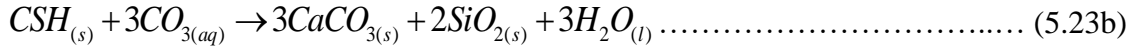
$$\begin{bmatrix} H \\ CSH \\ CH \\ C_3A\bar{C}H_{12} \\ FH_3 \\ \bar{C}H_2 \end{bmatrix}^{M^{new}} = (\beta^{-1})^T \begin{bmatrix} H \\ C_3S \\ C_2S \\ C_3A \\ C_4AF \\ \bar{C}H_2 \end{bmatrix}^{M^{old}} = \begin{bmatrix} 1 & -\frac{3y+z-x}{y}\alpha_{C_3S} & -\frac{2y+z-x}{y}\alpha_{C_2S} & -10\alpha_{C_3A} & -14\alpha_{C_4AF} & 0 \\ 0 & \frac{1}{y}\alpha_{C_3S} & \frac{1}{y}\alpha_{C_2S} & 0 & 0 & 0 \\ 0 & \frac{3y-x}{y}\alpha_{C_3S} & \frac{2y-x}{y}\alpha_{C_2S} & 0 & \alpha_{C_4AF} & 0 \\ 0 & 0 & 0 & \alpha_{C_3A} & \alpha_{C_4AF} & 0 \\ 0 & 0 & 0 & 0 & \alpha_{C_4AF} & 0 \\ 0 & 0 & 0 & -\alpha_{C_3A} & -\alpha_{C_4AF} & 1 \end{bmatrix} \begin{bmatrix} H \\ C_3S \\ C_2S \\ C_3A \\ C_4AF \\ \bar{C}H_2 \end{bmatrix}^{M^{old}} \quad (5.21b)$$

Equations 5.11 and 5.21 can be used to estimate the amount of calcium hydroxide, calcium silicate hydrate, calcium monosulfoaluminate, katoite, and hydrated iron (II) oxide. In this study, however, equation 5.11 is used to predict the quantity of cement hydrates since XRD analysis of the unexposed specimens does not indicate the presence of calcium monosulfoaluminate.

It was noted in Section 4.3.1.3.1 that the calcite detected in the unaged specimen is likely due to the presence of atmospheric CO<sub>2</sub>, which is believed to have dissolved in the mix water used to prepare cement slurry and subsequently reacted with cement hydrates. CO<sub>2</sub> gas occupies about 0.039% of atmospheric air. Upon dissolution in water, the solubility of this gas in water at 77°F and 14.65 psi is about 1.9485\*10<sup>-4</sup> mol/kg of water. This dissolution also changes the pH of the fluid from 7 to about 5.1. The chemical reactions between dissolved CO<sub>2</sub> and cement hydrates are:

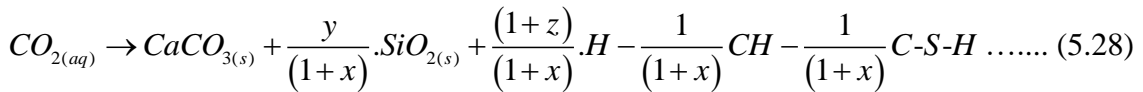
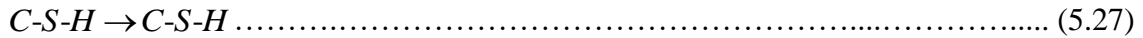
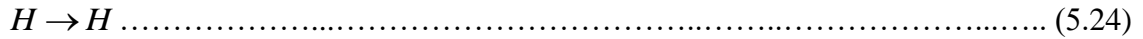


When  $x = 3$ ,  $y = 2$ , and  $z = 3$ , equation 2.17a becomes:



These governing equations are combined and re-expressed using components with known compositions (i.e. H<sub>2</sub>O, SiO<sub>2</sub>, Ca(OH)<sub>2</sub>, and (CaO)<sub>x</sub>.(SiO<sub>2</sub>)<sub>y</sub>.(H<sub>2</sub>O)<sub>z</sub>, and CO<sub>2</sub>) as the subject of the reactions. Dummy chemical reactions are included for H<sub>2</sub>O, SiO<sub>2</sub>, Ca(OH)<sub>2</sub>, and (CaO)<sub>x</sub>.(SiO<sub>2</sub>)<sub>y</sub>.(H<sub>2</sub>O)<sub>z</sub> to determine the residual amount of these components after the dissolved CO<sub>2</sub> has completely reacted.

Thus,



Equations 5.24 to 5.28 are expressed in matrix form as:

$$\begin{bmatrix} H \\ CO_2 \\ SiO_2 \\ CH \\ C-S-H \end{bmatrix} = \begin{bmatrix} 1 & 0 & 0 & 0 & 0 \\ \frac{(1+z)}{(1+x)} & 1 & \frac{y}{(1+x)} & -\frac{1}{(1+x)} & -\frac{1}{(1+x)} \\ 0 & 0 & 1 & 0 & 0 \\ 0 & 0 & 0 & 1 & 0 \\ 0 & 0 & 0 & 0 & 1 \end{bmatrix} \begin{bmatrix} H \\ CaCO_3 \\ SiO_2 \\ CH \\ C-S-H \end{bmatrix} \dots\dots\dots (5.29)$$

Therefore, the mole numbers of the new components are:

$$\begin{bmatrix} H \\ CaCO_3 \\ SiO_2 \\ CH \\ C-S-H \end{bmatrix}^{M^{new}} = \begin{bmatrix} 1 & \frac{(1+z)}{(1+x)} & 0 & 0 & 0 \\ 0 & 1 & 0 & 0 & 0 \\ 0 & \frac{y}{(1+x)} & 1 & 0 & 0 \\ 0 & -\frac{1}{(1+x)} & 0 & 1 & 0 \\ 0 & -\frac{1}{(1+x)} & 0 & 0 & 1 \end{bmatrix} \begin{bmatrix} H \\ CO_2 \\ SiO_2 \\ CH \\ C-S-H \end{bmatrix}^{M^{old}} \dots\dots\dots (5.30a)$$

Assuming  $x = 3$ ,  $y = 2$ , and  $z = 3$ ,

$$\begin{bmatrix} H \\ CaCO_3 \\ SiO_2 \\ CH \\ C-S-H \end{bmatrix}^{M^{new}} = \begin{bmatrix} 1 & 1 & 0 & 0 & 0 \\ 0 & 1 & 0 & 0 & 0 \\ 0 & \frac{1}{2} & 1 & 0 & 0 \\ 0 & -\frac{1}{4} & 0 & 1 & 0 \\ 0 & -\frac{1}{4} & 0 & 0 & 1 \end{bmatrix} \begin{bmatrix} H \\ CO_2 \\ SiO_2 \\ CH \\ C-S-H \end{bmatrix}^{M^{old}} \dots\dots\dots (5.30b)$$

**5.4.1.3 Modeling Transport Properties**

The degrees of hydration and chemical shrinkage are used to predict the initial porosity after hydration and hardening of cement. It is assumed that the 0.1 gallon/sack antifoam agent that was added during slurry preparation (Section 4.1.2) completely eliminated air entrainment; thus, the unreacted water (i.e. extra water) solely creates and fills the pores of cement. Assuming no air entrainment during mixing, extra water after hydration is computed using equation 5.11 or 5.21. Subsequently, equation 5.31 is used to estimate the initial porosity ( $\phi$ ). Assuming homogeneous volumetric shrinkage during setting, the pores will be smaller (Thomas and Jennings, 2003). Thus, chemical shrinkage ( $v_{chsh}$ ) is included to account for pore reduction.

$$\phi = \frac{M_{mw} M_w^{extr} (1 - v_{chsh})}{\left( w/c + \frac{\rho_w}{\rho_{cem}} \right) m_{cem}} \dots\dots\dots (5.31)$$

where,

$M_{mw}$  = molar mass of water (0.01801528 kgmol<sup>-1</sup>)

$M_w^{extr}$  = mole number for extra water (determined using equation 5.11 or 5.21)

$v_{chsh}$  = degree of chemical shrinkage

$w/c$  = water-to-cement ratio

$\rho_w$  = density of water at the curing temperature (kgm<sup>-3</sup>)

$\rho_{cem}$  = density of cement (about 3150 kgm<sup>-3</sup>)

$m_{cem}$  = mass of cement (kg)

$$k = a\phi^b + \frac{c}{\phi^d} + e \dots\dots\dots (5.32),$$

where a, b, c, d, and e are experimentally-determined constants. For the cement formulation used in this study, **Table 5.1** presents the values of these constants.

**Table 5.1 Constants in permeability-porosity correlation**

Cement class	a	b	c	d	e
G	5.00	3.00	5.00	-4.50	-0.09
H	5.00	2.80	5.00	-4.00	-0.10

#### 5.4.1.4 Modeling Stable Mineral Assemblage in Ca(OH)<sub>2</sub>-SiO<sub>2</sub>-CO<sub>2</sub>-NaCl-H<sub>2</sub>O System

Geochemical modeling involves the prediction of thermodynamically stable minerals after chemical reactions have occurred. Reaction between cementitious materials and aggressive fluid results in the precipitation and dissolution of minerals. It is generally agreed among geochemists that four constitutive laws govern chemical reactions. These include the law of mass action, the law of mass conservation, the law of charge balance, and the law of solute transport. The first three laws are mathematically expressed as (Bethke, 2008; Steefel, 1992):

$$M_w = n_w \left[ 55.55 + \sum_j \frac{v_{wj}}{K_j \gamma_j} \left\{ a_w^{v_{wj}} \cdot \prod_i (\gamma_i m_i)^{v_{ij}} \cdot \prod_k a_k^{v_{kj}} \cdot \prod_g f_g^{v_{gj}} \right\} \right] \dots\dots\dots (5.33)$$

$$M_i = n_w \left[ m_i + \sum_j \frac{v_{ij}}{K_j \gamma_j} \left\{ a_w^{v_{wj}} \cdot \prod_i (\gamma_i m_i)^{v_{ij}} \cdot \prod_k a_k^{v_{kj}} \cdot \prod_g f_g^{v_{gj}} \right\} \right] \dots\dots\dots (5.34)$$

$$M_k = n_k + n_w \sum_j \frac{v_{kj}}{K_j \gamma_j} \left\{ a_w^{v_{wj}} \cdot \prod_i (\gamma_i m_i)^{v_{ij}} \cdot \prod_k a_k^{v_{kj}} \cdot \prod_g f_g^{v_{gj}} \right\} \dots\dots\dots (5.35)$$

$$M_g = n_w \sum_j \frac{v_{gj}}{K_j \gamma_j} \left\{ a_w^{v_{wj}} \cdot \prod_i (\gamma_i m_i)^{v_{ij}} \cdot \prod_k a_k^{v_{kj}} \cdot \prod_g f_g^{v_{gj}} \right\} \dots\dots\dots (5.36)$$

$$m_j = \frac{1}{K_j \gamma_j} \left\{ a_w^{v_{wj}} \cdot \prod_i (\gamma_i m_i)^{v_{ij}} \cdot \prod_k a_k^{v_{kj}} \cdot \prod_g f_g^{v_{gj}} \right\} \dots\dots\dots (5.37)$$

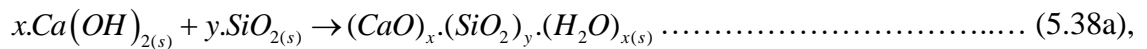
where, g, i, j, k, and w represents gas, aqueous species in the basis, aqueous species not in the basis (secondary species), minerals, and water respectively. The other terms in the above equations are defined as:

- $M$  = initial mole number
- $n$  = residual mole number after speciation
- $v$  = stoichiometric reaction coefficient
- $K$  = equilibrium constant of the governing chemical reaction
- $\gamma$  = activity coefficient
- $a$  = activity
- $m$  = molality
- $f$  = fugacity

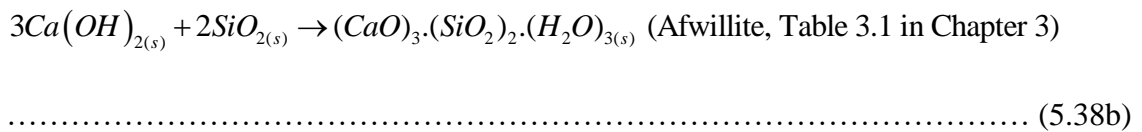
The ultimate goal of this modeling is to determine the amount of all minerals after exposure to CO<sub>2</sub>-rich brine. Equation 5.35 means that the residual amount of mineral k at any point in time is its initial amount less the amount of all aqueous species that have been derived from k. For instance, if calcium hydroxide (Ca(OH)<sub>2</sub>) dissolves in the pore solution of cement, the solute species that will be present in the pore solution are Ca<sup>2+</sup>

and OH<sup>-</sup>. If the equilibrium molality (concentration) of Ca<sup>2+</sup> and OH<sup>-</sup> are known, then equation 5.35 can be used to compute  $n_{Ca(OH)_2}$ , which is the residual amount of Ca(OH)<sub>2</sub> after dissolution.

In this study, only CH, CSH and SiO<sub>2</sub> are considered as the minerals in the initial chemical system. C<sub>3</sub>AH<sub>6</sub> and FH<sub>3</sub> are excluded because the quantity of these minerals produced after hydration are negligible when compared to the amount of CH, CSH and SiO<sub>2</sub>. In addition, XRD analyses (Chapter 4) before and after exposure of the specimens indicates that the reactivity of katoite is low. Dissolution of CH and progressive decalcification of CSH in solution both produce Ca<sup>2+</sup>, which brings about a common ion effect. This introduces a computational complexity into the multi-component chemical system. To manage this difficulty CSH is modeled as Ca(OH)<sub>2</sub> chemically bounded to SiO<sub>2</sub> and H<sub>2</sub>O; hence, the system Ca(OH)<sub>2</sub>-SiO<sub>2</sub>-CO<sub>2</sub>-NaCl-H<sub>2</sub>O is considered. In addition, selection of basis components (aqueous species and minerals) requires that it must not be possible to write a balanced chemical reactions between constituents in the basis (Bethke, 2008). It is known, however, that pozzolanic reaction occurs between portlandite and silica at high temperature which forms CSH (equation 5.38). Thus, the exclusion of CSH ensures that this requirement is met.



When x = 3 and y = 2,

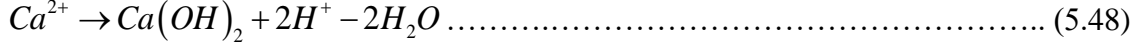
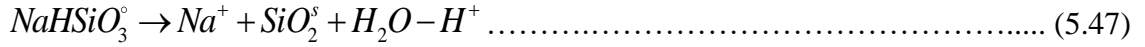
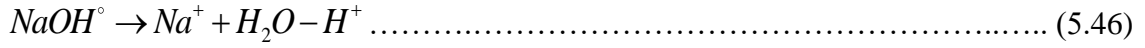
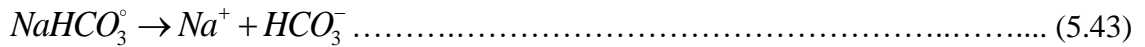
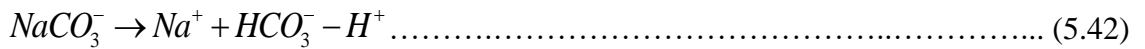
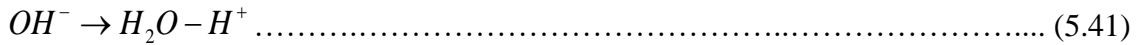
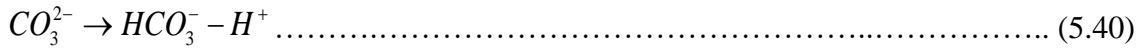
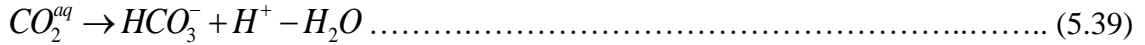


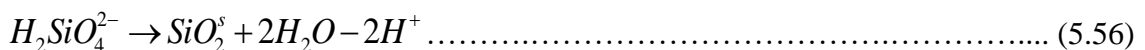
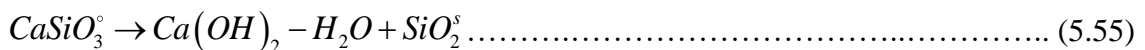
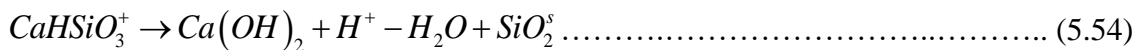
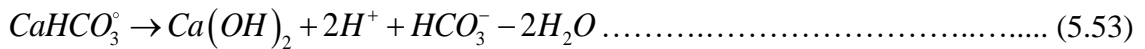
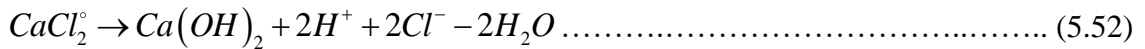
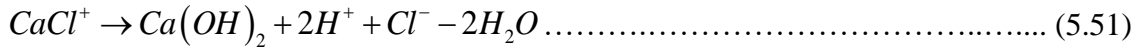
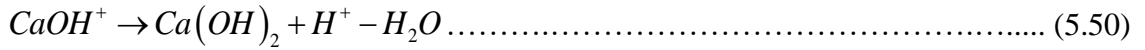
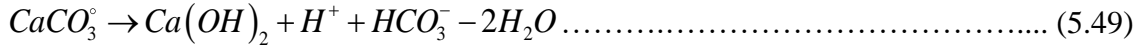
CO<sub>2</sub> is included to account for atmospheric CO<sub>2</sub> while NaCl accounts for the salt in solution. For the chemical system under consideration, **Table 5.2** shows the basis (primary) components and secondary species that are considered.

**Table 5.2 Initial components in Ca(OH)<sub>2</sub>-SiO<sub>2</sub>-CO<sub>2</sub>-NaCl-H<sub>2</sub>O chemical system**

Basis components	Secondary species
w: H <sub>2</sub> O i: H <sup>+</sup> , HCO <sub>3</sub> <sup>-</sup> , Cl <sup>-</sup> , Na <sup>+</sup> k: CH, CSH, SiO <sub>2</sub> <sup>s</sup>	j: CO <sub>2</sub> <sup>o</sup> , CO <sub>3</sub> <sup>2-</sup> , OH <sup>-</sup> , NaCO <sub>3</sub> <sup>-</sup> , NaHCO <sub>3</sub> <sup>o</sup> , NaCl <sup>o</sup> , HCl <sup>o</sup> , NaOH <sup>o</sup> , NaHSiO <sub>3</sub> <sup>o</sup> , Ca <sup>2+</sup> , CaCO <sub>3</sub> <sup>o</sup> , CaOH <sup>+</sup> , CaCl <sup>+</sup> , CaCl <sub>2</sub> <sup>o</sup> , CaHCO <sub>3</sub> <sup>+</sup> , CaHSiO <sub>3</sub> <sup>+</sup> , CaSiO <sub>3</sub> <sup>o</sup> , H <sub>2</sub> SiO <sub>4</sub> <sup>2-</sup> , H <sub>3</sub> SiO <sub>4</sub> <sup>-</sup> , H <sub>4</sub> SiO <sub>4</sub> <sup>o</sup> , HSiO <sub>3</sub> <sup>-</sup> , SiO <sub>3</sub> <sup>2-</sup> , SiO <sub>2</sub> <sup>o</sup>

Selection of the basis constituents is based on the components with known bulk composition. To obtain the governing equations, each secondary specie is expressed in terms of the components in the basis only. Thus, the governing equations are:





In equations 5.33 to 5.37 above,  $M_w$ ,  $M_i$ , and  $M_k$  are computed from the mass of water (typically equal to 1 kg, but is equal to the amount of pore water in this study), electron neutrality condition, amount of salt in solution and equation 5.11.  $v_w$ ,  $v_i$ ,  $v_j$ , and  $v_k$  are determined from the governing chemical reactions for the secondary species (equations 5.38 to 5.60).  $K_j$ ,  $\gamma_j$ , and  $a_w$  are temperature- and pressure-dependent; thus, they are determined from HKF (Helgeson-Kirkham-Flowers) model (Sverjensky et al., 1997; Shock et al., 1992; Shock et al., 1989; Shock and Helgeson, 1988) and Pitzer model



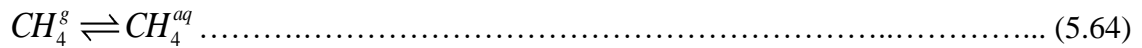
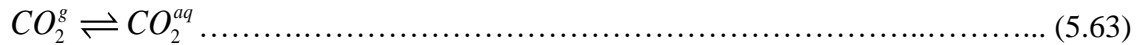
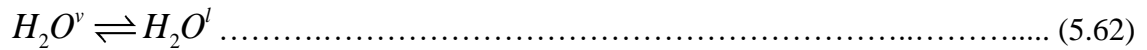
(Pitzer, 1973 and 1975; Møller, 1988; Millero, 1983).  $f_g$  is estimated from the gas-liquid phase equilibria model (presented in Section 5.4.2.1). Therefore, the only unknown parameters are  $n_w$ ,  $n_k$ ,  $m_i$ , and  $m_j$ . These parameters are evaluated through numerical solution of equations 5.33 to 5.37. In this study, the Newton-Raphson numerical technique is adopted.

As stated previously, CH, CSH and SiO<sub>2</sub> are the minerals in the initial chemical system. However, the collection of minerals in the chemical system changes as reaction progresses. This depends on whether or not the initial minerals dissolve and/or new minerals precipitate. As the aqueous species interact in the pore fluid, the status of these minerals must be evaluated in order to accurately predict the true state of chemical equilibrium. In a multi-component chemical system, minerals are in either undersaturated state or supersaturated state. Undersaturated minerals are the minerals with negative amounts which makes no practical sense. Supersaturated minerals are minerals that are ready to precipitate out of solution. If any mineral becomes undersaturated, it must be expunged from the system and the equilibrium state re-evaluated. Similarly, supersaturated minerals must be allowed to precipitate out of solution. The basis switching technique is often used by geochemist to switch undersaturated minerals out of solution and supersaturated minerals into solution. A true state of chemical equilibrium is reached when no mineral is undersaturated or supersaturated. At this state, all minerals in the chemical system constitute the stable mineral assemblage.

## 5.4.2 Modeling Cement Exposure to CO<sub>2</sub>-Saturated Brine in an HPHT Autoclave

### 5.4.2.1 Modeling Gas-Liquid Phase Equilibria in CO<sub>2</sub>-H<sub>2</sub>O<sup>v</sup>-CH<sub>4</sub> System

The fugacity and solubility of CO<sub>2</sub> gas are required inputs for modeling the bulk fluid chemistry. Under high temperature condition, water vaporizes thereby co-existing with the injected CO<sub>2</sub> and CH<sub>4</sub> in the headspace of the HPHT autoclave. At equilibrium between the gas phase and the liquid phase (bulk fluid), the following reactions occur:



The goal of modeling the gas-liquid phase equilibria is to determine the fugacity of H<sub>2</sub>O<sup>v</sup>, CO<sub>2</sub><sup>g</sup>, and CH<sub>4</sub><sup>g</sup> and the solubility of CO<sub>2</sub><sup>g</sup> and CH<sub>4</sub><sup>g</sup> (i.e. the concentration of CO<sub>2</sub><sup>aq</sup>, and CH<sub>4</sub><sup>aq</sup>). In a gas mixture, the fugacity coefficient of each gas is often determined from:

$$\ln \phi_g = \frac{b_g}{b_{mix}} (Z_{mix} - 1) - \ln(Z_{mix} - B_{mix}) - \frac{A_{mix}}{2\sqrt{2}B_{mix}} \left\{ \frac{2}{a_{mix}} \sum_{g_i, j} y_{g_i} a_{g_i - g_j} - \frac{b_g}{b_{mix}} \right\} \ln \left\{ \frac{Z_{mix} + (1 + \sqrt{2})B_{mix}}{Z_{mix} + (1 - \sqrt{2})B_{mix}} \right\}$$

..... (5.65)

where,  $a_{mix}$ ,  $b_{mix}$ ,  $b_i$ ,  $A_{mix}$ , and  $B_{mix}$  are defined as:

$$a_{mix} = \sum_{g_i}^N \sum_{g_j}^N y_{g_i} y_{g_j} \sqrt{a_{g_i} a_{g_j}} (1 - k_{g_i - g_j})$$

$$b_{mix} = \sum_g^N y_g b_g$$

$$A_{mix} = \frac{a_{mix} P}{(RT)^2}$$

$$B_{mix} = \frac{b_{mix} P}{RT}$$

$$a_g = 0.45724 \frac{(RT_{c,g})^2}{P_{c,g}} \left\{ 1 + (0.37464 + 1.54226\omega_g - 0.26992\omega_g^2) \left( 1 - \sqrt{\frac{T}{T_{c,g}}} \right) \right\}^2$$

$$b_g = 0.0778 \frac{RT_{c,g}}{P_{c,g}}$$

$\phi_g$  = fugacity coefficient of each gas component in the gas mixture.

$Z_{mix}$  = gas compressibility factor of the gas mixture.

$y_g$  = fraction of each gas component in the gas mixture.

The gas mixture compressibility factor is obtained from the numerical solution of the following equation:

$$Z_{mix}^3 - (1 - B_{mix})Z_{mix}^2 + (A_{mix} - 2B_{mix} - 3B_{mix}^2)Z_{mix} - (A_{mix}B_{mix} - B_{mix}^2 - B_{mix}^3) = 0 \dots\dots\dots (5.66)$$

For each gas in the gas mixture, the relationship between the gas fugacity coefficient and the gas fugacity is:

$$f_g = \phi_g y_g P \dots\dots\dots (5.67)$$

Since water vaporizes at high temperature, it co-exists with the injected gases to maintain pressure at the pre-set value. The vapor pressure of water at the temperature of interest is determined using the Antoine equation, which is expressed in equation 5.68. This pressure corresponds to the partial pressure of water vapor at the point of co-

existence with  $\text{CO}_2^g$  and  $\text{CH}_4^g$ . Thus, equation 5.69, 5.70, and 5.71 are the gas-phase fractions of water vapor, carbon dioxide gas, and methane gas respectively.

$$\log_{10} P_{vp} = A - \frac{B}{C + T} \quad (\text{T is measured in } ^\circ\text{C}) \dots\dots\dots (5.68),$$

where, A, B, and C are constants whose values are shown in **Table 5.3**. The unit of  $P_{vp}$  in equation 5.68 is torr.

**Table 5.3 Constants in Antoine equation**

A	B	C	Validity ( $^\circ\text{C}$ )
8.07131	1730.63	233.426	$1 \leq T \leq 99$
8.14019	1810.94	244.485	$100 \leq T \leq 374$

$$y_{\text{H}_2\text{O}^v} = \frac{P_{vp}}{P} \dots\dots\dots (5.69)$$

$$y_{\text{CO}_2^g} = r(1 - y_{\text{H}_2\text{O}^v}) \dots\dots\dots (5.70)$$

$$y_{\text{CH}_4^g} = (1 - r)(1 - y_{\text{H}_2\text{O}^v}) \dots\dots\dots (5.71),$$

where  $r$  is the composition of  $\text{CO}_2$  gas injected relative to the composition of  $\text{CH}_4$  gas.

The solubilities of  $\text{CO}_2^g$  and  $\text{CH}_4^g$  (i.e. the molality of  $\text{CO}_2^{\text{aq}}$ , and  $\text{CH}_4^{\text{aq}}$ ) are determined using the following abridged forms of equation 5.37.

$$m_j = \frac{f_m}{K_j \gamma_j} \quad (j = \text{CO}_2^{\text{aq}}, \text{CH}_4^{\text{aq}} \text{ and } m = \text{CO}_2^g, \text{CH}_4^g) \dots\dots\dots (5.72)$$

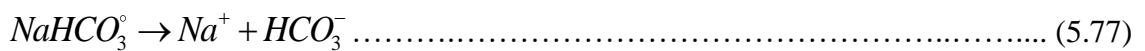
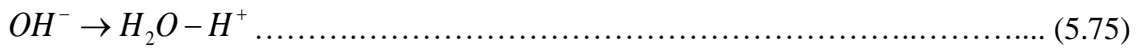
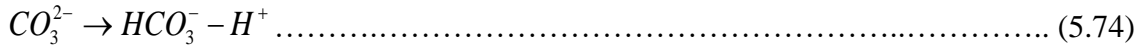
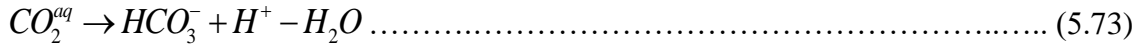
#### 5.4.2.2 Modeling Bulk Fluid Equilibria in $\text{CO}_2\text{-NaCl-H}_2\text{O}$ System

The physical model of the bulk fluid was described in Section 5.3. Hence, the following basis components and secondary species are considered (**Table 5.4**).

**Table 5.4 Components in CO<sub>2</sub>-NaCl-H<sub>2</sub>O chemical system**

Basis components	Secondary species
w: H <sub>2</sub> O i: H <sup>+</sup> , Cl <sup>-</sup> , Na <sup>+</sup> g: CO <sub>2</sub> <sup>g</sup>	j: CO <sub>2</sub> <sup>o</sup> , CO <sub>3</sub> <sup>2-</sup> , HCO <sub>3</sub> <sup>-</sup> , OH <sup>-</sup> , NaCO <sub>3</sub> <sup>-</sup> , NaHCO <sub>3</sub> <sup>o</sup> , NaCl <sup>o</sup> , NaOH <sup>o</sup>

The governing equation for each secondary specie are:



Equations 5.33 to 5.37 are applied to equations 5.72 to 5.79. The resulting equations are numerically solved to determine the molality of the aqueous species in the basis as well as the secondary species.

**5.4.2.3 Modeling Reactive Transport of Aqueous Species**

When cement comes into contact with aggressive fluid whose solutes (i.e. ions) concentration differ from the solutes concentration in the pore solution of the cement, solutes transport between the pore and bulk solutions is triggered due to concentration gradient. In the pore solution, chemical interactions occur among the solutes leading to the formation of secondary minerals and aqueous complexes. These

chemical interactions are limited by the transport of solutes between the two solutions. This results in a reactive transport phenomenon. For transport involving calcium ion, calcium-bearing hydrates in the cement matrix dissolves into pore solution to restore chemical equilibrium between the pore fluid and the solid matrix of the cement. Solute transport between the pore and bulk fluids is governed by the following equation:

$$\nabla_{\Omega} \cdot (\bar{D}_{m_{i,j}} \nabla_{\Omega} \cdot (m_{i,j})) - \bar{v} \nabla_{\Omega} \cdot (m_{i,j}) + R_{i,j} = \nabla_t \cdot (m_{i,j}) \dots\dots\dots (5.81),$$

where,

$\nabla_{\Omega}$  = divergent operator  $\nabla$  applied over the arbitrary domain  $\Omega$  in space

$\nabla_t$  = divergent operator  $\nabla$  applied over the time domain  $t$

$\bar{D}_{M_i}$  = effective diffusion coefficient of the mobile (aqueous) species in the basis

$m_{i,j}$  = Molality of the mobile species (i and j species)

$R_{i,j}$  = Reaction rate involving the mobile specie (positive for precipitation and negative for dissolution)

$\bar{v}$  = velocity of the bulk fluid

It is important to model the temperature field in the specimen because the reactions involved in cement degradation process are highly temperature-dependent, especially the computation of equilibrium constant  $K$ , fugacity and solubility of the injected gases. Equation 5.82 is the governing equation for temperature transport through the specimen.

$$\nabla_{\Omega} \cdot (\bar{D}_T \nabla_{\Omega} \cdot (T)) - \bar{v} \nabla_{\Omega} \cdot (T) = \nabla_t \cdot (T) \dots\dots\dots (5.82)$$

In this study,  $\Omega$  is a cylindrical domain (2D axisymmetric). In addition, the bulk fluid is static; hence, the velocity tensor  $\vec{v}$  is zero. Therefore, equations 5.80 and 5.81 become:

$$\nabla_{\Omega} \cdot (\vec{D}_{m_{i,j}} \nabla_{\Omega} \cdot (m_{i,j})) + R_{i,j} = \nabla_{r'} \cdot (m_{i,j}) \dots\dots\dots (5.83),$$

$$\nabla_{\Omega} \cdot (\vec{D}_T \nabla_{\Omega} \cdot (T)) = \nabla_{r'} \cdot (T) \dots\dots\dots (5.84)$$

The stable mineral assemblage after exposure to CO<sub>2</sub>-saturated brine is predicted using the Ca(OH)<sub>2</sub>-SiO<sub>2</sub>-CO<sub>2</sub>-NaCl-H<sub>2</sub>O system discussed in Section 5.4.1.4.

### 5.4.3 Modeling Mechanical Compression Test

Compressive strengths are predicted at two stages of the degradation process which include: strength before (i.e. after curing) and after CO<sub>2</sub> exposure test.

#### 5.4.3.1 Compressive Strength Model before CO<sub>2</sub> Exposure Test

Compressive strength development during cement curing is mostly affected by the degree of hydration and the water-to-cement ratio. In this study, a modified version of the strength model proposed by Powers (1958) is used.

$$\sigma_c = \sigma_{\infty} \left( \frac{0.71\alpha}{0.32\alpha + w/c} \right)^{13-16*(w/c)} \dots\dots\dots (5.85)$$

In equation 5.85,  $\sigma_{\infty}$  is the ultimate strength which is defined as (Maekawa et al. 2009):

$$\sigma_{\infty} = \frac{Ax_{C_3S} + Bx_{C_2S}}{x_{C_3S} + x_{C_2S}} x_{pc} + Cx_{SF} \dots\dots\dots (5.86),$$

where  $A$ ,  $B$  and  $C$  are material constants with values, 215 MPa, 250 MPa and 300 MPa respectively.  $x_{pc}$  and  $x_{SF}$  are weight fractions of Portland cement and silica flour, where  $x_c + x_{SF} = 1$ .  $x_{C_2S}$  and  $x_{C_3S}$  are volume fractions of C<sub>2</sub>S and C<sub>3</sub>S respectively.

### **5.4.3.2 Compressive Strength Models after CO<sub>2</sub> Exposure Test**

As reviewed in Chapter 2 (Section 2.4), previous strength models generally assume that mechanical strength deterioration is solely due to the loss of calcium from the solid matrix of cement. In this hypothesis, the distribution of solid-phase calcium in the invaded zone is correlated to the loss of strength. This assumption is reasonable if either secondary minerals are not formed during the degradation process or the secondary minerals dissolve after formation as the specimen traces its path toward chemical equilibrium. Therefore, two compressive strength models are developed. In the first model, it is assumed that secondary minerals, such as calcium carbonate, completely dissolve through leaching. In the second model, dimensional analysis is used to relate compressive strength to porosity, volume of the specimen, stress loading rate during compression test, and the average density of all minerals in cement after degradation.

#### **5.4.3.2.1 Model 1**

Carde et al. (1996) proposed a methodology for developing compressive strength models from solid-phase calcium profile in the leached zone of cement based on elasto-plasticity theory. Their model was developed for the case in which hardened cement is exposed to deionized non-acidic water. In this case, calcium leaching, through ionic diffusion, is the only mechanism of cement degradation. In the present study, the hardened cement is exposed to carbonated brine. Therefore, the specimen undergoes both carbonation and leaching with solid-phase calcium profile that is distinct from specimen that has undergone pure calcium leaching.

Consider a thin infinitesimal strip of thickness  $dx$ , located at distance  $x$  from the surface of the specimen and under the action of compressive stress  $\sigma_c$ , which is



distributed as  $\sigma_{c,x}$  as illustrated in **Figure 5.3**. In Figure 5.3a, zone 1 is the bi-carbonated and leached zone, zone 2 is the fully carbonated zone, zone 3 is the calcium-depleted zone, and zone 4 is the sound (unpenetrated) zone. In Figure 5.3b, however, the bi-carbonated and leached zone is masked by the fully carbonated zone (zone 1); thus, resulting in non-linear (power-law) behavior of the solid-phase calcium distribution. Zones 2 and 3 are the calcium-depleted and sound zones respectively. The axial force exerted on this strip under compression loading is:

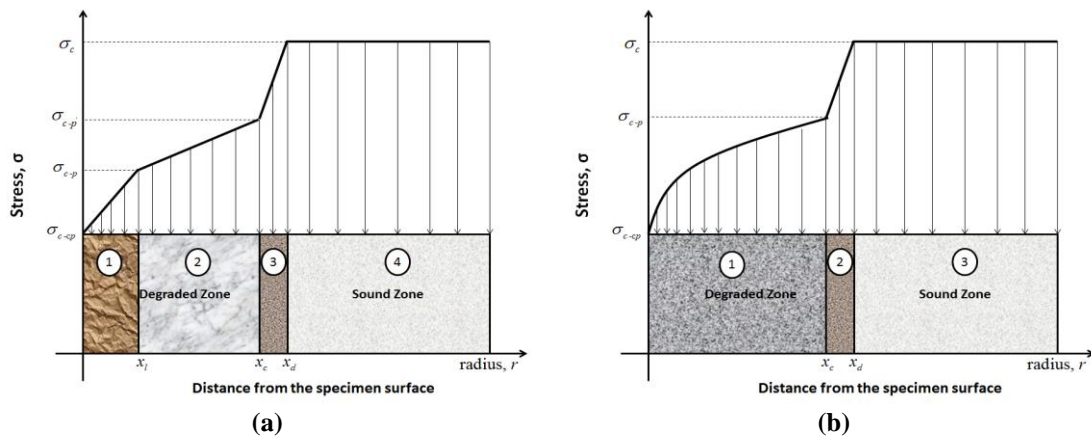
$$dF = \sigma_{c,x} dA \dots\dots\dots (5.87),$$

where,  $dA = 2\pi(r-x)dx$  and  $\sigma_{c,x}$  is a function of the degraded depth

Integrating both sides of equation 5.87, the total axial force gives:

$$F_T = \int_{x_1}^{x_2} dF = \int_{x_1}^{x_2} \sigma_{c,x} 2\pi(r-x) dx \dots\dots\dots (5.88),$$

Where,  $\sigma_{c,x}$  is the stress distribution.



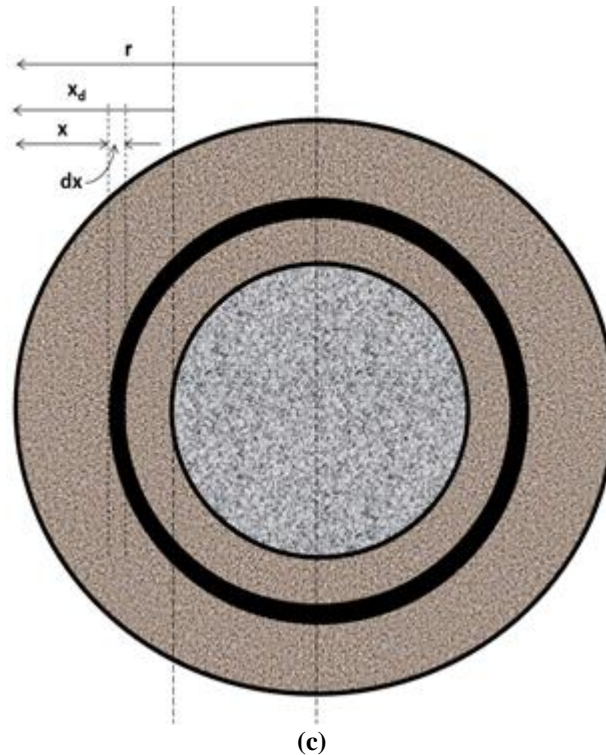


**Figure 5.3 (a) Typical profile of the solid-phase calcium in half section of the exposed specimen with bi-carbonated and leached zone distinct from the fully carbonated zone; (b) typical profile of the solid-phase calcium in half section of the exposed specimen with bi-carbonated and leached zone masked by the fully carbonated zone; (c) physical model of the degraded zone**

For the unexposed specimen,  $\sigma_{c,x}$  is evenly-distributed (i.e. constant) and is equal to  $\sigma_c$  since no degraded zone exist and solid-phase calcium is evenly-distributed throughout the specimen. Using equation 5.88, it is shown in the appendix that the axial force exerted on this specimen is:

$$F_T = \sigma_c \pi r^2 \dots\dots\dots (5.89)$$

For the exposed specimen, the distribution of stress aligns with the solid-phase calcium profile since degraded zones exist. For Figure 5.3a, it is shown in the appendix that the degraded strength ratio, ratio of the change in the axial force after exposure to the axial force of the unexposed specimen, is:

$$\frac{\Delta F}{F_T} = 1 - \frac{1}{\pi r^2} \left( \frac{F_1}{\sigma_c} + \frac{F_2}{\sigma_c} + \frac{F_3}{\sigma_c} + \frac{F_4}{\sigma_c} \right) \dots\dots\dots (5.90),$$

where,

$$\frac{F_1}{\sigma_c} = \frac{\pi}{3x_l} \left\{ (R_p - R_{cp}) (3rx_l^2 - 2x_l^3) + 3R_p x_l (2rx_l - x_l^2) \right\}$$

$$\frac{F_2}{\sigma_c} = \frac{\pi}{3(x_c - x_l)} \left[ (R'_p - R_p) \left\{ 3r(x_c^2 - x_l^2) - 2(x_c^3 - x_l^3) \right\} + 3(R_p x_c - R'_p x_l) \left\{ 2r(x_c - x_l) - (x_c^2 - x_l^2) \right\} \right]$$

$$\frac{F_3}{\sigma_c} = \frac{\pi}{3(x_d - x_c)} \left[ (1 - R'_p) \left\{ 3r(x_d^2 - x_c^2) - 2(x_d^3 - x_c^3) \right\} + 3(R'_p x_d - x_c) \left\{ 2r(x_d - x_c) - (x_d^2 - x_c^2) \right\} \right]$$

$$\frac{F_4}{\sigma_c} = \pi \left[ 2r(r - x_d) - (r^2 - x_d^2) \right]$$

The corresponding equation for Figure 5.3b is:

$$\frac{\Delta F}{F_T} = 1 - \frac{1}{\pi r^2} \left( \frac{F_1}{\sigma_c} + \frac{F_2}{\sigma_c} + \frac{F_3}{\sigma_c} \right) \dots \dots \dots (5.91),$$

where,

$$\frac{F_1}{\sigma_c} = \frac{\pi}{3x_c} \left\{ (R_p - R_{cp}) \left( \frac{6r}{n+1} x_c^2 - \frac{6}{n+2} x_c^3 \right) + 3R_{cp} x_c (2rx_c - x_c^2) \right\}$$

$$\frac{F_2}{\sigma_c} = \frac{\pi}{3(x_d - x_c)} \left[ (1 - R_p) \left\{ 3r(x_d^2 - x_c^2) - 2(x_d^3 - x_c^3) \right\} + 3(R_p x_d - x_c) \left\{ 2r(x_d - x_c) - (x_d^2 - x_c^2) \right\} \right]$$

$$\frac{F_3}{\sigma_c} = \pi \left[ 2r(r - x_d) - (r^2 - x_d^2) \right]$$

$x_c$  = carbonated depth

$x_l$  = leached depth

$x_d$  = degraded depth

$x_c$ ,  $x_l$ , and  $x_d$  are determined from the solid-phase calcium profile generated from the  $\text{Ca}(\text{OH})_2\text{-SiO}_2\text{-CO}_2\text{-NaCl-H}_2\text{O}$  system. Other variables are defined in the nomenclature.

### 5.4.3.2.2 Model 2

In this model, dissolution of calcium carbonate is assumed to be gradual so that its contribution to strength development can be investigated. The model accounts for porosity reduction in the penetrated zone. **Figure 5.4** illustrates the typical distribution of solid minerals after exposure to carbonic acid environment. Due to the complexity of solid-phase calcium distribution after cement is exposed to carbonic acid, a compressive strength model is developed using dimensional analysis. The model relates compressive strength to porosity ( $\phi$ ), sample volume ( $V$ ), stress loading rate ( $\dot{r}$ ), and average density ( $\rho_{cem}$ ) of minerals in cement. The choice of these parameters as the independent variables in the strength model is based on the common knowledge in solid mechanics that the stress-strain response of rigid materials (e.g. rocks) is influenced by these parameters. Therefore,

$$\sigma_c = \frac{k\rho_{cem}^a}{\phi V^b \dot{r}^c} \dots\dots\dots (5.92),$$

where,

$$\rho_{cem} = \frac{\sum_{k=1}^N n_k M_{w,k}}{\sum_{k=1}^N V_k} \dots\dots\dots (5.93),$$

$$a = \frac{1}{3}, b = -\frac{2}{9}, \text{ and } c = -\frac{2}{3} \text{ (from dimensional analysis)}$$

$$k = \alpha x^2 + \beta x + \gamma \text{ (}\alpha, \beta, \text{ and } \gamma \text{ are determined from experiment)}$$

$N$  = Total number of minerals (primary and secondary) after degradation

$n_k$  = residual mole number of each mineral, determined from equation 4.35 (mol)

$M_{w,k}$  = molar weight of each mineral ( $\text{kgmol}^{-1}$ )

$V_k$  = volume of each mineral, computed in each mesh during numerical simulation (kg)

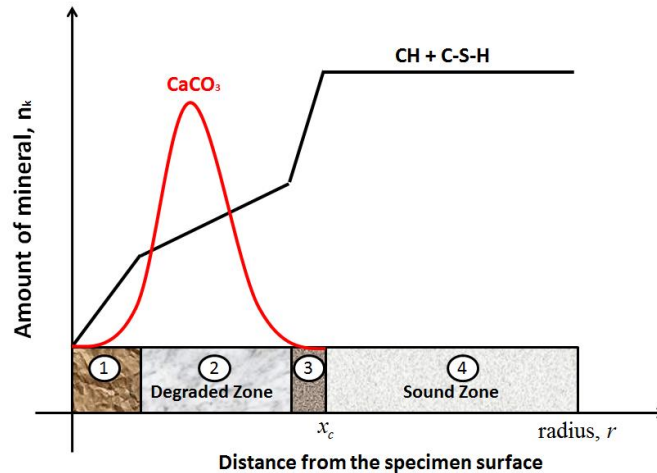


Figure 5.4 Typical distribution of solid minerals in cement exposed to carbonic acid

## 5.5 Model Results and Validation

### 5.5.1 Degree of Hydration and Chemical Shrinkage

The overall degree of hydration and chemical shrinkage were computed using the model described in Section 5.4.1.1. The input data were taken from Section 4.2.1 and Tables 2.2 and 4.1. **Figure 5.5a** shows the model predictions for the degrees of hydration and chemical shrinkage using the clinker compositions presented in Table 4.1. Since the clinker compositions, Blaine fineness, and water-to-cement ratio differ in the two classes of cement, about 56% of Class H was hydrated while about 65% of the clinker compounds in Class G reacted with water (Fig 5.6a). Similarly, Class H cement shrinks by about 5% while Class G cement shrinks by about 5.4%. **Figure 5.5b** compares the degrees of hydration and chemical shrinkage of both classes of cement when the clinker compositions and Blaine fineness of Class G is used for Class H but only the water-to-cement ratio is different. Under this condition, nearly 62% of Class H cement is hydrated with chemical shrinkage of about 5.5%. This underscores the significance of variability in the composition of cement from the manufacturer. Duguid (2009) and Taylor (1997) noted that only about 70% degree of hydration is possible in 28 days of curing. Thus, the

low degree of hydration predicted for Class H cement is mainly due to the short period of curing and the less amount of water available to facilitate hydration of clinker materials.

Three stages of hydration are identified in the plot for the degree of hydration (Figure 5.5b). Stage 1 is the slow induction period, Stage 2 is the acceleration period, and Stage 3 is the slow reaction period. The induction period is characterized with low heat evolution and gradual nucleation of hydration products (i.e. CH and CSH). The cement begins to set during the acceleration period and early compressive strength development begins with accelerating growth of principal product of hydration (i.e. CSH). At the late stage, gradual densification of microstructure around residual un-hydrated  $C_3S$  and CH re-crystallization occur (Bensted and Barnes, 2002).

In Figure 5.5a, Class G cement attained ultimate degree of hydration at approximately 120 hours. However, only about 50% of cementitious materials in Class H cement has hydrated after this time. Model validation was conducted using experimental data originally published by Lerch and Ford (1948) and reported by Lin and Meyer (2009). The model predictions appear to reasonably match the experimental data (Figure 5.6).

As noted in Section 3.2 of Chapter 3, the rates of hydration differ in the clinker compounds;  $C_3S$  and  $C_3A$  hydrate faster than  $C_2S$  and  $C_4AF$ . XRD analysis presented in Section 4.3.1.3.1 confirms this because  $C_3S$  and  $C_3A$  were completely hydrated while unhydrated  $C_2S$  and  $C_4AF$  were identified by XRD. Therefore, the overall degrees of hydration predicted above are applied to  $C_2S$  and  $C_4AF$  only.  $C_3S$  and  $C_3A$  are assumed to be completely hydrated.

## 5.5.2 Composition of Cement after Hydration

The information provided by the manufacturers of the cement used in this study (Table 4.1) does not indicate the presence of gypsum. Calcium monosulfoaluminate was not identified by XRD either (Section 4.3.1.3.1). However, katoite was detected by XRD. Thus, equation 5.11 and 5.30b are used to estimate the amount of hydrates and other components after curing. **Table 5.5** summarizes the results for different values of  $\alpha$ . The quantities of CH and CSH produced by both classes of cement are almost the same but the amount of extra water is higher in Class G than Class H.

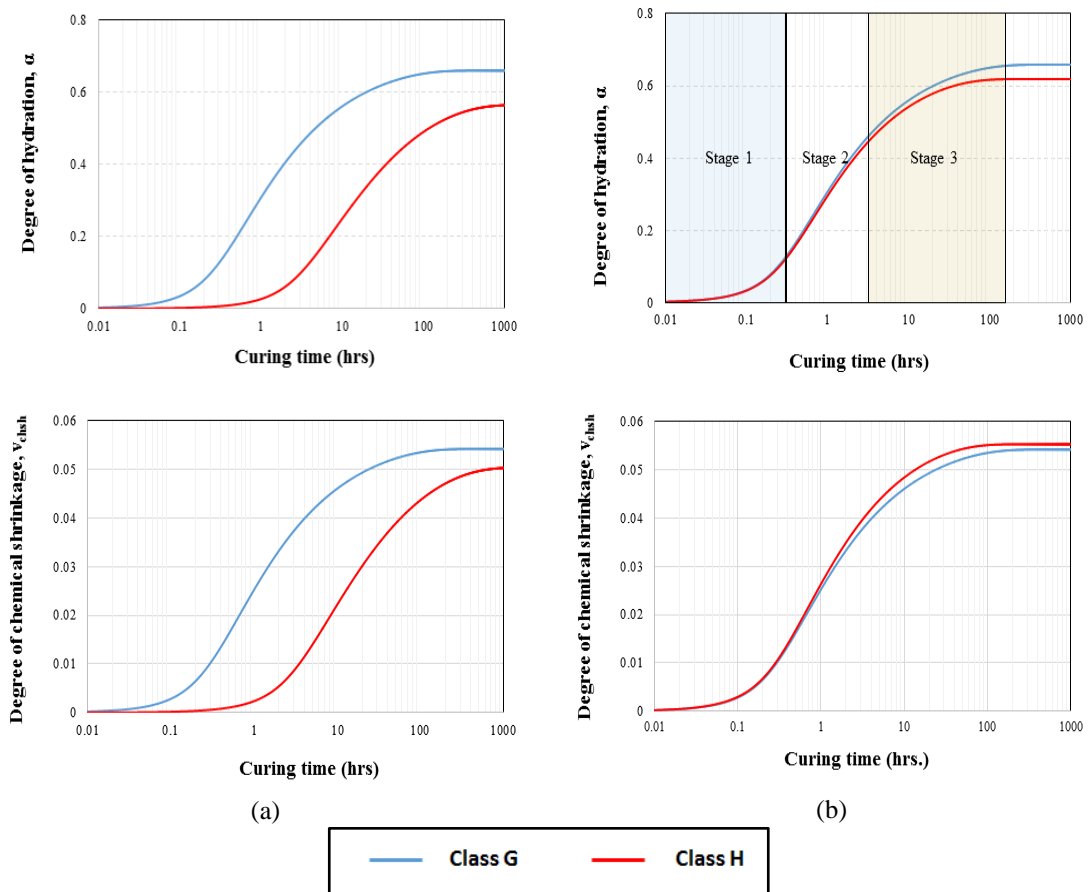


**Figure 5.5** Model predictions for the degrees of hydration and chemical shrinkage of cement: (a) with clinker compositions in Table 4.1; (b) with clinker composition of Class H the same as Class G

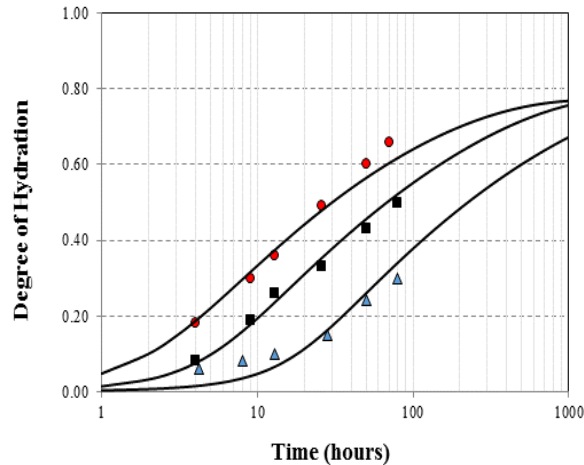


Figure 5.6 Validation of hydration model with experimental data

Table 5.5 Quantity of hydrates after hydration of cement

Before hydration			After hydration				
Components	Mole numbers		Components	Mole numbers			
	Class G	Class H		Case 1: $\alpha$ in Section 5.6.1		Case 2: $\alpha = 100\%$	
				Class G	Class H	Class G	Class H
H	21.00	18.14	H	10.86	8.95	9.56	6.49
C <sub>3</sub> S	2.18	2.21	CSH	1.39	1.36	1.54	1.61
C <sub>2</sub> S	0.90	1.01	CH	3.70	3.72	3.92	4.11
C <sub>3</sub> A	0.19	0.01	C <sub>3</sub> AH <sub>6</sub>	0.32	0.16	0.39	0.30
C <sub>4</sub> AF	0.19	0.29	FH <sub>3</sub>	0.13	0.15	0.19	0.29
SiO <sub>2</sub>	5.01	5.01	SiO <sub>2</sub>	5.01	5.01	5.01	5.01

Table 5.6 shows the composition by weight of all compounds, including the unhydrated compounds, after 5 days of curing. In the presence of 35% BWOC silica flour, CSH and CH make up approximately 58% (Case 1) and 64% (Case 2) in both classes of cement. Without silica flour, however, these hydrates constitute approximately 76% of the products of hydration (48% CSH and 28% CH) for Case 1 and 84% of the products of hydration (54% CSH and 30% CH) for Case 2. The typical compositions of CSH and CH in hardened cement paste are 50 to 70% and 20 to 25% respectively (Duguid, 2008;



Nelson, 1990). As noted in Section 2.2.1 (Chapter 2), 70-85% is the range widely adopted for the total composition of both hydrates. Thus, the model prediction is satisfactory. CSH and CH are the major compounds produced after hydration and the exclusion of katoite and hydrated iron (II) oxide in the chemical degradation model is reasonably justified.

**Table 5.6 Composition of chemical compounds after curing**

<b>Case 1 in Table 5.5</b>							
<b>Class G</b>					<b>Class H</b>		
	<b>Molar wt. (gmol<sup>-1</sup>)</b>	<b>Mole number (mol)</b>	<b>Weight (g)</b>	<b>Composition by wt. (%)</b>	<b>Mole number (mol)</b>	<b>Weight (g)</b>	<b>Composition by weight (%)</b>
C <sub>3</sub> S	228.31	0.00	0.00	0.00	0.00	0.00	0.00
C <sub>2</sub> S	172.23	0.31	53.39	4.15	0.50	86.12	6.64
C <sub>3</sub> A	270.19	0.00	0.00	0.00	0.00	0.00	0.00
C <sub>4</sub> AF	485.96	0.07	33.96	2.64	0.15	72.89	5.62
CSH	342.21	1.39	475.67	36.97	1.36	465.41	35.88
CH	74.02	3.70	273.87	21.29	3.72	275.35	21.23
C <sub>3</sub> AH <sub>6</sub>	378.05	0.32	120.98	9.40	0.16	64.27	4.95
FH <sub>3</sub>	213.75	0.13	27.79	2.16	0.15	32.06	2.47
SiO <sub>2</sub>	60.08	5.01	301.00	23.39	5.01	301.00	23.21
Total		1286.66			1297.10		
<b>Case 2 in Table 5.5</b>							
<b>Class G</b>					<b>Class H</b>		
	<b>Molar wt. (gmol<sup>-1</sup>)</b>	<b>Mole number (mol)</b>	<b>Weight (g)</b>	<b>Composition by wt. (%)</b>	<b>Mole number (mol)</b>	<b>Weight (g)</b>	<b>Composition by weight (%)</b>
C <sub>3</sub> S	228.31	0.00	0.00	0.00	0.00	0.00	0.00
C <sub>2</sub> S	172.23	0.00	0.00	0.00	0.50	0.00	0.00
C <sub>3</sub> A	270.19	0.00	0.00	0.00	0.00	0.00	0.00
C <sub>4</sub> AF	485.96	0.00	0.00	0.00	0.15	0.00	0.00
CSH	342.21	1.54	527.00	40.35	1.61	550.96	41.38
CH	74.02	3.92	290.16	22.21	4.11	304.22	22.85
C <sub>3</sub> AH <sub>6</sub>	378.05	0.39	147.44	11.29	0.30	113.42	8.52
FH <sub>3</sub>	213.75	0.19	40.61	3.11	0.29	61.99	4.66
SiO <sub>2</sub>	60.08	5.01	301.00	23.04	5.01	301.00	22.60
Total		1306.22			1331.60		

### 5.5.3 Transport and Mechanical Properties before CO<sub>2</sub> Exposure

From Table 5.5, the extra water in Class G cement is 10.86 moles while Class H cement contains 8.95 moles of extra water. Using equations 5.22 and 5.23, the initial porosity and permeability estimated for Class G is 28% and 0.036 mD, respectively. For Class H, the estimates are 26% and 0.038 mD. **Figure 5.7a** shows that the model predictions match the measured values reasonably. For permeability, comparison between model prediction and experimental data is shown in **Figure 5.7b**.

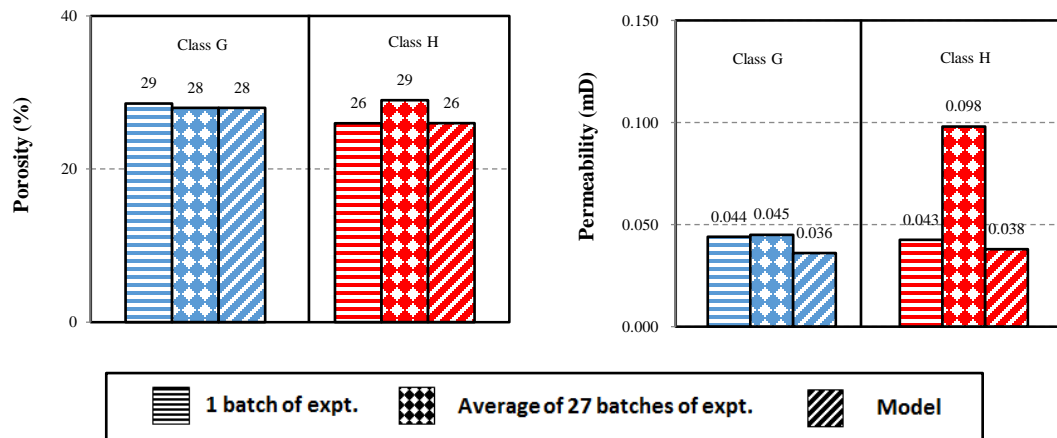


Figure 5.7 Validation of transport properties model with experimental data: (a) porosity; (b) permeability

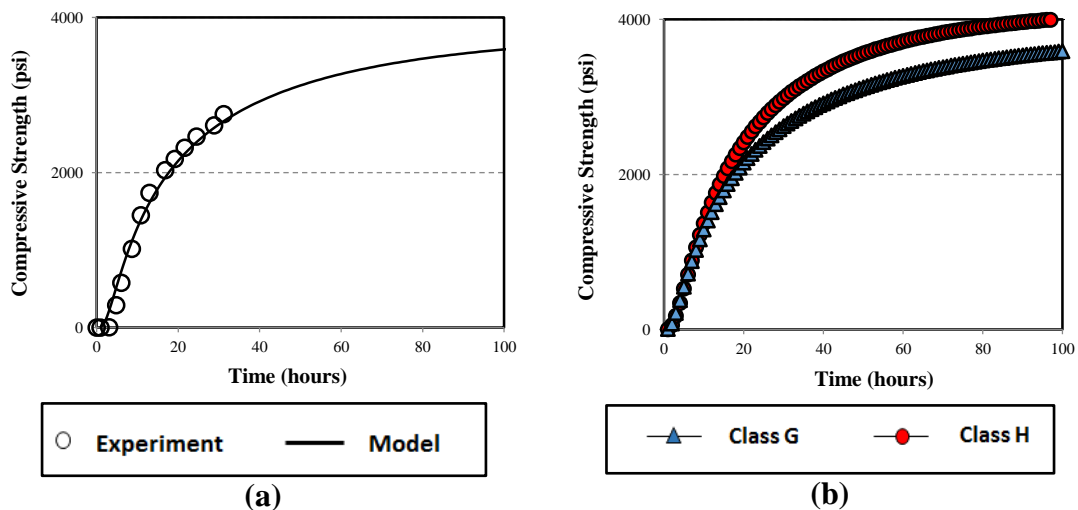


Figure 5.8 Comparison between: (a) model prediction and experimental data from previous study (Voigt and Shah, 2003); (b) model predictions for Classes G and H cement

The compressive strength model presented in Section 5.4.3.1 is used to predict compressive strength development during the curing process. **Figure 5.8a** compares the model prediction with literature data at w/c ratio of 0.5 (Voigt and Shah, 2003). The match between the model and experimental measurement is satisfactory. Furthermore, comparison is made between model predictions for Classes G and H cement (**Figure 5.8b**). Clearly, the initial strength after curing Class H cement is higher than the strength of Class G cement, although less degree of hydration was attained. **Figure 5.9** shows the model prediction and the average compressive strength of unaged specimens of Classes G and H cement that were presented in Chapter 4. The model reasonably predicts the experimental data.

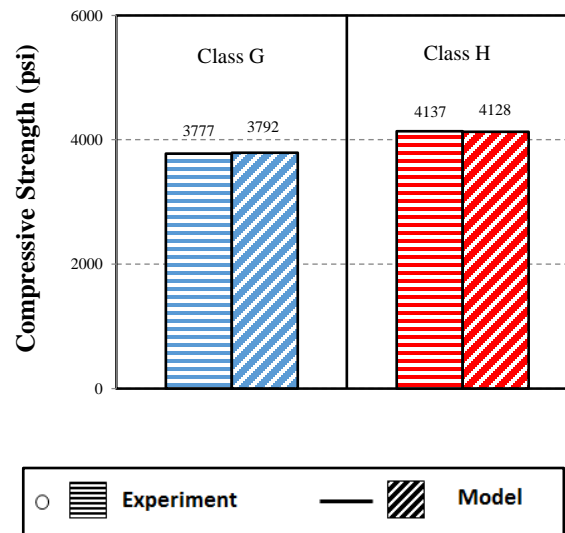


Figure 5.9 Comparison between model prediction and experimental data from this study

#### 5.5.4 Stable Mineral Assemblage and Pore Chemistry after Curing

Using the curing temperature and pressure condition, equations 5.33 to 5.37 are applied to the governing chemical reactions (equations 5.38 to 5.60). The molality of the primary and secondary species in Table 5.2 are computed by solving the resulting

equations with Newton-Raphson numerical scheme until the solution converges to  $1 \times 10^{-20}$  tolerance. Three minerals are included in the basis components, which include CH, CSH, and SiO<sub>2</sub>. The initial amount of these minerals are shown in Table 5.5. The quantity of extra water for each class of cement is used as the initial amount of pore water before the commencement of equilibration. **Table 5.7** shows the pH, molality (concentration) of aqueous species in the pore water and the residual amount of minerals. The amount of these components represent the initial conditions before commencement of reactive transport during CO<sub>2</sub> experiment. Many authors (Duguid, 2009; Kutchko et al., 2007; Berner, 1992; Reardon, 1992) have reported that the pH of the pore water in cement is between 11 and 14. These studies were either conducted at lower temperature or fewer components were included in the chemical system. The following six case studies are investigated to understand the effects of solid-phase compounds and temperature on the pH of pore water and to ascertain whether the pH value of 9.82 is truly reasonable.

Case 1: Without dissolved carbonate, only CH at 77°F (25°C) and 14.5 psi (1 bar)

Case 2: Without dissolved carbonate, only CH at 200°F (93°C) and 14.5 psi (1 bar)

Case 3: Without dissolved carbonate, only SiO<sub>2</sub> at 200°F and 14.5 psi

Case 4: Without dissolved carbonate, both CH and SiO<sub>2</sub> at 77°F and 14.5 psi

Case 5: Without dissolved carbonate, both CH and SiO<sub>2</sub> at 200°F and 14.5 psi

Case 6: With dissolved carbonate from atmospheric CO<sub>2</sub>, both CH and SiO<sub>2</sub> at 200°F and 14.5 psi

**Table 5.8** shows the results. Therefore, the pH in the present study (Table 5.7) is out of the range reported by previous investigators because of the high curing temperature adopted in this study (200°F) and the addition of silica to the baseline cement.

**Table 5.7 Concentration of species in the pore water of cement and the amount of minerals**

<b>Components in the pore fluid chemical system</b>	<b>Class G</b>	<b>Class H</b>
pH	9.82	9.82
<b>Concentration of species in the pore fluid (mol/kg)</b>		
H <sup>+</sup>	1.52E-10	1.52E-10
HCO <sub>3</sub> <sup>-</sup>	1.33E-08	1.33E-08
Na <sup>+</sup>	1.63E-01	1.62E-01
Cl <sup>-</sup>	2.86E-01	2.86E-01
CO <sub>2</sub> <sup>aq</sup>	4.53E-12	4.53E-12
CO <sub>3</sub> <sup>2-</sup>	7.27E-09	7.28E-09
OH <sup>-</sup>	2.92E-03	2.92E-03
Ca <sup>2+</sup>	8.53E-02	8.53E-02
CaCO <sub>3</sub> <sup>aq</sup>	6.49E-06	6.49E-06
CaOH <sup>+</sup>	3.07E-02	3.07E-02
CaHCO <sub>3</sub> <sup>+</sup>	2.79E-08	2.79E-08
NaCO <sub>3</sub> <sup>-</sup>	4.36E-09	4.36E-09
NaHCO <sub>3</sub> <sup>aq</sup>	1.95E-09	1.95E-09
NaCl <sup>aq</sup>	1.52E-02	1.52E-02
NaOH <sup>aq</sup>	3.58E-04	3.58E-04
CaCl <sup>+</sup>	3.53E-02	3.53E-02
CaCl <sub>2</sub> <sup>aq</sup>	2.41E-03	2.41E-03
NaHSiO <sub>3</sub> <sup>aq</sup>	1.64E-01	1.64E-01
CaHSiO <sub>3</sub> <sup>+</sup>	1.03E-01	1.03E-01
CaSiO <sub>3</sub> <sup>+</sup>	2.51E-01	2.51E-01
H <sub>2</sub> SiO <sub>4</sub> <sup>2-</sup>	6.96E-05	6.96E-05
H <sub>3</sub> SiO <sub>4</sub> <sup>-</sup>	1.53E-01	1.53E-01
H <sub>4</sub> SiO <sub>4</sub> <sup>aq</sup>	1.15E-02	1.15E-02
HSiO <sub>3</sub> <sup>-</sup>	5.79E-02	5.79E-02
SiO <sub>3</sub> <sup>2-</sup>	5.76E-04	5.76E-04
SiO <sub>2</sub> <sup>aq</sup>	8.58E-03	8.58E-03
<b>Mole number of minerals (mole)</b>		
CH	3.19	3.21
CSH	1.38	1.36
SiO <sub>2</sub>	4.26	4.26

**Table 5.8 Effect of temperature and the presence of silica in the pH of pore water**

	Case 1	Case 2	Case 3	Case 4	Case 5	Case 6
pH	12.38	10.50	5.05	11.67	9.82	9.82

### 5.5.5 Gas Fugacity and Solubility

The model described in Section 5.4.2.1 is implemented using the test conditions in Table 4.4. **Table 5.9** shows the fugacity of water vapor ( $f_{H_2O}$ ),  $CO_2$  gas ( $f_{CO_2}$ ), and  $CH_4$  gas ( $f_{CH_4}$ ). Generally, the fugacity of  $CO_2$  gas (i.e. the effective partial pressure of  $CO_2$  gas after injection) is substantially lower than its mechanical partial pressure. However, this pressure mostly increases with temperature, total test pressure, and  $CO_2$  gas composition. In addition, vapor pressure generally increases with temperature, but decreases with total test pressure and  $CO_2$  gas composition.

**Figure 5.10** compares the mutual solubility of carbon dioxide and methane gases at 50% compositions of each gas. In general,  $CO_2$  gas is about 8 times more soluble than  $CH_4$  gas; hence, the effect of its dissolved component on bulk fluid chemistry is neglected in this study. Therefore, as noted previously in Chapter 4,  $CO_2$  is the major driver of the chemical degradation of cement. The presence of  $CH_4$  gas merely helps to boost and sustain pressure during the  $CO_2$  exposure test.

**Table 5.9 Model prediction for the fugacity of water vapor,  $CO_2$  gas, and  $CH_4$  gas**

Expt. No.	T (°F)	P (psi)	$CO_2$ (%)	$CH_4$ (%)	$f_{H_2O}$ (psi)	$f_{CO_2}$ (psi)	$f_{CH_4}$ (psi)
1	100	6,000	10	90	0.05	232	3780
2	100	6,000	40	60	0.03	744	2719
3	100	6,000	100	0	0.01	1484	0
4	225	3,000	10	90	6.44	216	2373
5	225	3,000	40	60	5.46	805	1622
6	225	3,000	100	0	3.44	1866	0
7	225	6,000	10	90	3.35	378	4705

8	225	6,000	40	60	2.56	1350	3264
9	225	6,000	100	0	1.36	3010	0
10	225	9,000	10	90	2.35	556	7450
11	225	9,000	40	60	1.72	1945	5203
12	225	9,000	100	0	0.91	4281	0
13	350	3,000	10	90	67.76	243	2475
14	350	3,000	40	60	62.69	942	1677
15	350	3,000	100	0	53.23	2290	0
16	350	6,000	10	90	44.70	472	5166
17	350	6,000	10	90	44.70	472	5166
18	350	6,000	10	90	44.70	472	5166
19	350	6,000	40	60	38.80	1776	3531
20	350	6,000	100	0	28.68	4208	0
21	350	9,000	10	90	34.92	721	8282
22	350	9,000	40	60	29.27	2667	5688
23	350	9,000	100	0	20.52	6228	0
24	430	3,000	100	0	171.42	2315	0
25	430	6,000	10	90	144.64	497	5210
26	430	6,000	40	60	131.40	1909	3548
27	430	6,000	100	0	108.41	4632	0
28	430	9,000	100	0	82.93	7075	0

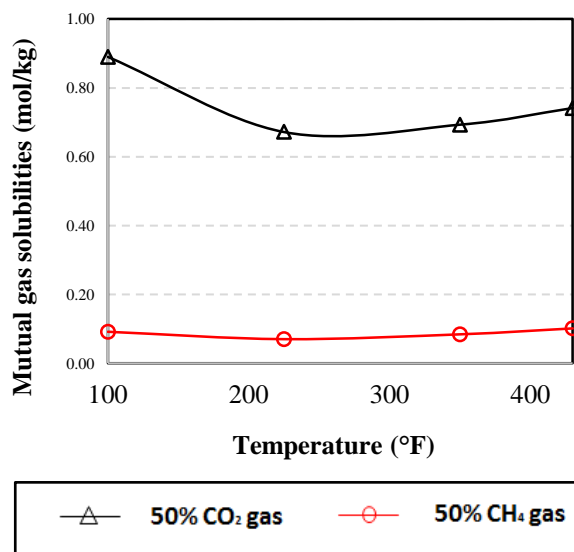
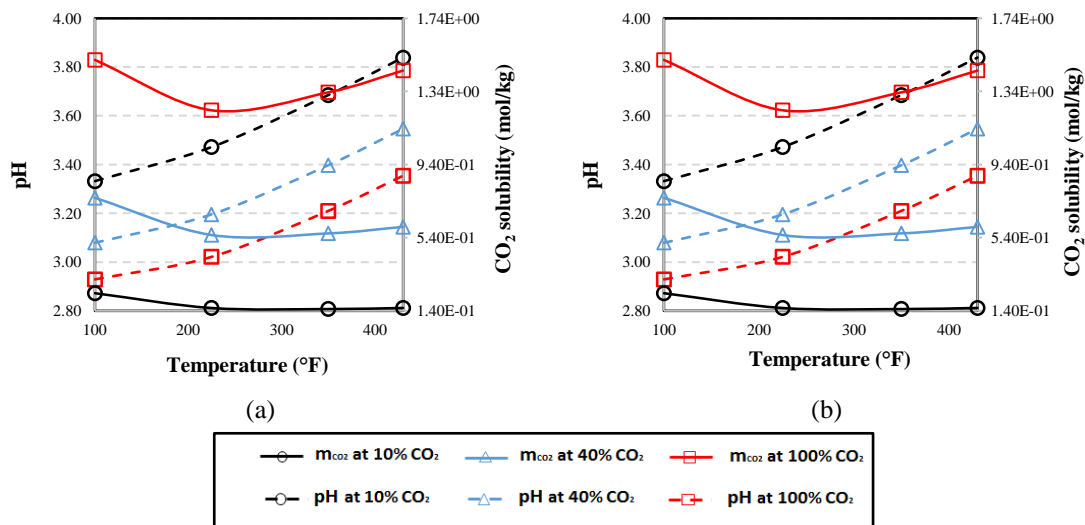


Figure 5.10 Comparison of the mutual solubility of CO<sub>2</sub> and CH<sub>4</sub> gases in 2% NaCl solution

## 5.5.6 Molality of Bulk Fluid Aqueous Species

Using the fugacity of CO<sub>2</sub> gas presented in Table 5.9, the model presented in Section 5.4.2.2 is implemented and the bulk fluid pH and molality (concentration) of aqueous species are determined at the different test conditions presented in Table 4.4. **Figure 5.11** presents the effects of temperature and pressure at different CO<sub>2</sub> gas composition on the pH of the bulk fluid and the solubility of CO<sub>2</sub> gas in 2% NaCl solution ( $m_{CO_2}$ ). The trends mostly agree with Duan and Sun's model (Section 3.9). As expected, increase in CO<sub>2</sub> gas composition and total test pressure increases the strength of the carbonic acid (bulk fluid) due to increasing CO<sub>2</sub> gas solubility. However, it is intriguing that the bulk fluid is less acidic as temperature increases, with a dramatic increase in sharpness above 200-250°F. This, perhaps, explains why carbonation of cement specimens was dominant at low temperature. Normally, the pH of pure water decreases as temperature increases, not because water becomes more acidic at elevated temperature, but due to a shift in equilibrium position (Le Châtelier's Principle) thereby increasing the equilibrium constant of water ( $K_w$ ).



**Figure 5.11** Fluid pH and solubility of CO<sub>2</sub> gas ( $m_{CO_2}$ ) in 2% NaCl solution: (a) effect of temperature at 6000 psi; (b) effect of pressure at 350°F



**Table 5.10** presents the concentrations of aqueous species for some of the test conditions (experiments 3, 9, 20, and 27). These concentrations constitute the initial boundary condition at the outer surface of the exposed specimen. Thus, the initial condition in the specimen (Table 5.7) and the boundary condition at the surface of the specimen (i.e. bulk fluid) are used to solve the reactive transport model presented in Section 5.4.2.3. At the boundary, the initial concentration of species such as  $\text{Ca}^{2+}$ ,  $\text{CaCO}_3^{\text{aq}}$ ,  $\text{CaOH}^+$ ,  $\text{CaHCO}_3^+$ , etc. is zero. At each computational time step, minerals are allowed to precipitate and dissolve without violating the constitutive laws presented in Section 5.4.1.4. The problem is solved in a cylindrical (2D axisymmetric) domain and the results are presented in Section 5.6.1.7.

**Table 5.10 Concentration of aqueous species in the bulk fluid**

Components in the bulk fluid chemical system	Expt. 3	Expt. 9	Expt. 20	Expt. 27
<b>pH</b>	<b>2.93</b>	<b>3.02</b>	<b>3.21</b>	<b>3.35</b>
$\text{H}^+$	1.18E-03	9.52E-04	6.17E-04	4.43E-04
$\text{Cl}^-$	3.25E-01	3.10E-01	2.78E-01	2.43E-01
$\text{Na}^+$	3.25E-01	3.10E-01	2.77E-01	2.42E-01
$\text{CO}_2^{\text{aq}}$	1.51E+00	1.24E+00	1.33E+00	1.45E+00
$\text{CO}_3^{2-}$	8.13E-11	1.01E-10	4.79E-11	2.00E-11
$\text{HCO}_3^-$	1.01E-03	7.40E-04	3.77E-04	2.09E-04
$\text{OH}^-$	3.04E-11	1.08E-09	9.77E-09	2.47E-08
$\text{NaCO}_3^-$	3.13E-10	8.18E-11	1.32E-11	3.32E-12
$\text{NaHCO}_3^{\text{aq}}$	1.69E-04	2.13E-04	2.39E-04	2.34E-04
$\text{NaCl}^{\text{aq}}$	1.71E-02	3.21E-02	6.41E-02	9.92E-02
$\text{NaOH}^{\text{aq}}$	5.80E-12	2.38E-10	2.54E-09	7.27E-09

### 5.5.7 Mineral Assemblage and Pore Chemistry after $\text{CO}_2$ Exposure

The transport of aqueous species between the bulk and pore fluids is implemented in Comsol Multiphysics software while the computation of mineral

assemblage is executed in Matlab. **Figure 5.12** shows a picture of the cut section of an exposed specimen and the typical distribution of some species in the pore solution. Formation of  $\text{CaCO}_3$  is expected in the outer zone, where the concentrations of  $\text{Ca}^{2+}$  and  $\text{HCO}_3^-$  overlaps.

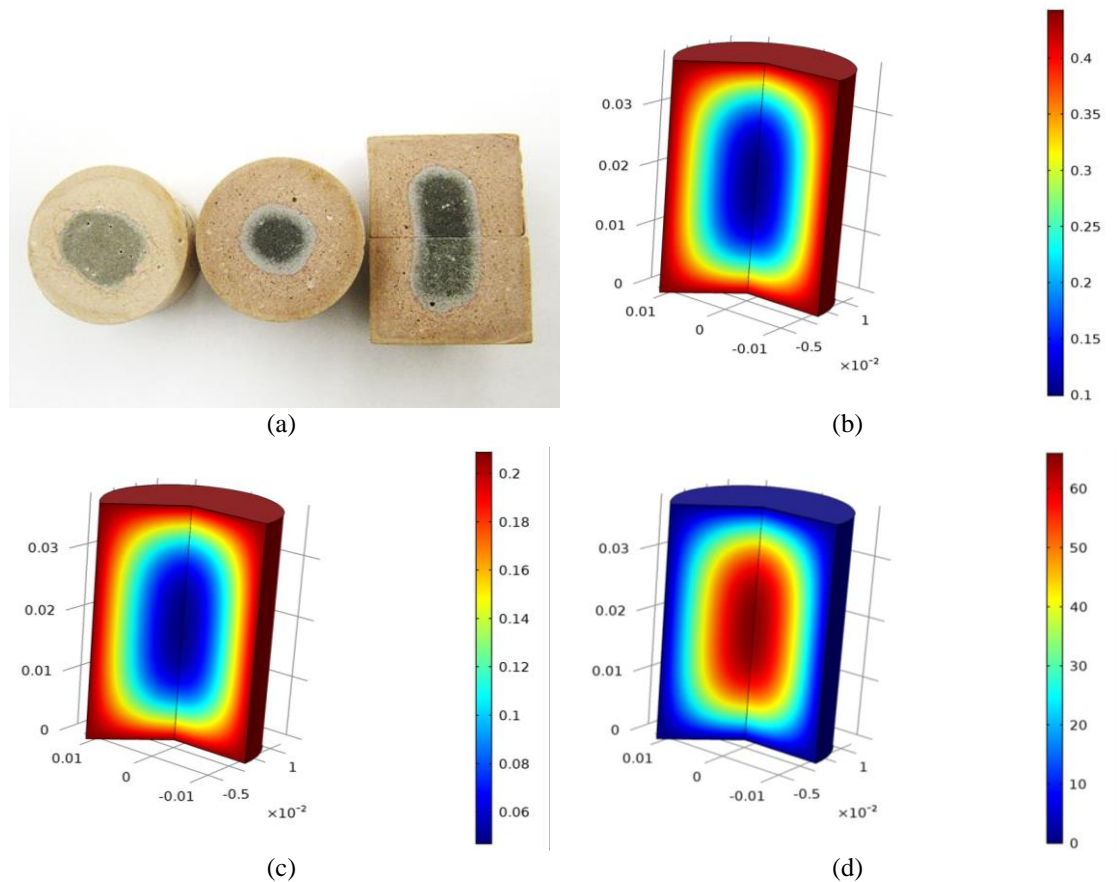


**Figure 5.12** (a) Cut section of exposed specimen; and typical concentration of aqueous species ( $\text{mol/m}^3$ ) after solute transport between the bulk and the pore fluids: (b)  $\text{H}^+$ ; (c)  $\text{HCO}_3^-$ ; (d)  $\text{Ca}^{2+}$

The effect of water-to-cement ratio on solid phase calcium is presented in **Figure 5.13a**. With less water requirement, Class H is more  $\text{CO}_2$  resistant than Class G. This agrees with experimental observation noted by Bruckdorfer (1986). Therefore, Class H cement, with the same clinker composition as Class G cement but different amount of mixing water, will typically show better mechanical strength as previously noted in Chapter 4. Similar study conducted for composition of  $\text{CO}_2$  gas shows deeper penetration

of acid as the composition of CO<sub>2</sub> gas increases (**Figure 5.13b**); thus, resulting in chemical degradation. The chemical degradation is due to the shift in equilibrium position in response to increased production of carbonic acid, which result in dissolution of precipitated calcite. Besides, temperature effect was also investigated (**Figure 5.13c**). Although the precipitation of calcite is likely at temperatures below 200-250°F, as previously discussed in Section 3.9.1 (Chapter 3), the dissolution of calcium hydroxide into pore solution decreases with temperature; hence, the degree of carbonation is minimized. Similarly, less dissolution of portlandite limits further corrosion of cement by carbonic acid at higher temperature, although dissolution of calcite is more likely to occur at high temperature due to shift in equilibrium. This further explains the mixed trend in experimental data presented in Chapter 4 for temperature effect study.

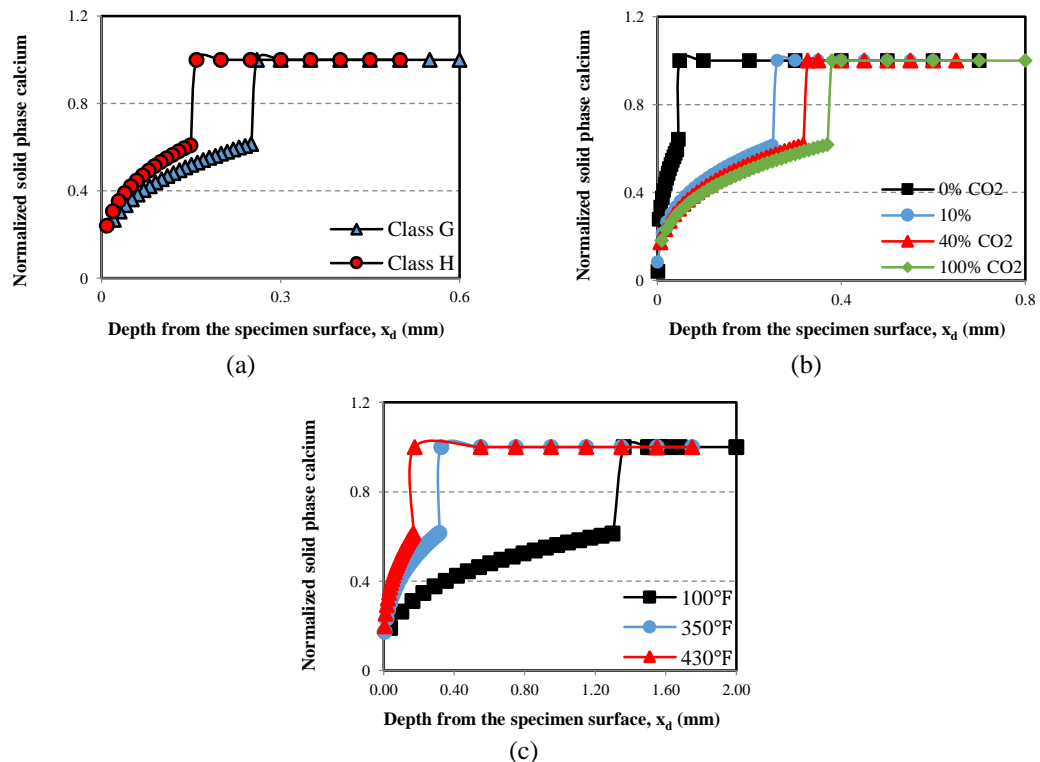


**Figure 5.13** (a) comparison between the solid-phase calcium profiles of Classes G and H cement at 6000 psi, 350°F, and 10% CO<sub>2</sub>; (b) CO<sub>2</sub> gas composition effect on the solid-phase calcium profile of Class G cement at 6000 psi and 350°F; (c) temperature effect on the solid-phase calcium profile of class G cement at 6000 psi and 40% CO<sub>2</sub>

**Figure 5.14a** shows the residual amounts of calcium in the solid phase (cement hydrates) and the calcium carbonate produced. This plot shows that the amount of calcium carbonate produced by Class H cement is higher than Class G cement. Also, the residual amount of calcium in the solid-phase of the cement is higher. This is attributed to the lower porosity in this class of cement, which limits further ingress of dissolved  $\text{CO}_2$  since the calcium carbonate produced from initial carbonation forms a protective layer. Effect of the alteration in the original solid phase composition on porosity is shown in **Figure 5.14b**. This model prediction supports the analysis presented in Chapter 4 that carbonation results in decrease in porosity while bicarbonation and leaching leads to increase in porosity. Thus, the higher amount of carbonate, in addition to the residual cementitious materials, account for the improved strength in Class H cement.

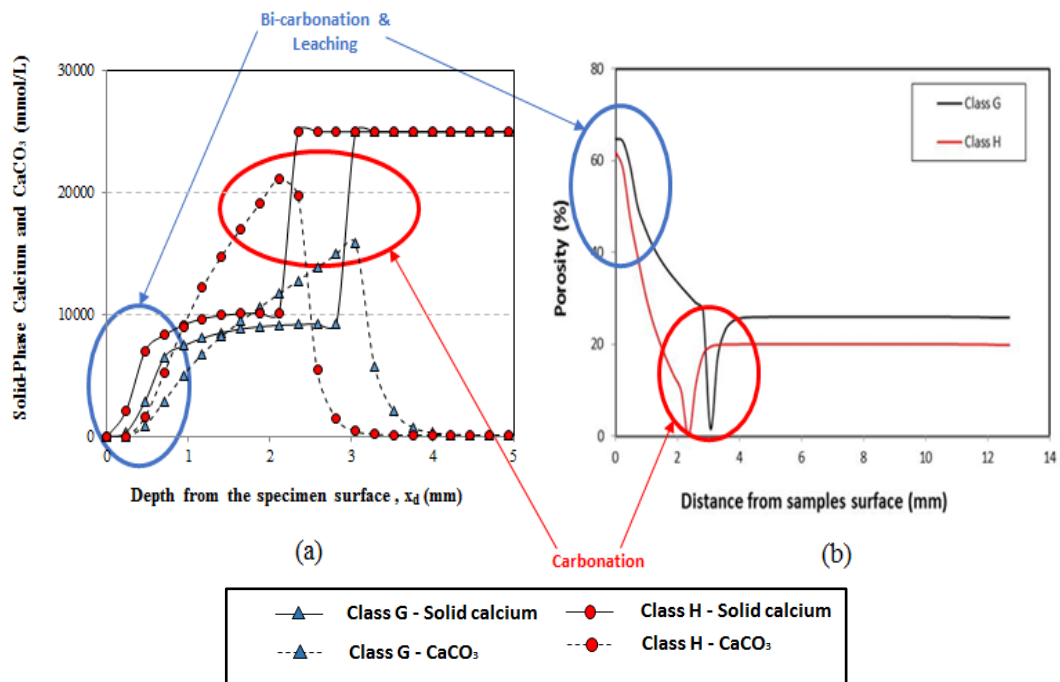


**Figure 5.14 (a)** model prediction of the solid-phase calcium from the residual cement hydrates and calcium carbonate after cement is exposed to carbonated-brine; **(b)** model prediction of the evolution of porosity after cement is exposed to carbonated-brine

## 5.5.8 Mechanical Strength after CO<sub>2</sub> Exposure

Compressive strength after exposure of specimens to CO<sub>2</sub> is predicted using the models presented in Section 5.4.3.2 (Models 1 and 2). Model validation is performed by comparing model predictions to experimental measurements presented in Chapter 4 for the effects of total test pressure and CO<sub>2</sub> gas composition on cement degradation. **Figure 5.15a** shows the experimental measurements and model predictions for pressure effect at 10% CO<sub>2</sub> and 350°F on Class G cement. The trend predicted by the model (Model 1) shows acceptable agreement with the overall trend of the experimental data. As test pressure increases, the model predicts a progressive reduction in strength while the measurement shows slight improvement in strength between 3000 and 6000 psi. This difference could be due to the assumption used in formulating the strength model or data scattering, which is inherent in compressive strength measurements of degraded cement. Since the strength model used in this prediction assumes that any secondary mineral formed during the degradation process is completely dissolved before the specimen attains chemical stability, the trend predicted by the model shows the dominance of leaching over carbonation. Thus, the overall effect of varying test pressure is the loss of mechanical strength, resulting from the increased solubility of CO<sub>2</sub> in brine. For the CO<sub>2</sub> gas composition effect, the model adequately predicts the trend in experimental measurement up to 40% CO<sub>2</sub> gas composition (**Figure 5.15b**). At 100% CO<sub>2</sub>, the effect of carbonation was not captured. As a result of this limitation, the model could not satisfactorily predict the compressive strength of Class H cement because the general trend of the strength measurement for this class of cement shows an overriding effect of carbonation over leaching.

To validate the model presented in Section 5.4.3.2.2 (Model 2), two experimental case studies with evidence of both carbonation and leaching are used (Figure 5.16). The first case study is presented in Figure 5.16a, which shows the effect of test pressure on mechanical degradation at 100% CO<sub>2</sub> and 430°F. The second case study, presented in Figure 5.16b, shows comparison between the model prediction and experimental measurements for CO<sub>2</sub> gas composition effect at 6000 psi and 430°F. In both cases, the match between model predictions and experimental measurements is very reasonable.

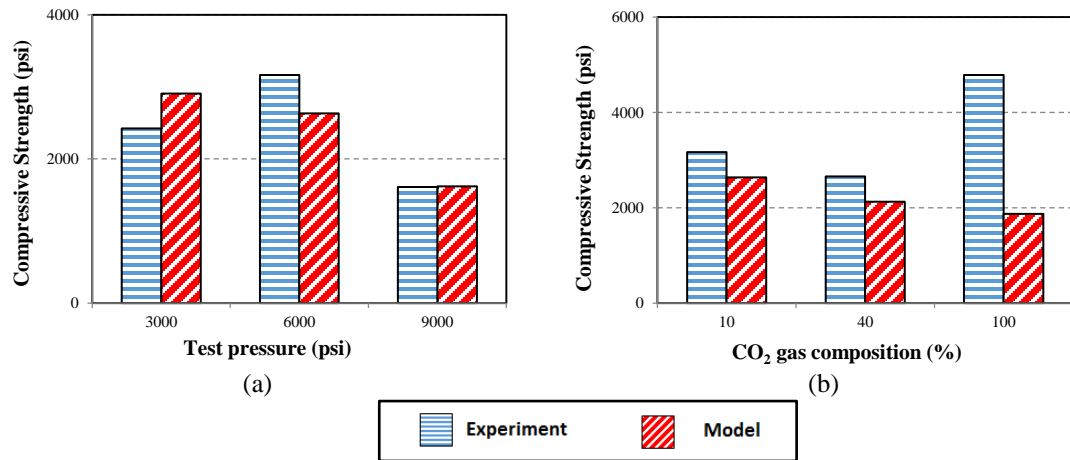


Figure 5.15 Comparison between model predictions and experimental measurements for Class G cement: (a) pressure effect at 10% CO<sub>2</sub> and 350°F; and (b) CO<sub>2</sub> effect at 6000 psi and 350°F

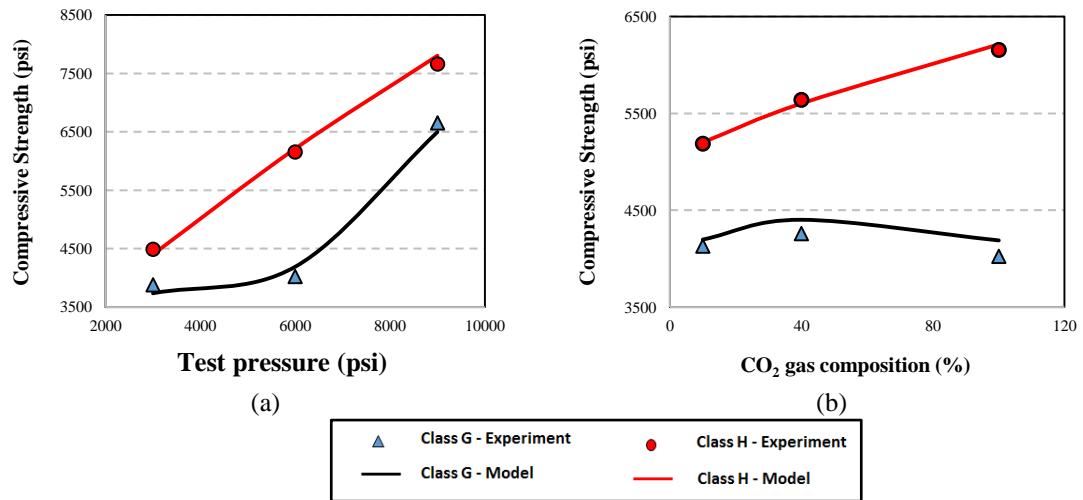


Figure 5.16 Comparison between model predictions and experimental measurements for Classes G and H cement: (a) pressure effect at 100% CO<sub>2</sub> and 430°F; and (b) CO<sub>2</sub> effect at 6000 psi and 430°F

## Chapter 6 Conclusions and Recommendations

### 6.1 Conclusions

The following are the major findings in this research:

1. Before exposure of cement to carbonated-brine, analysis of mineralogy shows that the clinker materials were incompletely hydrated; the hydration of  $C_3S$  is believed to be the major factor responsible for the initial development of mechanical strength. Relative to calcium silicate hydrate, evidence from mineralogy shows that portlandite is the most consumed as downhole parameters increases. Calcium silicate hydrate is predominantly preserved for the retention of strength. In some cases, the calcium silicate hydrate is either transformed to its crystalline polymorphs or incompletely carbonated to form calcium silicate carbonate.
2. When  $CO_2$  is dissolved in brine, the carbonic acid formed results in the degradation of oil well cement and subsequent corrosion of casing. Several mechanisms are involved but carbonation and leaching are the two major competing mechanisms, with the consumption of portlandite and calcium silicate hydrate in both cases. In most scenarios that were investigated, cement carbonation was dominant even though some level of leaching was observed. Under HPHT condition, structural transformation of uncarbonated C-S-H at elevated temperature also contributes to mechanical behavior.
3. The effect of temperature on the mechanical behavior of well cement shows mixed trend. Generally, strength increases with temperature up to 225°F and 350°F mainly due to carbonation of cement hydrates. This implies that the rate of attack is maximum between 225°F and 430°F. At 430°F, the loss of strength is minimized, especially in Class G cement, due to reduction in solubility of CH and C-S-H.

4. CO<sub>2</sub> gas composition shows insignificant influence on mechanical degradation at low temperature, although the specimens were chemically degraded. At elevated temperature, however, incremental gain in strength occurs due to the progressive carbonation of cement hydrates. In most cases that were investigated, cement carbonation was the dominant mechanism of degradation.

5. Variation in total test pressure facilitate the rate of acid attack on cement due to the increase in CO<sub>2</sub> solubility as pressure increases. Carbonation of cement hydrates and leaching of the resulting carbonate are the major drivers. Carbonation dominates at low to moderately high pressures (up to 6,000 psi), but leaching counterbalances the effect of carbonation at higher pressure.

6. Generally, the outcome of this study suggests that pressure and CO<sub>2</sub> gas composition have marginal influence on the degradation on cement in carbonic acid environment relative to temperature. Thus, temperature seems to be the most critical downhole condition that determines the performance of well cement after placement behind the casing.

7. Class H cement, as formulated in this study, demonstrates better structural integrity for casing support and zonal isolation than Class G cement after exposure to carbonic acid attack. Predominately, it exhibited increase in compressive strength and reduction in porosity and permeability after the exposure. Modeling and simulation of the curing process shows that less degree of hydration is attained in Class H cement due to the lower amount of mixing water used to prepare the slurry; hence, it is less porous and stronger than Class G.



8. In most cases investigated, comparison of model predictions with experimental data shows reasonable agreement.

## **6.2 Recommendations**

1. As previously noted, overall assessment of the mechanical behaviour of Class H cement after exposure to CO<sub>2</sub>-saturated brine under HPHT conditions shows that it demonstrates improved performance than Class G cement. However, there is strong evidence that both classes of cement were chemically degraded. Thus, Class H cement is recommended for further use with additives to explore the possibilities of engineering CO<sub>2</sub>-resistant cement.

2. In drilling applications, cement is placed behind the casing to seal off the annulus while drilling progresses and during the operational life of the well, even after the well has been abandoned. The analyses presented in this study are based on experiments that were conducted over short durations. Experimental investigations over long durations of exposure are recommended, as this may further expand the knowledge base in cement corrosion. For the most part, however, the analyses are consistent with observation from field retrieval of cement that had been exposed to CO<sub>2</sub> for 30 years (Carey et al., 2007).

3. Recent advances in cementing technology has shown the potential of high alumina cement and resin-based cement as possible replacement for conventional Portland-based cement. However, reliable data on the performance of these emerging cementing applications under extreme downhole conditions are presently unavailable or scarce. Extensive laboratory studies are recommended.

## Nomenclature

A	$\text{Al}_2\text{O}_3$
API	American Petroleum Industry
ASTM	American Society for Testing and Materials
BWOC	By Weight of Cement
BWOSF	By weight of silica flour
C	CaO
$\text{CaCO}_3$	Calcium carbonate
$\text{C}_3\text{A}$	Tricalcium aluminate, $3\text{CaO} \cdot \text{Al}_2\text{O}_3$ or $\text{Ca}_3\text{Al}_2\text{O}_6$
$\text{C}_4\text{AF}$	Tetracalcium aluminoferrite, $4\text{CaO} \cdot \text{Al}_2\text{O}_3 \cdot \text{Fe}_2\text{O}_3$ or $\text{Ca}_4\text{Al}_2\text{Fe}_2\text{O}_{10}$
CCS	Carbon Capture and Storage
CCUS	Carbon Capture, Utilization, and Storage
CH	Calcium hydroxide or portlandite, $\text{Ca}(\text{OH})_2$
$\text{CO}_2$	Carbon dioxide
$\text{C}_3\text{S}$	Tricalcium silicate, $3\text{CaO} \cdot \text{SiO}_2$ or $\text{Ca}_3\text{SiO}_5$
$\text{C}_2\text{S}$	Dicalcium silicate, $2\text{CaO} \cdot \text{SiO}_2$ or $\text{Ca}_2\text{SiO}_4$
CSH	Calcium silicate hydrate, $3\text{CaO} \cdot 2\text{SiO}_2 \cdot 3\text{H}_2\text{O}$
C-S-H	CSH and its polymorphs
C-S-C	Calcium silicate carbonate
DAQ	Data acquisition
EDTA	Ethylenediaminetetraacetic
EDX	Energy-dispersive X-ray
EOR	Enhanced Oil Recovery

F	Fe <sub>2</sub> O <sub>3</sub>
FTIR	Fourier Transform Infra-Red
H	H <sub>2</sub> O
HEC	Hydroxyl Ethyl Cellulose
MIT	Massachusetts Institute of Technology
NaCl	Sodium Chloride
NETL	National Energy Technology Laboratory
SEM	Scanning Electron Microscopy
XRD	X-Ray Diffraction
NMR	Nuclear Magnetic Resonance spectroscopy
S	SiO <sub>2</sub>
<i>t</i>	Time from commencement of degradation process
<i>D</i>	Effective diffusion coefficient
<i>C<sub>s</sub></i>	Specie concentration in solid phase
<i>Blaine</i>	Cement fineness
<i>α</i>	Degree of hydration
<i>E<sub>a</sub></i>	Activation energy
<i>R</i>	Universal gas constant
<i>w/c</i>	Water-to-cement ratio
<i>ε</i>	Dimensionless variable
<i>ξ<sub>d</sub></i>	Dimensionless degraded depth
<i>x<sub>d</sub></i>	Degraded depth
<i>x<sub>c</sub></i>	Carbonated depth

$x_l$	Leached depth
$x_{pc}$	Weight fraction of Portland cement
$x_{SF}$	Weight fraction of silica flour
$x_{C_2S}$	Volume fraction of C <sub>2</sub> S
$x_{C_3S}$	Volume fraction of C <sub>3</sub> S
$\sigma_\infty$	Ultimate strength
$v_{chsh}$	Chemical shrinkage
$T$	Absolute Temperature, K
$P$	Total pressure, bar
$y$	Mole fraction
$m$	Molality
$M$	Molar number
$\varphi$	Fugacity coefficient
$\sigma_1$	Peak stress
$\sigma_3$	Confining stress
$r$	Radius of cement specimen
$\sigma_c$	Initial uniform stress in sample
$\sigma_{c-p}$	First intermediate stress in the leached zone
$\sigma_{c-cp}$	Minimum stress in the leached zone
$\sigma_{c-p'}$	Second intermediate stress in the leached zone
$\sigma_c$	Stress in sound zone

## References

- 9<sup>th</sup> Annual HPHT Wells Summit: HPHT World Map and Developments. (2013). Retrieved from <http://www.hphtwells.com>.
- 11<sup>th</sup> Annual HPHT Wells Summit: High Pressure High Temperature, High Costs, High Stakes? (2015). Retrieved from <http://www.hphtwells.com>.
- Adamson, K., Birch, G., Gao, E., Hand, S., Macdonald, C., Mack, D., Quadri, A., 1998. High-Pressure, High-Temperature Well Construction. *Oilfield Review*: 36-49.
- Aiex, C., Campos, G., Deshpande, A., Chiney, A., Patil, S., & Ravi, K. (2015). An Experimental Study on Effects of Static CO<sub>2</sub> on Cement under High-Pressure/High-Temperature Conditions. *Offshore Technology Conference*. doi:10.4043/25659-ms.
- Alawode, O., & Idowu, O. I. (2011). Effects of Water-Cement Ratios on the Compressive Strength and Workability of Concrete and Lateritic Concrete Mixes. *The Pacific Journal of Science and Technology*, 12(2), pp. 99-105.
- Alnes, H., Eiken, O., Nooner, S., Sasagawa, G., Stenvold, T., & Zumberge, M. (2011). Results from Sleipner gravity monitoring: Updated density and temperature distribution of the CO<sub>2</sub> plume. *Energy Procedia*, 4, 5504–5511. doi:10.1016/j.egypro.2011.02.536.
- API Specification 10A (1995). Specification for cements and materials for well cementing (twenty second edition). American Petroleum Institute.
- API RP 10B (1997). Recommended practice for testing well cements. American Petroleum Institute.
- ASTM C39/C39M-12 (2012). Standard Test Method for Compressive Strength of Cylindrical Concrete Specimens. West Conshohocken, PA: ASTM.
- Baciu, D., & Simitzis, J. (2007). Synthesis and Characterization of a Calcium Silicate Bioactive Glass. *Journal of Optoelectronics and Advanced Materials*, 9, 3320-3324.
- Backe, K. R., Skalle, P., Lile, O. B., Lyomov, S. K., Justnes, H., & Sveen, J. (1998). Shrinkage of Oil Well Cement Slurries. *Journal of Canadian Petroleum Technology*, 37(09), 63-67. doi:10.2118/98-09-06.
- Backe, K. R., Lile, O. B., & Lyomov, S. K. (2001). Characterizing Curing Cement Slurries by Electrical Conductivity. *SPE Drilling & Completion*, 16(04), 207–207. doi:10.2118/74694-pa.

- Barlèt-Gouédard, V., Rimmelé, G., Goffé, B., & Porcherie, O. (2006). Mitigation Strategies for the Risk of CO<sub>2</sub> Migration Through Wellbores. Proceedings of IADC/SPE Drilling Conference. doi:10.2523/98924-ms.
- Barlèt-Gouédard, V., Rimmelé, G., Porcherie, O., Quisel, N., & Desroches, J. (2009). A solution against well cement degradation under CO<sub>2</sub> geological storage environment. *International Journal of Greenhouse Gas Control*, 3(2), 206–216. doi:10.1016/j.ijggc.2008.07.005.
- Baumgarte, C., Thiercelin, M., & Klaus, D. (1999). Case Studies of Expanding Cement to Prevent Microannular Formation. Proceedings of SPE Annual Technical Conference and Exhibition. doi:10.2523/56535-ms.
- Bearden, W. G. (1959). Effect of Temperature and Pressure on the Physical Properties of Cement. In *Oil Well Cementing Practices in the United States*. New York: American Petroleum Institute.
- Beirute, R., & Tragesser, A. (1973). Expansive and Shrinkage Characteristics of Cements Under Actual Well Conditions. *Journal of Petroleum Technology*, 25(08), 905–909. doi:10.2118/4091-pa.
- Bensted, J., & Barnes, P. (2002). *Structure and Performance of Cements*, Second Edition. London and New York: Spon Press.
- Bentz, D. P. (2006). Influence of Water-to-Cement Ratio on Hydration Kinetics: Simple Models Based on Spatial Considerations. *Cement and Concrete Research*, 36(2), 238–244. doi:10.1016/j.cemconres.2005.04.014
- Berner, U. R. (1988). Modelling the Incongruent Dissolution of Hydrated Cement Minerals. *Radiochimica Acta*, 44-45(2), 387-394. doi:10.1524/ract.1988.4445.2.387.
- Berner, U. R. (1992). Evolution of Pore Water Chemistry During Degradation of Cement in a Radioactive Waste Repository Environment. *Waste Management*, 12(2-3), 201–219. doi:10.1016/0956-053x(92)90049-o.
- Bethke, C. M., 2008. *Geochemical and Biogeochemical Reaction Modeling*, Second Edition. Edinburgh: Cambridge University Press.
- Bolio-Arceo, H., & Glasser, F. P. (1990). Formation of Spurrite, Ca<sub>5</sub>(SiO<sub>4</sub>)<sub>2</sub>CO<sub>3</sub>. *Cement and Concrete Research*, 20(2), 301–307. doi:10.1016/0008-8846(90)90084-b.
- Bois, A.-P., Vu, M.-H., Ghabezloo, S., Sulem, J., Garnier, A., & Laudet, J.-B. (2013). Cement Sheath Integrity for CO<sub>2</sub> Storage – An Integrated Perspective. *Energy Procedia*, 37, 5628–5641. doi:10.1016/j.egypro.2013.06.485.

- Bourgoyne Jr., A. T., Millheim, K. K., Chenevert, M. E., & Young Jr., F. S. (1986). *Applied Drilling Engineering*, Volume 2. Texas: SPE Richardson.
- Brandl, A., Cutler, J., Seholm, A., Sansil, M., & Braun, G. (2011). Cementing Solutions for Corrosive Well Environments. *SPE Drilling & Completion*, 26(02), 208–219. doi:10.2118/132228-pa.
- Bresson B., Meducin, F., & Zanni, H. (2002). Hydration of Tricalcium Silicates (C<sub>3</sub>S) at High Temperature and High Pressure. *Journal of Materials Science*, 37(24), 5355-5365.
- Bruckdorfer, R. A. (1986). Carbon Dioxide Corrosion in Oilwell Cements. Proceedings of SPE Rocky Mountain Regional Meeting. doi:10.2523/15176-ms.
- Bureau of Ocean Energy Management, Regulation and Enforcement (BOEMRE), Washington, D. C. (2011). Report Regarding the Causes of the April 20, 2010 Macondo Well Blowout. Retrieved from, [http://www.bsee.gov/uploadedfiles/bsee/bsee\\_newsroom/publications\\_library/ocs\\_archives/deepwaterhorizon/boemre%20final%20dwh%20sept2011.pdf](http://www.bsee.gov/uploadedfiles/bsee/bsee_newsroom/publications_library/ocs_archives/deepwaterhorizon/boemre%20final%20dwh%20sept2011.pdf).
- Calvert, D. J., & Smith, D. K. (1990). API Oilwell Cementing Practices. Proceedings of Offshore Technology Conference. doi:10.4043/6210-ms.
- Cao, H. T., Bucea, L., Ray, A., & Yozghatlian, S. (1997). The Effect of Cement Composition and pH of Environment on Sulfate Resistance of Portland Cements and Blended Cements. *Cement and Concrete Composites*, 19(2), 161–171. doi:10.1016/s0958-9465(97)00011-5.
- Carde, C., François, R., & Torrenti, J.-M. (1996). Leaching of both Calcium Hydroxide and C-S-H from Cement Paste: Modeling the Mechanical Behavior. *Cement and Concrete Research*, 26(8), 1257–1268. doi:10.1016/0008-8846(96)00095-6.
- Carde, C., & François, R. (1997). Effect of the Leaching of Calcium Hydroxide from Cement Paste on Mechanical and Physical Properties. *Cement and Concrete Research*, 27(4), 539–550. doi:10.1016/s0008-8846(97)00042-2.
- Carde, C., & François, R. (1999). Modelling the Loss of Strength and Porosity Increase due to the Leaching of Cement Pastes. *Cement and Concrete Composites*, 21(3), 181–188. doi:10.1016/s0958-9465(98)00046-8.
- Carey, J. W., Wigand, M., Chipera, S. J., WoldeGabriel, G., Pawar, R., Lichtner, P. C., Wehner, S. C., Raines, M. A., Guthrie, G. D. (2007). Analysis and Performance of Oil Well Cement with 30 Years of CO<sub>2</sub> Exposure from the SACROC Unit, West Texas, USA. *International Journal of Greenhouse Gas Control*, 1(1), 75–85. doi:10.1016/s1750-5836(06)00004-1.

- Carter, L. G., Waggoner, H. F., & George, C. (1966). Expanding Cements for Primary Cementing. *Journal of Petroleum Technology*, 18(05), 551–558. doi:10.2118/1235-pa.
- Cervera, M., Faria, R., Oliver, J., & Prato, T. (2002). Numerical Modelling of Concrete Curing, Regarding Hydration and Temperature Phenomena. *Computers & Structures*, 80(18-19), 1511–1521. doi:10.1016/s0045-7949(02)00104-9.
- Cervera, M., Oliver, J., & Prato, T. (1999). Thermo-Chemo-Mechanical Model for Concrete. I: Hydration and Aging. *Journal of Engineering Mechanics*, 125(9), 1018–1027. doi:10.1061/(asce)0733-9399(1999)125:9(1018).
- Ceyhan, I., Santra, A. K., & Cullick, A. S. (2011). Carbon Dioxide, Geochemical, and Rate-of-Dissolution Simulation for Deep Storage Environments. *Proceedings of SPE International Symposium on Oilfield Chemistry*. doi:10.2118/141031-ms.
- Chenevert, M. E., & Shrestha, B. K. (1991). Chemical Shrinkage Properties of Oilfield Cements (includes associated paper 23477). *SPE Drilling Engineering*, 6(01), 37–43. doi:10.2118/16654-pa.
- Churakov, S. V. (2009). Structural position of H<sub>2</sub>O molecules and hydrogen bonding in anomalous 11Å tobermorite. *American Mineralogist*, 94(1), 156–165. doi:10.2138/am.2009.2907.
- Clodic, L., and Meike, A. (1997). Thermodynamics of Calcium Silicate Hydrates. Development of a Database to Model Concrete Dissolution at 25°C using the EQ3/6 Geochemical Modeling Code. DOE Contract No. W-7405-Eng-48, UCRL-ID-132088 (August 18, 1997). doi:10.2172/2896.
- Condor, J., & Asghari, K. (2009). Experimental Study of Stability and Integrity of Cement in Wellbores Used for CO<sub>2</sub> Storage. *Energy Procedia*, 1(1), 3633–3640. doi:10.1016/j.egypro.2009.02.159.
- Crank, J. (1975). *The Mathematics of Diffusion*, Second Edition. Oxford: Clarendon Press.
- Craft, B. C., Johnson, T. J., & Kirkpatrick, H. L. (1935). Effects of Temperature, Pressure and Water-cement Ratio on the Setting Time and Strength of Cement. *Transactions of the AIME*, 114(01), 62–68. doi:10.2118/935062-g.
- Dabić, P., Krstulović, R., Rušić, D., 2000. A New Approach in Mathematical Modeling of Cement Hydration Development. *Cement and Concrete Research*, 30(7), 1017–1021. doi:10.1016/s0008-8846(00)00293-3.



- Danielson, U. (1962). Heat of Hydration of Cement as affected by Water–Cement Ratio. Proceedings of the 4th International Symposium on the Chemistry of Cement, Washington DC, USA, 1962, Paper IV-S7, 519–526.
- Development of Geothermal Well Completion Systems Final Report (1980). DOE Contract No. EG-77 -C02-4190, COO/4190-9.
- Deschner, F., Lothenbach, B., Winnefeld, F., & Neubauer, J. (2013). Effect of Temperature on the Hydration of Portland Cement Blended with Siliceous Fly Ash. *Cement and Concrete Research*, 52, 169–181. doi:10.1016/j.cemconres.2013.07.006.
- Deshpande, A., Chiney, A., Patil, S., Paiva, M. D. M., Ravi, K., Aiex, C., & Campos, G. (2015). Long-Term Study of Effects of CO<sub>2</sub> Exposure on Cement Integrity under Downhole Conditions. Proceedings of EUROPEC 2015. doi:10.2118/174329-ms.
- Duguid, A. (2008). The Effect of Carbonic Acid on Well Cements as Identified Through Lab and Field Studies. SPE Eastern Regional/AAPG Eastern Section Joint Meeting. doi:10.2118/119504-ms.
- Duguid, A. (2009). An Estimate of the Time to Degrade the Cement Sheath in a Well Exposed to Carbonated Brine. *Energy Procedia*, 1(1), 3181–3188. doi:10.1016/j.egypro.2009.02.101.
- Eiken, O., Ringrose, P., Hermanrud, C., Nazarian, B., Torp, T. A., & Høier, L. (2011). Lessons learned from 14 years of CCS operations: Sleipner, In Salah and Snøhvit. *Energy Procedia*, 4, 5541–5548. doi:10.1016/j.egypro.2011.02.541.
- Eilers, L. H., Nelson, E. B., & Moran, L. K. (1983). High-Temperature Cement Compositions - Pectolite, Scawtite, Truscottite, or Xonotlite: Which Do You Want? *Journal of Petroleum Technology*, 35(07), 1373–1377. doi:10.2118/9286-pa.
- Fabbri, A., Jacquemet, N., & Seyedi, D. M. (2012). A Chemo-Poromechanical Model of Oilwell Cement Carbonation under CO<sub>2</sub> Geological Storage Conditions. *Cement and Concrete Research*, 42(1), 8–19. doi:10.1016/j.cemconres.2011.07.002.
- Foster, A., Pollema, A., Petitt, I. H., Heathman, J. F., Johnson, C. R., & Schlepers, R. (2011). Contemporary Approach Coupled with Traditional Techniques Tackle Extreme Wellbore Environment in Schoonebeek Heavy Oil Field. Proceedings of SPE Heavy Oil Conference and Exhibition. doi:10.2118/150022-ms.
- Frech, R., Wang, E. C., & Bates, J. B. (1980). The I.R. and Raman Spectra of CaCO<sub>3</sub> (Aragonite). *Spectrochimica Acta Part A: Molecular Spectroscopy*, 36(10), 915–919. doi:10.1016/0584-8539(80)80044-4.

- Frittella, F., Babbo, M., & Muffo, A. I. (2009). Best Practices and Lesson Learned from 15 Years of Experience of Cementing HPHT Wells in Italy. Proceedings of Middle East Drilling Technology Conference & Exhibition. doi:10.2118/125175-ms.
- Gallus, J. P., Watters, L. T., & Pyle, D. E. (1979). Performance of Oilwell Cementing Compositions in Geothermal Wells. Society of Petroleum Engineers Journal, 19(04), 233–241. doi:10.2118/7591-pa.
- Garnier, A., Laudet, J. B., Patil, S., Patil, R., Ravi, K., & Ferreira, L. (2012). Effect of Acid Gas on Cement Sheath Integrity: Experimental Findings. Proceedings of SPE Saudi Arabia Section Technical Symposium and Exhibition. doi:10.2118/160890-ms.
- Gérard, B., Le Bellego, C., & Bernard, O. (2002). Simplified modelling of calcium leaching of concrete in various environments. Materials and Structures, 35(10), 632–640. doi:10.1007/bf02480356.
- Ghabezloo, S., Sulem, J., & Saint-Marc, J. (2009). Evaluation of a Permeability-Porosity Relationship in a Low Permeability Creeping Material Using a Single Transient Test. International Journal of Rock Mechanics and Mining Sciences, 46(4), 761–768. doi:10.1016/j.ijrmms.2008.10.003.
- Ghabezloo, S. (2011). Effect of the Variations of Clinker Composition on the Poroelastic Properties of Hardened Class G Cement Paste. Cement and Concrete Research, 41(8), 920–922. doi:10.1016/j.cemconres.2011.03.022.
- Glasser, F. P. (1973). The Formation and thermal Stability of Spurrite,  $\text{Ca}_5(\text{SiO}_4)_2\text{CO}_3$ . Cement and Concrete Research, 3(1), 23–28. doi:10.1016/0008-8846(73)90058-6.
- Glasser, F. P., Marchand, J., & Samson, E. (2008). Durability of Concrete-Degradation Phenomena Involving Detrimental Chemical Reactions. Cement and Concrete Research, 38(2), 226–246. doi:10.1016/j.cemconres.2007.09.015.
- Ghofrani, R., & Plack, H. (1993). CaO- and/or MgO-Swelling Cements: A Key for Providing a Better Annular Sealing? Proceedings of SPE/IADC Drilling Conference. doi:10.2523/25697-ms.
- Gunasekaran, S., Anbalagan, G., & Pandi, S. (2006). Raman and Infrared Spectra of Carbonates of Calcite Structure. Journal of Raman Spectroscopy, 37(9), 892–899. doi:10.1002/jrs.1518.
- Hara, N., Chan, C. F., & Mitsuda, T. (1978). Formation of 14 Å Tobermorite. Cement and Concrete Research, 8(1), 113–115. doi:10.1016/0008-8846(78)90064-9.

- Haga, K., Sutou, S., Hironaga, M., Tanaka, S., & Nagasaki, S. (2005). Effects of Porosity on Leaching of Ca from Hardened Ordinary Portland Cement Paste. *Cement and Concrete Research*, 35(9), 1764–1775. doi:10.1016/j.cemconres.2004.06.034.
- Heinold, T., Dillenbeck, R., & Rogers, M. (2002). The Effect of Key Cement Additives on the Mechanical Properties of Normal Density Oil and Gas Well Cement Systems. *Proceedings of SPE Asia Pacific Oil and Gas Conference and Exhibition*. doi:10.2523/77867-ms.
- Henmi, C. (1992). Clinotobermorite,  $\text{Ca}_5\text{Si}_6(\text{O},\text{OH})_{18}\cdot 5\text{H}_2\text{O}$ , a New Mineral from Fuka, Okayama Prefecture, Japan. *Mineralogical Magazine*, 56(384), 353–358. doi:10.1180/minmag.1992.056.384.07
- Hewlett, P.C. (2004). *Lea's Chemistry of Cement and Concrete*, Fourth edition. Oxford: Elsevier Science.
- Holt, E. (2005). Contribution of mixture design to chemical and autogenous shrinkage of concrete at early ages. *Cement and Concrete Research*, 35(3), 464–472. doi:10.1016/j.cemconres.2004.05.009.
- Horkoss, S., Lteif, R., & Rizk, T. (2011). Influence of the Clinker  $\text{SO}_3$  on the Cement Characteristics. *Cement and Concrete Research*, 41(8), 913–919. doi:10.1016/j.cemconres.2011.04.015.
- Huerta, N. J., Bryant, S. L., Strazisar, B. R., Kutchko, B. G., & Conrad, L. C. (2009). The Influence of Confining Stress and Chemical Alteration on Conductive Pathways within Wellbore Cement. *Energy Procedia*, 1(1), 3571–3578. doi:10.1016/j.egypro.2009.02.151.
- Ilesanmi, O. R., Hilal, B., Gill, S., Brandl, A. (2013). Long-term Wellbore Isolation in a Corrosive Environment. *Proceedings of SPE/IADC Middle East Drilling Technology Conference & Exhibition*. doi:10.2118/166769-ms.
- James, S. G., & Boukhelifa, L. (2008). Zonal Isolation Modeling and Measurements - Past Myths and Today Realities. *SPE Drilling & Completion*, 23(01), 68–75. doi:10.2118/101310-pa.
- Justnes, H., van Loo, D., Reyniers, B., Skalle, P., Sveen, J., & Sellevold, E. J. (1995). Chemical shrinkage of oil well cement slurries. *Advances in Cement Research*, 7(26), 85–90. doi:10.1680/adcr.1995.7.26.85.
- Krilov, Z., Loncaric, B., & Miksa, Z. (2000). Investigation of a Long-Term Cement Deterioration Under a High-Temperature, Sour Gas Downhole Environment. *Proceedings of SPE International Symposium on Formation Damage Control*. doi:10.2523/58771-ms.

- Kulik, D. A., & Kersten, M. (2001). Aqueous Solubility Diagrams for Cementitious Waste Stabilization Systems: II, End-Member Stoichiometries of Ideal Calcium Silicate Hydrate Solid Solutions. *Journal of the American Ceramic Society*, 84(12), 3017–3026. doi:10.1111/j.1151-2916.2001.tb01130.x.
- Kulik, D. A. (2011). Improving the Structural Consistency of C-S-H Solid Solution Thermodynamic Models. *Cement and Concrete Research*, 41(5), 477–495. doi:10.1016/j.cemconres.2011.01.012.
- Kutchko, B. G., Strazisar, B. R., Dzombak, D. A., Lowry, G. V., & Thaulow, N. (2007). Degradation of Well Cement by CO<sub>2</sub> under Geologic Sequestration Conditions. *Environ. Sci. Technol.*, 41(13), 4787–4792. doi:10.1021/es062828c.
- Kutchko, B. G., Strazisar, B. R., Lowry, G. V., Dzombak, D. A., & Thaulow, N. (2008). Rate of CO<sub>2</sub> Attack on Hydrated Class H Well Cement under Geologic Sequestration Conditions. *Environ. Sci. Technol.*, 42(16), 6237–6242. doi:10.1021/es800049r.
- Kutchko, B. G., Strazisar, B. R., Hawthorne, S. B., Lopano, C. L., Miller, D. J., Hakala, J. A., & Guthrie, G. D. (2011). H<sub>2</sub>S–CO<sub>2</sub> Reaction with Hydrated Class H Well Cement: Acid-gas Injection and CO<sub>2</sub> Co-Sequestration. *International Journal of Greenhouse Gas Control*, 5(4), 880–888. doi:10.1016/j.ijggc.2011.02.008.
- Laudet, J.-B., Garnier, A., Neuville, N., Le Guen, Y., Fourmaintraux, D., Rafai, N., Burlion, N., Shao, J.-F. (2011). The Behavior of Oil Well Cement at Downhole CO<sub>2</sub> Storage Conditions: Static and Dynamic Laboratory Experiments. *Energy Procedia*, 4, 5251–5258. doi:10.1016/j.egypro.2011.02.504.
- Lécolier, E., Rivereau, A., Le Saoût, G., & Audibert-Hayet, A. (2007). Durability of Hardened Portland Cement Paste used for Oilwell Cementing. *Oil & Gas Science and Technology - Revue de l'IFP*, 62(3), 335–345. doi:10.2516/ogst:2007028.
- Lécolier, E., Ferrer, N., Lamy, F., et al. 2008. Behavior of Permeable Steel/Cement Interface in Contact with CO<sub>2</sub> - Saturated brine. GHGT-9, Washington.
- Lehr, D. J., & Collins, S. (2015). The High-Pressure/High-Temperature Completion Landscape-Yesterday, Today, and Tomorrow. *SPE Drilling & Completion*, 30(03), 187–197. doi:10.2118/170919-pa.
- Lerch, W., Ford, C. L., 1948. The Long-Term Study of Cement Performance in Concrete: Chapter 3. Chemical and Physical Tests of the Cements. *ACI Journal* 19(8): 745-795.
- Le Saoût, G., Lécolier, É., Rivereau, A., & Zanni, H. (2004). Study of Oilwell Cements by Solid-state NMR. *Comptes Rendus Chimie*, 7(3-4), 383–388. doi:10.1016/j.crci.2003.10.018.

- Le Saoût, G., Lécolier, E., Rivereau, A., & Zanni, H. (2005). Micropore Size Analysis in Oil Well Cement by Proton Nuclear Relaxation. *Magnetic Resonance Imaging*, 23(2), 371–373. doi:10.1016/j.mri.2004.11.052.
- Le Saout, G., Lécolier, E., Rivereau, A., & Zanni, H. (2006a). Chemical Structure of Cement Aged at Normal and Elevated Temperatures and Pressures, Part I: Class G Oilwell Cement. *Cement and Concrete Research*, 36(1), 71–78. doi:10.1016/j.cemconres.2004.09.018.
- Le Saoût, G., Lécolier, E., Rivereau, A., & Zanni, H. (2006b). Chemical Structure of Cement Aged at Normal and Elevated Temperatures and Pressures, Part II: Low Permeability Class G Oilwell Cement. *Cement and Concrete Research*, 36(3), 428–433. doi:10.1016/j.cemconres.2005.11.005.
- Lesti, M., Tiemeyer, C., & Plank, J. (2013). CO<sub>2</sub> Stability of Portland Cement Based Well Cementing Systems for Use on Carbon Capture & Storage (CCS) Wells. *Cement and Concrete Research*, 45, 45–54. doi:10.1016/j.cemconres.2012.12.001.
- Lin, F., & Meyer, C. (2009). Hydration Kinetics Modeling of Portland Cement Considering the Effects of Curing Temperature and Applied Pressure. *Cement and Concrete Research*, 39(4), 255–265. doi:10.1016/j.cemconres.2009.01.014.
- Liteanu, E., Spiers, C. J., & Peach, C. J. (2009). Failure Behavior Wellbore Cement in the Presence of Water and Supercritical CO<sub>2</sub>. *Energy Procedia*, 1(1), 3553–3560. doi:10.1016/j.egypro.2009.02.149.
- Long Term Integrity of CO<sub>2</sub> Storage – Well Abandonment Technical Study Report. IEA Greenhouse Gas R&D Programme No. 2009 / 08 (November 2009).
- Lothenbach, B., Matschei, T., Möschner, G., & Glasser, F. P. (2008). Thermodynamic Modelling of the Effect of Temperature on the Hydration and Porosity of Portland Cement. *Cement and Concrete Research*, 38(1), 1–18. doi:10.1016/j.cemconres.2007.08.017.
- Maekawa, K., Ishida, T. and Kishi, T. (2009). *Multi-scale Modeling of Structural Concrete*. London and New York: Taylor and Francis Group.
- Maheshwari, H., 2014. Effects of CO<sub>2</sub> on Degradation of Oilwell Cement under HPHT Environment. MS Thesis, University of Oklahoma.
- Mainguy, M., & Coussy, O. (2000). Propagation Fronts during Calcium Leaching and Chloride Penetration. *Journal of Engineering Mechanics*, 126(3), 250–257. doi:10.1061/(asce)0733-9399(2000)126:3(250).

- Mainguy, M., Tognazzi, C., Torrenti, J.-M., & Adenot, F. (2000). Modelling of Leaching in Pure Cement Paste and Mortar. *Cement and Concrete Research*, 30(1), 83–90. doi:10.1016/s0008-8846(99)00208-2.
- Mason, H. E., Du Frane, W. L., Walsh, S. D. C., Dai, Z., Charnvanichborikarn, S., & Carroll, S. A. (2013). Chemical and Mechanical Properties of Wellbore Cement Altered by CO<sub>2</sub>-Rich Brine Using a Multianalytical Approach. *Environ. Sci. Technol.*, 47, 1745-1752. doi:10.1021/es3039906.
- Massachusetts Institute of Technology (MIT). 2015. Carbon Capture and Sequestration Project Database, <https://sequestration.mit.edu>, (accessed on 10/31/2015).
- Matsuda, Y., Tsukada, M. (1995). Identification of Calcium Carbonate Contained as Body in Modern Paints by FTIR Spectroscopy. *IRUG 2 Postprints*, 25-34.
- Matsushita, F., Aono, Y., & Shibata, S. (2004). Calcium silicate structure and carbonation shrinkage of a tobermorite-based material. *Cement and Concrete Research*, 34(7), 1251–1257. doi:10.1016/j.cemconres.2003.12.016.
- Matteo, E. N., & Scherer, G. W. (2012). Experimental Study of the Diffusion-Controlled Acid Degradation of Class H Portland Cement. *International Journal of Greenhouse Gas Control*, 7, 181–191. doi:10.1016/j.ijggc.2011.07.012.
- Méducin, F., Noïk, C., Rivereau, A., & Zanni, H. (2002). Complementary Analyses of a Tricalcium Silicate Sample Hydrated at High Pressure and Temperature. *Cement and Concrete Research*, 32(1), 65–70. doi:10.1016/s0008-8846(01)00630-5.
- Merlino, S., Bonaccorsi, E., & Armbruster, T. (2001). The Real Structure of Tobermorite 11Å: Normal and Anomalous Forms, OD Character and Polytypic Modifications. *Eur.j.mineral.*, 13(3), 577–590. doi:10.1127/0935-1221/2001/0013-0577.
- Milestone, N. B., Sugama, T., Kukacka, L. E., & Carciello, N. (1986). Carbonation of geothermal grouts — Part 1: CO<sub>2</sub> Attack at 150°C. *Cement and Concrete Research*, 16(6), 941–950. doi:10.1016/0008-8846(86)90018-9.
- Millero, F. J., Pierrot, D., Lee, K., Wanninkhof, R., Feely, R., Sabine, C. L., Key, R. M., Takahashi, T. (2002). Dissociation Constants for Carbonic Acid Determined from Field Measurements. *Deep Sea Research Part I: Oceanographic Research Papers*, 49(10), 1705–1723. doi:10.1016/s0967-0637(02)00093-6.
- Millero, F. J. (1983). The Estimation of the pK\*HA of Acids in Seawater Using the Pitzer Equations. *Geochimica et Cosmochimica Acta*, 47(12), 2121–2129. doi:10.1016/0016-7037(83)90037-6.

- Mirza, W. H., Al-Noury, S. I., & Al-Bedawi, W. H. (1991). Temperature Effect on Strength of Mortars and Concrete Containing Blended Cements. *Cement and Concrete Composites*, 13(3), 197–202. doi:10.1016/0958-9465(91)90020-i.
- Møller, N. (1988). The Prediction of Mineral Solubilities in Natural Waters: A Chemical Equilibrium Model for the Na-Ca-Cl-SO<sub>4</sub>-H<sub>2</sub>O system, to High Temperature and Concentration. *Geochimica et Cosmochimica Acta*, 52(4), 821–837. doi:10.1016/0016-7037(88)90354-7.
- Moran, L. K., Murray, T. R., & Moyer, W. R. (1991). Cement Expansion: A Laboratory Investigation. *Proceedings of SPE Production Operations Symposium*. doi:10.2523/21685-ms.
- Mulder, W. H., & Hassan, I. (2011). The Effect of Orientational Disorder of the Anion in Calcite on the Aragonite (Pmcn) ↔ Calcite (R3c) Equilibrium. *The Canadian Mineralogist*, 49(4), 1035–1043. doi:10.3749/canmin.49.4.1035.
- Nakarai, K., Ishida, T., & Maekawa, K. (2006). Modeling of Calcium Leaching from Cement Hydrates Coupled with Micro-Pore Formation. *ACT*, 4(3), 395–407. doi:10.3151/jact.4.395.
- National Energy Technology Laboratory. 2015. NETL's Carbon Capture and Storage Database – Version 5 (May 2015 revision). Retrieved from <http://www.netl.doe.gov/research/coal/carbon-storage/strategic-program-support/database> (accessed 27 April 2016).
- Nelson, E. B. (1979). Development of Geothermal Well Completion Systems. Final Report. doi:10.2172/5987961.
- Nelson, E. B., Eilers, L. H., & Kalousek, G. L. (1981). Formation and Behavior of Calcium Silicate Hydrates in a Geothermal Environment. *Cement and Concrete Research*, 11(3), 371–381. doi:10.1016/0008-8846(81)90109-5.
- Nelson, E. B., & Eilers, L. H. (1985). Cementing Steamflood and Fireflood Wells-Slurry Design. *Journal of Canadian Petroleum Technology*, 24(05). doi:10.2118/85-05-06.
- Nelson, E. B. (1990). *Well Cementing*. Sugar Land, Texas: Schlumberger Educational Services.
- Neuville, N., Aouad, G., Lecolier, E., & Damidot, D. (2012). Innovative Leaching Tests of an Oilwell Cement Paste for CO<sub>2</sub> Storage: Effect of the Pressure at 80°C. *Energy Procedia*, 23, 472–479. doi:10.1016/j.egypro.2012.06.065.

- Newell, D. L., & Carey, J. W. (2013). Experimental Evaluation of Wellbore Integrity Along the Cement-rock Boundary. *Environ. Sci. Technol.*, 47(1), 276–282. doi:10.1021/es3011404.
- Noik, C., & Rivereau, A. (1999). Oilwell Cement Durability. Proceedings of SPE Annual Technical Conference and Exhibition. doi:10.2118/56538-ms.
- Omoisebi, O., Maheshwari, H., Ahmed, R., Shah, S., Osisanya, S., Santra, A., & Saasen, A. (2015a). Investigating Temperature Effect on Degradation of Well Cement in HPHT Carbonic Acid Environment. *Journal of Natural Gas Science and Engineering*, 26, 1344–1362. doi:10.1016/j.jngse.2015.08.018.
- Omoisebi, O., Ahmed, R., Shah, S., & Osisanya, S. (2015b). Mechanical Integrity of Well Cement Under Geologic Carbon Sequestration Conditions. Proceedings of Carbon Management Technology Conference. doi:10.7122/439562-ms.
- Pang, X., Meyer, C., Funkhouser, G. P., & Darbe, R. (2015). Depressurization Damage of Oil Well Cement Cured for 3days at Various Pressures. *Construction and Building Materials*, 74, 268–277. doi:10.1016/j.conbuildmat.2014.07.022.
- Parcevaux, P. A., & Sault, P. H. (1984). Cement Shrinkage and Elasticity: A New Approach for a Good Zonal Isolation. Proceedings of SPE Annual Technical Conference and Exhibition. doi:10.2523/13176-ms.
- Pitzer, K. S. (1973). Thermodynamics of Electrolytes. I. Theoretical Basis and General Equations. *J. Phys. Chem.*, 77(2), 268–277. doi:10.1021/j100621a026.
- Pitzer, K. S. (1975). Thermodynamics of Electrolytes. V. Effects of Higher-Order Electrostatic Terms. *J Solution Chem*, 4(3), 249–265. doi:10.1007/bf00646562.
- Powers, T. C. (1958). *The Physical Structure and Engineering Properties of Concrete*. PCA Research & Development Laboratories, Bulletin 90, Chicago.
- Rahmani, K., Shamsai, A., Saghafian, B., & Peroti, S. (2012). Effect of Water and Cement Ratio on Compressive Strength and Abrasion of Microsilica Concrete. *Middle-East Journal of Scientific Research*, 12(8), 1056-1061.
- Raouf, A., Nick, H. M., Wolterbeek, T. K. T., & Spiers, C. J. (2012). Pore-scale Modeling of Reactive Transport in Wellbore Cement under CO<sub>2</sub> Storage Conditions. *International Journal of Greenhouse Gas Control*, 11, S67–S77. doi:10.1016/j.ijggc.2012.09.012.
- Ravi, K., Biezen, E., Lightford, S., Hibbert, A., & Greaves, C. (1999). Deepwater Cementing Challenges. Proceedings of SPE Annual Technical Conference and Exhibition. doi:10.2523/56534-ms.



- Reardon, E. J. (1992). Problems and Approaches to the Prediction of the Chemical Composition in Cement/Water Systems. *Waste Management*, 12(2-3), 221–239. doi:10.1016/0956-053x(92)90050-s.
- Reddy, B. R., Xu, Y., Ravi, K., Gray, D. W., & Pattillo, P. (2009). Cement Shrinkage Measurement in Oilwell Cementing--A Comparative Study of Laboratory Methods and Procedures. *SPE Drilling & Completion*, 24(01), 104–114. doi:10.2118/103610-pa.
- Richardson, I. G. (2008). The Calcium Silicate Hydrates. *Cement and Concrete Research*, 38(2), 137–158. doi:10.1016/j.cemconres.2007.11.005.
- Ringrose, P., Eiken, O. (2011). Sleipner and Snøhvit Projects. CSLF Interactive Workshop, Saudi Arabia, 01–02 March 2011, Carbon Sequestration Leadership Forum.
- Root, R. L., & Calvert, D. G. (1971). The Real Story of Cement Expansion. *Proceedings of SPE Rocky Mountain Regional Meeting*. doi:10.2523/3346-ms.
- Rubiandini R.S., (2000). New Additive for Improving Shearbond Strength in High Temperature and Pressure Cement. *Proceedings of IADC/SPE Asia Pacific Drilling Technology*. doi:10.2118/62750-ms.
- Rutt, H. N., & Nicola, J. H. (1974). Raman Spectra of Carbonates of Calcite Structure. *Journal of Physics C: Solid State Physics*, 7(24), 4522–4528. doi:10.1088/0022-3719/7/24/015.
- Sahmaran, M., Kasap, O., Duru, K., & Yaman, I. O. (2007). Effects of Mix Composition and Water–Cement Ratio on the Sulfate Resistance of Blended Cements. *Cement and Concrete Composites*, 29(3), 159–167. doi:10.1016/j.cemconcomp.2006.11.007.
- Salim, P., Amani, M. (2013). Special Considerations in Cementing High Pressure High Temperature Wells. *International Journal of Engineering and Applied Sciences*, 1(4), 120-143.
- Santra, A., Reddy, B. R., Liang, F., et al. 2009. Reaction of CO<sub>2</sub> with Portland Cement at Downhole Conditions and the Role of Pozzolanic Supplements. Paper SPE 121103 presented at the SPE International Symposium on Oilfield Chemistry, The Woodlands, Texas, 20 – 22 April.
- Santra, A. K., Reddy, B. R., Liang, F., & Fitzgerald, R. (2009). Reaction of CO<sub>2</sub> with Portland Cement at Downhole Conditions and the Role of Pozzolanic Supplements. *Proceedings of SPE International Symposium on Oilfield Chemistry*. doi:10.2118/121103-ms.

- Sauki, A. B. and Irawan, S. (2010). Effects of Pressure and Temperature on Well Cement Degradation by Supercritical CO<sub>2</sub>. *International Journal of Engineering & Technology IJET-IJENS* 10 (4): 53 – 61.
- Saunders, C. D., & Walker, W. A. (1954). Strength of Oil Well Cements and Additives Under High Temperature Well Conditions. *Proceedings of Fall Meeting of the Petroleum Branch of AIME*. doi:10.2118/390-g.
- Scherer, G. W., Kutcho, B., Thaulow, N., Duguid, A., & Mook, B. (2011). Characterization of Cement from a Well at Teapot Dome Oil Field: Implications for Geological Sequestration. *International Journal of Greenhouse Gas Control*, 5(1), 115–124. doi:10.1016/j.ijggc.2010.06.010.
- Scherer, G. W., & Huet, B. (2009). Carbonation of Wellbore Cement by CO<sub>2</sub> Diffusion from Caprock. *International Journal of Greenhouse Gas Control*, 3(6), 731–735. doi:10.1016/j.ijggc.2009.08.002.
- Shado, Y., and Joel, O. (2011). Challenges and Remedy for Cementing of HPHT Wells in Nigerian Operation. *Proceedings of Nigeria Annual International Conference and Exhibition*. doi:10.2118/150751-ms.
- Shock, E. L., & Helgeson, H. C. (1988). Calculation of the Thermodynamic and Transport Properties of Aqueous Species at High Pressures and Temperatures: Correlation Algorithms for Ionic Species and Equation of State Predictions to 5 kb and 1000°C. *Geochimica et Cosmochimica Acta*, 52(8), 2009–2036. doi:10.1016/0016-7037(88)90181-0.
- Shock, E. L., Helgeson, H. C., & Sverjensky, D. A. (1989). Calculation of the Thermodynamic and Transport Properties of Aqueous Species at High Pressures and Temperatures: Standard Partial Molal Properties of Inorganic Neutral Species. *Geochimica et Cosmochimica Acta*, 53(9), 2157–2183. doi:10.1016/0016-7037(89)90341-4.
- Shock, E. L., Oelkers, E. H., Johnson, J. W., Sverjensky, D. A., & Helgeson, H. C. (1992). Calculation of the Thermodynamic Properties of Aqueous Species at High Pressures and Temperatures. Effective Electrostatic Radii, Dissociation Constants and Standard Partial Molal Properties to 1000 °C and 5 kbar. *J. Chem. Soc., Faraday Trans.*, 88(6), 803–826. doi:10.1039/ft9928800803.
- Sverjensky, D. A., Shock, E. L., & Helgeson, H. C. (1997). Prediction of the Thermodynamic Properties of Aqueous Metal Complexes to 1000°C and 5 kb. *Geochimica et Cosmochimica Acta*, 61(7), 1359–1412. doi:10.1016/s0016-7037(97)00009-4.
- Smith, D. K. (1991). *Worldwide Cementing Practices*, First Edition. American Petroleum Institute.

- Soler, J. M. 2007. Thermodynamic Description of the Solubility of C-S-H Gels in Hydrated Portland Cement: Literature Review. Working Report 88 (November 2007).
- Steefel, C. I. (1992). Coupled Fluid Flow and Chemical Reaction: Model Development and Application to Water-Rock Interaction. Ph.D. Dissertation, Yale University.
- Stiles, D. (2006). Effects of Long-Term Exposure to Ultrahigh Temperature on the Mechanical Parameters of Cement. Proceedings of IADC/SPE Drilling Conference. doi:10.2523/98896-ms.
- Sweatman, R. E., Santra, A. K., Kulakofsky, D. S., & Calvert, D. G. (2009). Effective Zonal Isolation for CO<sub>2</sub> Sequestration Wells. Proceedings of SPE International Conference on CO<sub>2</sub> Capture, Storage, and Utilization. doi:10.2118/126226-ms.
- Tarco, J. C., & Asghari, K. (2010). Experimental Study of Stability and Integrity of Cement in Wellbores Used for CO<sub>2</sub> Storage. *Journal of Canadian Petroleum Technology*, 49(10), 37–44. doi:10.2118/142004-pa.
- Taylor, H. F. W. (1964). *The Chemistry of Cements*. London: Academic Press.
- Taylor, H. F. W. 1997. *The Chemistry of Cements*, 2<sup>nd</sup> Edition. London: Thomas Telford Publishing.
- Teodoriu, C., Yuan, Z., Schubert, J., & Amani, M. (2012). Experimental Measurement of Mechanical Parameters of Class G Cement. Proceedings of SPE/EAGE European Unconventional Resources Conference and Exhibition. doi:10.2118/153007-ms.
- Teodoriu, C., Reinicke, K.M. and Fichter, C. et al. 2010. Investigations on of the Mechanical Properties of Class G Cement and their Effect on Well Integrity. *International Journal of Engineering and Applied Sciences*, 3(2), 1-7.
- Thomas, J. J., & Jennings, H. M. (2003). Changes in the Size of Pores During Shrinkage (or Expansion) of Cement Paste and Concrete. *Cement and Concrete Research*, 33(11), 1897–1900. doi:10.1016/s0008-8846(03)00167-4.
- United States Coast Guard (USCG), Washington, D. C. (2011). Report of Investigation into the Circumstances Surrounding the Explosion, Fire, Sinking and Loss of Eleven Crew Members Aboard The Mobile Offshore Drilling Unit Deepwater Horizon in The Gulf of Mexico April 20-22, 2010, Volume I, MISLE Activity Number: 3721503. Retrieved from [http://www.bsee.gov/uploadedFiles/BSEE/BSEE\\_Newsroom/Publications\\_Library/OCS\\_Archives/DeepwaterHorizon/2\\_DeepwaterHorizon\\_ROI\\_USCG\\_Volume%20I\\_20110707\\_redacted\\_final.pdf](http://www.bsee.gov/uploadedFiles/BSEE/BSEE_Newsroom/Publications_Library/OCS_Archives/DeepwaterHorizon/2_DeepwaterHorizon_ROI_USCG_Volume%20I_20110707_redacted_final.pdf) (accessed on 11/10/2015).

- Vagenas, N. V., Gatsouli, A. and Kontoyannis, C. G. (2003). Quantitative Analysis of Synthetic Calcium Carbonate Polymorphs Using FT-IR Spectroscopy. *Talanta*, 59(4), 831–836. doi:10.1016/s0039-9140(02)00638-0.
- Voigt, T., Shah, S. P. (2003). Nondestructive monitoring of setting and hardening of portland cement mortar with sonic methods. Northwestern University, Evanston, USA, 1-8.
- Xyla, A. G., & Koutsoukos, P. G. (1989). Quantitative Analysis of Calcium Carbonate Polymorphs by Infrared Spectroscopy. *J. Chem. Soc., Faraday Trans. 1*, 85(10), 3165. doi:10.1039/f19898503165.
- Ylmén, R., Jäglid, U., Steenari, B.-M., & Panas, I. (2009). Early Hydration and Setting of Portland Cement Monitored by IR, SEM and Vicat Techniques. *Cement and Concrete Research*, 39(5), 433–439. doi:10.1016/j.cemconres.2009.01.017.
- Ylmén, R., & Jäglid, U. (2013). Carbonation of Portland Cement Studied by Diffuse Reflection Fourier Transform Infrared Spectroscopy. *Int J Concr Struct Mater*, 7(2), 119–125. doi:10.1007/s40069-013-0039-y.
- Zaki, M. I., Knözinger, H., Tesche, B., & Mekhemer, G. A. H. (2006). Influence of Phosphonation and Phosphation on Surface Acid–Base and Morphological Properties of CaO as Investigated by in Situ FTIR Spectroscopy and Electron Microscopy. *Journal of Colloid and Interface Science*, 303(1), 9–17. doi:10.1016/j.jcis.2006.07.011.
- Zhang, Q., & Ye, G. (2012). Dehydration Kinetics of Portland Cement Paste at High Temperature. *Journal of Thermal Analysis and Calorimetry*, 110(1), 153–158. doi:10.1007/s10973-012-2303-9.
- Zhang, Y.-Q., Radha, A. V., & Navrotsky, A. (2013). Thermochemistry of Two Calcium Silicate Carbonate Minerals: Scawtite,  $\text{Ca}_7(\text{Si}_6\text{O}_{18})(\text{CO}_3)\cdot 2\text{H}_2\text{O}$ , and Spurrite,  $\text{Ca}_5(\text{SiO}_4)_2(\text{CO}_3)$ . *Geochimica et Cosmochimica Acta*, 115, 92–99. doi:10.1016/j.gca.2013.03.031.

## Appendix – Compressive Strength Model

Recall equation 5.88, the total axial force gives:

$$F_T = \int_{x_1}^{x_2} dF = \int_{x_1}^{x_2} \sigma_{c,x} 2\pi(r-x) dx$$

(i) Unexposed Sample

$$\sigma_T = \sigma_c, \quad 0 < x \leq r$$

Therefore,

$$F_T = \int_0^r \sigma_T dA = \int_0^r \sigma_c dA = \sigma_c \int_0^r 2\pi(r-x) dx$$

$$\frac{F_T}{\sigma_c} = 2\pi \left( r \int_0^r dx - \int_0^r x dx \right) = \pi r^2 = A$$

Where, A = cross sectional area of sample

Thus,

$$F_T = \sigma_c \pi r^2$$

(ii) Exposed Sample

The following relationships are defined:

$$R_p = \frac{\sigma_{c-p}}{\sigma_c}; \quad R_{cp} = \frac{\sigma_{c-cp}}{\sigma_c}; \quad R_p' = \frac{\sigma_{c-p}'}{\sigma_c}$$

$$\sigma_{c-p} = R_p \sigma_c; \quad \sigma_{c-cp} = R_{cp} \sigma_c; \quad \sigma_{c-p}' = R_p' \sigma_c$$

Case 1: Figure 5.3a

Zone 1: Ca (HCO<sub>3</sub>)<sub>2</sub> leached zone (amorphous and porous silica)

$$\sigma_{c,x} = \frac{\sigma_{c-p} - \sigma_{c-cp}}{x_l} x + \sigma_{c-cp}, \quad 0 < x \leq x_l$$

Therefore,

$$F_1 = \int_0^{x_l} \sigma_{c,x} dA = \int_0^{x_l} \left( \frac{\sigma_{c-p} - \sigma_{c-cp}}{x_l} x + \sigma_{c-cp} \right) 2\pi(r-x) dx$$

$$F_1 = \sigma_c \int_0^{x_l} \left( \frac{R_p - R_{cp}}{x_l} x + R_{cp} \right) 2\pi(r-x) dx$$

$$\frac{F_1}{\sigma_c} = \frac{\pi}{3x_l} \left\{ (R_p - R_{cp})(3rx_l^2 - 2x_l^3) + 3R_{cp}x_l(2rx_l - x_l^2) \right\}$$

Zone 2: Fully carbonated zone

$$\sigma_{c,x} = \frac{\sigma_{c-p} - \sigma_{c-p}}{x_c - x_l} x + \frac{\sigma_{c-p}x_c - \sigma_{c-p}x_l}{x_c - x_l}, \quad x_l < x \leq x_c$$

$$F_2 = \int_{x_l}^{x_c} \left( \frac{\sigma_{c-p} - \sigma_{c-p}}{x_c - x_l} x + \frac{\sigma_{c-p}x_c - \sigma_{c-p}x_l}{x_c - x_l} \right) 2\pi(r-x) dx$$

$$F_2 = \sigma_c \int_{x_l}^{x_c} \left( \frac{R_p' - R_p}{x_c - x_l} x + \frac{R_p'x_c - R_p'x_l}{x_c - x_l} \right) 2\pi(r-x) dx$$

$$\frac{F_2}{\sigma_c} = \frac{\pi}{3(x_c - x_l)} \left[ (R_p' - R_p) \left\{ 3r(x_c^2 - x_l^2) - 2(x_c^3 - x_l^3) \right\} + 3(R_p'x_c - R_p'x_l) \left\{ 2r(x_c - x_l) - (x_c^2 - x_l^2) \right\} \right]$$

Zone 3: Calcium-depleted zone

$$\sigma_{c,x} = \frac{\sigma_c - \sigma_{c-p}}{x_d - x_c} x + \frac{\sigma_{c-p}x_d - \sigma_c x_c}{x_d - x_c}, \quad x_c < x \leq x_d$$

$$F_3 = \int_{x_c}^{x_d} \left( \frac{\sigma_c - \sigma_{c-p}}{x_d - x_c} x + \frac{\sigma_{c-p}x_d - \sigma_c x_c}{x_d - x_c} \right) 2\pi(r-x) dx$$

$$F_3 = \sigma_c \int_{x_c}^{x_d} \left( \frac{1 - R_p'}{x_d - x_c} x + \frac{R_p'x_d - x_c}{x_d - x_c} \right) 2\pi(r-x) dx$$

$$\frac{F_3}{\sigma_c} = \frac{\pi}{3(x_d - x_c)} \left[ (1 - R_p') \left\{ 3r(x_d^2 - x_c^2) - 2(x_d^3 - x_c^3) \right\} + 3(R_p'x_d - x_c) \left\{ 2r(x_d - x_c) - (x_d^2 - x_c^2) \right\} \right]$$

Zone 4: Sound zone

$$\sigma_{c,x} = \sigma_c, \quad x_d < x \leq r$$

$$F_4 = \sigma_c \int_{x_d}^r 2\pi(r-x) dx$$

$$\frac{F_4}{\sigma_c} = \pi \left[ 2r(r-x_d) - (r^2 - x_d^2) \right]$$

Therefore,

$$F_d = \left( \frac{F_1}{\sigma_c} + \frac{F_2}{\sigma_c} + \frac{F_3}{\sigma_c} + \frac{F_4}{\sigma_c} \right) \sigma_c$$

Degraded ratio,

$$\frac{\Delta F}{F} = \frac{F_T - F_d}{F_T} = \frac{\sigma_c \pi r^2 - \left( \frac{F_1}{\sigma_c} + \frac{F_2}{\sigma_c} + \frac{F_3}{\sigma_c} + \frac{F_4}{\sigma_c} \right) \sigma_c}{\sigma_c \pi r^2} = 1 - \frac{1}{\pi r^2} \left( \frac{F_1}{\sigma_c} + \frac{F_2}{\sigma_c} + \frac{F_3}{\sigma_c} + \frac{F_4}{\sigma_c} \right)$$

Case 2: Figure 5.3b

Zone 1: Ca (HCO<sub>3</sub>)<sub>2</sub> leached zone + Fully-carbonated zone

$$\sigma_{c,x} = \frac{\sigma_{c-p} - \sigma_{c-cp}}{x_c^n} x^n + \sigma_{c-cp}, \quad 0 < x \leq x_c$$

Therefore,

$$F_1 = \int_0^{x_c} \sigma_{c,x} dA = \int_0^{x_c} \left( \frac{\sigma_{c-p} - \sigma_{c-cp}}{x_c^n} x^n + \sigma_{c-cp} \right) 2\pi(r-x) dx$$

$$F_1 = \sigma_c \int_0^{x_c} \left( \frac{R_p - R_{cp}}{x_c^n} x^n + R_{cp} \right) 2\pi(r-x) dx$$

$$\frac{F_1}{\sigma_c} = \frac{\pi}{3x_c} \left\{ (R_p - R_{cp}) \left( \frac{6r}{n+1} x_c^2 - \frac{6}{n+2} x_c^3 \right) + 3R_{cp} x_c (2rx_c - x_c^2) \right\}$$

Zone 2: Calcium-depleted zone

$$\sigma_{c,x} = \frac{\sigma_c - \sigma_{c-p}}{x_d - x_c} x + \frac{\sigma_{c-p} x_d - \sigma_c x_c}{x_d - x_c}, \quad x_c < x \leq x_d$$

$$F_2 = \int_{x_c}^{x_d} \left( \frac{\sigma_c - \sigma_{c-p}}{x_d - x_c} x + \frac{\sigma_{c-p} x_d - \sigma_c x_c}{x_d - x_c} \right) 2\pi (r - x) dx$$

$$F_2 = \sigma_c \int_{x_c}^{x_d} \left( \frac{1 - R_p}{x_d - x_c} x + \frac{R_p x_d - x_c}{x_d - x_c} \right) 2\pi (r - x) dx$$

$$\frac{F_2}{\sigma_c} = \frac{\pi}{3(x_d - x_c)} \left[ (1 - R_p) \{ 3r(x_d^2 - x_c^2) - 2(x_d^3 - x_c^3) \} + 3(R_p x_d - x_c) \{ 2r(x_d - x_c) - (x_d^2 - x_c^2) \} \right]$$

Zone 3: Sound zone

$$\sigma_{c,x} = \sigma_c, \quad x_d < x \leq r$$

$$F_3 = \sigma_c \int_{x_d}^r 2\pi (r - x) dx$$

$$\frac{F_3}{\sigma_c} = \pi \left[ 2r(r - x_d) - (r^2 - x_d^2) \right]$$

Therefore,

$$F_d = \left( \frac{F_1}{\sigma_c} + \frac{F_2}{\sigma_c} + \frac{F_3}{\sigma_c} \right) \sigma_c$$

Degraded ratio,

$$\frac{\Delta F}{F} = 1 - \frac{1}{\pi r^2} \left( \frac{F_1}{\sigma_c} + \frac{F_2}{\sigma_c} + \frac{F_3}{\sigma_c} \right)$$